The Dissertation Committee for Ripudaman Manchanda Certifies that this is the approved version of the following dissertation:

A General Poro-Elastic Model for Pad-Scale Fracturing of Horizontal Wells

Committee:

Mukul M. Sharma, Supervisor

Jon E. Olson

David Nicolas Espinoza

Mark W. McClure

Nicolas P. Roussel

A General Poro-Elastic Model for Pad-Scale Fracturing of Horizontal Wells

by

Ripudaman Manchanda, B.Tech.; M.S.E.

Dissertation

Presented to the Faculty of the Graduate School of

The University of Texas at Austin

in Partial Fulfillment

of the Requirements

for the Degree of

Doctor of Philosophy

The University of Texas at Austin

December 2015

Dedication

Dedicated to my loving family for the sacrifices, inspiration and encouragement.

Acknowledgements

I would like to express my sincere gratitude to my advisor, Dr. Mukul M. Sharma for his patience, guidance and support throughout the duration of my studies at UT Austin. Despite his extremely busy schedule, he was always able to make time for discussions focusing on my research. The ideas he shared and the suggestions he made over the course of this dissertation broadened my understanding of not only the topic of my research but also gave me a holistic understanding of the oil and gas industry. I would also like to thank my dissertation committee members who provided valuable advice to make this document more complete and made me think hard and learn more.

I am thankful to my friends and colleagues at the department for their support and encouragement during my stay in Austin. I have learnt a lot from them and they made the experience enjoyable. Jin Lee deserves a special mention for providing invaluable support during the course of these studies and for always being there to listen to any problems the students may have thus facilitating success. The FROGG team has been crucial to the success of this work. I would specially like to thank Dr. Philip Cardiff and Eric C. Bryant, for guiding all the members of the team during this collaborative effort. Acknowledgements are also due to the Texas Advanced Computing Center for providing high-performance computing resource for this research.

I have been blessed to have some of the best friends one could hope for. Their friendship has kept me sane and level-headed during the turbulent periods of this journey. Majority of this credit goes to Sheena Patel. Her spirit, love, care, patience and forgiveness have inspired me to aim higher and achieve more. Her constant encouragement helped in achieving all the targets in this work successfully. Thank you Sheena.

Ever since I was a kid, there has been one person who has been a pillar of support and motivation for me – Dr. Harpreet Gulati. He has been the guiding light in my path thus far and I hope I can be an inspiration to others like he has been to me.

Finally, I would like to thank my grandparents, my parents and my brother for their unconditional love, support and encouragement.

A General Poro-Elastic Model for Pad-Scale Fracturing of Horizontal Wells

Ripudaman Manchanda, Ph.D.

The University of Texas at Austin, 2015

Supervisor: Mukul M. Sharma

Economic production of oil and gas from tight rocks requires horizontal well drilling with multiple hydraulic fractures along the length of the horizontal wells. Multiple horizontal wells are drilled and fractured close to each other to increase the recovery of oil and gas from a single location or pad. Interference between fractures in a horizontal well pad is commonly observed in the field. There is no clear understanding of the impact of various operational and reservoir parameters on the observed interference. This inter-well interference can occur through the creation of complex fracture networks and/or poro-elastic stress changes.

In this research, the development of a poro-elastic numerical simulator was undertaken to evaluate hydraulic fracturing practices in pad-scale scenarios. The primary motivation was to assess the impact of various operational parameters such as fracture spacing, well spacing and fracture sequencing on the geometry of the created fractures.

Two approaches were used to understand the problem at hand. In the first approach, static fractures were simulated in 3-D and the impact of their stress shadow on subsequent fractures was studied. It was observed that fracture spacing, injection volume, and time between successive fractures were the most important parameters that could be

used to optimize the creation of fractures in a well. Formation properties such as Young's modulus and horizontal stress contrast modified the magnitude and spatial extent of the stress shadow and the extent of stress reorientation. It was shown that stage spacing, well spacing and fracture sequencing together with fracture designs (volume of sand pumped and fluids used) can be adjusted to obtain non-intersecting, transverse fractures that efficiently drain the reservoir. A hypothesis, time dependent closure of induced unpropped fractures, was presented to explain why zipper fracturing often outperforms conventional sequential fracturing. The hypothesis was tested and confirmed with a field data set made available to us by Shell from the Eagle Ford shale.

In the second approach, a novel finite volume based 3-D, geomechanical, field-scale numerical simulator was developed to simulate propagation of multiple fractures simultaneously in a poro-elastic reservoir. This provided a more realistic model of the pad-scale fracturing process. The ability of the model to perform realistic pad-scale simulations was demonstrated for a variety of field situations such as multi-cluster multi-stage fracturing, infill-well fracturing, re-fracturing, mini-frac analysis and fracture network simulations. The inclusion of poro-elastic effects and reservoir heterogeneity in the model allowed us to examine the effects of reservoir depletion on fracture geometry in refraced and infill wells.

Table of Contents

List of Tables

List of Figures

Chapter 1: Introduction

Horizontal completions are extremely important for the effective drainage of shale reservoirs. Pad scale development of unconventional oil and gas reservoirs is gaining importance. The decisions taken to improve production performance in such environments are not always guided by engineering processes that tie production performance to completion designs. Economics and lease-holding are the main drivers for deciding on well locations, timing and other aspects of strategic planning. Once these have been decided, the design of the fracturing treatment and the location and spacing of the wells must be done on the basis of field experience and sound engineering principles. Operators have tried various strategies based on historical data from their respective plays. Very few comprehensive analyses including the geo-mechanics of the hydraulic fracturing process and the depletion process have been discussed in the literature.

In this dissertation we attempt to understand the science governing the performance of hydraulic fractures in such unconventional oil and gas reservoirs.

1.1 Overview of Tight Oil and Gas Reservoirs

Figure 1.1 shows the location of the unconventional reservoirs driving the growth of oil and gas production in the U.S. The growth in production from these reservoirs has reduced the net energy import and has helped in meeting the rising levels of oil and gas consumption in the U.S. (Figure 1.2). However, recovering oil and gas from these reservoirs is difficult and capital intensive. Hydraulic fracturing of these reservoirs is a necessity to be able to economically produce hydrocarbons. The thin pay-zones as well as more efficient recovery make horizontal well hydraulic fracturing to be the most viable option to stimulate these highly impermeable reservoirs (King 2010).

Several such reservoirs are present all over the U.S. (Figure 1.1). However lessons learnt from one reservoir are not directly applicable to each of the other reservoirs (King 2010). There are marked differences in the geology, in situ stresses, pore pressure, depths and several other important features. These differences have a common denominator in the science that can describe the occurrences. This science is predominantly geo-mechanics.

Geo-mechanics provides the governing physics that helps in deciding the: -

- Drilling direction
- Hydraulic fracture propagation direction
- Interaction between hydraulic fractures and natural fractures
- Stress interference due to hydraulic fractures
- Well spacing, fracture spacing and fracture sequencing
- Infill well drilling and stimulation
- Re-fracturing

In everyday engineering practice, empirical approaches are used to design pad scale horizontal well and hydraulic fracturing treatments. These are trial-and-error approaches that are not firmly grounded in an understanding of the science behind the decisions.

1.2 OBJECTIVES

In this work a sound engineering basis for stimulating unconventional shale oil and gas reservoirs is presented. The principles of geo-mechanics and poro-elasticity are used to help design wells and fractures that best drain oil and gas reservoirs.

The main research objectives are: -

1. Develop a general, computationally efficient, poro-elastic model that includes the effects of pore pressure and stress shadowing induced by the creation of fractures and pore pressure depletion.
2. Apply the model to study geo-mechanical effects observed in an oil and gas reservoir including both near fracture and pad-scale effects in 3-D.
3. Perform calculations to predict fracture reorientation and development of fracture complexity due to interaction with existing fracture networks and simulate realistic pad-scale hydraulic fracture designs.
4. Develop strategies to increase oil and gas recovery by optimizing fracture spacing, well spacing, fracture sequencing and fracture complexity. Test the viability of infill wells and re-fracturing existing wells to increase the estimated ultimate recovery (EUR) of a region in the reservoir.

1.3 STRUCTURE OF THE DISSERTATION

This dissertation is divided into six chapters. The analysis in Chapters 2 and 3 is based on the impact of non-propagating static fractures while Chapters 4 and 5 explain the development and application of a novel geomechanics simulator to pad-scale problems using propagating fractures.

Chapter 2 extends the work done by Roussel (2011) to horizontal well fracturing. Using static non-propagating fractures in a poro-elastic simulator, the influence of various reservoir and operational parameters on potential fracture trajectories in a horizontal well is discussed. Optimization of fracture spacing and fracture sequencing is recommended to increase the EUR of hydrocarbons.

Chapter 3 extends the results in Chapter 2 to multi-well scenarios. A workflow for pad-scale fracture modeling is discussed that can be used to simulate inter-well and inter-

fracture interference in multi-well hydraulic fracturing pads. An Eagle Ford basin case study is presented to depict the field observation of the theories put forward in Chapter 2. Understanding from the field case study is extended to explain the impact of interference between fractures in multiple wells in a pad. Based on the understanding developed in this work new strategies are recommended to increase hydraulic fracture efficiency in horizontal well pads.

Chapter 4 discusses the model development for the geomechanical poro-elastic reservoir simulator to simulate fracture propagation in various pad scale scenarios. Model verification cases are analyzed and a numerical analysis is performed to showcase the capabilities of the system. Features such as dynamic mesh refinement, parallelization and fluid-solid interaction algorithms are also discussed.

Chapter 5 describes the application of the simulator described in Chapter 4 to various pad scale scenarios. Parametric analysis is performed to describe the impact of various parameters on simultaneous multiple fracture propagation. Insights are obtained by simulation of multi-stage hydraulic fracture treatments and infill well fracturing treatments. Other model applications (re-fracturing, mini-frac analysis, and fracture network simulation) are proposed and illustrated.

Finally, Chapter 6 summarizes the contributions of the research, draws conclusions and makes recommendations for future work.

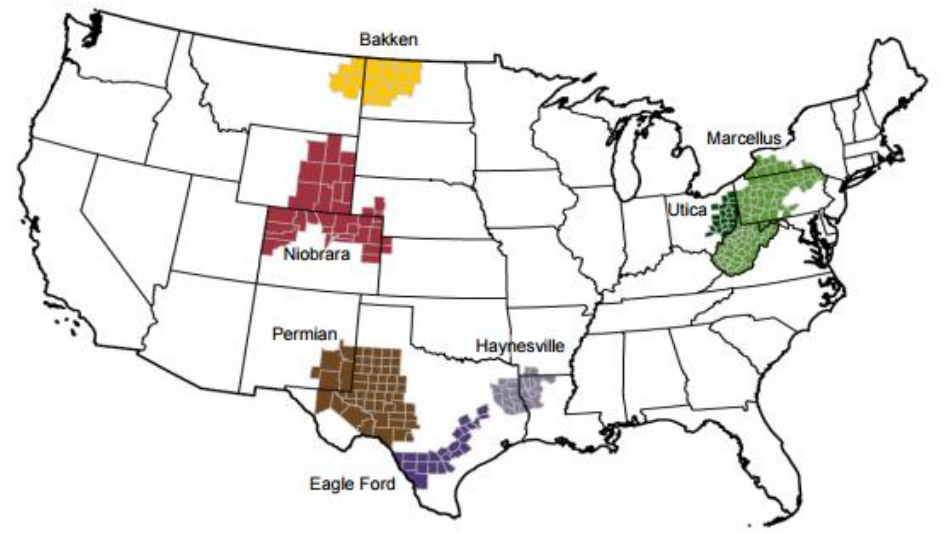

Figure 1.1 Location of the seven regions accounting for 92% of domestic oil production growth and all domestic natural gas production growth during 2011-14 (EIA, 2015).

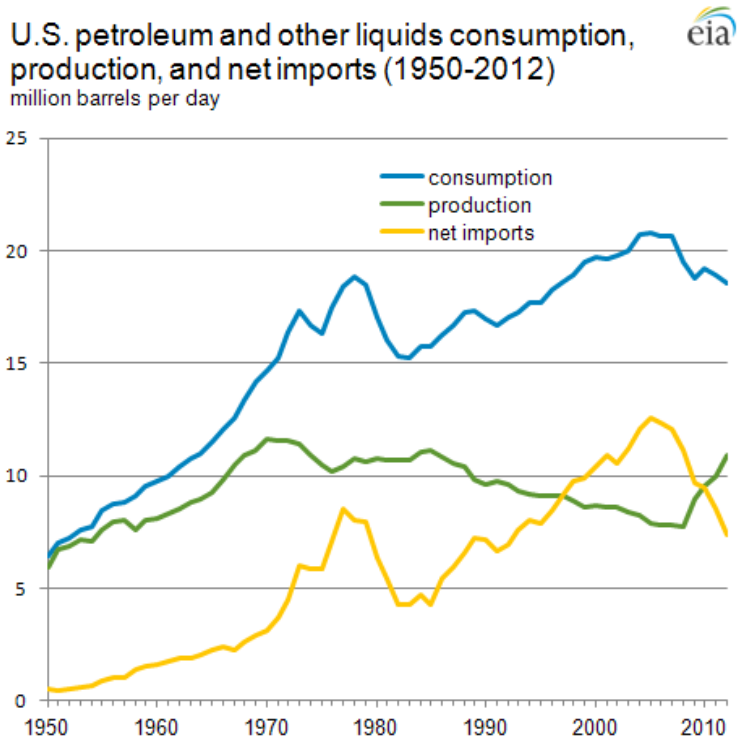

Figure 1.2 U.S. petroleum consumption, production and net imports (EIA, 2013)

Chapter 2: Single Well Fracturing Optimization: Static Fractures

In this chapter[1] we investigate some of the important variables that could impact the quality of the hydraulic fractures created in a horizontal well. The results presented in this chapter provide operators with tools to design completions and fracture treatments (proppant volume, fracture spacing, and sequencing) to maximize reservoir drainage and increase EURs. This should lead to more effective completion designs.

The creation of a hydraulic fracture changes the stress distribution in the vicinity of the fracture. This stress shadow can influence the growth of subsequent fractures. We use the principle of stress interference caused by open fractures to guide the propagation direction of subsequent fractures. A sensitivity analysis of the factors that affect the stress shadow was performed. These factors include both formation properties as well as treatment variables. A three-dimensional geomechanical model was used to observe the behavior of three typical shale gas reservoirs: Bakken, Barnett and Eagle Ford. We estimate optimum spacing values for the three cases that allow fractures to follow trajectories that are transverse and orthogonal to the wellbore. We also provide an understanding of the variables that an operator can control to have an efficient drainage of the reservoir and avoid intersecting fractures. A relation between the efficiency of the fracture treatment and the net closure pressure response observed in the field was provided. Use of the net closure pressure values from the fracture treatments as a diagnostic tool for generating more efficient completion design was also explained.

[1] Many of the ideas expressed in this chapter were first presented in Manchanda et al. (2012, 2013), Roussel et al. (2012), Manchanda and Sharma (2013, 2014). Sharma supervised all the above projects. Roussel contributed with the corresponding papers towards the end of his PhD and helped with the start of the continuation of the project with the corresponding papers. Holzhauser provided field data for validation and collaborated on the analysis. The field analysis will be discussed in the next chapter.

The stress re-orientation caused by an open fracture was simulated and horizontal stress contrast contour maps were generated. The reduction in horizontal stress contrast can lead to increased fracture complexity. We describe ways to increase fracture complexity by varying the completion design. The Young's modulus of the rock and the *in-situ* horizontal stress contrast are shown to be significant factors controlling the extent of fracture complexity generated in a given reservoir. In addition, the effect of proppant mass injected per stage is also shown to significantly impact fracture complexity. We provide optimum ranges of fracture spacing and proppant volume for the various shale formations analyzed. The use of these guidelines should result in more fracture complexity than would otherwise be observed.

The impact of closure of fractures is also taken into consideration to estimate their impact on the induced stress interference. Immediately after a hydraulic fracture treatment is pumped, the width of the propped fracture and the associated induced unpropped (IU) fracture network is at its maximum. The hydraulic fracture and the induced unpropped fractures close as a result of fluid leak-off over time. This implies that the stress shadow in their vicinity also decreases over time. Complete closure of induced, unpropped fractures can significantly reduce the stress shadow and make subsequent fracture stages less susceptible to fracture interference and more efficient by avoiding wastage of fluid / proppant into pre-existing fractures. This suggests that increasing the time between successive fractures in a wellbore will lead to improved fracture performance.

Using geomechanical computations we show that waiting for longer times between successive stages of a horizontal well allows for a reduction in the stress shadow and less fracture interference leading to a more efficient fracture network by successive fractures in a horizontal well. The idea of establishing a minimum time between

successive fracture stages in a well is proposed. The time required for the induced un-propped fractures to close can be calculated from our models and varies based on the reservoir and fluid properties but is of the order of hours.

2.1 LITERATURE REVIEW

2.1.1 Impact of Stress Shadow on Fracture Trajectory

The mechanical stress interference caused by propped open fractures impacts the direction of propagation of fractures in horizontal wells. These fractures can curve towards or away from each other (Olson 2008; Roussel and Sharma 2011a, 2011b, 2012; Bunger et al. 2012). In some cases, the fractures that curve towards the previous stages intersect the previous fracture. The stress interference effect is called stress shadowing and has been demonstrated in the field by microseismic measurements (Fisher et al. 2004; Mayerhofer et al. 2006).

In work done previously, an attraction zone has been identified in the vicinity of a fracture deviating from a transverse orthogonal path (Roussel and Sharma 2011a, 2011b, 2012). They hypothesized that a fracture initiated within this attraction zone will propagate toward the previous stage. This fracture could intersect the previous fracture if the fracture enters the stress-reversal region. Such fracture-to-fracture interactions may lead to sub-optimal drainage of the reservoir by the fracture treatment. Transverse growth of fractures should be promoted to improve the reservoir drainage efficiency of multi-stage fracture treatments in horizontal wells. In this chapter we propose a careful analysis of stress interference effects to promote the transverse growth of these fractures.

Most operators these days have resorted to small spacing of fracture stages and multiple perforation clusters per stage in horizontal wells in ultra-low-permeability environments. Though it may seem as though such treatment designs will create greater

reservoir drainage, one must pay attention to mechanical stress interactions. We present a sensitivity analysis of stress-shadowing effects in horizontal completions to provide insight into the spacing of subsequent fracture stages and how smaller spacing between fractures can also lead to non-transverse fractures.

Shale plays are characteristically very heterogeneous. Evidence has been presented to show the inactivity of a significant share of perforation clusters that do not contribute to the well's production (Miller et al. 2011). One hypothesis is that one perforation cluster dominates over its neighbors accepting most of the fluid and proppant being pumped during a stage. Furthermore, past field data has also suggested merging of fractures initiated from multiple perforation clusters (Daneshy 2011). Also, a wide variability of production rates is observed in the fields for similar completion designs and well locations (Cipolla et al. 2011). All the above mentioned factors suggest that significant opportunities exist to improve overall completion effectiveness in horizontal wells.

Propagation of fractures initiated simultaneously from multiple perforation clusters should be impacted by the stress interference created by consecutive fractures. Though this chapter does not specifically address this topic, we do understand the importance of stress interference in completions (Cipolla et al. 2011; Daneshy 2011; Miller et al. 2011). The topic of simultaneous multiple fracture propagation will be discussed in a later chapter.

2.1.2 Impact of Stress Shadow on Fracture Complexity

Characterization of the fracture network has remained a debatable and challenging topic. Advancements in the field of diagnostics have helped in this and allowed for an improved assessment of the completion effectiveness. Such advancements include the use

of diagnostic tools like microseismic measurements, mini-frac treatments, fracture injection tests (Barree et al. 2009), fluid and proppant flowback tests (King and Leonard 2011), and distributed temperature sensing (DTS) measurements (Huckabee 2009). One source of data that is readily available but rarely used is the evolution of fracture closure pressure from one stage to the next. An analysis of this fracture closure pressure from one stage to the next can reveal useful information about the fracture-to-fracture interaction and requires no additional equipment (Vermylen and Zoback 2011). It has been shown that intersection of fractures causes the net closure stress to vary in an up-and-down trend through fracture stages (Roussel and Sharma 2011a, 2011b, 2012). In this chapter, we show how the formation properties, fracture spacing, fracture width, etcetera, affect the change in the net closure pressure during sequential fracturing.

Many of the reservoirs in unconventional oil and gas reservoirs are naturally fractured i.e. contain planes of weaknesses that are non-uniformly distributed in the reservoir. The natural fractures can exist because of shear, extension or tensile events (Olsen et al. 2009). Natural fractures are considered to be crucial for production from unconventional reservoirs (Brown et al. 1995; Mayerhofer et al. 2006). These natural fractures are zones of high permeability that if connected to the hydraulic fracture can create efficient pathways to transfer hydrocarbons from the reservoir to the hydraulic fracture and as such govern the gas (or oil) producibility from the rock matrix (Brown et al. 1995; Olsen et al. 2009).

Certain diagnostic methods such as microseismic (MS) methods are used to map the location of shear failure events during a hydraulic fracturing treatment (Fisher et al. 2004; Cipolla et al. 2010). These shear failure events often occur because of pressure and temperature effects (such as those induced by hydraulic fracturing) leading to slippage at the planes of weakness in the reservoir. The MS data can be used as a tool to diagnose the

presence of shear failure planes during the treatment. The use of microseismic monitoring and tracers has shown that the creation of propped hydraulic fractures in most cases leads to the formation of complex fracture networks (Cipolla et al. 2010). The complexity of the fracture networks is often associated with the interaction of the hydraulic fracture with the pre-existing heterogeneity in the rock fabric. The location and orientation of these natural fractures in the reservoir rock can provide an important description of the stimulated rock volume (SRV) which in turn allows us to more accurately describe the well productivity and the well's ultimate recovery (EUR) (Mayerhofer et al. 2010).

Complex fractures can have a substantial effect on the production response of wells because of the change in fracture length, width and loss of fluid because of the secondary fractures and fissures (Warpinski 1990; Warpinski et al. 1990; Cipolla et al. 2000, 2007; Cipolla, Peterman, et al. 2005). In some cases this complex fracturing can improve production by maximizing the contact area of the reservoir with the well. Understanding this fracture network complexity and using it to better design hydraulic fracturing treatments has remained a challenge for the industry. From microseismic and tiltmeter data collected over the last 10 years, a huge diversity in fracture propagation patterns has been observed (Warpinski et al. 1996; Griffin et al. 2003; Fisher et al. 2004, 2005; Cipolla, Shucart, et al. 2005; Weijers et al. 2005; Wolhart et al. 2005, 2006; Mayerhofer et al. 2006). These patterns can guide us in understanding the importance of different variables and hence help us to identify the best stimulation strategy to characterize and induce the appropriate degree of fracture complexity for a given reservoir.

Significant advances have been made to describe the natural fracture networks and include their influence in simulating the propagation of hydraulic fractures. Meyer & Bazan (2011) have developed a discrete fracture network (DFN) model for naturally

fractured formations in which hydraulic fracturing could induce Mode I (Jaeger et al. 1979; Zoback 2007) natural fracture networks. This is similar to the wire-mesh model (Xu et al. 2010) in which a Hydraulic Fracture Network (HFN) model is proposed that uses perpendicular sets of vertical planar fractures through which the hydraulic fracture propagates and is represented by a growing ellipsoidal volume of the stimulated formation. Nagel, Gil, & Sanchez-nagel (2011) have proposed a discrete element model (DEM) that uses a predefined DFN to propagate hydraulic fractures. The DFN can be stimulated in both tensile and shear modes based on the injection fluid and the developed pressures and stresses. Dahi-Taleghani and Olson (2011) use an Extended Finite Element Method (XFEM) approach to solve the problem of complex fractures based on a two-dimensional plane strain elasticity approach. A description of the existing natural fracture network is required in all these approaches to simulate propagating fractures. Data on such pre-existing networks is almost impossible to obtain. Some core analysis can be done to assess the natural fracture density in the core samples (Gale et al. 2007). However, the use of the core-scale natural fracture density for the entire reservoir is debatable.

Several authors such as (Wu and Pollard 2002) and Olsen et al. (2009) have explained that a hydraulic fracture can intersect and induce the propagation of existing natural fractures. They have further shown that the width at the intersection of the hydraulic fracture and the natural fractures is dependent on a variety of factors such as the difference between the magnitudes of maximum and minimum principal stresses. A decrease in the horizontal stress contrast enables greater fracture widths at the intersection hence allowing more proppant communication into the natural fractures. Weng et al. (2011) have shown that a decrease in stress anisotropy changes the induced fracture geometry from a bi-wing fracture to a complex fracture network. Low values of

stress anisotropy can enable Mode I opening of some of these natural fractures. Proppant transport into the natural fractures is assisted when these fractures open in Mode I. Increased fracture complexity suggests an increase in the surface area of the created fractures and associated fracture network. A larger fracture surface area and a complex fracture network will result in better drainage of the reservoir in the vicinity of the fracture. Ideally this should lead to improved productivity of a particular stage and collectively for the horizontal well. In the absence of proppant transport into the stimulated natural fractures, these natural fractures might not connect to the primary hydraulic fracture and hence might not contribute to the production of the hydrocarbons directly. Thus, a low horizontal stress contrast can facilitate propped opening of natural fractures and help in sustaining greater production.

In this chapter we show that in addition to causing fractures to intersect each other the stress shadow effect can significantly reduce the horizontal stress contrast leading to more fracture complexity when creating multiple fractures from a single horizontal wellbore. A fracturing treatment in a region of low horizontal stress contrast can help to improve well productivity and EUR by stimulating natural fractures. We define how the location of this low horizontal stress contrast region varies with fracture geometry, mechanical properties, reservoir properties, and completion design. The completion design mentioned primarily focusses on optimizing the fracture spacing in a horizontal well and deciding the volume of proppant to pump in each fracturing treatment. The simulation results are used to identify the optimal spacing values between fractures in a horizontal well to be able to tap into the natural fracture networks in the formation. We further focus on the alternate fracturing sequence that was proposed earlier (East et al. 2011; Roussel and Sharma 2011a). Using our numerical simulations we discuss ways to optimize the fracture spacing to obtain maximum fracture complexity for the middle

fractures. In this chapter we suggest a new strategy for designing completions. This strategy takes into consideration an optimal way to obtain fracture complexity.

2.1.3 Impact of Fracture Closure and Induced Stress Shadow

The effectiveness of a hydraulic fracturing treatment in horizontal wells is dependent on a number of variables. Importance of treatment variables (such as fluid rheology, flow rates, proppant etc.), completion variables (stage spacing, number of clusters per stage, fracture sequencing etc.) and reservoir variables (natural fracture density, stiffness, etc.) has been emphasized in work done by numerous researchers (Cipolla et al. 2000, 2007; Ribeiro and Sharma 2013; Malhotra et al. 2014).

It is important to understand the effect of these treatment variables in order to effectively design fractures that stimulate a large portion of the reservoir. Fluid rheology governs the pressure drop along a fracture and hence its width and the settling of proppant in the fracture. A high viscosity fluid is crucial for proppant transport and usually leads to the creation of wider fractures (Gidley et al. 1990). Slick water fluids generally yield longer created fracture lengths but may result in smaller propped fracture lengths (Mayerhofer and Economides 1997; Walker et al. 1998; Britt et al. 2006; Palisch et al. 2010). Alternate innovative strategies have been developed using combinations of viscous and non-viscous fluids to create longer more conductive propped fractures (Ribeiro and Sharma 2013; Malhotra et al. 2014).

Although the treatment, completion and reservoir parameters are extremely important in the design of fracture treatments to effectively stimulate horizontal wells, one very important variable that has not been considered by the industry is the time between adjacent fractures in a horizontal well. In this chapter, with the help of geomechanical stimulations and field data we show that the time between adjacent

fractures in a horizontal well affects the effectiveness of the fractures. We suggest that the increase in time between two successive fractures in a given wellbore causes the stress shadow of the created fractures and the associated induced unpropped fractures to decrease because of fracture closure and hence allow for the creation of larger stimulated reservoir volumes and more effective stimulation.

In this chapter we use analytical derivations and geomechanical simulations to go a step further and understand the concept of fracture closure and its impact on the time dependent stress shadow. We explain the crucial variables involved in the process and extend the understanding to isolate the impact of induced unpropped (IU) fractures and the main hydraulic fracture.

In summary, this chapter discusses the following:

- Using fracture pressure data as a diagnostic for fracture interference.
- Optimizing fracture spacing to get transverse fractures
- Optimizing fracture spacing to get fracture complexity
- Understanding the impact of fracture closure on stress shadow and stress interference.

2.2 Model Formulation

A poroelastic model to simulate the stress interference between fractures in horizontal wells was formulated as described earlier (Roussel 2011; Roussel and Sharma 2011a, 2011b). In these calculations a hydraulic fracture was represented by PKN geometry (Perkins and Kern 1961; Nordgren 1972). The model was built using FLAC3D®, a three-dimensional numerical model that allows us to compute stresses in the rock. The reservoir is modeled as a homogeneous, isotropic, elastic, and bounded

medium to capture the stress distribution around propped-open fractures. The governing equations that are used to model a linear elastic solid material are discussed below.

2.2.1 Poroelastic Model

The coupled fluid-flow/mechanical isothermal response of a linear isotropic poroelastic material is governed by differential equations that relate pore pressure, stresses, strains and the variation of fluid content introduced by Biot (1955). Temperature is assumed constant in all simulations, thus thermo-elastic effects are not modeled. In the numerical formulation, space and time derivatives are approximated using finite-difference schemes.

Fluid affects only the volumetric response which can be described by three independent mechanical parameters (i.e. α, K and K_u). K is the drained bulk modulus, the bulk modulus of a porous material where fluid escapes without resistance ($\Delta p = 0$) while K_u, the undrained modulus corresponds to a zero flux material in which fluid cannot escape as a volumetric force is applied. In Biot's poroelastic formulation, the material's shear deformation is not influenced by the presence of fluid, and is thus described by the shear modulus G of the solid matrix.

In the literature, there are numerous formulations of the volumetric response of a poroelastic material. The chosen approach here is a continuum formulation where the fluid-filled porous material is treated as a whole Detournay & Cheng (1993). The constitutive equations of the poroelastic material are given in Eq. (2-1) and Eq. (2-2):

$$\sigma_{ij} = 2G\varepsilon_{ij} + \left(K - \frac{2}{3}G\right)\varepsilon_{kk}\delta_{ij} - \alpha\delta_{ij}p \tag{2-1}$$

$$\varsigma = \alpha\varepsilon_{kk} + \frac{p}{M}$$
$$with\ \frac{1}{M} = \frac{\alpha - \phi}{K_s} + \frac{\phi}{K_f}\ and\ \alpha = 1 - \frac{K}{K_s} \tag{2-2}$$

The constitutive equations contain two poroelastic quantities expressed in function of porosity ϕ and bulk moduli K, K_s and K_f, Biot's coefficient α and Biot's modulus M. Biot's coefficient α compares the material's deformation from the solid matrix and from the grains that compose it. In the special case of incompressible solid constituents (K_s>>K), and Biot's coefficient equals 1. The inverse of Biot's modulus M is defined as the change in the rock's fluid content resulting from a change in pore pressure, for a constant volumetric strain (Eq. (2-3)):

$$\frac{1}{M} = \left.\frac{\partial\varsigma}{\partial p}\right|_{\varepsilon_{kk}} \tag{2-3}$$

The fluid transport is modeled by Darcy's law of the fluid discharge in a porous material, (Eq. (2-4)):

$$q_i = -\frac{k}{\mu}\left(p_{,i} - \rho_f g_i\right) \tag{2-4}$$

Assuming that the equilibrium state is established at all times, the balance of local stresses in the fluid-filled porous material takes the form (Eq. (2-5)):

$$\sigma_{ij,j} + \rho g_i = 0$$
$$\text{where } \rho = (1 - \phi)\rho_s + \phi\rho_f \tag{2-5}$$

with ρ_s and ρ_f, the densities of the solid and the fluid phase, respectively.

When incorporating Eq. (2-5) into Eq. (2-1), we can highlight the contributions of mechanical strains and pore-pressure gradients in the poroelastic equilibrium equations solved at each grid-point of the numerical model (Eq. (2-6)):

$$\underbrace{2G\varepsilon_{ij} + \left(K - \frac{2}{3}G\right)\varepsilon_{kk}\delta_{ij}}_{mechanical\ stresses} - \underbrace{\alpha\delta_{ij}p}_{pore\ pressure\ gradients} + \underbrace{\rho g_i}_{body\ forces} = 0 \qquad (2\text{-}6)$$

where $p_{,j}$ are the gradients in pore pressure along x_j

The geometry of interest is modeled using the commercial code, FLAC3D®. Using a finite-difference and explicit-numerical scheme, the software couples fluid flow and the stress state in the reservoir. The poroelastic coupling is based on Biot's theory. The reservoir is homogeneous, isotropic, purely elastic, and is bounded by layers with a different value of shear modulus. Flow only occurs within the reservoir and does not leak into the bounding layers. The bounding layers in our simulations are defined as the top and bottom layers.

The far-field, no-flow boundaries are located at a distance (from the fracture) equal to at least three times the fracture half-length l_f. The model boundary conditions are detailed below:

Uniform fluid pressure in the fracture:

$$p = p_f \text{ at } -l_f < x < l_f,\ y = 0,\ -h_f < z < h_f$$

Constant stress applied at outside boundaries:

$$\sigma_{zz} = -\sigma_v,\ \sigma_{xx} = -\sigma_{hmax} \text{ and } \sigma_{yy} = -\sigma_{hmin}$$

No-flow reservoir boundaries at:

$$x = \pm x_r,\ y = \pm y_r \text{ and } z = \pm z_r$$

The above system of equations is solved to estimate the impact of hydraulic fractures on the stresses around them. In this section we focus on the mechanical

reorientation of stresses. The poroelastic effect, because of leak-off, has been excluded because of the extremely low permeability of the shale reservoirs. Stress reorientation caused by poroelastic effects is usually significant only over longer durations of injection and production (Roussel and Sharma 2011b; Warpinski and Branagan 1989; Weng and Siebrits 2007).

2.2.2 Fracture Closure and Fluid Leak-off

The Carter equation (Eq. (2-7)) is commonly used to describe the leak-off rate,

$$q_L = \frac{C_L}{\sqrt{t}} \tag{2-7}$$

Using an overall material balance and combining Carter's concept, the change in volume of a fracture because of leak-off has been derived elsewhere (Ehlig-Economides and Economides 2000). A general form of the expression is given in Eq. (2-8)

$$V_i = V + 2Ar_p\left(\kappa C_L\sqrt{t} + S_P\right) \tag{2-8}$$

In the absence of propagating fractures we assume that the entire surface area of the fracture opens at the first moment of pumping and hence assume the maximum value of κ as 2. Also, we ignore spurt-loss, a reasonable assumption for tight rocks. Thus the simplified expression for the variation in fracture volume is given by Eq. (2-9)

$$V = V_i - 4AC_L\sqrt{t} \tag{2-9}$$

Assuming a PKN like geometry, the volume of a fracture wing is the product of the average width and the face area. Thus the variation in fracture width can now be expressed as,

$$\overline{w_c} = \overline{w_i} - 4C_L\sqrt{t} \tag{2-10}$$

For a PKN geometry fracture the average width and maximum width are related by,

$$\overline{w} = 0.628w_{max} \tag{2-11}$$

Thus, the fracture width at the wellbore varies with time as given by Eq. (2-12)

$$w_c = w_i - 6.37C_L\sqrt{t} \tag{2-12}$$

Eq. (2-12) can be adapted to a form in which the change in width between two time steps can be evaluated as shown in Eq. (2-13)

$$w_t = w_{t-\Delta t} - 6.37C_L\left(\sqrt{t} - \sqrt{t-\Delta t}\right) \tag{2-13}$$

Where, Δt is the time step. This discretization is important for our numerical implementation to enable fluid and mechanical coupling in our model. This now allows us to capture the closure of the fracture after a fracture treatment is completed.

2.2.3 Fracture Trajectory Algorithm

Using the above fracture closure algorithm, the stress interference effects can be captured as a function of time. The intermediate principal stress direction and the minimum principal stress value can be used to govern the direction of propagation of this fracture. It can be assumed that the fracture will propagate in the direction of S_2 and will have less resistance in the direction with lower S_3. This is used to estimate the fracture trajectory. Figure 2.1 shows the steps involved in estimating the trajectory of successive fractures.

2.3 Results and Discussion

In this section, results are presented from both analytical and numerical analysis to estimate the stress shadow around static hydraulic fractures. The primary assumption for the results presented in this chapter is that the stress shadow is a result of a hydraulic fracture that has already been created and is not growing, i.e. a static fracture. Figure 2.2 shows a schematic of a half-fracture used in most of the simulation cases. The advantage of studying the stress interference for static fractures is that the problem is simplified

significantly and it is possible to simulate multiple hydraulic fractures in a horizontal well pad in a reasonable time frame (a few hours).

2.3.1 Stress Distribution Around a Single Transverse Fracture

In this section first an analytical representation of the stress shadow induced by a hydraulic fracture is presented. Then the stress shadow model obtained from a numerical simulator (FLAC3D®) is used to estimate the impact of various completion and reservoir variables on the stress shadow and the stress interference between fractures within a horizontal well.

2.3.1.1 Analytical assessment of stresses in the vicinity of a fracture

For a penny shaped crack, a set of equations can be derived to estimate the impact of fracture closure on the stresses in the vicinity of the fracture. The maximum width of a penny shaped crack open under uniform effective pressure (Perkins and Kern 1961) is given by,

$$w_{max} = \frac{8(1-\upsilon^2)p_{net}h_f}{\pi E} \tag{2-14}$$

The crack is open due a net pressure given by p_{net} and the half height (or the radius) of the crack is given by h_f. Thus the decrease in the width caused by fracture closure can be analytically coupled with the net pressure opening the fracture and hence the stress distribution around the crack. The expressions for the stress variation at a distance from a 2-D semi-infinite crack are (Sneddon 1946; Sneddon and Elliot 1946; Warpinski and Branagan 1989; Roussel 2011; Vermylen and Zoback 2011). The reduced solution for the stresses along the axis perpendicular to the plane of a penny shaped crack along the axis of the fracture are presented below,

$$\sigma_{yy} = -\frac{2p_{net}}{\pi}\left[\frac{\zeta(\zeta^2-1)}{(\zeta^2+1)^2} - \tan^{-1}\left(\frac{1}{\zeta}\right)\right]$$

$$\sigma_{xx} = -\frac{p_{net}}{\pi}\left[\frac{3\zeta}{(\zeta^2+1)^2} + \frac{2\upsilon\zeta}{(\zeta^2+1)^2} - (1+2\upsilon)\tan^{-1}\left(\frac{1}{\zeta}\right)\right] \quad (2\text{-}15)$$

Here, $\zeta = y/h_f$ is the dimensionless distance along the Y-axis away from the crack. The stresses can be plotted as dimensionless quantities vs. the dimensionless distance from the crack. We can couple Eqs. (2-12), (2-13) and (2-14) and plot the variation in stress as a function of time. Figure 2.3 shows how the "stress shadow" of a fracture is affected by the opening/closure of the fracture. Clearly, the stress perturbation caused by a crack is a nonlinear function of the distance from the fracture.

Figure 2.4 shows the normalized stress perturbation as a function of square root of time. Eq. (2-12) shows that the width of the fracture decreases as the square root of time. Since the width of the fracture is proportional to the generated stress perturbation, the stress perturbation also decreases with the square root of time. Figure 2.5 shows this dependence and how the stress perturbation decreases in time at a particular distance away from the fracture face. Clearly the gradient is much steeper close to the fracture and decreases further away from the fracture. Figure 2.5b shows that the decrease in stress perturbation for various values of the leak-off coefficient. Increasing the leak-off coefficient decreases the closure time. Thus, in a very low permeability formation, the stress perturbation caused by the fracture at a particular distance from the fracture decreases much slower than in a higher permeability formation. Since, in the transient flow regime the leak-off coefficient is a function of square root of permeability (Schechter 1992), the leak-off coefficient is inversely proportional to time. Thus if the permeability of the formation decreases by 100 times, the leak-off coefficient decreases by 10 times and the time of closure increases by 100 times.

Figure 2.6 shows the impact of the initial fracture width on the stress shadow. For all other parameters remaining the same, a fracture with a larger initial width will take a longer time to close than a fracture with a smaller initial width.

The stress interference because of a fracture is a function of a number of variables. The two main variables we are concerned with here are the time between consecutive fractures and the distance between fractures. Using Eq. (2-12), Eq. (2-14), and Eq. (2-15) we can show that the normalized stress interference caused by a fracture is a function of time and distance from the fracture expressed in terms of the following dimensionless quantities,

$$\frac{\Delta\sigma_{yy}}{p_{neti}} = \left(1 - 6.37\sqrt{\tau}\right) f(\zeta)$$

where,

$$f(\zeta) = -\frac{2}{\pi}\left[\frac{\zeta(\zeta^2-1)}{(\zeta^2+1)^2} - \tan^{-1}\left(\frac{1}{\zeta}\right)\right]$$
$$\tau = \frac{t}{\left(\left(w_i - w_f\right)/C_L\right)^2} \qquad (2\text{-}16)$$
$$p_{neti} = \frac{\pi E w_i}{8(1-\upsilon^2)h_f}$$

This relation has been plotted for various dimensionless times (τ) in Figure 2.7. A completion engineer must aim to minimize the stress shadow. The relation presented above allows an engineer to estimate the time needed for the stress shadow to decay to an acceptable value. This time will depend on various factors such as the fracture spacing, the elastic moduli etc. which are all accounted for in the simple dimensionless relation presented above.

The primary assumption when applying the above analytical model to estimate the stress shadow in the vicinity of a hydraulic fracture is the assumption of a circular fracture geometry. In order to estimate the stress shadow around fractures of geometries other than a circular geometry, a numerical model is required.

2.3.1.2 Numerical assessment of stresses in the vicinity of a fracture

We use a three layer model in which we ascribe different mechanical properties to the boundary layers and the pay zone. The rock layers bounding the reservoir may have mechanical properties (E_b, ν_b) different from the pay zone (E_p, ν_p) (Figure 2.7). However, for the cases considered in this work we have assumed that the pay zone height and fracture height are equal.

The fluid pressure inside a hydraulic fractures keeps it open. When the fluid pressure in the fracture decreases, the fracture closes until the fracture reaches its propped dimensions. To model a propped hydraulic fracture we use the amount of sand pumped during a stage to estimate the final fracture width using Eq. (2-17). This equation describes the mass of proppant required to fill up a PKN geometry fracture of prescribed length (L_f), height (H_f), porosity (ϕ_{frac}), and width (w_{max}) at the wellbore. A PKN fracture geometry is a simplification, since we know that the fracture geometry is likely to be a lot more complex. We assume that during the fracture treatment process at least one dominant long hydraulic fracture is created. The primary effect of the stress shadow created is captured by the dominant fracture. We do not use a displacement boundary condition but use an iterative process to converge to the designed width at the wellbore by varying the net stress in the fracture. This procedure has been discussed in great detail in Roussel (2011).

$$m_{prop} = \frac{\pi}{4} w_{max} L_f H_f \rho_{prop} \left(1 - \phi_{frac}\right) \tag{2-17}$$

The initial value of pressure inside the fracture is used from the field data. Thereafter the fracture net pressure is varied based on Eq. (2-18) till the simulated fracture width, w_{max}^{k} approaches the design fracture width, w_{max} where k is the iteration cycle number (Eq. (2-13)).

$$p_{net}^{k+1} = p_{net}^{k} - \frac{1}{cf}\left(\frac{w_{max}^{k} - w_{max}}{w_{max}}\right)\left(p_{net}^{k} + \sigma_{hmin}\right) \tag{2-18}$$

In order to couple fluid flow with mechanical effects a unique strategy was applied. The treatment pumping time is assumed to be about 2 hours. For the first 30 minutes the fluid pressure inside the fracture and the stress on the fracture faces is ramped up to a chosen/provided value of pressure in small steps of time. Thereafter, the converged value of pressure is used to perform fluid flow calculation and coupled with mechanical stress on the fracture face for the remaining treatment time. This allows us to model the creation of a fracture while considering poroelastic stresses.

It is also important to consider the impact of stress interference when treating the next hydraulic fracture stage in the same well. Figure 2.9 represents one such scenario where Fracture 1 has closed to a certain width and the treatment for Fracture 2 is about to start. Figure 2.9 shows the contour map of the local horizontal stress contrast in the presence of a fracture. The *in-situ* horizontal stress contrast is 400 psi. The red dashes show the direction of the local σ_{hmax}, which guides the direction of fracture propagation. For this scenario, Fracture 1 has a 400 ft. fracture half-length, 200 ft. fracture height, 500 M-lbm proppant which gives a maximum fracture width of 0.77 in. at the wellbore (for 50% proppant pack porosity and 165.4 lb/ft^3 proppant density). The mechanical properties for this case are a Young's modulus of 6 MMpsi in the pay zone and the Poisson's ratio is 0.2 in the pay zone. The *in-situ* σ_{hmax} direction is parallel and the *in-situ* σ_{hmin} direction is perpendicular to the fracture in Figure 2.9. After creating the fracture,

the stresses around the fracture are altered. Figure 2.9b shows the contour map of the local σ_{hmin} value in the presence of the fracture. The increase in stress perpendicular to the fracture is more than the increase in stress parallel to the fracture in the vicinity of the fracture. This leads to a reversal in the direction of the intermediate principal stress close to the fracture. Moving away from the fracture leads to a reduction in the minimum principal stress value and we encounter a region of negligible horizontal stress contrast where the intermediate principal stress and the minimum principal stress are approximately equal in magnitude. This is also where the direction of intermediate principal stress reorients itself along the *in-situ* far field direction of σ_{hmax}. The direction of the intermediate principal stress is important because it guides the direction of propagation of the subsequent fracture. However, in the regions where the local horizontal stress contrast magnitude has a low value, the local heterogeneity of the reservoir can take precedence in deciding the direction of hydraulic fracture propagation. Thus, if the subsequent fracture in the current case of Figure 2.9 is initiated in the marked region of low horizontal stress contrast in Figure 2.9a, there is a much higher probability that it will tap into the natural fracture system in the reservoir and eventually create a complex fracture network.

The impact of pressure changes on the stresses is negligible at the fracturing time scale. Figure 2.10 and Figure 2.11 show the mechanical and poroelastic effects induced by a propped fracture. The simulations used to produce the results presented in Figure 2.10 assume a permeability of 1 mD while the results presented in Figure 2.11 assume a permeability of 1 μD. In this model, a propped fracture is simulated with 500,000 lbs of proppant. The initial pressure inside the fracture is assumed to be the average treatment pressure. In this simulation the fracture treatment time is 2 hours and for the duration of the treatment time the fluid calculations in the matrix are done with fixed fracture

geometry and a constant pressure equivalent to the fracture treatment pressure inside the fracture. Thereafter, the pressure inside the fracture is allowed to dissipate into the reservoir in time as the pressure inside the fracture is greater than the reservoir pressure. This allows us to simulate fluid leak-off from the fracture into the reservoir. This fluid leak-off increases the pressure in the vicinity of the fracture over time, thus giving rise to poroelastic effects and changing the stresses in the reservoir (Zhai and Sharma 2007). The fracture width is maintained constant during this time to eliminate the impact of fracture closure on the stresses in the vicinity of the fracture. This effect of fracture closure is discussed in Section 2.3.5. As seen in the figure, a significant decrease in the minimum principal stress is observed in the immediate vicinity of the fracture over time. However, this variation in the minimal principal stress reduces very quickly away from the propped fracture. This effect is more prominent in the high permeability case where the pressure dissipates more.

Some assumptions have been made to simplify the simulations. Most of the assumptions have been stated above. Some other important assumptions are listed below:

- In this set of results we have assumed PKN type fractures with a uniform proppant density. We recognize that this is not likely to occur in the field. The proppant bank formed inside the fracture is prone to settle near the bottom of the fracture because of proppant settling. This may cause the propped fracture to be below the zone of interest. As the actual proppant distribution is unknown, we have made the simplifying assumption that it is uniform.
- In this set of results a single planar fracture per stage has been assumed. In the scenario in which there is evidence of multiple fractures per stage, the simulation results will need to be modified to include the impact of the multiple fractures on the stress reorientation observed in the field.

2.3.2 Superposition of Stresses for Multiple Transverse Fractures

Instead of creating several fractures in a single numerical model, we use a model of the mechanical stress perturbation caused by a single fracture. The solution of this model is superposed to allow us to obtain the stress distribution around the n^{th} fracture. The resulting stress reorientation map can be used to deduce the direction of propagation of the $(n+1)^{th}$ fracture (Figure 2.12). This workflow was first presented by Roussel and Sharma (2011a, 2011b) and detailed explanation is given in Roussel (2011).

The stress effects of one fracture on the next fracture in a sequential fracturing sequence depend on the rock deformation resulting from the propped nature of the previous fracture. Thus, we model this rock deformation by applying a uniform stress along the hydraulic fracture at the time of closure. This fracture closure stress is equal to the net closing pressure, p_{net}, plus the minimum *in-situ* horizontal stress, σ_{hmin}. This closure pressure can be observed operationally if the pressure gauges are allowed to capture pressures for long periods of time after completing each stage. However fracture closure pressure is rarely measured in the field. Several methods exist to estimate the fracture closing pressure based on knowledge of the initial shut-in pressure, including G-function analysis (Weng et al. 2002).

After we model the propped-open fracture, the rock deformation is used to generate the stress distribution in the vicinity of the opened fracture. We generate stress re-orientation maps using the stress distribution. From the results obtained we extract two parameters which are used as input for modeling the subsequent fracture stage: (a) the net closure stress and (b) the propagation direction at a given distance from the fracture equal to the fracture spacing s_f.

In order to keep the simulations fast and computationally efficient, we have used a superposition technique that allows us to superpose the effect of one fracture on the

subsequent fracture. We calculate the stress interference caused by the previous fracture at the location of the next fracture. This extra stress is then added to the local S_{hmin} estimate. The net closure stress in the subsequent fracture is the sum of the net closure stress of the previous fracture (without stress shadow) and the extra stresses generated due to the stress shadow of the previous fracture as shown in Eq. (2-19). The net pressure required to achieve the specified fracture width varies with each additional fracture:

$$p_{net}^{n+1} = p_{net}^{n} + \sigma_{yy}^{n}(s_f) - \sigma_{hmin} \tag{2-19}$$

In order to track the trajectory we use the stress distribution around a fracture to track the trajectory of the subsequent fracture assuming that it will follow the direction of maximum horizontal stress. Thereafter, an average angle of deviation from the orthogonal trajectory, θ_f (s_f), is calculated from the coordinates of the final fracture position (Figure 2.12).

There are several motivations for not modeling multiple propped-open fractures in the same grid. Firstly, in the FLAC3D® finite difference model, the geometry of all fractures must be set from the beginning. This would be a difficult task, as the angle of propagation of subsequent transverse fractures will depend on the mechanical stress perturbation generated by the previous fractures. This would require a complex and time consuming re-meshing after every single fracture stage. Secondly, having multiple fractures in a single model represents a significant computing task. Using a simplified strategy, we are able to generate maps of the propagation direction of multiple sequential transverse fractures in a horizontal well in a matter of minutes.

Next we assess the impact of various field parameters such as Young's Modulus and Poisson's Ratio of rock layers, amount of proppant mass injected, fracture spacing and *in-situ* horizontal stress contrast on the geometry of the fractures obtained. For the

following simulation results a propped fracture geometry is assumed for all the simulated fractures.

2.3.3 Impact of Field Parameters on Fracture Trajectories

Typical formation and fracture properties for the Barnett, Bakken and Eagle Ford shales that were taken from the literature are shown in Table 2.1 and are used in our simulations**.** These values are used as base cases for the sensitivity analysis performed on each of the formations. These base case values were obtained from field data presented in the literature (Kuhlman et al. 1992; Cipolla et al. 2009; Mullen 2010; Stegent et al. 2010; Centurion 2011).

21 fracture stages have been simulated for each of the base cases. Net pressure values for the base cases are shown in Figure 2.13 together with fracture trajectories shown in Figure 2.14. Figure 2.13a shows the evolution of net closure pressure values from stage to stage for the three formations described above. A distinct contrast in the trends for the different formations is observed for the three shale gas plays owing to the varying properties of the three formations. As we will see later, the Young's modulus of the formation has a major influence on the characteristic trends observed. The Barnett shale, which has the highest Young's modulus and the lowest horizontal stress contrast, shows a very different trend primarily because of higher stress interference. Figure 2.13b depicts the total pressure inside the fracture at closure. The Bakken values are a lot higher primarily because the pay zone is located about 2000 feet deeper than the other two formations.

The net closure pressure trends plateau after the first few stages for the Bakken and the Eagle Ford cases. The Barnett cases on the other hand show a characteristic up-and-down trend through the stages. Figure 2.14 depicts the fracture trajectories obtained

for the three formations considered. We get intersecting fractures in the Barnett case while there are no intersecting fractures in the Bakken and the Eagle Ford cases. However, the Bakken case shows greater fracture deviation than the Eagle Ford case. In the simulations conducted it was assumed that a longitudinal fracture extended along the wellbore till it intersected an existing fracture. These fracture trajectory trends can be directly correlated with the net pressure trends observed. For the Barnett case, an intersecting longitudinal fracture is directly correlated with higher net closure pressures. For the fracture after the longitudinal fracture we observe a dominant transverse trajectory and a drop in the net closure pressure value. The net closure pressure value for a propped fracture should be non-zero. A longitudinal fracture does not alter the stresses in the y direction as much as a transverse fracture. Thus, we get a drop in the net closure pressure value due to the lack of mechanical interference after a longitudinal fracture. The higher net closure pressure values for the Bakken case (in comparison to the Eagle Ford case) can be attributed to the greater deviation of fractures in the Bakken case. This greater deviation is evidence of greater mechanical interference and thus higher net closure pressure values are observed.

As shale formations can be highly heterogeneous, a broad sensitivity analysis can help in understanding the implications of a variety of parameters that cannot be accurately ascertained in the field. Also, extreme values of some parameters were used in the sensitivity analysis when representative values were not found in literature. The ranges of various parameter values are presented in Table 2.2, Table 2.2 and Table 2.3. The sensitivity analysis has been presented as charts of net closure pressure vs. stage number in Figure 2.15 to Figure 2.20. Each figure compares the effect of one variable parameter on the net closure pressure variation from stage-to-stage in the three formations.

2.3.3.1 Effect of formation properties

The formation properties include the horizontal stress contrast, the Young's modulus and the Poisson's ratio. Figure 2.15 and Figure 2.16 show the variation in the net closure pressure trend with changes in Young's modulus, the Poisson's ratio and the *in-situ* horizontal stress contrast for the different formations.

The figures show that varying the Young's modulus and the Poisson's ratio, leads to a variation in the range of net closure pressure values as well as a change in the trend. We believe that the low stress contrast chosen for the Barnett leads to the oscillatory trend whereas a higher stress contrast in the Bakken and the Eagle Ford as well as a greater fracture spacing in the Eagle Ford leads to a monotonic increase in the net closure pressure values observed. Everything else remaining the same, an increase in the value of Young's modulus leads to an increase in the stress interference and the value of net closure pressure observed in all the formations. A change in Poisson's ratio leads to significant changes in the Barnett case. However, an increase in the Poisson's ratio value in the other two cases leads to a slight, almost insignificant, increase in the net closure pressure response.

The stress contrast in the formations has a strong impact on the onset of fracture intersection as seen in Figure 2.17. From the figure we observe that a critical value of the stress contrast should exist, above which an increase in the stress contrasts does not lead to significant changes in the response of net closure pressure. Formations with a low value of the stress contrast such as the Barnett shale are more likely to feature intersecting fracture stages. A change in the percentage of intersecting fractures has a strong impact on net closure pressure trends and magnitudes. But a different value of the *in-situ* horizontal stress contrast does not systematically imply different net closure pressure values, in particular when all fractures remain transverse.

2.3.3.2 Effect of completion variables

Completion variables such as fracture length, proppant mass per stage, and fracture spacing have a strong influence on the net closure pressure trends as observed in Figure 2.18, Figure 2.19 and Figure 2.20.

The fracture length and proppant mass have an interrelated effect on the trends observed. For the same proppant mass, an increase in length implies a decrease in the fracture width and for the same fracture length an increase in proppant mass leads to an increase in fracture width (Eq. (2-17)). Thus, an increase in fracture length depicts a trend that is qualitatively similar to the trend observed when decreasing proppant mass. This shows that the fracture width is the main reason for the trends observed. The fracture length determines the spatial extent of the stress shadow, but the fracture width controls the magnitude of stress interference.

One interesting result that we observe is the effect of the fracture tip. Figure 2.18c shows that for a very short fracture (100 ft. half-length), the stress reorientation leads to a reduction in the net closure pressure from stage 1 to stage 2.

Figure 2.20a shows that decreasing the fracture spacing leads to an increase in the amplitude of the fluctuations observed in the Barnett case. For the other two cases, no fluctuations are observed but instead net closure pressure gradually increases through all stages. This is because the mechanical interference is cumulative and this leads to a progressive increase in the net closure pressure of the propped-open fractures. For larger fracture spacing, in all three cases, we observe that the net closure pressure plateaus after the first few stages.

2.3.3.3 Effect of fracture spacing on fracture trajectory

Figure 2.21, Figure 2.22, and Figure 2.23 show the fracture trajectories for the different fracture spacing for the three formations. We see that as the fracture spacing is

reduced subsequent fractures tend to be in the stress repulsion zone for the Bakken and the Eagle Ford whereas for the Barnett the reduction in fracture spacing leads to fractures sometimes growing into the stress attraction zone. For example, Figure 2.23 shows that almost every transverse/oblique fracture is followed by a longitudinal fracture thus depicting fractures growing in the stress attraction zones. The fracture trajectory pictures can also be tied to the net pressure profiles. For the Bakken and the Eagle Ford, the curving of the fractures at smaller fracture spacing shows significant stress interference and this is depicted in Figure 2.20 with increasing net closure pressure values at smaller spacing. Also, for the Barnett, increasing the fracture spacing leads to a relief in the stress interference and leads to lower net pressure values as shown in Figure 2.20a for the 200-ft fracture spacing case. Another correlation between the net closure pressure and the fracture trajectory can be established by comparing the stages where we get longitudinal fractures. In Figure 2.23b we get longitudinal fractures in stage numbers 6, 9, 12, 15, 18 and 21. These stages clearly correspond to the peaks on the net closure pressure plot for 100-ft fracture spacing shown in Figure 2.20a. Thus an up-and-down trend in the net closure pressure can clearly be used as a diagnostic to identify inefficient fracture stages.

2.3.3.4 Effect of proppant mass on the percentage of intersecting fractures

We have established in the previous sections that amongst the treatment variables that affect the net closure pressure response, the proppant mass per stage and the fracture spacing are the most significant. Proppant mass per stage is the only variable that an operator can directly control after the formation has been perforated. Thus, it is important to evaluate the efficiency of a fracture treatment and the effect of varying proppant mass per stage as well as fracture spacing.

We define the efficiency of a fracture treatment as the percentage of intersecting fractures in a particular fracture treatment. Figure 2.24 and Figure 2.25 show plots for the Barnett and the Bakken shales. The parameter values chosen for these plots are given in Table 2.5. We studied a wide range of fracture spacing and average proppant mass per stage.

The Barnett shale, owing to its brittle character and high Young's modulus values, shows a very dynamic response. The characteristic properties of the Barnett make it almost impossible to have an efficient fracture treatment at small fracture-spacing. It was observed that for smaller fracture spacing an exceptionally small amount of proppant per stage would be required to avoid intersecting fractures. This small amount of proppant per stage would imply extremely small fracture widths which might lead to an inefficient completion. This effect is rather subdued at greater values of fracture spacing, for example, for fracture spacing greater than 150 ft., we do not observe any intersection of fractures for a proppant mass below 225 M-lbs.

The Bakken shale, on the other hand, provides evidence of very contrasting behavior. The characteristic properties of the Bakken shale make it possible to have efficient fracture treatments at very low fracture spacing. Even at an unreasonably small fracture spacing of 25ft, and about 150 M-lbs of proppant for the Bakken shale we only have around 25% intersection of fractures. We have assumed a 150-ft fracture half-length in our simulations for the Bakken cases here. Thus, if there is a way to increase the propped fracture length, we should be able to pump in more proppant into the formation without causing any intersection of fractures and this should lead to much more efficient reservoir drainage. Opting for 250 M-lbs of proppant pumped per stage, we can design a fracture spacing of 75 ft. and avoid fractures from intersecting each other. We believe

that closely spaced, non-intersecting transverse fractures will maximize reservoir contact and drain the shale reservoir most effectively.

The sensitivity analysis presented above covers some of the most important parameters that affect the stress shadow around a hydraulic fracture. The conclusion is that Young's modulus, horizontal stress contrast, fracture spacing, fracture length, and proppant mass all have a strong influence on the spatial extent of the stress shadow and the magnitude of the stress interference.

2.3.4 Impact of Field Variables on Fracture Complexity

In the above analysis we primarily looked at optimizing trajectories of the dominant fracture created in multiple stages of hydraulic fracturing in a single well. Numerous researchers have demonstrated the existence of complex fracture networks in unconventional shale oil and gas formations. Here we study how we can use hydraulic fracturing to create regions that may induce high fracture complexity.

We have run simulations to observe the effect of the parameters discussed above on the magnitude of horizontal stress contrast observed in the horizontal plane going through the middle of the fracture. We look in detail at the variation in horizontal stress contrast along the wellbore at the point of initiation of the subsequent fracture. This gives us an estimate of how the fracture will tap into the stress complexity of the reservoir.

2.3.4.1 Stress reorientation around a single transverse fracture.

Figure 2.26a shows the variation in horizontal stress contrast with distance from the fracture along the wellbore. Figure 2.26b shows the angle of reorientation of the intermediate principal stress direction in the horizontal plane along the wellbore with distance from the fracture. For this scenario, the initial fracture has 200 ft. fracture height, 300 M-lbm proppant which gives a corresponding maximum fracture width at the

wellbore (shown in the legend) (for 50% proppant pack porosity and 165.4 lb/ft^3 proppant density). The mechanical properties for this case are a Young's modulus of 6 MMpsi and the Poisson's ratio is 0.2 in the pay zone. The *in-situ* horizontal stress contrast is 200 psi. Roussel and Sharma (2011a) show that an increase in fracture width increases the extent of stress reversal along the horizontal well away from the fracture. Figure 2.26a shows that with increasing maximum fracture width the minimum value of horizontal stress contrast is obtained at a larger distance from the fracture location. As explained in Figure 2.9 this minimum value provides the optimal fracture spacing that will generate complex fracture networks in the reservoir. Thus, it is evident from the figure that the optimal fracture spacing decreases with increase in fracture length. Also, the optimal fracture spacing decreases with a decrease in maximum fracture width. Another important consideration is the orientation of the intermediate principal stress direction at the point of initiation of the subsequent fracture. This reorientation angle, shown in Figure 2.26b, should be close to 0 degrees so that the initiated fracture propagates orthogonally away from the wellbore and leads to an efficient completion. The extent of the stress reversal region can be estimated from the extent of the high angle region (greater than 80 degrees) from the curves in Figure 2.26b. Comparing Figure 2.26a and Figure 2.26b, it is evident that the extent of the stress reversal coincides with the location of the region of minimum horizontal stress contrast. It is clear from the figure that the extent of the stress reversal region decreases with an increase in fracture length. Please note that the widths presented in the figure are higher than what would be expected in real scenarios. This chart represents a parametric analysis. In the set of simulation results presented in this chart, the proppant mass per fracture and the height of the fracture were kept constant for different values of fracture lengths. Thus using volume conservation inside the fracture the width of the fracture is calculated to be high for the shorter fracture lengths.

It is interesting to note the fluctuation in the horizontal stress contrast profile shown in Figure 2.26a. As seen in the figure, the horizontal stress contrast attains a peak value close to the fracture face. Roussel and Sharma (2011a) have shown that both intermediate principal stress and minimum principal stress decrease with distance from an open fracture. The gradient of these stresses from the fracture face are, however, different. An open fracture causes the gradient of intermediate principal stress to be smaller than the gradient of the minimum principal stress in its vicinity. This trend reverses at a certain distance from the fracture. Thus the horizontal stress contrast attains a peak vs. distance from the fracture and the horizontal stress contrast curve attains a minimum value before increasing back to the *in-situ* stress state at larger distances from the fracture. The fluctuation in the horizontal stress contrast is discussed in more detail by Roussel and Sharma (2011a) in which they have discussed the variation in the generated stress contrast caused by an open fracture as a function of fracture geometry and formation properties.

2.3.4.2 Effect of in-situ horizontal stress contrast.

Figure 2.27 **(**Young's modulus of the pay zone is 6 MMpsi) and Figure 2.28 **(**Young's modulus of the pay zone is 4 MMpsi) depict the optimum fracture spacing (as defined above) as a function of the proppant mass per stage. The range of values assumed for the proppant mass per stage is realistic based on knowledge of the values used in the industry. Figure 2.27a represents the relation between optimum fracture spacing and proppant mass for an *in-situ* horizontal stress contrast of 200 psi and Figure 2.27b represents the relation between optimum fracture spacing and proppant mass for an *in-situ* horizontal stress contrast of 400 psi. The Young's modulus of the pay zone in the model corresponding to Figure 2.27 is 6,000,000 psi while the Young's modulus of the

pay zone in the model corresponding to Figure 2.28 is 4,000,000 psi. Figure 2.28a and Figure 2.28b represent the relation between optimum fracture spacing and proppant mass for an *in-situ* horizontal stress contrast of 250 psi and 500 psi, respectively. The error bars in the figures define the range of optimum fracture spacing. This range is computed by observing the extent of the region along the wellbore for which the local horizontal stress contrast is less than 50 psi and the angle of the intermediate principal stress in the region is less than 45 degrees. Using this definition we observe that the range of fracture spacing for the cases represented in Figure 2.28 are approximately $\pm$ 0 ft., $\pm$ 5 ft., and $\pm$ 7.5 ft. for fracture half-lengths 200 ft., 300 ft., and 400 ft., respectively.

The above figures show that with an increase in proppant mass the optimum fracture spacing increases. For the same fracture length a variation in proppant mass leads to a variation in the maximum fracture width because the height of the fracture is constant for all the cases described above, at 200 ft. An increased fracture width causes greater stress interference which explains the increase in the optimum fracture spacing with increase in proppant mass per stage. Similarly, a change in the fracture length for the same proppant mass per stage leads to a change in the maximum fracture width and hence leads to drastically different values of optimum fracture spacing.

From Figure 2.27 and Figure 2.28, we can observe large variations in the optimal fracture spacing value caused by changes in horizontal stress contrast. For example, Figure 2.27 shows that for a proppant mass of 300,000 lbm, at a lower horizontal stress contrast of 200 psi, the optimum fracture spacing varied from approximately 130 ft. to approximately 250 ft. while at the higher horizontal stress contrast of 400 psi, the optimum fracture spacing varies from approximately 25 ft. to approximately 140 ft. A similar scenario is represented in Figure 2.28. For the case of a higher *in-situ* horizontal stress contrast the fracture needs to create enough mechanical interference to be able to

reduce the horizontal stress contrast appreciably. This can be achieved by increasing the width of the fracture. Hence, for the same fracture length and optimum fracture spacing, a much greater amount of proppant mass per stage is required. For example, according to Figure 2.28, to obtain an optimum fracture spacing of 50 ft. for a fracture with half-length 400 ft. we need approximately 300,000 lbm of proppant per stage at an *in-situ* horizontal stress contrast of 250 psi, however, to obtain the same optimum fracture spacing for the same fracture length we need approximately 600,000 lbm of proppant per stage for a 500 psi *in-situ* horizontal stress contrast.

It is clear from these results that the optimum fracture design (fracture spacing, proppant mass per stage, and so forth) is closely tied to the reservoir properties and the *in-situ* stresses. The horizontal stress contrast considerations described here are seldom taken into account in fracture design. However, as shown here the choice of proppant mass and stage spacing should be based on the considerations discussed above.

2.3.4.3 Effect of Young's modulus.

Figure 2.29, like Figure 2.27 and Figure 2.28, represents the variation in the optimum fracture spacing as a function of the proppant mass per stage. Figure 2.29a represents the case of a low Young's modulus (2.25 MMpsi) while Figure 2.29b represents the case of higher Young's modulus (4 MMpsi). The *in-situ* horizontal stress contrast for both the cases is 250 psi.

For similar values of proppant mass and fracture length we get much smaller optimum fracture spacing values for the lower Young's modulus case. For example, for a proppant mass of 400 M-lbm per stage, the optimum fracture spacing varies from approximately 25 ft. to approximately 120 ft. for the lower Young's modulus case, while the optimum fracture spacing varies from approximately 80 ft. to approximately 180 ft.

for the higher Young's modulus case. This happens because the mechanical interference caused in a low stiffness environment is significantly smaller than the mechanical interference caused in the higher stiffness environment.

2.3.4.4 Stress reorientation between two fractures.

The impact of fracture sequencing has been established in previous work (Roussel and Sharma 2011a, 2011b). Roussel and Sharma (2011b) have shown that the fracture spacing required for orthogonal fractures in a horizontal well is much lower for the scenario of alternate fracturing in comparison with the consecutive fracturing technique. For a synthetic case of the Barnett shale they prescribed a recommended fracture spacing that was over 50% lower using the alternate fracturing sequence compared to consecutive fracturing.

The alternate fracturing sequence strategy involves placing the third fracture (based on distance from the toe) before the second fracture. After the third fracture is created the second fracture is stimulated between the first and the third fracture (East et al. 2011). The notations first, second, third here correspond to the respective locations in the horizontal well from the toe and should not be confused with the order of the fracturing. The order of fracturing with the alternate fracturing sequence thus becomes 1-3-2-5-4-… and so on. On the other hand, the order of fracturing with the consecutive fracturing sequence is 1-2-3-4-5. As explained in the reference (Roussel and Sharma 2011b), because the third fracture is placed a large distance away from the first fracture, the third fracture propagates in a region of negligible stress interference and can be considered more or less orthogonal to the wellbore.

Roussel and Sharma (2011a) mention a region of low horizontal stress contrast that is developed between the two created fractures. This region of low horizontal stress

contrast coincides with the initiation point of the second fracture. Figure 2.30 illustrates the evolution of a region of low horizontal stress contrast with the variation in spacing between the first fracture and the third fracture. In the cases presented the fracture half-length is 200 ft., the fracture height is 200 ft., the proppant mass in each fracture is 200 M-lbm, the Young's modulus of the pay zone is 2 MMpsi, the Poisson's ratio is 0.2 and the *in-situ* horizontal stress contrast is 200 psi. For this particular scenario, a region of low horizontal stress contrast is developed for 200 ft. bookend fracture spacing, the spacing between the first fracture and the third fracture; however the direction of the intermediate stress in the middle of the bookend fractures is longitudinal. Thus, there is a high probability that if we try propagating a fracture in the middle of the two existing fractures for this case, it would create an inefficient completion by intersecting either or both of the existing fractures. Whereas, increasing the bookend fracture spacing to 205 ft., the low horizontal stress contrast region becomes larger and we get a small zone of transversely directed intermediate principal stress. This increases the probability of the fracture that is initiated between the two bookend fractures to grow transverse and away from the wellbore while tapping into the pre-existing complex fracture network. A region of low horizontal stress contrast is consistently obtained between the bookend fractures till approximately 225 ft. bookend fracture spacing. At this spacing, a small region of higher horizontal stress contrast (local horizontal stress contrast greater than 50 psi is classified as higher horizontal stress contrast here) is observed close to the wellbore between the bookend fractures. This implies that a fracture that initiates in this region will propagate transverse and away from the wellbore and will tap into the natural fracture network in the low horizontal stress contrast region. However, beyond a bookend fracture spacing of 230 ft. the low horizontal stress contrast region disappears from the middle of the bookend fractures and hence now though we still have a transverse second

fracture there is a much lower probability of this fracture tapping into the existing natural fracture network.

Figure 2.31 and Figure 2.32 help in quantifying the observations from Figure 2.30. Figure 2.31 shows the variation in the horizontal stress contrast and reorientation angle along the wellbore between the two bookend fractures. Figure 2.31a illustrates the decrease in horizontal stress contrast between the two bookend fractures. At the smallest fracture spacing considered (200 ft.) we observe only one minimum in the curve of horizontal stress contrast vs. the distance between the fractures. At larger fracture spacing we get two minima and with an increase in the fracture spacing these minima are seen to move closer to the bookend fractures. As these minima move away, the horizontal stress contrast peaks to a high value between the minima. This local maximum between the minima increases with an increase in the bookend fracture spacing. Figure 2.31b, shows the reorientation angle along the wellbore between the two bookend fractures. At the lowest bookend fracture spacing considered (200 ft.) it is evident that the local stresses completely reverse direction, while at higher fracture spacing the region of stress reversal between the bookend fractures decreases with the increase in bookend fracture spacing. Based on these plots, if the bookend fracture spacing is between 205 ft. and 215 ft., the middle fracture will initiate in a region of extremely low horizontal stress contrast and hence possibly tap into the natural fracture network in the reservoir. This range of optimal bookend fracture spacing is narrow. Technological advances should allow the operators to achieve this range of depth tolerance. If such depth tolerance is not achievable in the field it would be more practical to err on the higher side of the suggested range. For example, in this particular example if the depth tolerance of 10 ft. is not achievable, the chosen bookend fracture spacing should be such that the attained bookend fracture spacing is not less than 205 ft. This is because less than a 205 ft.

bookend fracture spacing the probability of getting longitudinal fractures will be high thus leading to an inefficient completion.

Figure 2.32 shows the variation in horizontal stress contrast and reorientation angle away from the wellbore in the middle of the two bookend fractures. Figure 2.32b shows that the angle of reorientation is less than 10 degrees for bookend fracture spacing more than 205 ft. in the middle of the bookend fractures. Thus the middle fractures in these cases of higher bookend fracture spacing should propagate transverse from the wellbore. For the particular case of bookend fracture spacing equal to 205 ft., the middle fracture will tend to initiate away from the wellbore and then should change direction based on the reorientation angle as well as the low horizontal stress contrast. Figure 2.32a shows that for the case of bookend fracture spacing equal to 205 ft. the horizontal stress contrast in the middle of the bookend fractures stays at a value less than 30 psi. This makes the conditions conducive for the middle fracture to tap into the existing natural fracture network. On the other hand, the horizontal stress contrast in the middle region increases with an increase in the bookend fracture spacing. Thus the fractures in these cases of higher fracture spacing will tend to propagate transverse and away from the wellbore yet will have a lower probability of taping into the existing natural fracture network.

2.3.4.5 Effect of in-situ horizontal stress contrast and Young's modulus.

Figure 2.33 and Figure 2.34 describe the effect of the *in-situ* horizontal stress contrast, Young's modulus of the pay zone, and the proppant mass per stage on the optimum bookend fracture spacing. The optimal bookend fracture spacing is defined by the following two criteria:-

- The middle fracture should initiate in a region of negligible stress reorientation angle, and
- The region in the middle of the bookend fractures should fall in a region of horizontal stress contrast less than 50 psi.

Thus, based on Figure 2.31 and Figure 2.32, bookend fracture spacing of 205 ft. – 225 ft. satisfy both these criteria. Thus the optimal fracture spacing is defined by the mean of the range i.e. 215 ft. with a tolerance of $\pm$ 10 ft.

From Figure 2.33 and Figure 2.34 we observe that an increase in proppant mass per stage leads to an increase in the optimum fracture spacing. As explained in an earlier section of this chapter, this happens because of increased stress interference caused by a wider fracture for a higher proppant mass per stage.

Figure 2.33 represents the analysis done on a pay zone with a Young's modulus of 4,000,000 psi for fractures that are 200 ft. in height and have half-lengths between 200 and 400 ft. (as presented). We notice that the *in-situ* horizontal stress contrast is highly consequential in defining the amount of proppant mass to be placed into the fracture. For example, for a fracture half-length of 300 ft. and the optimal bookend fracture spacing of 200 ft., we require approximately 150,000 lbm proppant per stage for a horizontal stress contrast of 200 psi while we require approximately 225,000 lbm proppant per stage for a horizontal stress contrast of 400 psi. Similarly from Figure 2.34, we need 200,000 lbm proppant per stage for a horizontal stress contrast of 200 psi for an optimal bookend fracture spacing of 300 ft. for a 300 ft. half-length fracture while we need 300,000 lbm proppant per stage for a horizontal stress contrast of 400 psi for the same bookend fracture spacing and fracture length.

Comparing Figure 2.33 and Figure 2.34 we see that we need less proppant per stage in a higher Young's modulus environment to get the same optimal fracture spacing.

For example for an *in-situ* horizontal stress contrast of 200 psi, fracture half-length of 300 ft. and optimal fracture spacing of 300 ft., we need 200,000 lbm proppant in the case of higher Young's modulus (6,000,000 psi) and 300,000 lbm proppant in the case of lower Young's modulus (4,000,000 psi). Another noticeable feature of the figure is that the error bar associated with the different cases increases in size with an increase in Young's modulus but decreases in size with an increase in horizontal stress contrast.

2.3.5 Impact of Fracture Closure on Stress Shadow

In the previous section (2.3.1) an analytical method to study the impact of fracture closure on the stress shadow around the main closing fracture was discussed. In this section, we study numerical fracture closure. Then we study the impact of the closure of Induced Unpropped (IU) fractures. IU fractures are unpropped fractures that are created during a hydraulic fracturing treatment.

The analytical expressions presented in (2-16) provide one way of understanding the relation between fracture spacing and the time between stages. However these methods are only valid for cases where fractures are radial. Predicting the time of closure of fractures of arbitrary shapes requires the use of numerical simulations.

Figure 2.35 shows the contour of the minimum principal stress for various times during fracture closure. The figure depicts the decrease in the stress shadow with fracture closure. The stress distribution near the tip represents singularity effects. Though the figure depicts a decrease in the stress shadow in the vicinity of the fracture during fracture closure, the tip effects persist. This stress singularity exists after fracture closure due to the application of a fixed displacement boundary condition. This set of figures should be treated as a schematic.

Figure 2.36 and Figure 2.37 attempt at quantifying the impact of fracture closure on the stresses in the vicinity of the factures for a particular set of *in-situ* parameters. The fracture is created by assuming an average treatment pressure value (~10,000 psi). The *in-situ* minimum principal stress (S_{hmin}) is assumed to be 7372 psi and is assumed to be in the direction perpendicular to the simulated fractures. The *in-situ* intermediate principal stress (S_{hmax}) is assumed to be 7472 psi and is assumed to be in the direction along the fracture length. Reservoir pressure is assumed to be 6000 psi. Reservoir permeability and porosity are assumed to be 1 micro-Darcy and 5%. The fracture is located at 0 ft. in the chart. The fracture in this simulation was assumed to have a half-length of 300 ft., and total height of 100 ft.

This average treatment pressure is higher than the pressure required to prop-open a fracture to the propped fracture width. Thus the fracture is opened to a greater width than before because of the excess fluid pressure. The fracture treatment time is assumed to be 2 hours during which the pressure inside the fracture is assumed to be constant at the average treatment pressure value. After this the above mentioned fracture closure procedure is applied to get the fracture to close. In this simulation the fracture closed from its initial width to the final propped width in about 200 minutes. A good explanation of the time of closure and its dependence on various factors such as reservoir permeability, existing fracture networks etc. is discussed above. This time of closure in the simulation is not representative of the values observed in the field because of several reasons. The permeability assumed here is greater than the permeability of the reservoir matrix. The effective surface area of fracture contact with the reservoir is not correctly modeled in this simulation since the presence of a network of fractures connected to the main hydraulic fracture is not modeled. This network of fractures can be very efficient in driving the fluid away from the main hydraulic fracture. However, the closure time has a

similar order of magnitude as the fracture closure times observed in the field in mini-frac and DFIT tests. The closure times in our simulations have not been calibrated against field data and only provide a possible impact of leak-off and fracture closure on the stress interference. In direct comparison between the simulation results and the field results we need to include a lot of other factors, such as, the amount of fluid pumped in the field test, the effect of fluid rheology and including the actual treatment data in the simulations. This will be discussed in detail in the next chapter.

Figure 2.36 shows that the minimum principal stress caused by the open fracture reduces in the vicinity of the fracture in time. The time shown in the figure is the time after the pumping into the fracture is stopped. The high stresses seen in this figure are a direct result of the treating pressure assumed. Immediately next to the fracture face this pressure increases the *in-situ* stress. Clearly this high stress region is transient (as shown in the figure) and localized (spatially). The figure depicts that the decreasing width of the fracture over time quickly decreases the stress shadow in the vicinity of the fracture. Figure 2.37 shows the effect of fracture closure on the horizontal stress contrast over time. Fracture closure leads to sharp changes in the horizontal stress contrast at distances up to 400 ft. from the fracture face. From the figure it is easy to observe that the stress contrast decreases from about 1200 psi to about 400 psi at a distance of 100 ft. from the fracture in about 3.5 hours. Also, the region of almost negligible horizontal stress contrast shifts from about 600 ft. away from the fracture after 10 minutes to about 400 ft. from the fracture after 3.5 hours. This region of negligible horizontal stress contrast has been discussed to be the extent of the region of stress reversal. More on that is discussed above. Thus, the movement of the region of lowest horizontal stress contrast has implications on the trajectory of the successive fractures. A high value of horizontal stress contrast could suggest the opening of unpropped fractures in Mode II or Mode III

while a low value of horizontal stress contrast can enable the successive fractures to harness the heterogeneity of the reservoir in Mode I and allow the successive fracture to develop into a complex fracture network (Jaeger et al. 1979; Zoback 2007). Thus the effect of fracture closure over time on the stress shadow is an important consideration when designing hydraulic fracturing treatments.

2.3.5.1 Induced unpropped (IU) fracture closure and stress shadow

The effect of a propped fracture can be understood by assuming a propped width and calculating the stress shadow of the fracture at that width. IU fractures are created because of the local heterogeneities in the formation. These IU fractures are believed to be of a much smaller initial width.

It is likely that not all fractures created during a hydraulic fracturing treatment carry proppant. In Figure 2.38 we show the computed effect of opening propped fractures and unpropped fractures on the *in-situ* stresses. The figure shows a contour map of the minimum principal stress in the reservoir. In the simulation to generate Figure 2.38, three fractures of different lengths but the same fracture pressure were initially created at a distance of 75 ft. from each other. The middle fracture was chosen to be longer and was assumed to be a propped fracture in the simulation, while the two outer fractures were assumed to be unpropped fractures. The propped fracture's geometry was held constant during the course of the simulation while the unpropped fractures were allowed to close over time in the simulation. This simulation could be thought of as simulating a field scenario in which the three clusters in a single fracture stage are stimulated. Alternatively, this represents a propped fracture with two unpropped outer fractures. The middle fracture is assumed to be the longest and contains all the proppant. The outer fractures are assumed to be shorter and are assumed to not have any proppant. All the

fractures are, however, assumed to open at the same fracturing pressure. This fracture pressure is the fracture closure pressure for the propped fracture but should be considered as the initial pressure of the outer fractures. Once the fracture treatment is completed, the middle fracture retains the geometry but the outer fractures close because of pressure dissipation and fluid leak-off.

The figure shows that the stress shadow of the unpropped fractures is reduced as time progresses. This information is very consequential when fracturing consecutive stages in a horizontal well. The presence of a large stress shadow can lead to fracture interference. Open, induced unpropped (IU) fractures have a strong influence on the direction of growth of subsequent fractures. However, as these fractures close, the stress shadow shrinks. This implies that there is a clear advantage to establishing a time delay between two adjacent fractures.

Figure 2.39 quantifies the contour plots of Figure 2.38. Over the span of 10 hours (as shown in the figure) that it takes to close the unpropped fractures, the minimum principal stress in their vicinity decreases from about 8300 psi to 7800 psi. This 500 psi decrease could be deemed sufficient to reorient successive fracture treatments that allow fractures to propagate in the shadow of the open fracture networks of the previous stage. Thus the time between successive stages in a horizontal well can substantially change the interaction between spatially adjacent fractures in a wellbore.

The closure time is controlled by two factors, the leak-off coefficient and the initial width (Eq. (2-12)). For the same leak-off coefficient the IU fracture closure time is significantly smaller than the hydraulic fracture closure time. However, unlike hydraulic fractures, IU fractures generally will not have a large effective area for leak-off. Hence the effective leak-off coefficient used for the IU fractures should be considerably smaller than the effective leak-off coefficient for the hydraulic fracture.

In Figure 2.5 we showed that reducing the leak-off coefficient by 10 times increases the time of fracture closure by 100 times. Figure 2.6 shows that for the same leak-off coefficient a change in initial width leads to a change in the fracture closure time. Also note that the stress change in the bigger initial width case is much larger than the stress change in the smaller initial width case. The smaller initial width case is more representative of IU fractures. It is clearly seen that reduction in the leak-off coefficient and reduction in the initial width causes the closure time to be the same for the IU fracture as the main hydraulic fracture, however, the stress change because of an IU fracture is seen to be much lower than the stress change because of a hydraulic fracture. Thus the impact of an IU fracture on the stress shadow of a hydraulic fracture network is insignificant. However, the closure time remaining the same implies that the IU fracture remains propped open for a long time. One potential repercussion of this is that the fracture created in the subsequent stage may potentially lose fluid into the still open IU fracture created by the previous fracture stage. A schematic of how this overlap may lead to biased stimulated regions is presented in Figure 2.40. We assume that it requires t_p minutes to pump a fracture stage. The delay time Δt is defined as the time between the end of a treatment stage and the start of another treatment stage. We assume this delay time Δt to be constant for all stages in both the cases considered. Figure 2.40 qualitatively shows the stimulated areas for a consecutive fracturing sequence at different times during the fracturing. Figure 2.40a shows the stimulated area at the time pumping is stopped for the 1st stage of fracturing. Comparing Figure 2.40a and Figure 2.40b we can see that at the time the 2nd fracture has initiated the stimulated area of stage 1 has decreased. Figure 2.40c shows that while the stimulated area of the 1st stage continues decreasing, the stimulated area created by the 2nd hydraulic fracturing stage is preferentially oriented towards the previous stage and has excessive overlap with the fracture network of the

previous stage. Finally Figure 2.40d shows the overlap between the stimulated areas of the two stages when the 3rd stage fracture is initiated thus depicting wastage of fluid into pre-stimulated regions of the formation.

2.4 CONCLUSIONS

The analysis of the stress shadow of hydraulic fractures presented in the Chapter reveals the following conclusions that need to be considered when designing hydraulic fracturing treatments in the field:

- Hydraulic fractures alter the stress distribution in their vicinity. The spatial extent of the stress shadow decreases with time because of the closure of both propped and induced unpropped (IU) fractures.
- The spatial extent of the stress shadow region is large immediately after pumping a hydraulic fracturing treatment and reduces considerably with time because of fluid leak-off and fracture closure.
- The ISIP trends measured during the completion of a horizontal well have surprising implications with regard to fracture-to-fracture interference. These pressure trends can act as an inexpensive diagnostic method to evaluate the extent of fracture interference.
- The up-and-down variations of the net pressure from one stage to the next can indicate propagation of transverse fractures into previously stimulated regions of the reservoir and suggest an insufficient spacing of the fracture stages.
- Fracture spacing (which is affected by both stage spacing and cluster spacing), is the most important operator controlled parameter that can be used to control the extent of fracture interference. Non-intersecting fractures are obtained above a

critical value of the fracture spacing. Under such conditions transverse fractures are shown to propagate while still being subject to stress-shadowing effects.

- More data for estimating the closure pressures for each stage are required. Using accurate values of the net closure pressures from stage-to-stage, a better understanding of fracture orientation and interference can be obtained.
- The model provides qualitative trends for changes in the efficiency of the fracture treatment. However, the model-based conclusions should be coupled and confirmed with microseismic and production logging data.
- The stress shadow caused by fractures creates zones of reduced horizontal stress contrast in the vicinity of these fractures. These zones of low horizontal stress contrast are more conducive to the creation of complex fracture networks, the opening of natural fractures which can lead to better connectivity with a natural fracture network.
- The generated horizontal stress contrast initially increases and then reaches a minimum value at a certain distance from the fracture. In most cases this minimum value of horizontal stress contrast coincides with a change in the direction of the intermediate stress. Thus if successive fractures are initiated in this region of low horizontal stress contrast and negligible stress reorientation angle, the second fracture will be much more likely to tap into the natural fracture network existing in the reservoir.
- An alternate fracturing sequence has been discussed in previous work. This alternate fracturing sequence (sometimes referred to as the Texas Two-Step fracturing sequence) has been hypothesized to reduce the effective fracture spacing in a horizontal wellbore and lead to more efficient completions and possibly larger number of fractures. It has now become feasible to implement this

fracturing sequence with the use of new sliding sleeve tools on coiled tubing, that allow single fractures to be pumped in any desired sequence.

- In this work we have shown that an alternate fracturing sequence can be effectively used to tap into the natural fracture network. We observed that the stress reorientation caused by the presence of fractures causes the horizontal stress contrast in the middle of the bookend fractures to be reduced to negligible values for a range of bookend fracture spacing. Thus planning the completion design to make this happen can allow the middle fractures to tap into the naturally fractured reservoir.
- The most significant parameters that influence the location and extent of these low horizontal stress contrast zones between bookend fractures are Young's modulus of the pay zone, *in-situ* horizontal stress contrast, fracture geometry, and proppant mass per stage.
- Interference between fractures in a given wellbore depends on the stress shadow created by both the propped fracture and the induced unpropped (IU) fractures.
- More fracture interference is expected to occur if the time between successive fractures is small, which may lead to poorer fracture performance as a result of re-stimulation of previously fractured regions.
- Conversely, if the time between successive fractures in a wellbore is increased long enough for the IU fractures to close, the stress shadow region shrinks leading to less interference between fractures and better performing fractures. These effects are clearly shown to be significant through our geomechanical simulations and through analysis of field data.
- The closure time for IU fractures is dependent on the amount of fluid pumped, fluid rheology, reservoir permeability and the fracture face area. For

unconventional reservoirs with a large number of planes of weaknesses/natural fractures/other local heterogeneities, the time of fluid leak-off can be reduced considerably and hence the closure time can also be reduced considerably.

We make the following recommendations based on the analysis shown in this chapter:

- The net closure pressure values are sensitive to both formation properties and treatment variables. Amongst formation properties, Young's modulus and the *in-situ* horizontal stress contrast have a very significant impact. Amongst the treatment variables, while the fracture length and the proppant mass share a complementary effect, decreasing fracture spacing leads to increasing stress interference between the fractures.
- We recommend the alternate fracturing sequence or higher than usual stage spacing (200 ft. - 300 ft.) in the Barnett shale gas play because of its characteristic properties. A combination of high Young's modulus and low deviatoric stress in the Barnett Shale indicates a risk of underestimating fracture spacing.
- Unlike the Barnett, the Bakken and Eagle Ford shales are soft and a lower stage spacing should allow efficient reservoir drainage without the danger of fracture interference.
- Since the proppant mass pumped per stage controls the width of the fracture and hence the amount of rock deformation, decreasing the amount of proppant pumped per stage may allow fracture stages to be more closely spaced while maintaining transverse fracture propagation.
- The major parameters that influence the extent of the low stress region are Young's modulus, fracture half-length, fracture height, proppant mass-per-stage, and *in-situ* horizontal stress contrast.

- To obtain more fracture complexity using the alternate fracturing routine, an increase in proppant mass per stage, decrease in fracture lengths, increase in Young's modulus or decrease in horizontal stress contrast can independently lead to greater mechanical interference and hence the bookend fractures need to be spaced farther apart to enable the low horizontal stress contrast zone in the middle of the bookend fractures to be fully used.
- The relation presented above allows an engineer to estimate the time needed for the stress shadow to decay to an acceptable value. This time will depend on various factors such as the fracture spacing, the elastic moduli etc. which are all accounted for in the simple dimensionless relation presented above.
- We present a simple dimensionless analytical expression relating the variation of the stress interference to time between adjacent fractures (and all other important parameters). This relation can be used by a completions engineer to optimize both the spacing between adjacent fractures as well as the time required to reduce the stress interference to an acceptable value.

2.5 NOMENCLATURE

α	= Biot's coefficient	dimensionless
A	= fracture face area (one wing)	L^2, m^2
cf	= empirical convergence factor	dimensionless
C_L	= leak-off coefficient	$LT^{-0.5}$, $m/s^{0.5}$
ε_{ij}	= total stress tensor	$ML^{-1}T^2$, Pa
E	= Young's modulus	$ML^{-1}T^2$, Pa
E_b	= Young's modulus of bounding layers	$ML^{-1}T^2$, Pa
E_p	= Young's modulus of payzone layer	$ML^{-1}T^2$, Pa
ϕ	= porosity	dimensionless
ϕ_{frac}	= fracture porosity	dimensionless
g_i	= gravitation vector	LT^{-2}, m/s^2
G	= Shear modulus	$ML^{-1}T^2$, Pa
h_f	= fracture half-height	L, m
h_p	= payzone half-height	L, m
Hf	= fracture height	L, m
κ	= opening-time distribution factor	dimensionless
k	= permeability	L^2, m^2
K	= bulk modulus	$ML^{-1}T^2$, Pa
K_s	= bulk modulus of the solid	$ML^{-1}T^2$, Pa
K_f	= bulk modulus of the fluid	$ML^{-1}T^2$, Pa
l_f	= fracture half-length	L, m
L_f	= fracture length	L, m
μ	= fluid viscosity	$ML^{-1}T^{-1}$, Pa.s
m_{prop}	= mass of proppant	M, kg
M	= Biot's modulus	$ML^{-1}T^2$, Pa
υ	= Poisson's ratio	dimensionless
υ_p	= Poisson's ratio of payzone layer	dimensionless
υ_b	= Poisson's ratio of boundary layer	dimensionless
P	= pore pressure	$ML^{-1}T^2$, Pa
p_f	= bottom-hole fracture pressure	$ML^{-1}T^2$, Pa
p_{net}	= net closure stress	$ML^{-1}T^2$, Pa
p_{net}^k	= net closure pressure for iteration number k	$ML^{-1}T^2$, Pa
q_i	= specific discharge vector	LT^{-1}, m/s
q_L	= leak-off rate	LT^{-1}, m/s
ρ	= bulk density	ML^{-3}, kg/m^3
ρ_f	= fluid density	ML^{-3}, kg/m^3
ρ_s	= solid density	ML^{-3}, kg/m^3
ρ_{prop}	= proppant density	ML^{-3}, kg/m^3
r_p	= ratio of permeable area to total fracture area	dimensionless
u_i	= displacement vector of solid	L, m
ς	= variation of fluid content	LT^{-1}, m/s

σ_{ij}	= total stress tensor	$ML^{-1}T^{2}$, Pa
σ_{hmin}, S_{hmin}, S_3	= minimum principal stress	$ML^{-1}T^{2}$, Pa
σ_{hmax}, S_{hmax}, S_2	= intermediate principal stress	$ML^{-1}T^{2}$, Pa
σ_v, S_v, S_1	= maximum principal stress	$ML^{-1}T^{2}$, Pa
s_f	= fracture spacing,	L, m
S_p	= spurt loss coefficient	L, m
t	= time	T, s
τ	= dimensionless time	dimensionless
V_i	= initial volume of one wing of a bi-wing fracture	L^3, m^3
V	= current volume of one wing of a bi-wing fracture	L^3, m^3
$\overline{w}$	= average fracture width	L, m
$\overline{w_c}$	= current average fracture width	L, m
$\overline{w_i}$	= initial average fracture width	L, m
w_{max}	= maximum fracture width	L, m
w_{max}^{k}	= maximum fracture width for iteration number k	L, m
w_c	= current maximum fracture width	L, m
w_i	= initial maximum fracture width	L, m
w_f	= final maximum fracture width	L, m
w_t	= maximum fracture width at time t	L, m
ζ	= dimensionless distance from fracture	dimensionless

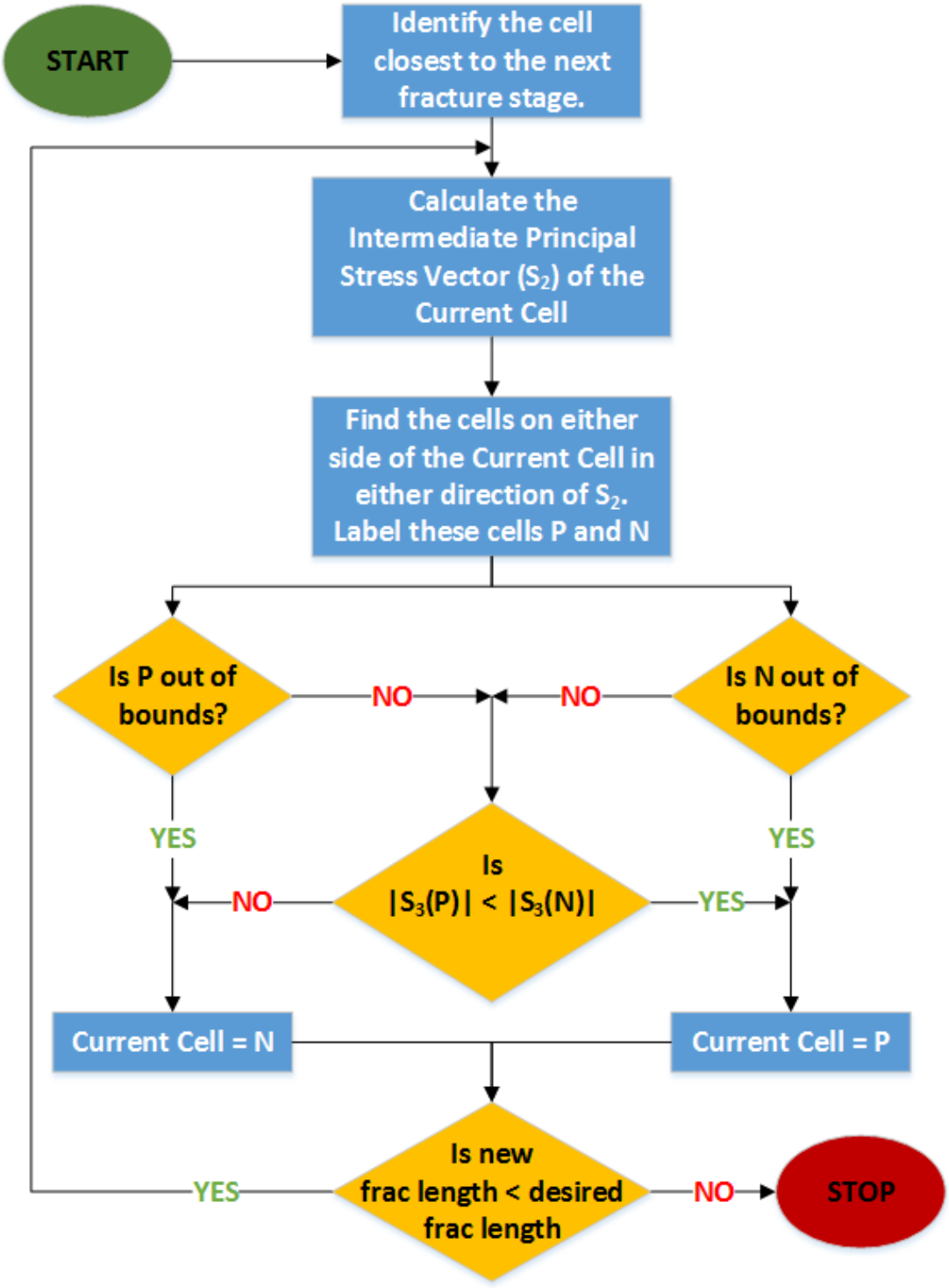

Figure 2.1 Fracture Trajectory Algorithm

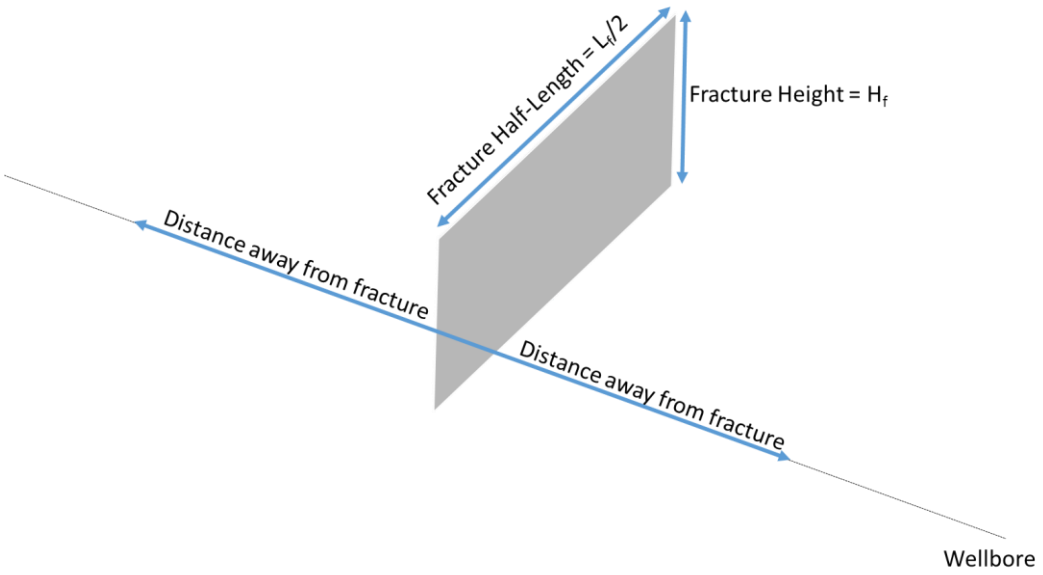

Figure 2.2 Schematic for fracture simulations.

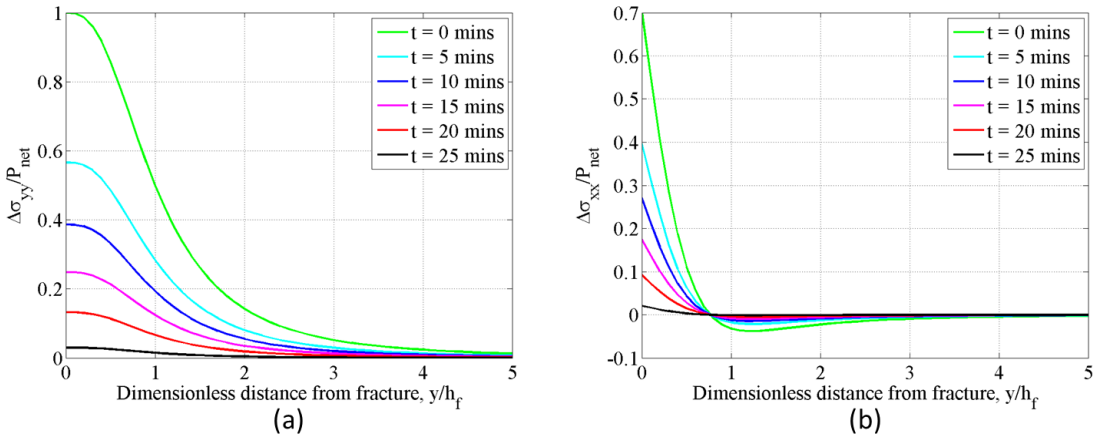

Figure 2.3 Stress variation as a function of distance from a circular crack face and time. Crack is in the XZ plane. (a) stress change perpendicular to the fracture face and (b) stress change in the direction of the fracture face, along the axis of the fracture.

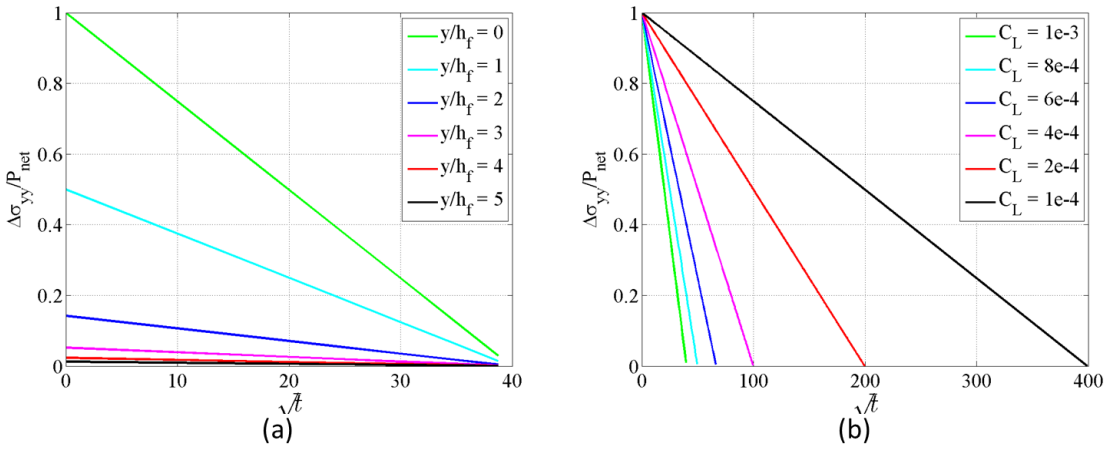

Figure 2.4 Normalized stress variation as a function of square-root of time and (a) as a function of normalized distance from fracture-face for leak-off coefficient=10^{-3} ft./min$^{1/2}$ (b) as a function of leak-off-coefficient for stress variation calculated at the surface of the fracture ($x/h_f = 0$). The leak-off coefficient values are presented in ft./min$^{1/2}$

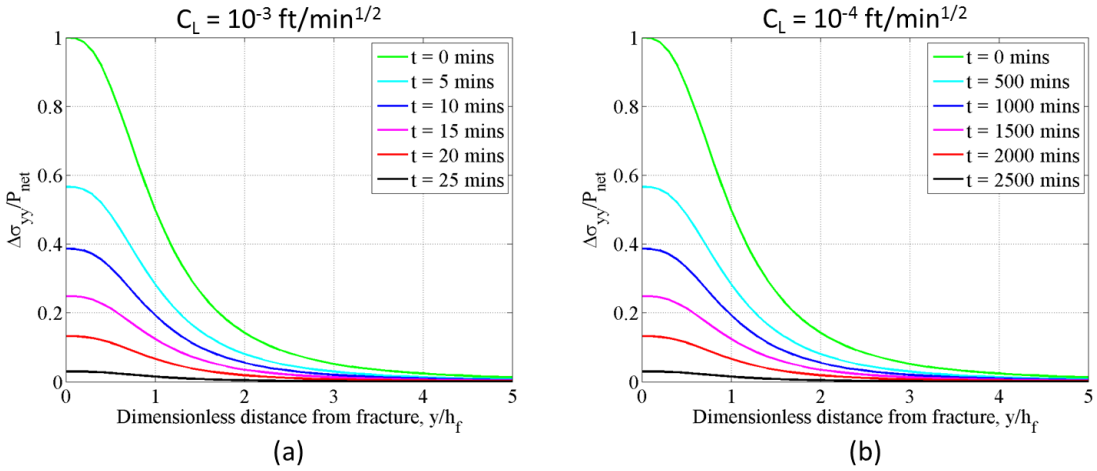

Figure 2.5 Impact of leak-off coefficient on the fracture closure. (a) Leak-off coefficient is 10^{-3} ft./min$^{1/2}$, (b) Leak-off coefficient is 10^{-4} ft./min$^{1/2}$. The leak-off coefficient values are presented in ft./min$^{1/2}$.

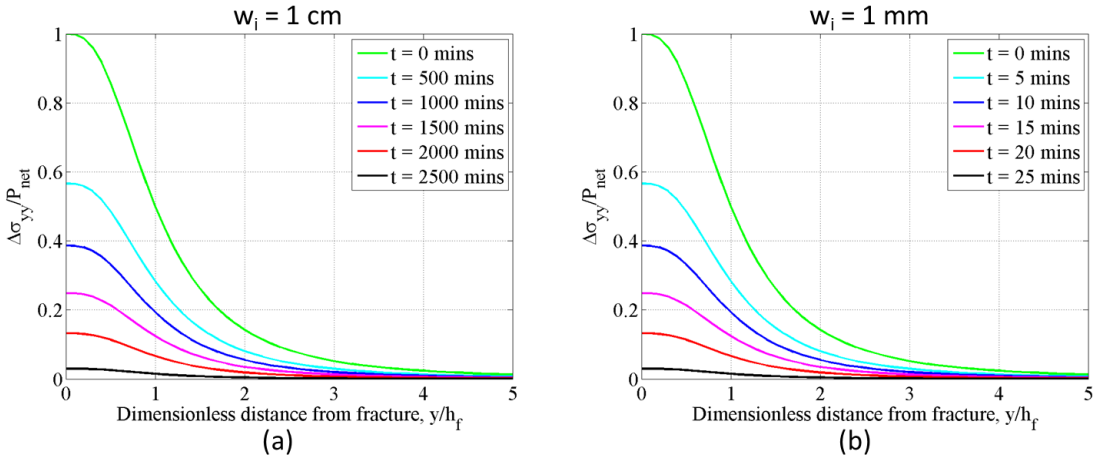

Figure 2.6 Stress change around a fracture over time. (a) Initial width of the fracture is 1 cm, (b) Initial width of the fracture is 1 mm.

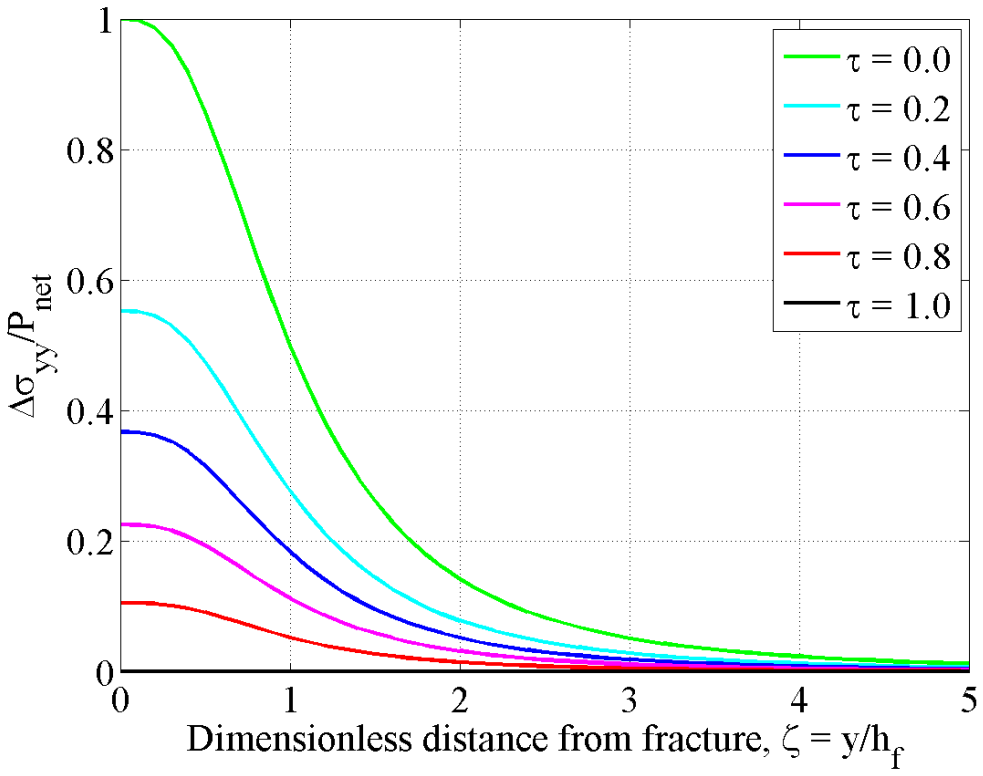

Figure 2.7 General type curves showing the dimensionless stress interference as a function of the dimensionless time and the dimensionless distance from the fracture face (based on Eq. (2-16)).

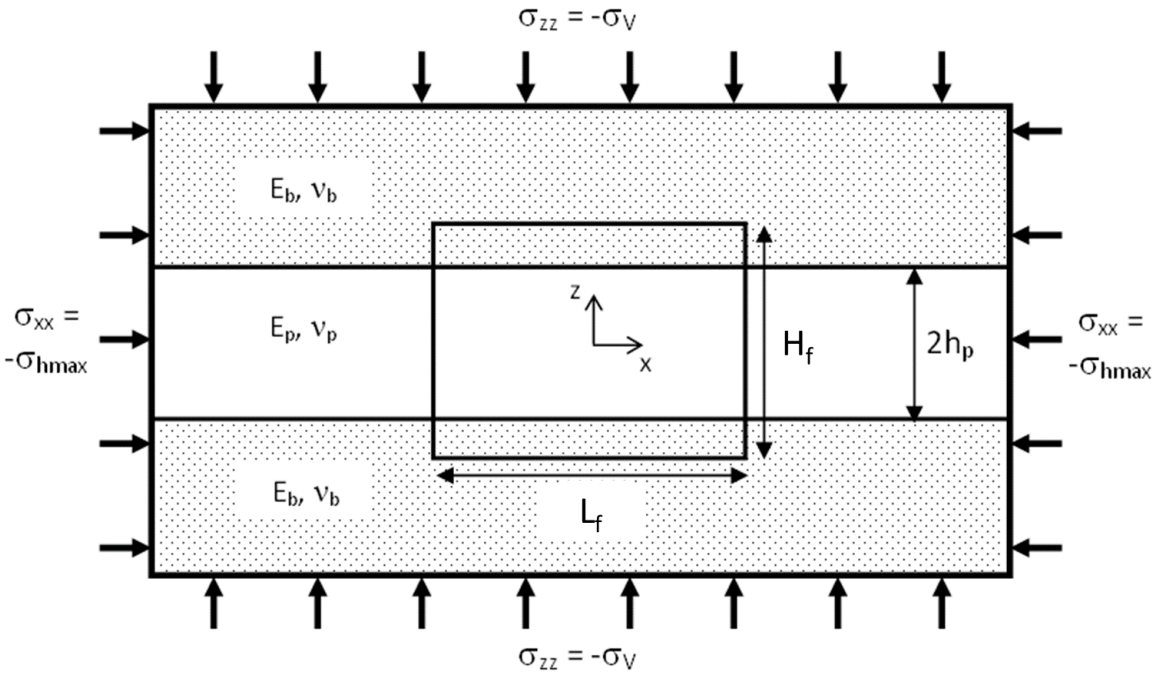

Figure 2.8 Geometry of a vertical fracture in a layered rock (vertical plane) (Roussel and Sharma 2011a, 2011b).

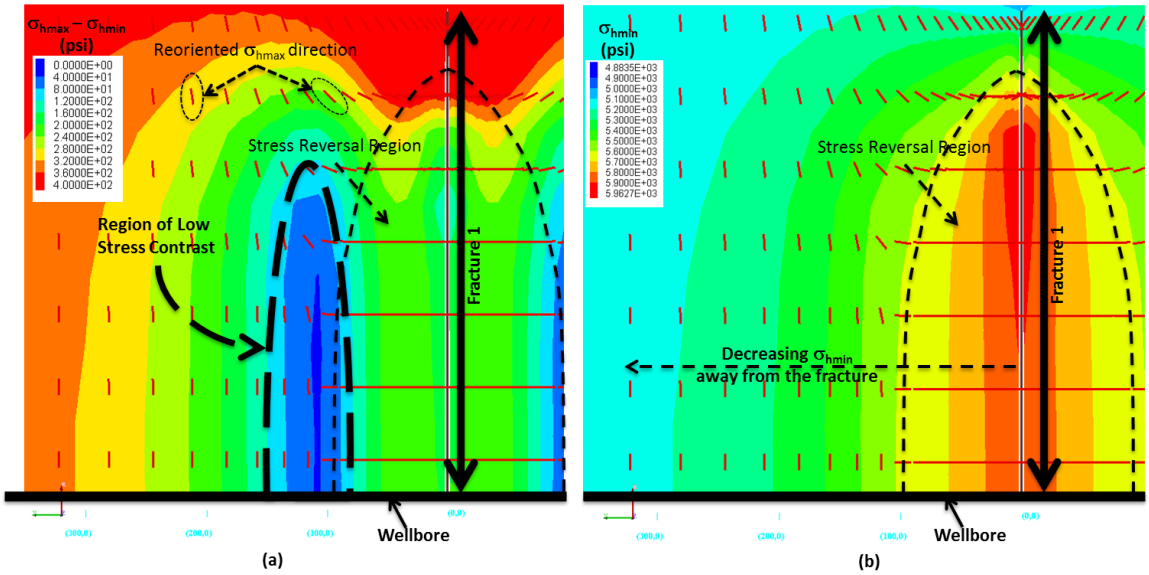

Figure 2.9 (a) Contour map shows the change in horizontal stress contrast ($\sigma_{hmax} - \sigma_{hmin}$), (b) Contour map shows the minimum principal stress magnitude (σ_{hmin}).

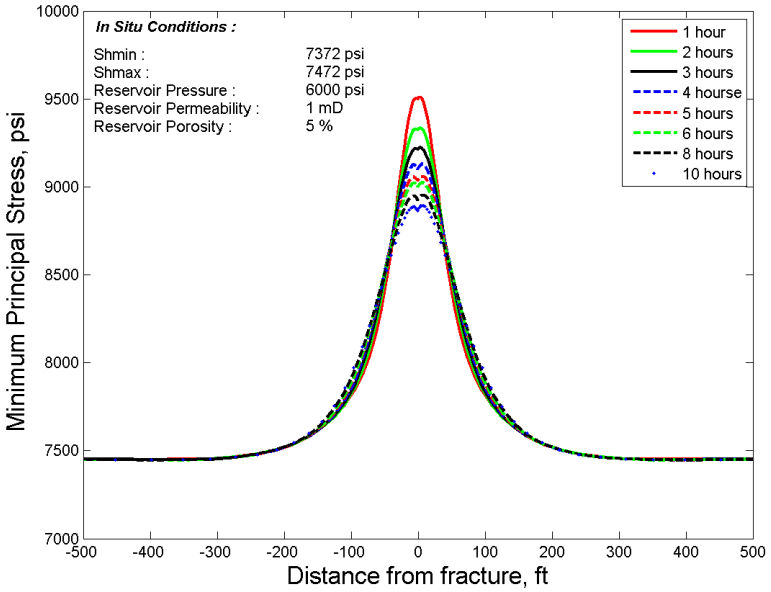

Figure 2.10 Changes in the local reservoir minimum principal stress caused by pressure depletion of a propped fracture. The permeability of the case here is 1 mD permeability.

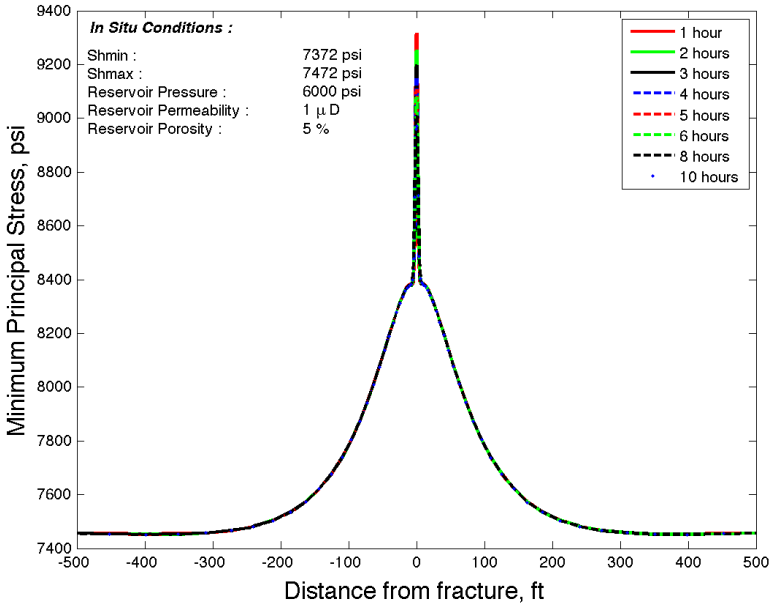

Figure 2.11 Changes in the local reservoir minimum principal stress caused by pressure depletion of a propped fracture with a permeability of 1 μD permeability.

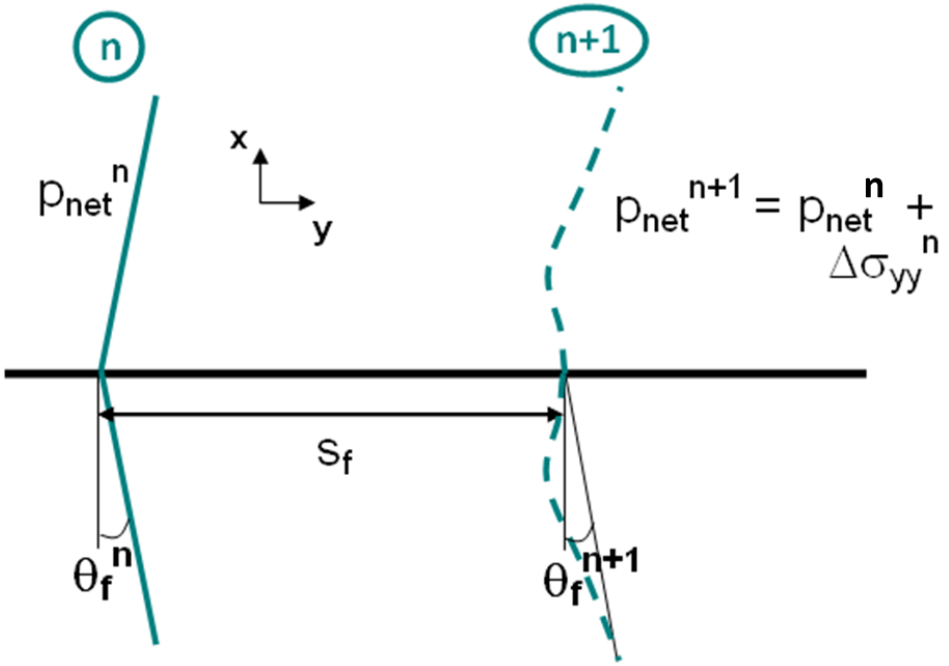

Figure 2.12 Method of calculation of the net closure stress and trajectory of the subsequent fracture in consecutive fracturing.

	Barnett	Bakken	Eagle Ford
Young's Modulus, MMpsi	6.00	2.25	1.50
Poisson's Ratio	0.22	0.25	0.26
Fracture Spacing, ft.	100	100	326
Fracture half-length, ft.	300	300	300
σ_{hmin}, psi	5100	7950	5750
σ_{hmax}, psi	5300	8933	6250
σ_v, psi	8000	9925	8195
Proppant mass, M-lbs	150	185	290.28
Fracture Height, ft.	200	300	400

Table 2.1 Chosen properties for the different base case scenarios

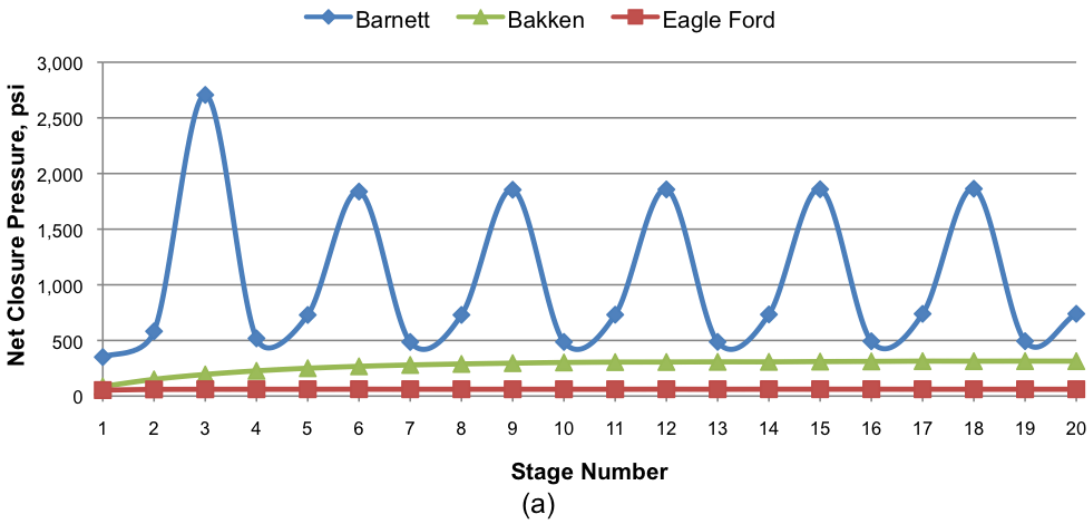

(a)

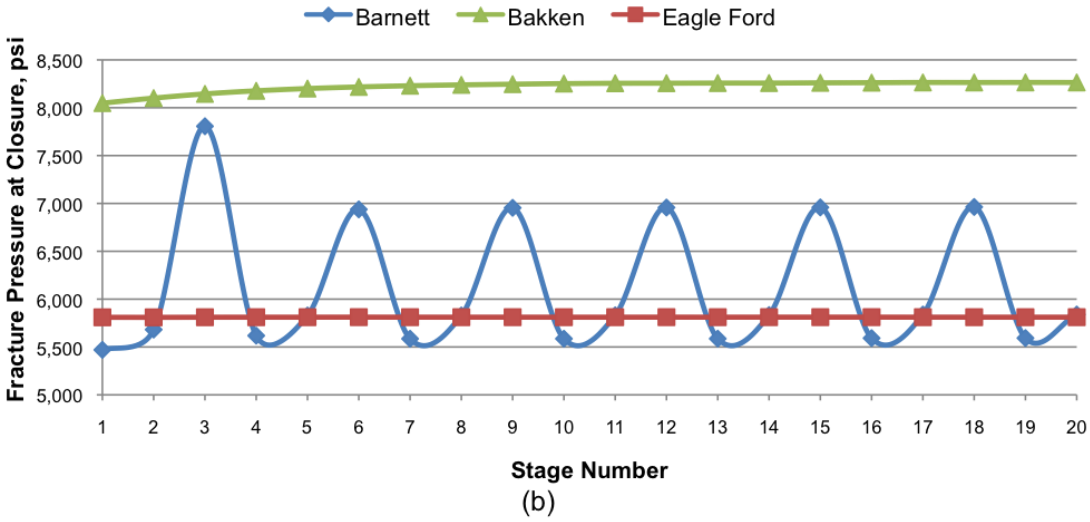

(b)

Figure 2.13 Comparison of the pressure response of the three assumed base cases of the Barnett, Bakken and Eagle Ford formations. (a) Net closure pressure vs. stage number, (b) Fracture closure pressure vs. stage number.

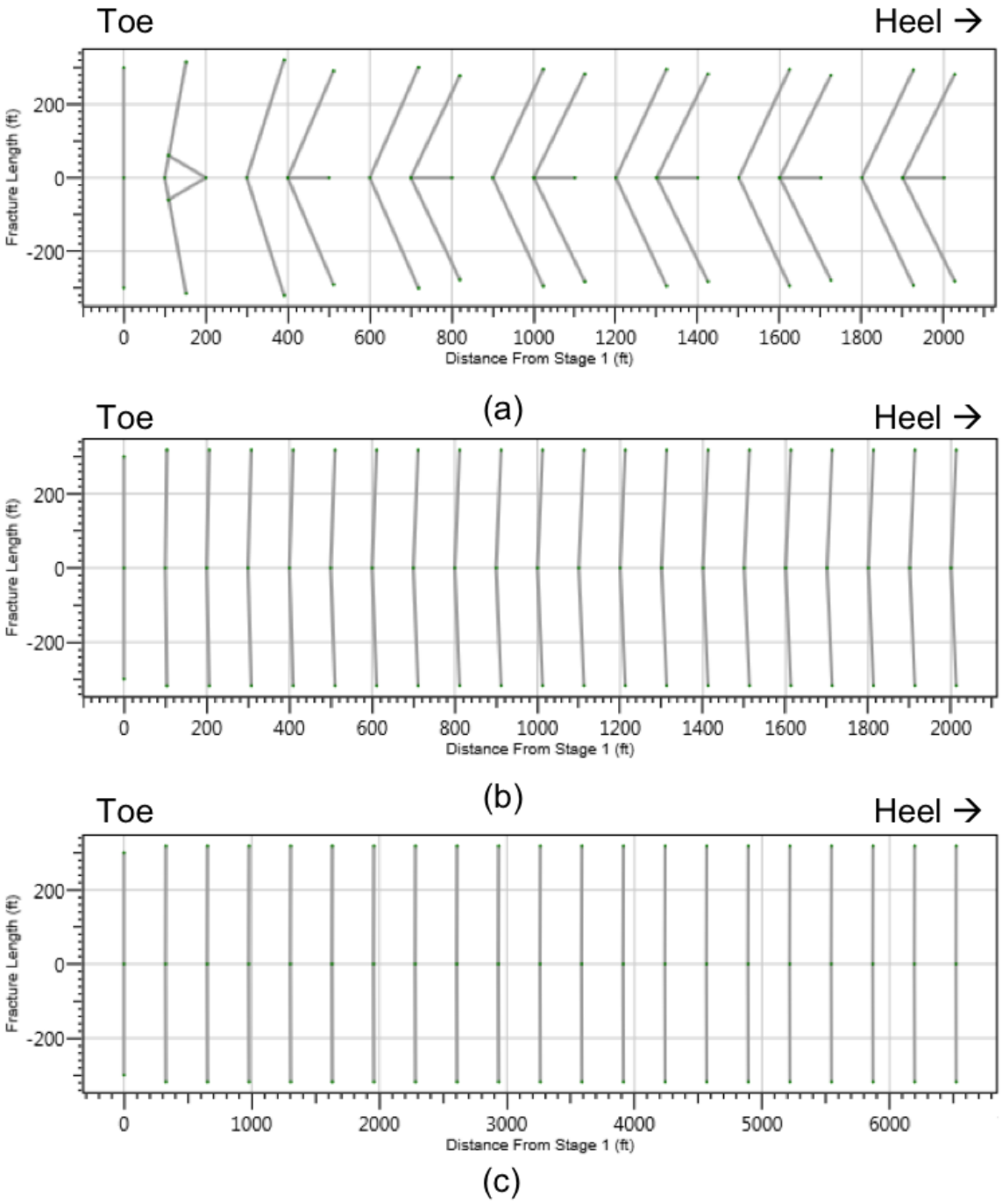

Figure 2.14 Fracture trajectories of the three base cases for 11 consecutive stages. (a) Barnett, (b) Bakken, (c) Eagle Ford.

	Base Case	Case 1	Case 2
Young's Modulus, MMpsi	6	3	9
Poisson's Ratio	0.22	0.18	0.26
Fracture Spacing, ft.	100	50	200
Fracture half-length, ft.	300	150	600
Horizontal stress contrast, psi	200	100	400
Proppant mass, M-lbs	150	75	300

Table 2.2 Chosen properties to study sensitivity for the Barnett base case.

	Base Case	Case 1	Case 2
Young's Modulus, MMpsi	2.25	1.5	4
Poisson's Ratio	0.25	0.1	0.35
Fracture Spacing, ft.	100	50	200
Fracture half-length, ft.	300	150	225
Horizontal stress contrast, psi	1000	250	500
Proppant mass, M-lbs	185	225	350

Table 2.3 Chosen properties to study sensitivity for the Bakken base case.

	Base Case	Case 1	Case 2
Young's Modulus, MMpsi	1.5	0.75	3
Poisson's Ratio	0.26	0.15	0.4
Fracture Spacing, ft.	326	151	609
Fracture half-length, ft.	300	100	450
Horizontal stress contrast, psi	500	100	1000
Proppant mass, M-lbs	290.28	180	473.36

Table 2.4 Chosen properties to study sensitivity for the Eagle Ford base case.

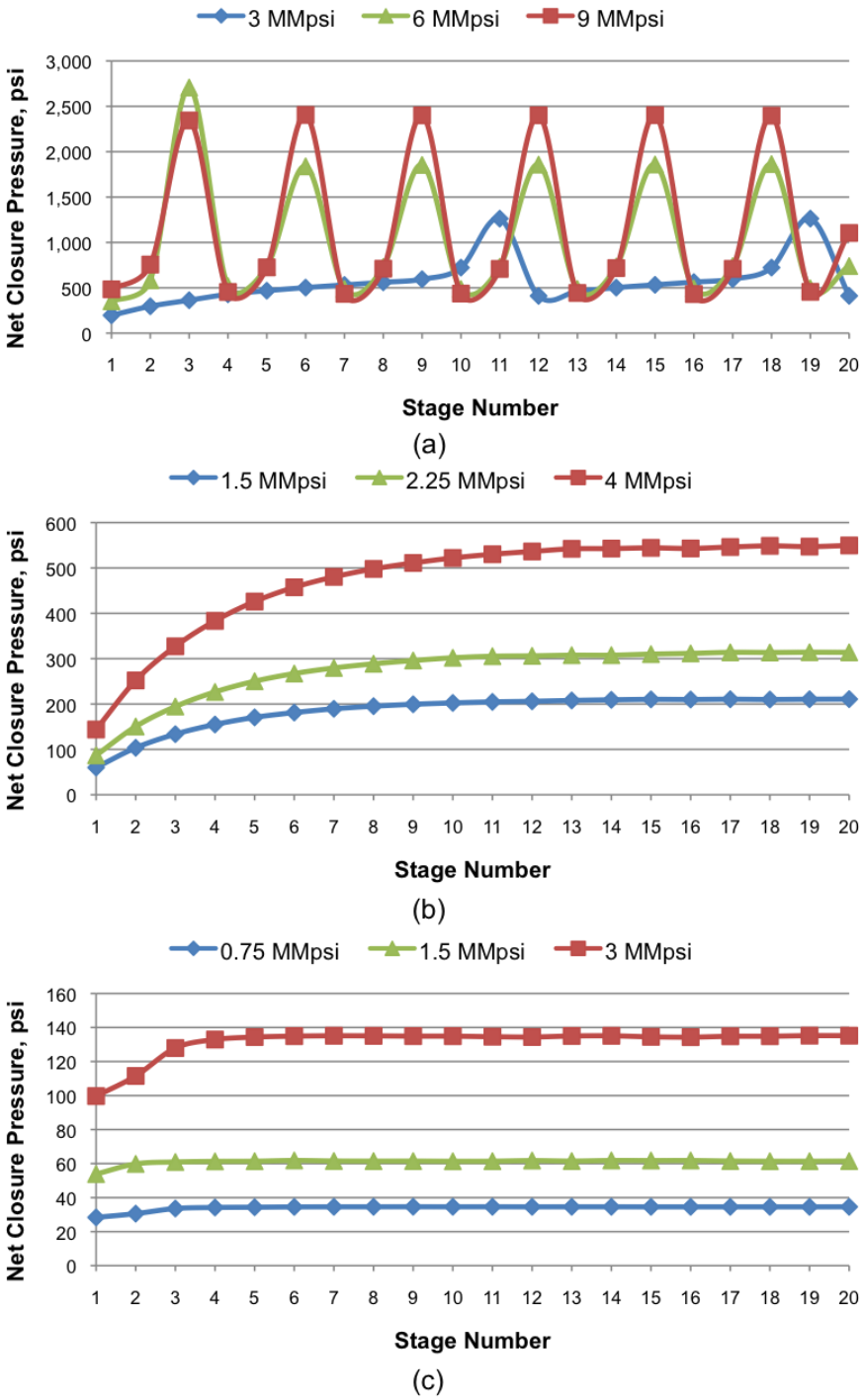

Figure 2.15 Effect of Young's modulus on the net closure pressure response for the (a) Barnett shale gas play, (b) Bakken shale gas play, and (c) Eagle Ford shale gas play.

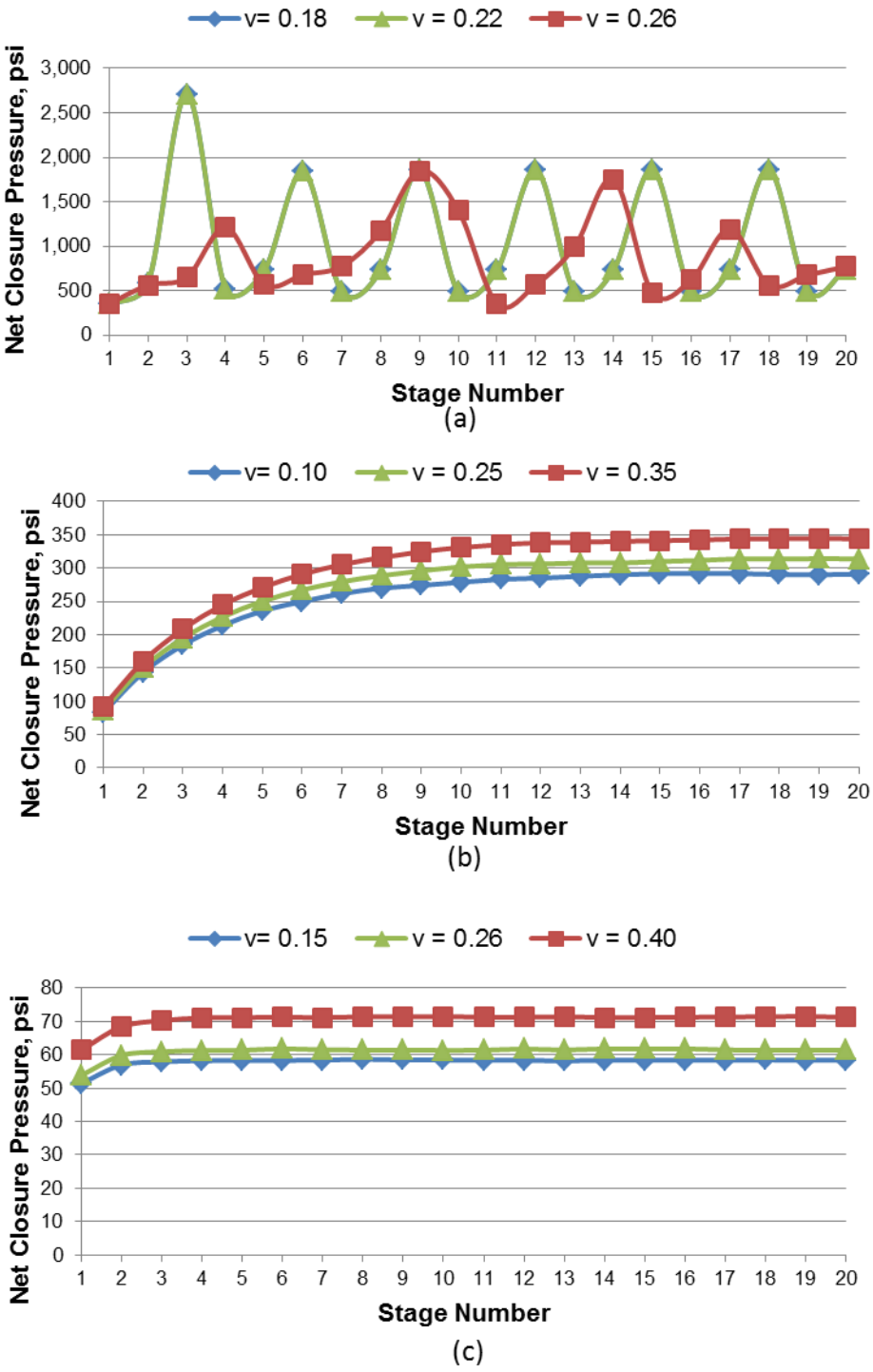

Figure 2.16 Effect of Poisson's ratio on the net closure pressure response for the (a) Barnett shale gas play, (b) Bakken shale gas play, and (c) Eagle Ford shale gas play.

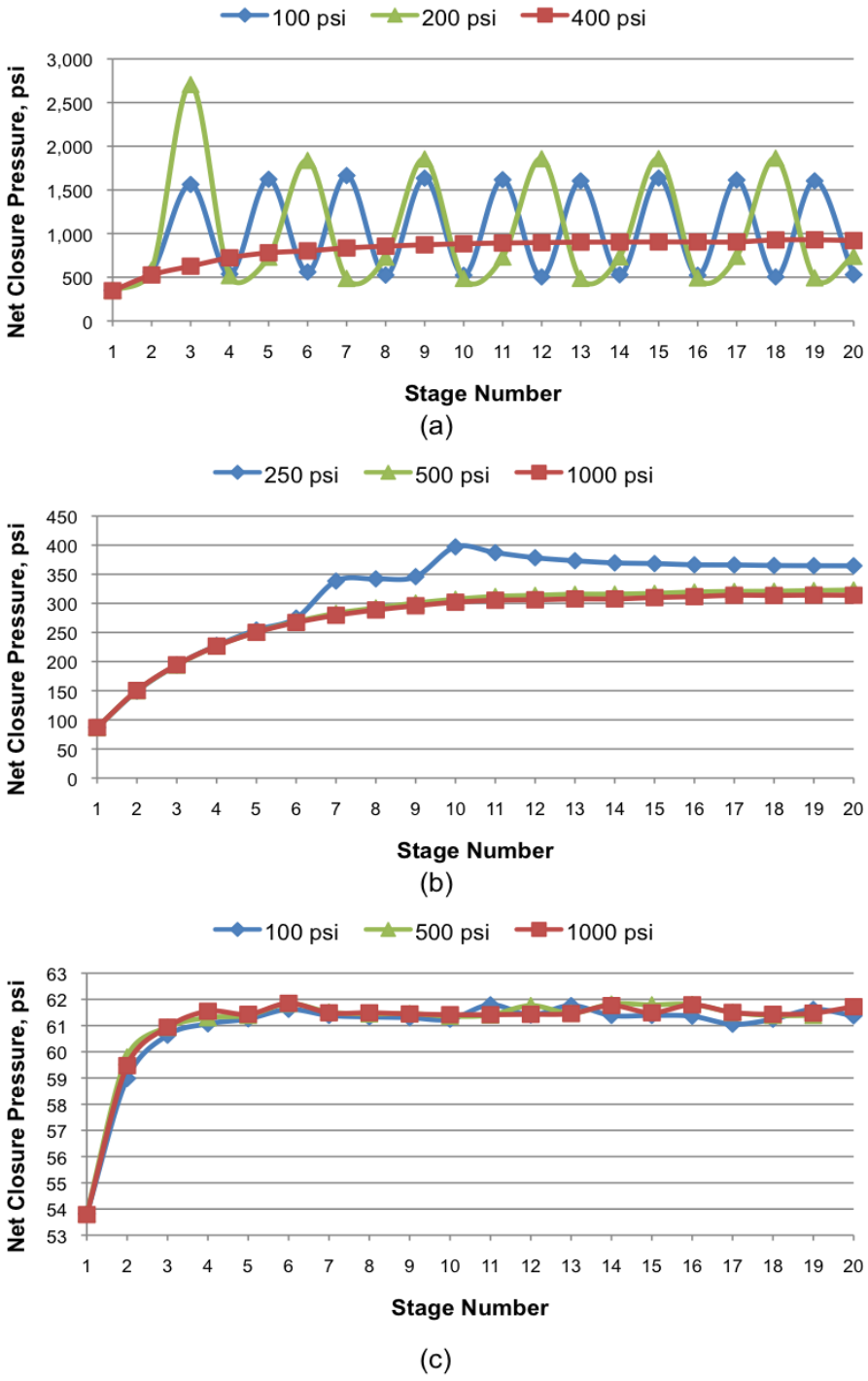

Figure 2.17 Effect of *in-situ* horizontal stress contrast on the net closure pressure response for the (a) Barnett shale gas play, (b) Bakken shale gas play, and (c) Eagle Ford shale gas play.

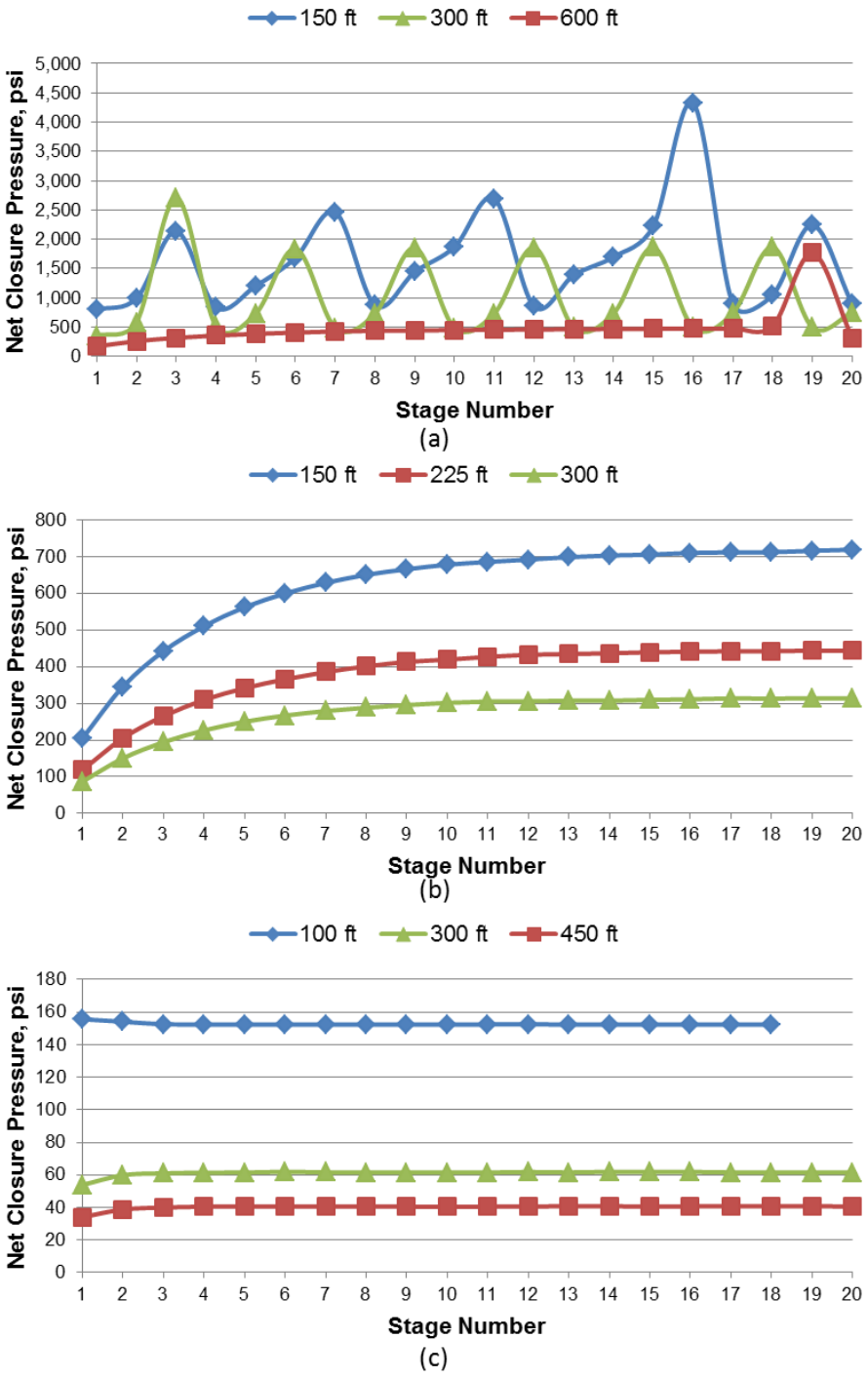

Figure 2.18 Effect of fracture half-length of the fractures on the net closure pressure response for the (a) Barnett shale gas play, (b) Bakken shale gas play, and (c) Eagle Ford shale gas play.

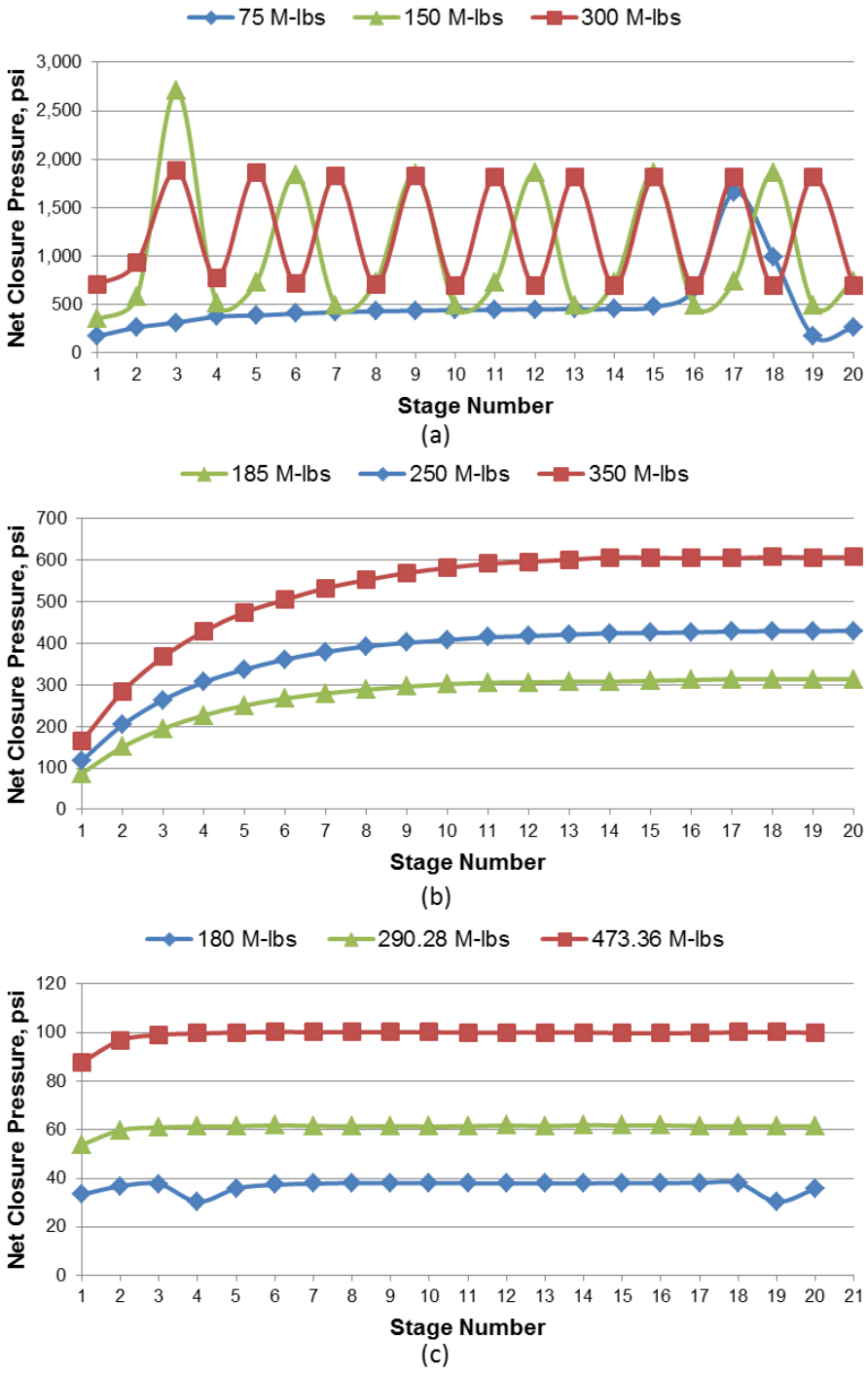

Figure 2.19 Effect of proppant mass per stage on the net closure pressure response for the (a) Barnett shale gas play, (b) Bakken shale gas play, and (c) Eagle Ford shale gas play.

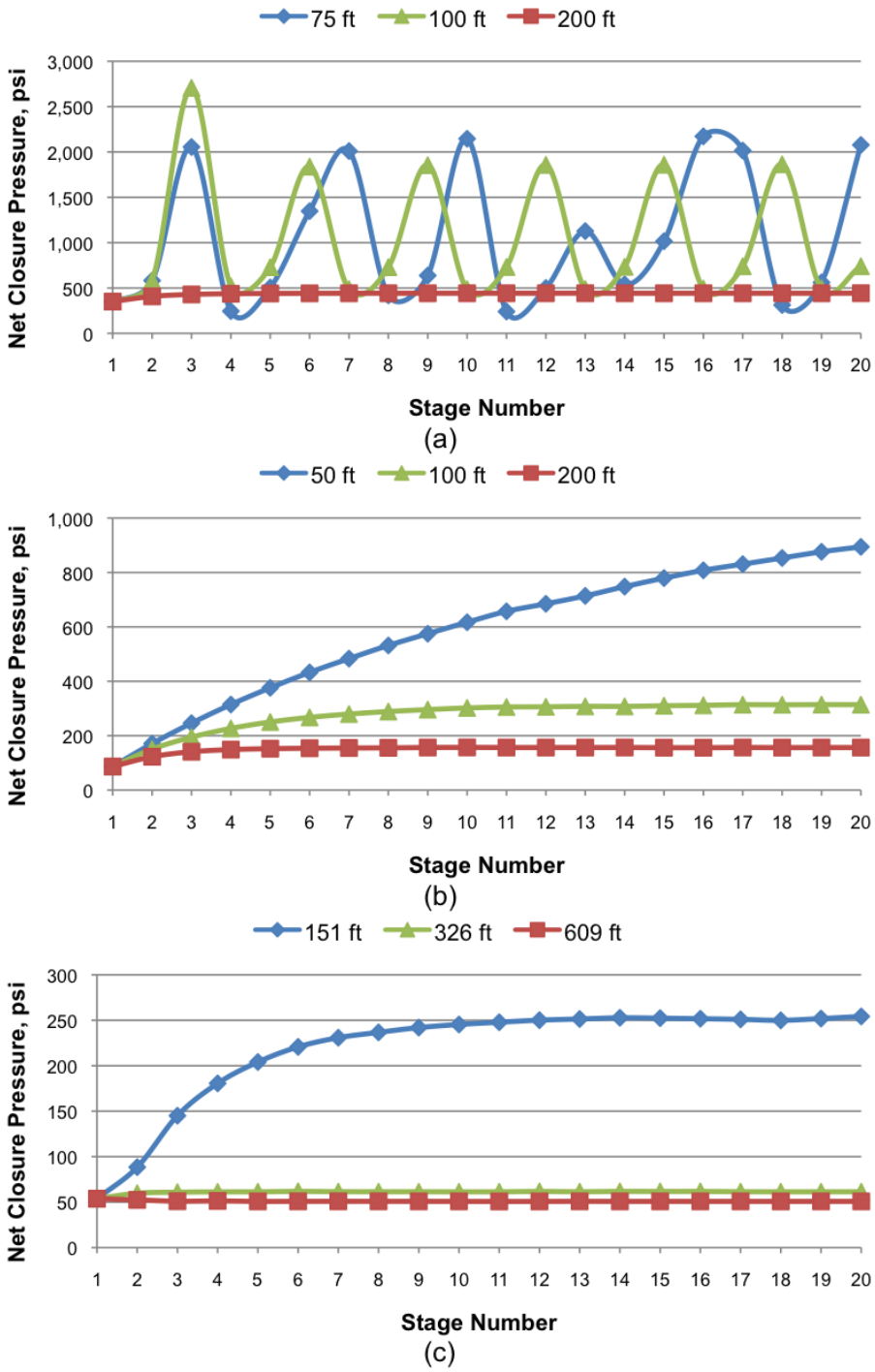

Figure 2.20 Effect of fracture spacing on the net closure pressure response for the (a) Barnett shale gas play, (b) Bakken shale gas play, and (c) Eagle Ford shale gas play.

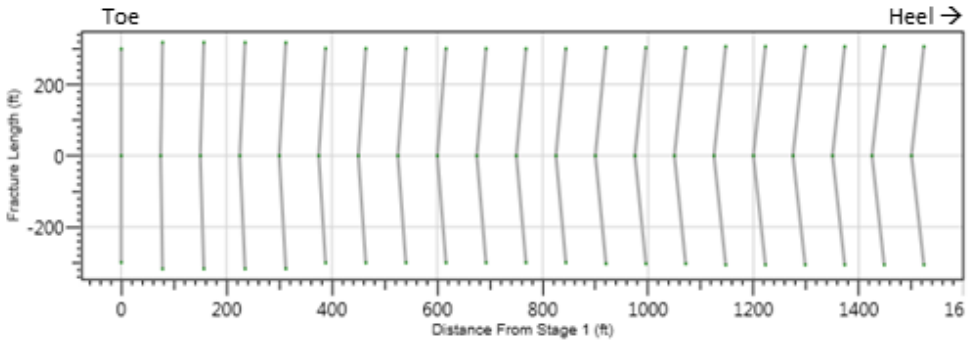

(a)

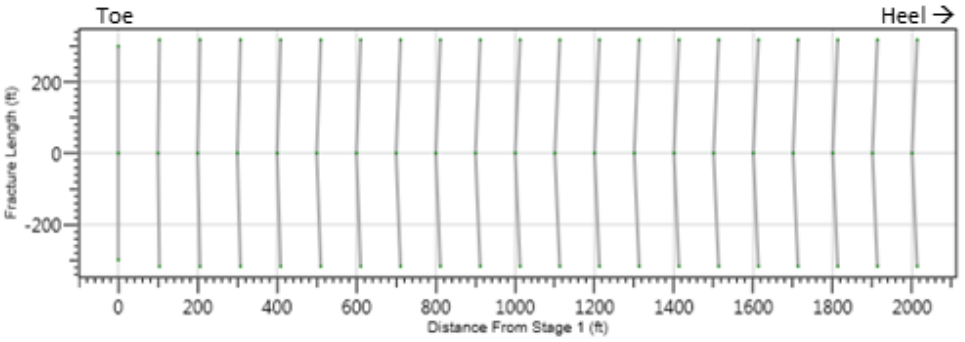

(b)

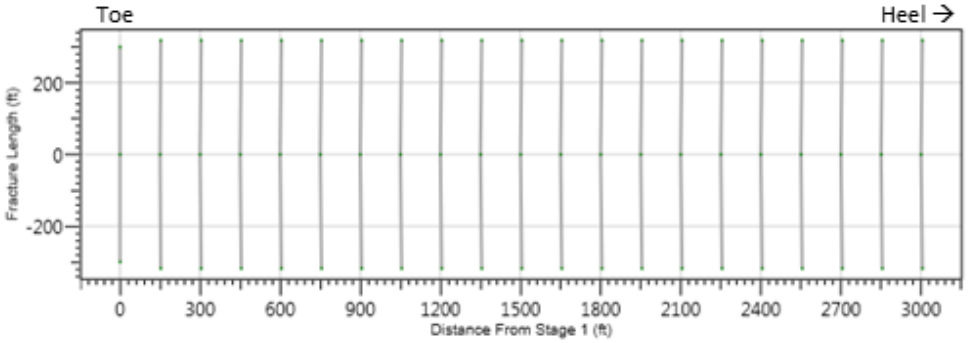

(c)

Figure 2.21 Variation in the fracture trajectories due to changes in stage spacing in the Bakken formation. Stage spacing of the cases (a), (b) and (c) are 75 ft., 100 ft. and 150 ft. respectively.

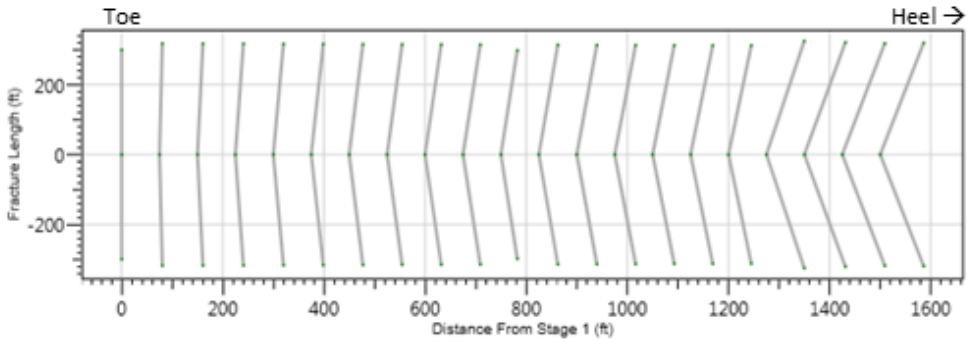

(a)

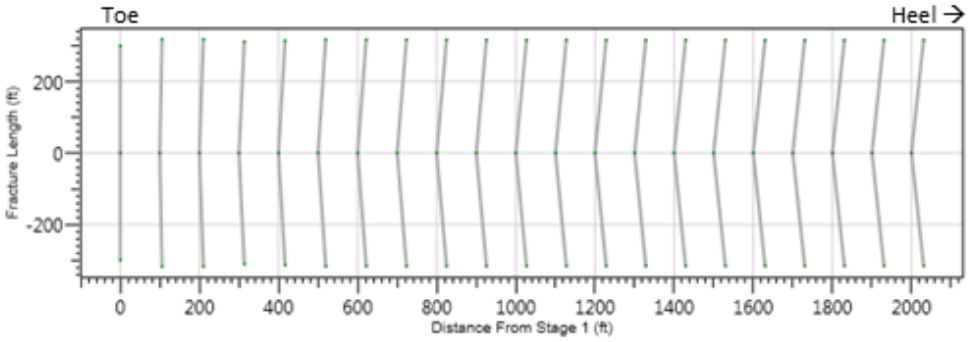

(b)

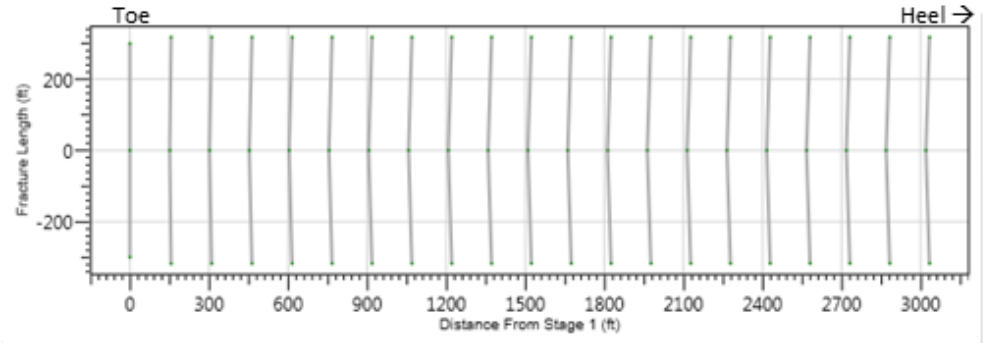

(c)

Figure 2.22 Variation in the fracture trajectories due to changes in stage spacing in the Eagle Ford formation. Stage spacing of the cases (a), (b) and (c) are 75 ft., 100 ft. and 150 ft. respectively.

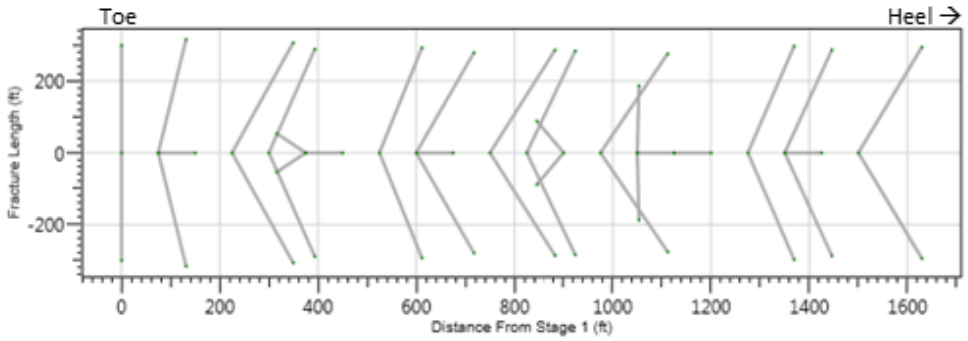

(a)

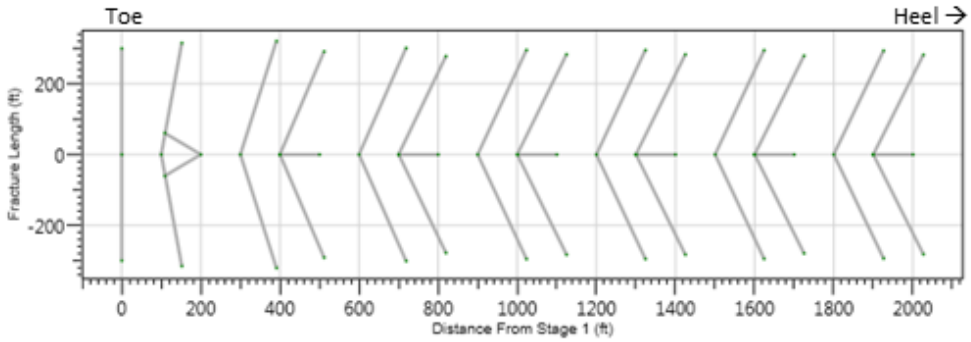

(b)

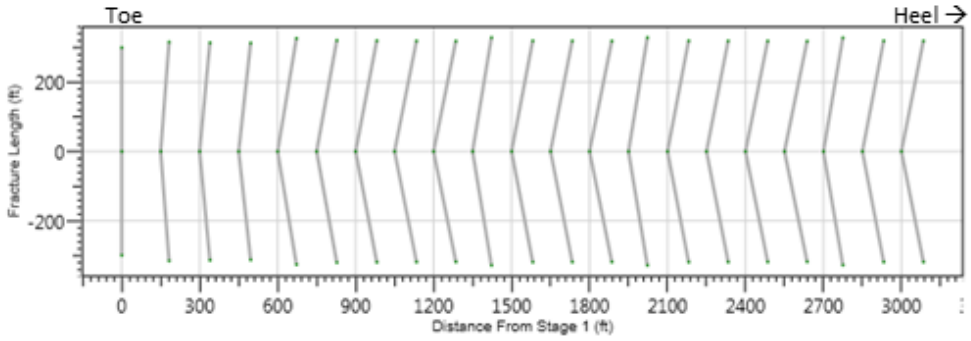

(c)

Figure 2.23 Variation in the fracture trajectories due to changes in stage spacing in the Barnett formation. Stage spacing of the cases (a), (b) and (c) are 75 ft., 100 ft. and 150 ft. respectively.

	Barnett	Bakken
Young's Modulus, MMpsi	6.00	2.25
Poisson's Ratio	0.22	0.25
Fracture half-length, ft.	300	150
σ_{hmin}, psi	5100	7950
σ_{hmax}, psi	5300	8933
σ_{v}, psi	8000	9925
Fracture Height, ft.	200	300

Table 2.5 Constant parameters in the study presented in

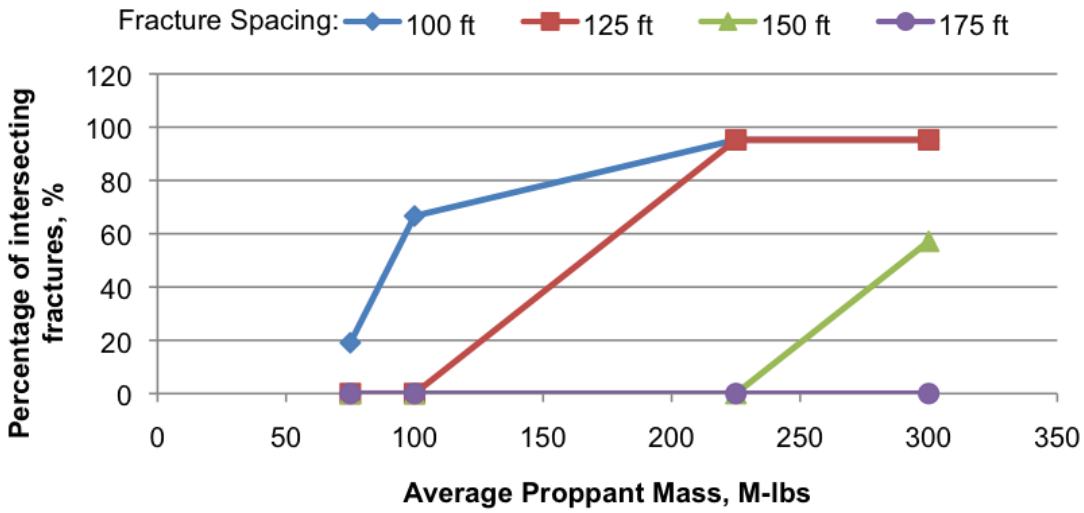

Figure 2.24 Variation in percentage of intersecting fractures with changes in fracture spacing and average proppant mass per stage for the Barnett play.

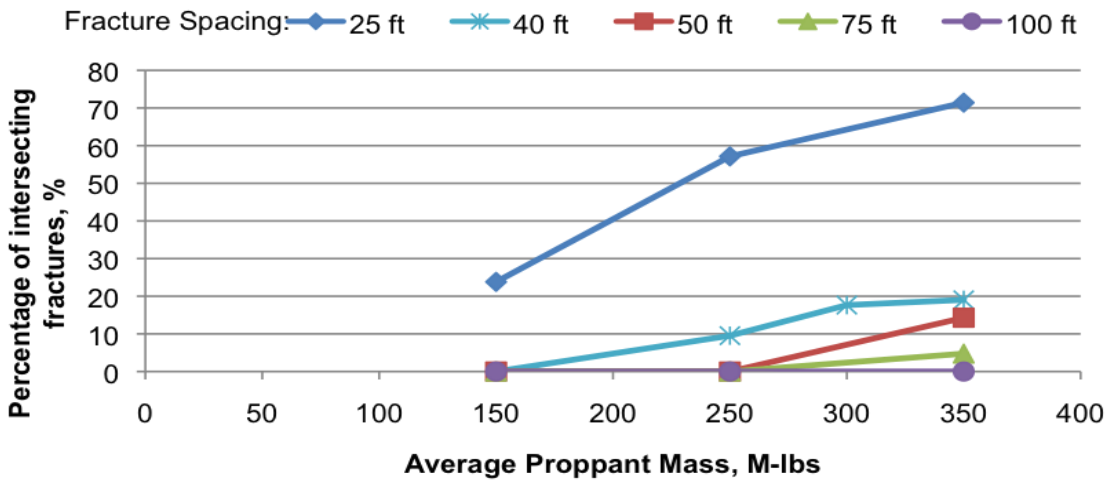

Figure 2.25 Variation in percentage of intersecting fractures with changes in fracture spacing and average proppant mass per stage for the Bakken play.

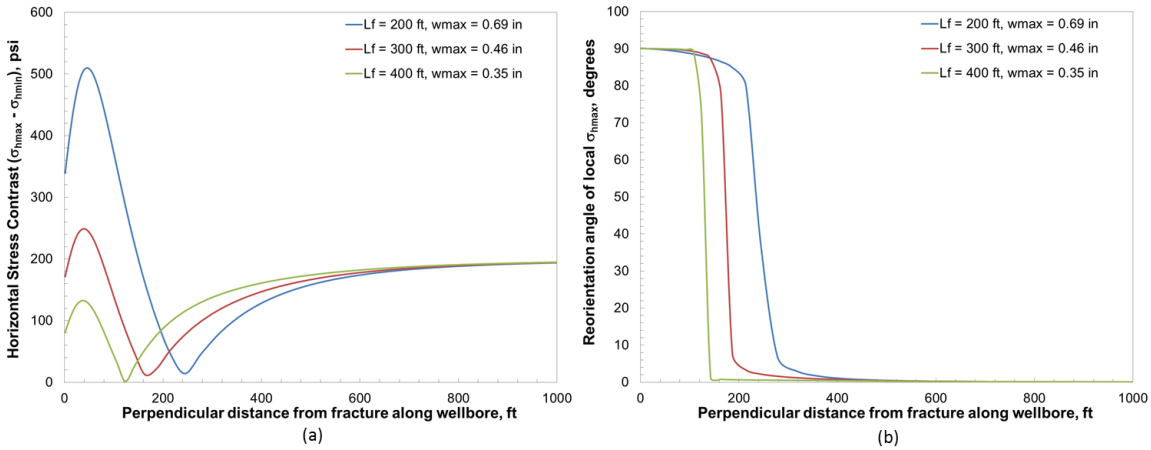

Figure 2.26 (a) Variation in the horizontal stress contrast with distance from the previous fracture along the horizontal wellbore. (b) Variation in the angle of reorientation of the local σ_{hmax} with distance from the previous fracture. Legend shows fracture half-lengths.

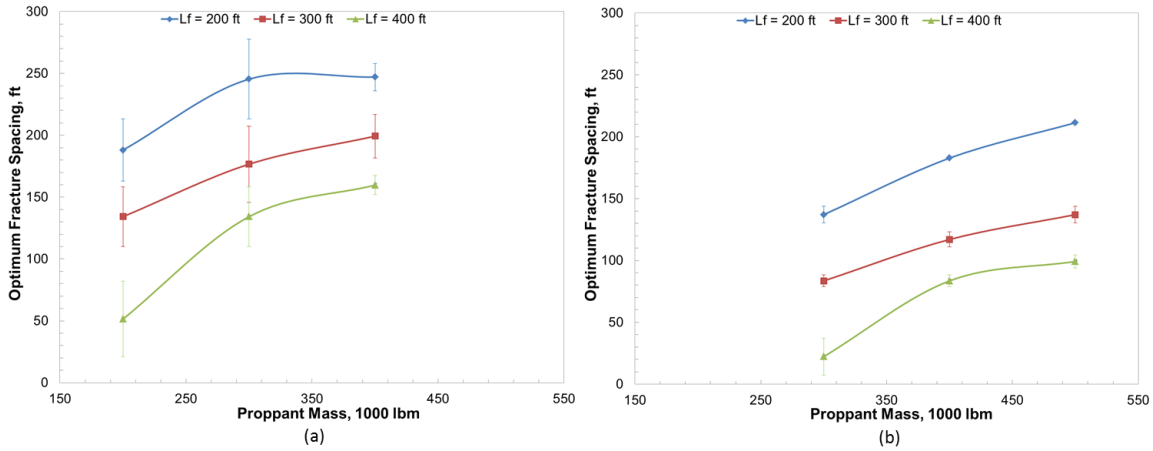

Figure 2.27 Variation in optimum fracture spacing vs. amount of proppant used per stage for different fracture lengths. The error bars represent the extent of the optimal fracturing zone. *In-situ* horizontal stress contrast used in the model is (a) 200 psi, (b) 400 psi. Legend shows fracture half-lengths.

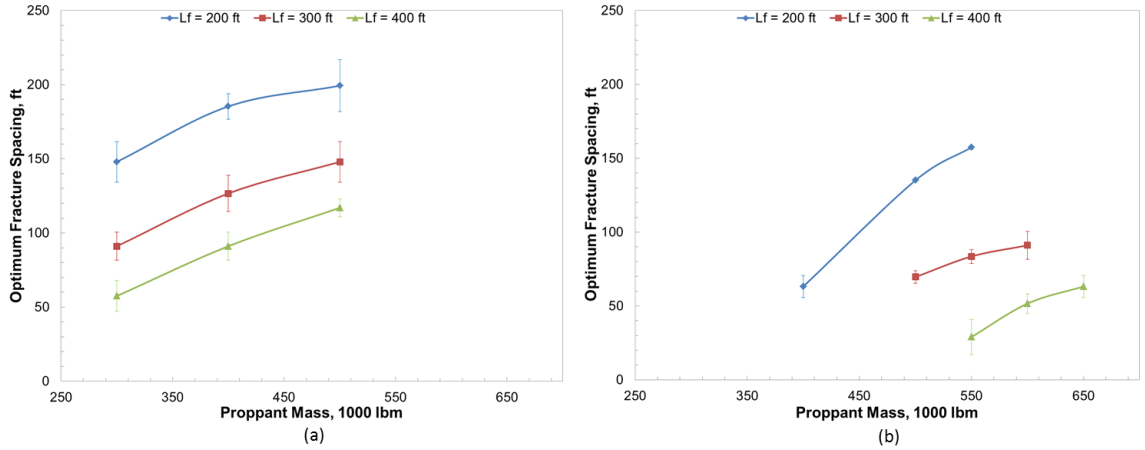

Figure 2.28 Variation in optimum fracture spacing vs. amount of proppant used per stage for different fracture lengths. The error bars represent the extent of the optimal fracturing zone. *In-situ* horizontal stress contrast used in the model is (a) 250 psi, (b) 500 psi. Legend shows fracture half-lengths.

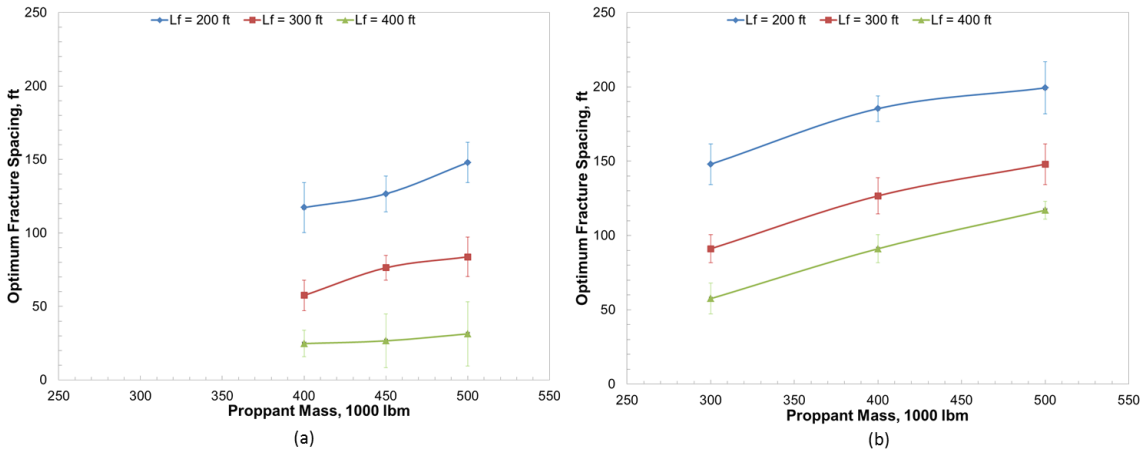

Figure 2.29 Variation in optimum fracture spacing vs. amount of proppant used per stage for different fracture lengths. The error bars represent the extent of the optimal fracturing zone. Young's modulus of the pay zone is (a) 2.25 MMpsi, (b) 4 MMpsi. Legend shows fracture half-lengths.

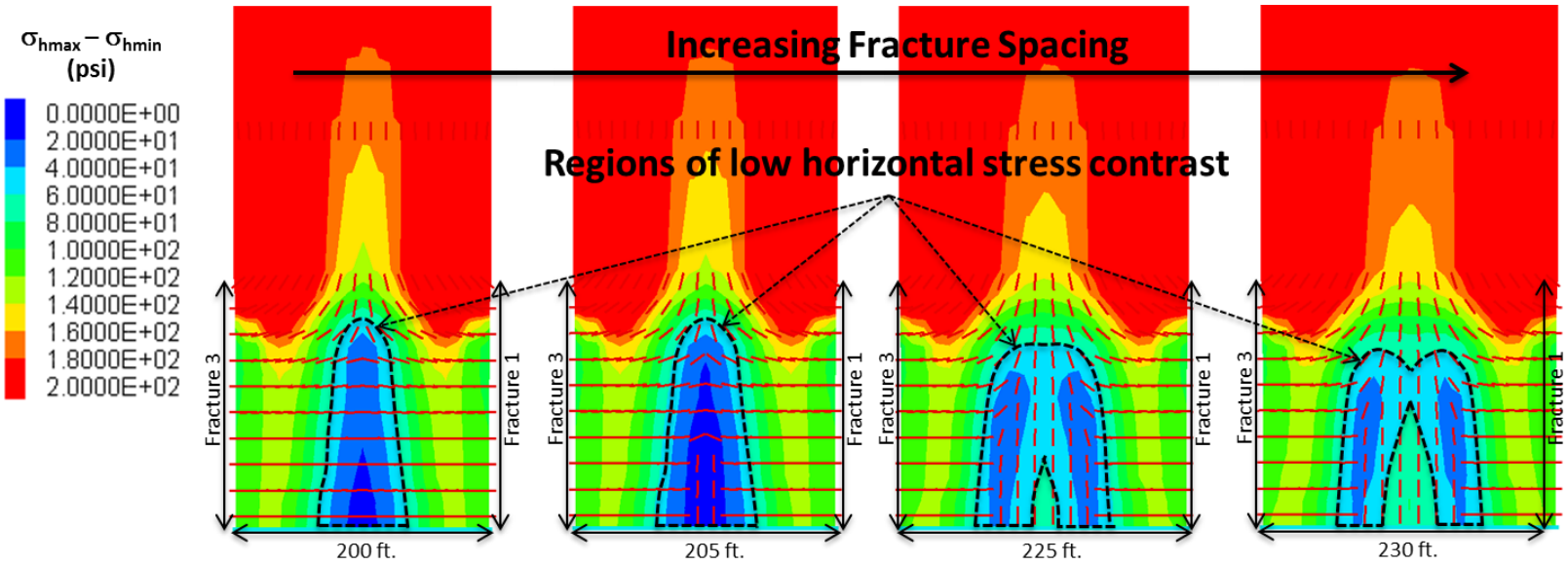

Figure 2.30 Illustration of the concept of alternate fracturing in which Fracture 2 is propagated in the middle of Fracture 1 and Fracture 3 after 1 and 3 have been created. The illustrations depict the change in the size and shape of the low horizontal stress contrast regions with the increase in spacing between the bookend fractures.

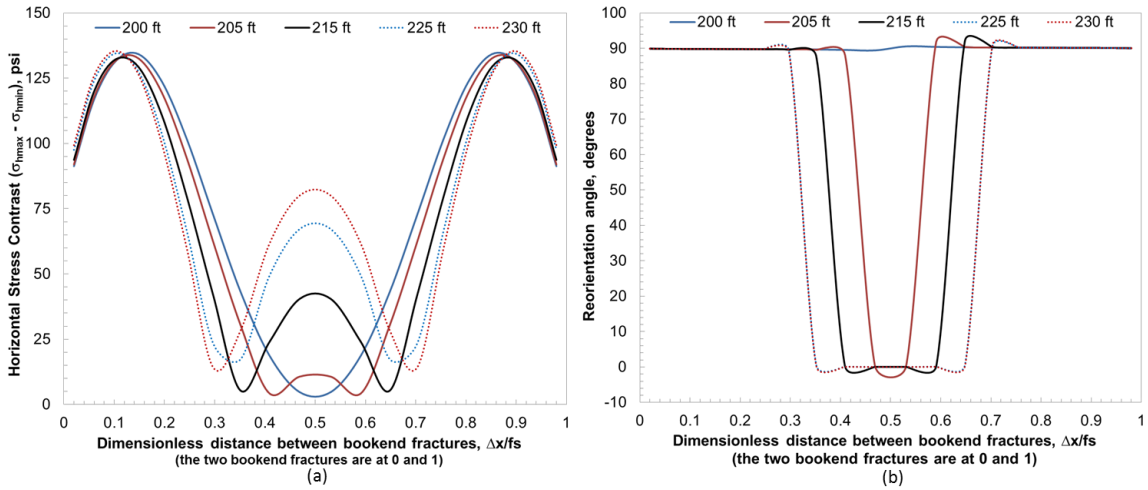

Figure 2.31 The influence of the bookend fractures on (a) horizontal stress contrast, (b) reorientation angle, along the wellbore between the two bookend fractures.

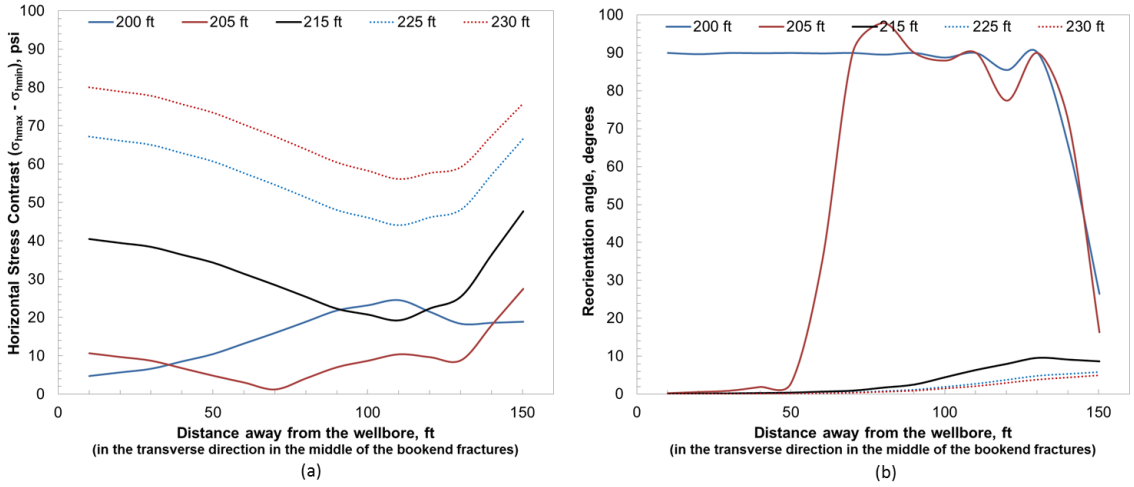

Figure 2.32 The influence of the bookend fractures on (a) horizontal stress contrast, (b) reorientation angle, away from the wellbore in the middle of the two bookend fractures.

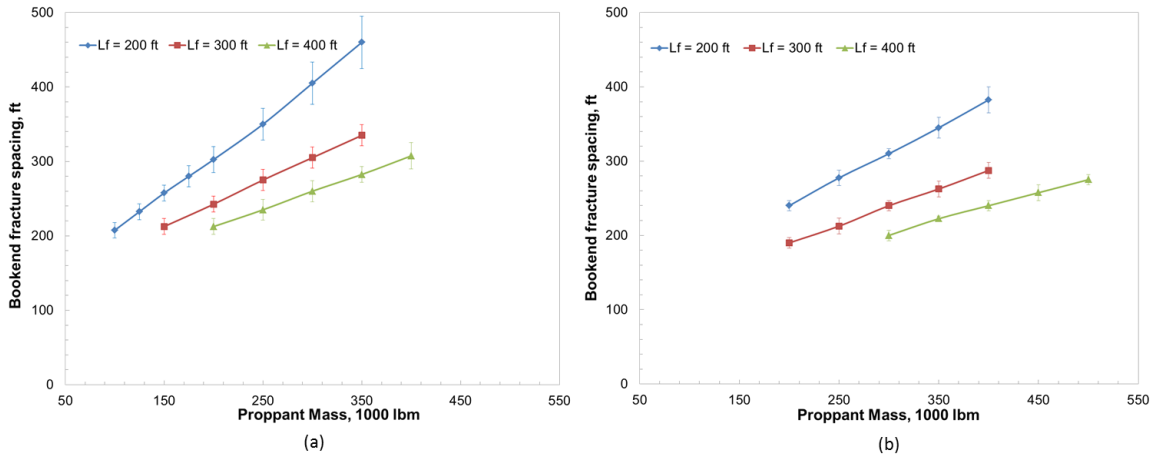

Figure 2.33 Effect of proppant mass on the bookend fracture spacing to obtain optimal middle fracture complexity in a soft environment (Young's modulus of pay zone = 4 MMpsi) and *in-situ* horizontal stress contrast = (a) 200 psi. (b) 400 psi. Legend shows fracture half-lengths.

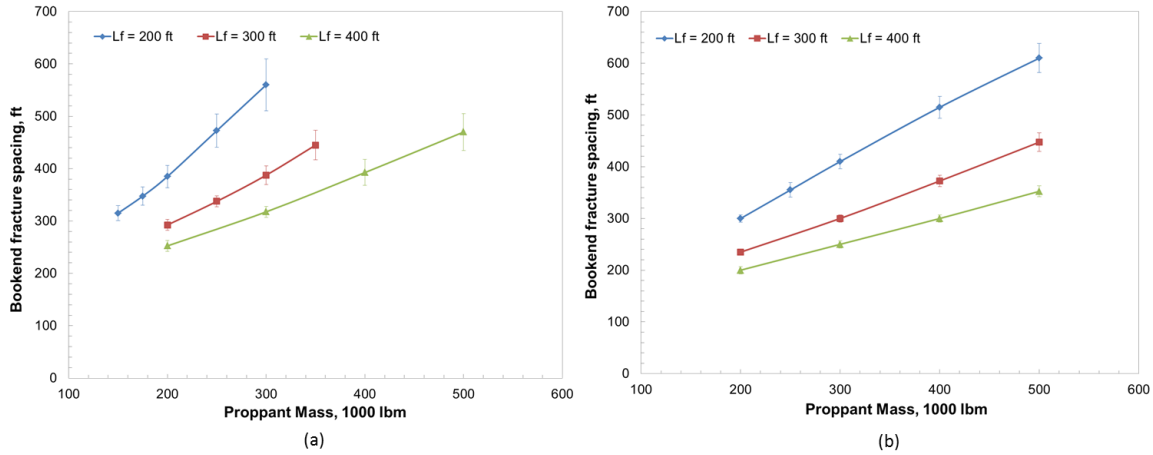

Figure 2.34 Effect of proppant mass on the bookend fracture spacing to obtain optimal middle fracture complexity in a stiff environment (Young's modulus of pay zone = 6 MMpsi) and *in-situ* horizontal stress contrast = (a) 200 psi. (b) 400 psi. Legend shows fracture half-lengths.

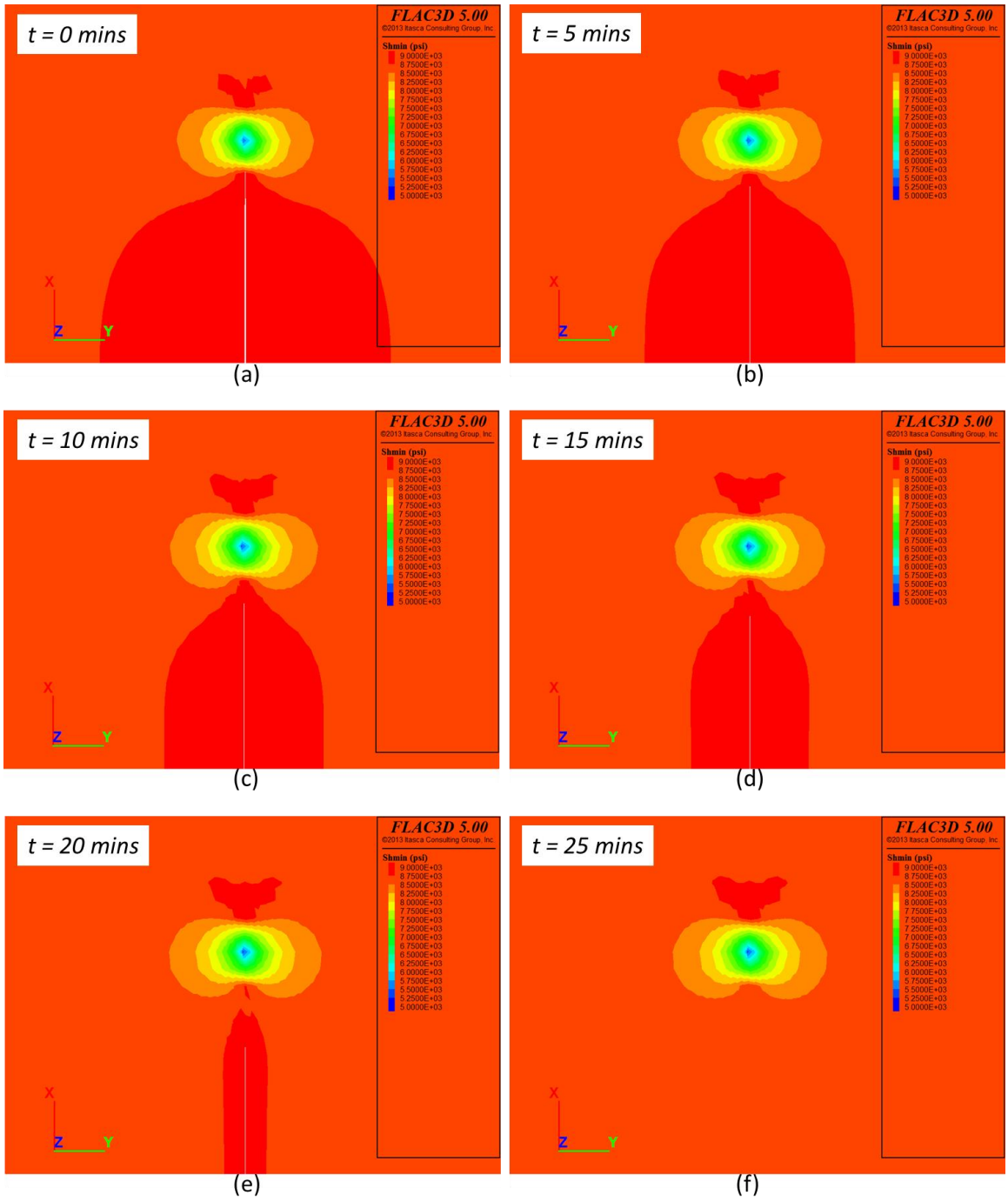

Figure 2.35 The contour of minimum principal stress in the vicinity of a closing fracture at different times. The fracture is seen as a thin white line in the middle of the grid. No poroelastic stresses were included in this simulation.

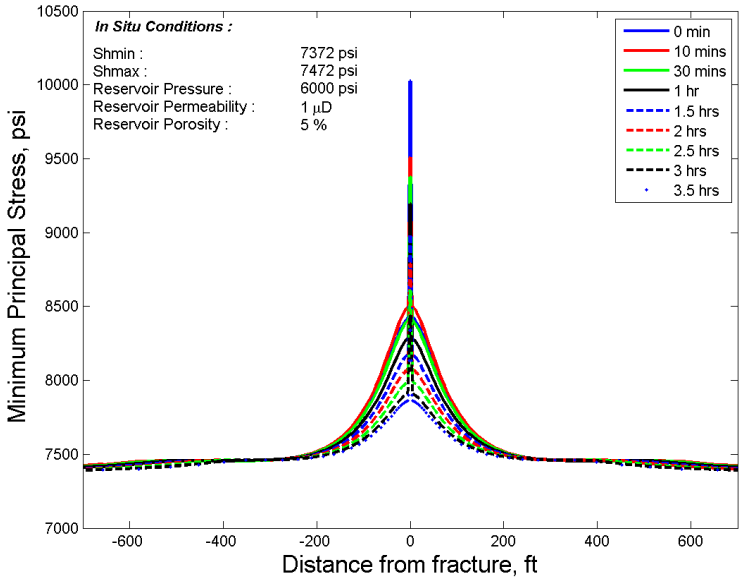

Figure 2.36 Changes in the local reservoir minimum principal stress (S_{hmin}) along the axis of the fracture because of fracture closure and pressure mitigation from the closing fracture.

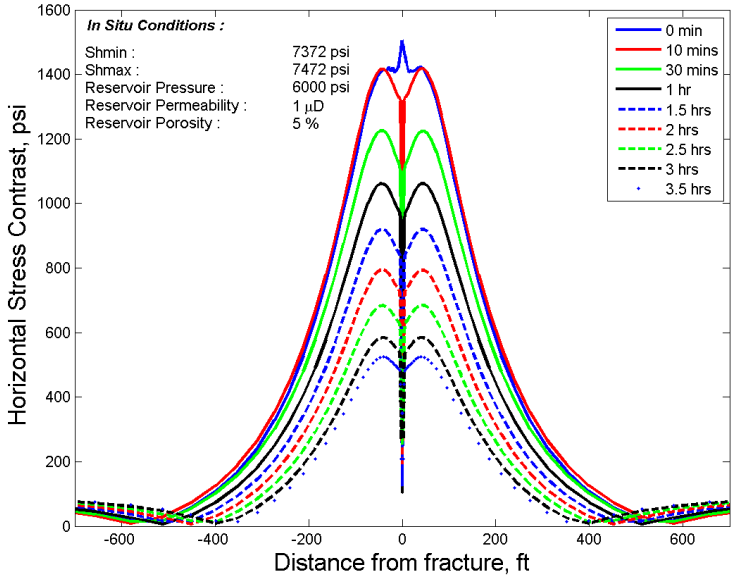

Figure 2.37 Changes in the local reservoir horizontal stress contrast (S_{hmax} - S_{hmin}) along the axis of the fracture because of fracture closure and pressure mitigation from the closing fracture.

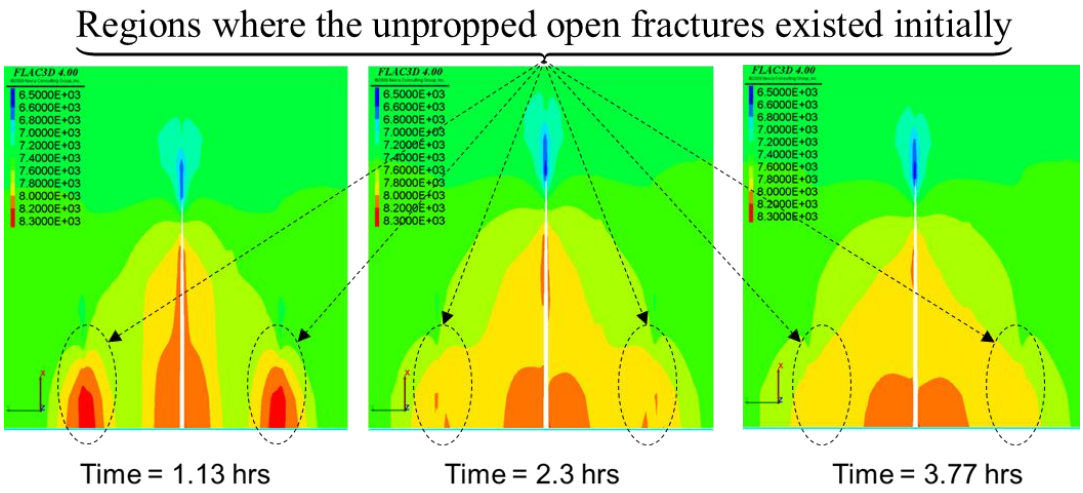

Figure 2.38 Effect of fracture closure on the minimum principal stress. The marked regions define the location of the initial unpropped open fractures. The middle white line represents the propped open fracture. The contour colors represent the local minimum principal stress.

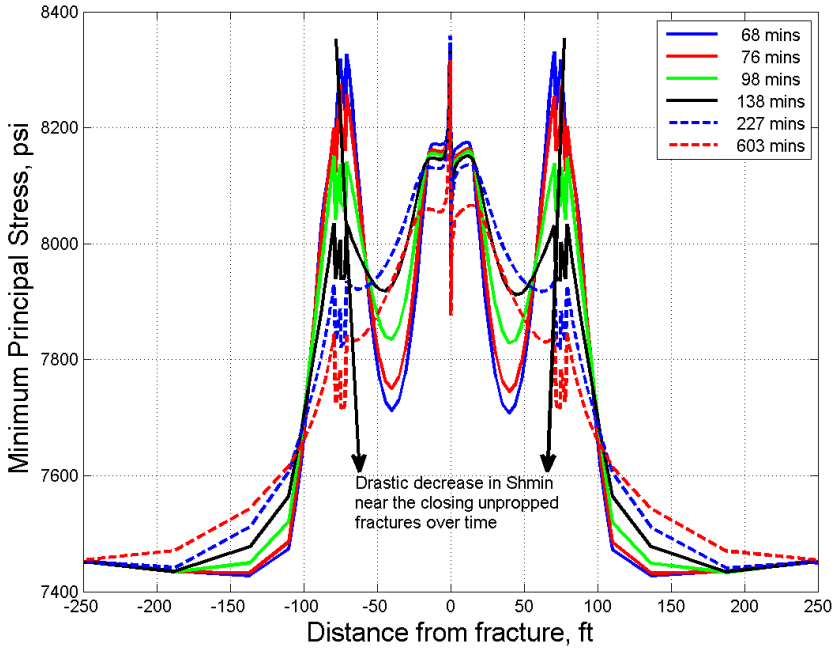

Figure 2.39 The effect of unpropped fracture closure on the minimum principal stress caused by fluid leak-off and pressure depletion over time. The middle fracture is located at 0 ft. and the outer fractures are located at -75 ft. and 75 ft.

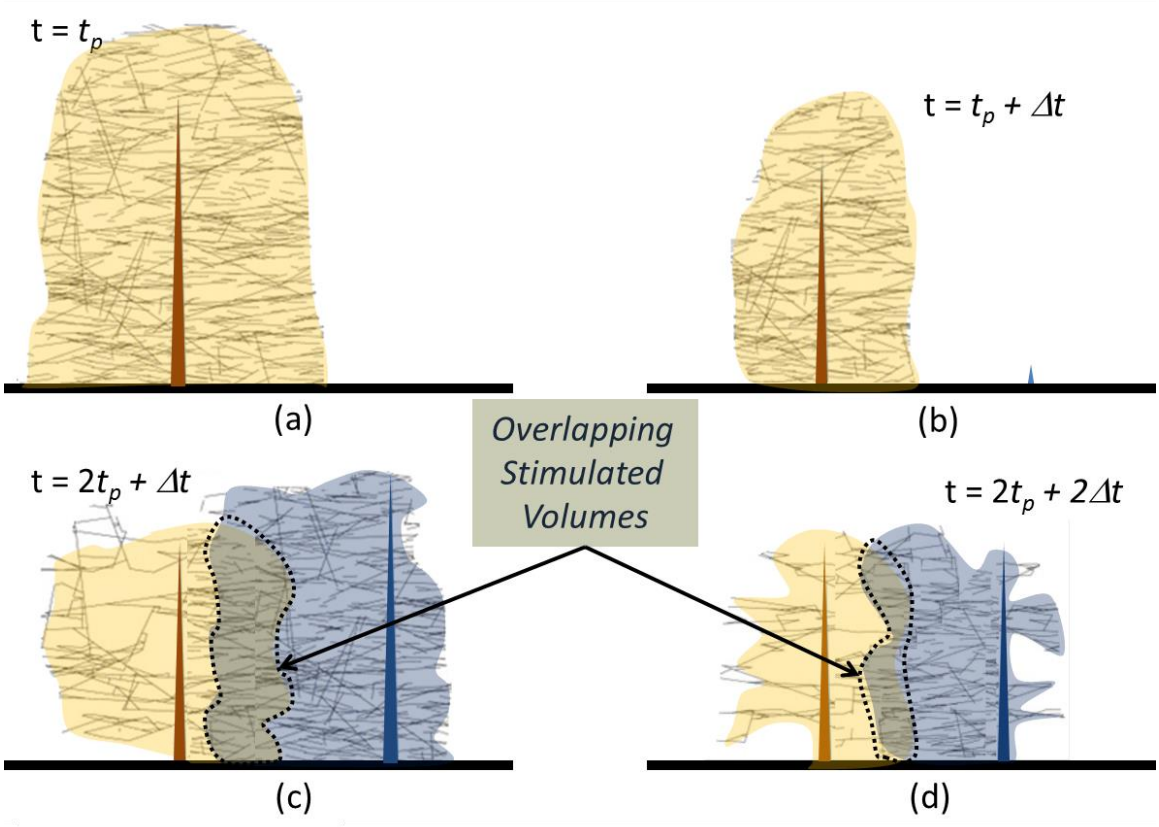

Figure 2.40 Stimulated regions for a consecutively fractured well (a) Fracture network stimulated at the end of the 1st hydraulic fracture treatment, (b) Fracture closure and the existing network at the start of the 2nd hydraulic fracture treatment, (c) Stimulated fracture networks at the end of the 2nd hydraulic fracture treatment, (d) Existing fracture network at the start of the 3rd hydraulic fracture treatment. A biased stimulation region is seen for the 2nd frac stage.

Chapter 3: Optimizing Fractures in Multiple Well Pads: Static Fractures

In this chapter[2], some of the issues involved with pad scale hydraulic fracturing are addressed. First, a review is provided of how other researchers and industry professionals address this problem. We present a workflow that has been devised based on the model formulated in the previous chapter. This is followed by results and discussion showing the most important parameters that need to be considered in the field. Thereafter, the designed workflow is applied to an actual field case study. A set of conclusions are provided while discussing limitations of the current method.

3.1 Literature Review

Fracturing horizontal wells has allowed us to produce oil and gas from shales and other low permeability formations. The success of these production methods is almost entirely dependent on our ability to successfully fracture and produce long sections of horizontal wellbores. As our experience with drilling and completing large numbers of wells in different kinds of shales has grown, it is becoming apparent that the best fracture design is closely integrated with the choice of well spacing, fracture spacing, geology and fluid properties of the shale.

In most unconventional shale plays, several horizontal wells are drilled and fractured in multiple stages from a single location or pad. There is limited work done on the analysis of these pad drilled wells. We focus on understanding the importance of optimizing pad scale parameters such as well spacing and fracture sequencing in this chapter.

[2] Many of the ideas expressed in this chapter were first presented in (Manchanda and Sharma 2013; Manchanda et al. 2014). Sharma supervised all the above projects. Holzhauser (Shell) provided field data for validation and collaborated on the analysis.

3.1.1 Fracture Networks

Complex fractures can have a substantial effect on the production response of wells (Warpinski et al. 1990; Warpinski 1991; Cipolla et al. 2000; Cipolla, Peterman, et al. 2005). Microseismic data has been used to infer the impact of stress interference on fracture complexity. From microseismic and tiltmeter data collected over the last 10 years, diverse fracture propagation patterns has been observed (Warpinski et al. 1996; Griffin et al. 2003; Fisher et al. 2004; Cipolla, Peterman, et al. 2005; Weijers et al. 2005; Wolhart et al. 2005, 2006; Mayerhofer et al. 2006). These patterns can guide us in understanding the importance of different variables and help us to identify the best stimulation strategy to characterize and induce the appropriate degree of fracture complexity for a given reservoir. In this chapter we discuss how the production response of wells can change the nature of the induced complex fractures and hence affect the production response of the new fractures because of poro-elastic stress interference.

3.1.2 Communication between Pad Wells

Several authors have presented data showing the pressure response in a well when an adjacent well is being fractured. Gupta et al. (2012) illustrate this effect in Figure 3.1. The fact that the pressure communication is virtually instantaneous shows quite conclusively that micro-fractures or high permeability channels are present between the wells during fracturing.

Figure 3.2 shows that the spikes in the bottom-hole pressure of Well 1 are correlated to the spikes observed in the production gas rate. This increase in gas rate and spike in bottom-hole pressure when fractures are created in offset wells suggest communication between the newly created fractures and the producing well (Well 1). After the spike in production rates and bottom-hole pressures both the rates and the pressures go back to their pre-offset-well-fracture trends. This shows that the network of

fractures that were created during fracturing in the offset wells have stopped contributing to the production of the producing well. This may suggest that the IU fractures that were created have closed and have stopped contributing to the production of the producing well.

Sardinha et al. (2014) provide an interesting data set showing the connectivity between wells on a pad. Figure 3.3 shows the 10 wells in three zones that were part of a pad study to observe inter-well pressure interactions during fracturing, and during flowback. Operational details are provided in the original paper. Fracture network surveillance was done by analyzing the inter-well pressure hits during fracturing, and analyzing early and late time production interference. The authors observed a high degree of pressure interaction and microseismic overlap between wellbores during the fracture stimulation treatments. This suggests the establishment of a well-connected and over-pressured fluid filled network of fractures during and immediately after the hydraulic fractures treatments are pumped. During the flowback period they observed a reduction in the degree of well-to-well connectivity. This pressure connectivity is further reduced after the long term production phase is established. During this production period many of the well-to-well connections disappear. Figure 3.4 shows strong communication between wells. The data clearly show that most wells deliver frac hits to nearby wells only.

During flowback, the pressure and flow rate of each well was monitored. In an event when a well's production was interrupted due to operational events, the degree of production response in offset wells was recorded. Figure 3.5 shows the flowback production interference between the wells. There is a marked decrease in the inter-well connectivity during this flowback production phase.

In this chapter we infer the communication between hydraulically fractured horizontal wells in a pad by using tracer data. We show that IU fracture networks created in one well can potentially connect between the wells depending on the timing and sequence of the fracturing jobs. The analysis is done for a real field case in the Eagle Ford formation.

3.1.3 Fracture Sequencing

Ramakrishnan, Yuyan, and Belhadi (2011) talk about the increased operational efficiency of zipper fracturing when compared to simultaneous fracturing. They recommend that zipper fracturing is operationally favorable when the wells being fractured are on the same pad and the wellheads of the wellbores are close together (as shown in Figure 3.6). This prevents the movement of crews between the wells and the entire operation can be completed using one stimulation and perforation crew. The stimulation and perforation crew can alternate between the wells one stage at a time thus saving most of the waiting time. Thus all the stages can be stimulated from toe to heel more efficiently than in a consecutive fracturing strategy.

Ramakrishnan, Yuyan, and Belhadi (2011) also suggested that the zipper fracturing technique can potentially help divert the fracture direction and help in increasing the effective stimulated volume by increasing the complexity in successive fracture stages. However, they did not provide any conclusive evidence of this derivative advantage of zipper fracturing.

Some authors (Roussel and Sharma 2011a; Vermylen and Zoback 2011) have shown how stress shadow effects can lead to the creation of larger microseismic volumes with zipper fractures when compared to simultaneous fracturing or consecutive fracturing sequences. Vermylen and Zoback (2011) suggested that poro-elastic effects might be

inducing the different pressure trends that are observed when comparing zipper fractured wells and simultaneously fractured wells. In this chapter we show that poro-elastic effects are negligible at a fracturing time scale and that fracture closure can help explain the differences between zipper fractured wells and simultaneously fractured wells.

Rios et al. (2013) performed geomechanical calculations to compare the stress interference effects between modified zipper fractured wells (Rafiee et al. 2012) and tip-to-tip zipper fractured wells. They concluded that the modified/staggered zipper fracturing might not be beneficial because of an increase in S_{hmin} and a decrease in the maximum shear stress between the fractures. They, however, suggested that tip-to-tip fracturing can reduce the S_{hmin} and increase the maximum shear stress which can potentially increase the stimulation of natural fractures. Thus multiple interacting hydraulic fractures from two wells can create an extensive region of increased normal stresses and decreased shear stresses which can potentially stabilize natural fractures rather than enhancing shear. Hence, it is important to understand inter-well stress interference on a case-by-case basis.

Neuhaus et al. (2012) showed using an integrated analysis for the Marcellus Shale that zipper fracturing can produce more fracture network surface area and increase production. Nagel et al. (2014) did a parametric study to understand the impact of different natural fracture orientations, in-situ stresses, and natural fracture friction angles for various geometries of hydraulic fractures in zipper fracturing scenarios. Their simulations suggested the need for a fully coupled hydro-mechanical modeling approach to understand the behavior of hydraulic fractures in naturally fractured reservoirs.

The importance of treatment parameters, completion parameters, reservoir parameters and time between adjacent fractures in a horizontal well in the design of fracture treatments was discussed in Chapter 2. In this chapter we apply that

understanding to a field case study. Results from this field study describes the reasons for the success of zipper fracturing sequences. It is shown that the increase in time between two successive fractures in a given wellbore (in zipper fracturing) causes the stress shadow of the created fractures and the associated induced unpropped fractures to decrease because of fracture closure and hence allow for the creation of larger stimulated reservoir volumes and more effective stimulation.

3.1.4 Pad Scale Completion Strategies

Gupta et al. (2012) suggest a workflow that combines the aspects of fracture analysis, reservoir analysis and geo-mechanics analysis in a pad location to help design field development strategies that include infill wells (Figure 3.7). Their conclusions from two example field cases helped in defining the problem of inter-well fracture interference. They exhibited evidence of early onset fracture interference using pressure transients. They suggested using material balance calculations to estimate fracture geometries to help customize well spacing. They showcased the importance of geomechanical stresses for both the impact on near fracture stress reorientation as well as far-field stress reorientation caused by long term production. As discussed in the previous chapter they suggested that the impact of stress reorientation on the trajectory of fracture propagation could result in more complex fractures in infill wells. They recommended that an analysis of the effectiveness of injection, production and shut-in strategies should be conducted to steer fracture propagation and avoid inter-well interference on a customized basis and suggested avoiding making general conclusions. Gupta et al. (2012) suggested several pad scale strategies that could be usefully applied in the field. In this chapter we try to conduct such an analysis to obtain additional knowledge and

understanding of pad scale techniques deployed in the industry today and suggest new strategies.

Roussel, Florez, & Rodriguez (2013) discuss the impact of production from outer wells in a pad on the stresses in the middle wells and estimate the corresponding trajectories of the fractures in the infill wells using a fully coupled geo-mechanics simulator. Such efforts are the first in the field to analyze the stresses in the field and design fracture treatments for infill wells. They performed a parametric study to understand the importance of various pad scale variables and attempt to optimize the timing of infill well fracturing by looking at the impact of stress reorientation on infill well fracture trajectories (Figure 3.8).

Ajani & Kelkar (2012) studied the production interference between infill wells and offset producers. They concluded that the interference is dependent on the age of an offset well and the distance from the offset well. They recommended developing an entire section by drilling all the infill wells. They note that interference between the wells was seen to follow the stress anisotropy in the field. They discussed the use of normalized initial production as a function of the well spacing and saw a strong correlation. In this chapter we normalize the well spacing to be a function of the fracture geometry since the fracture geometry controls the induced stress interference.

Sahai et al. (2013) compared the SRV overlap between hydraulic fractures from three parallel horizontal wells using reservoir simulations. They suggested that the recovery factor and NPV are reduced for zipper fracturing with overlapping SRVs. They suggested that infill wells were better. Geomechanical computations were not done hence the effect of fractures on the middle well SRV was not taken into consideration. In this chapter we try to address this issue and model the stress interference effect of outer wells on the middle wells to optimize the completion strategy.

In this chapter we add more knowledge and understanding to the pad scale techniques deployed in the industry today using geomechanical simulations. These simulations help in designing workflows to optimize fracture sequencing, well spacing, fracture spacing, and infill well timing.

3.2 Workflow for Pad Scale Fracture Modeling

In Chapter 2 a workflow for single well hydraulic fracture optimization was created using a geomechanical simulation model. It was shown that the most important parameters that influence the stress reorientation due to a created fracture are the geometry of the fracture (width, height and length), fracture surface area (representative of leak-off area), and fracture orientation. Using the same geomechanical model formulation, a new workflow to simulate fractures in multiple wells is presented below.

3.2.1 Modeling Multiple Hydraulic Fractures in a Pad

In a field treatment, a hydraulic fracture is opened by the pressure acting on its surface by the fluid pumped into the fracture. For each hydraulic fracture this is modelled by imposing two boundary conditions on the fracture face, a traction boundary condition for the mechanical opening and a fluid pressure boundary condition to accomplish fluid leak-off.

This is repeated for multiple fractures in a pad. All the fractures are modelled with their prescribed geometries at the chosen fracture spacing and well spacing for all the wells in a pre-defined sequence. Poro-elastic stress interference induced by fracturing is also modelled. The fracture closure algorithm is also incorporated. For the various wells in the pad this should enable an analysis of variable well spacing, fracture spacing and fracture sequencing.

These capabilities allow for the incorporation of custom fracture sequencing in the horizontal wells on the pad (zipper fractures, alternate fractures etc.). The impact of fracture sequencing is reflected in the treatment pressures, closure pressures, micro-seismic data as well as production data from wells. Thus using such numerical simulations a better understanding of the impact of fracture sequencing can be obtained.

3.2.2 Modeling Well History

Modeling the history of the well is important to capture the changes in the reservoir due to production, injection and shut-in of the wells in the pad. In unconventional shale reservoirs a Stimulated Reservoir Volume (SRV, Mayerhofer et al. 2010) is simulated to capture the high permeability of the high permeability region immediately around the main propped fracture. The SRV after fracture treatment (at the end of pumping) and the SRV obtained during production can potentially be very different. The closure of networks of fractures that form the initial SRV can potentially decrease the effective permeability of the reservoir rock. The SRV during production should be calibrated with the history matched reservoir production response. This estimate should then be included as the calculated SRV in the geo-mechanical reservoir simulator to simulate the well history (production, injection or shut-in) and hence capture the geo-mechanical impact of the well history. The main assumptions in this procedure are:

- We use pre-defined fracture and SRV dimensions. Estimation of the SRV dimensions as well as permeability make the problem a non-unique history matching problem. Thus, it is necessary to pre-define a few unknowns. The SRV extent along the wellbore is assumed to be half of the distance between the

fractures in most cases. In these cases we essentially assume an SRV to exist all along the horizontal wellbore.

- We assume a constant permeability in the entire SRV. The SRV permeability should vary with the density of the induced network of fractures. However, here we approximate the induced network of fractures with a region of enhanced but constant permeability.

The production of the horizontal well pads can be simulated by fixing the open widths of the fractures and simulating production pressures on the surface of the fractures. These production pressures are then applied as a boundary condition for the pressure equation to perform the geomechanical calculations in the reservoir and model poro-elastic stress changes.

Based on the simulated features for the various cases – single fracture, multiple fractures and multiple wells – we analyze the stress state to diagnose evidence of fracture complexity. The following rules can help to understand the impact of the stress state in a particular formation:

- At low values of horizontal stress contrast the chances of complex fracturing increase. Such contour diagrams can be especially useful in understanding the impact of inter-well stress interference before and after production of the wells in the pad, thus helping in deciphering the potential of refractured wells and infill wells in a pad setting.
- Shear failure contours provide an indication of MS events. It is hard to obtain *a priori* knowledge of the location and orientation of all the heterogeneities in the rocks. These heterogeneities could include natural fractures, planes of weaknesses and other discontinuities. All such heterogeneities have variable mechanical properties. Cohesion values can range from 0 psi to 2000 psi depending on the

mineralogy and extent of cementing of the discontinuities. Friction angles may range from 20 to 40 degrees. Changes in these mechanical properties potentially affect the stress state. The stress state in the reservoir also changes with well spacing, fracture spacing, fracture sequencing, production etc. Performing explicit Mohr-Coulomb calculations (using Eq. (3-1)) and choosing a range of values, we can characterize the evidence of failure for various scenarios (see Figure 3.9)

$$f^s = \sigma_1 - \sigma_3 N_\phi - 2c\sqrt{N_\phi}$$
$$N_\phi = \frac{1+\sin\phi}{1-\sin\phi} \tag{3-1}$$

- Pore pressure contours help diagnosing the extent of depletion. Before a decision to stimulate infill wells is executed it is important to assess if economical production can be obtained from the new well. Pore pressure contours can help in determining this.

The stress and pore pressure contour plots can help connect the stress state in the reservoir to field observations such as production data, micro-seismic data, tracer data, DTS and DAS data. For example, a probability distribution for shear failure can be computed (as shown in Figure 3.9) by using a distribution of cohesion and friction angle. An area with a higher probability of shear failure should represent a greater concentration of micro-seismic events.

3.3 Results and Discussion

In this section, we discuss the application of the above described model to study and analyze fractures in multi-well pads.

3.3.1 Inter-Well Stress Interference

Figure 3.10 shows a general schematic of the shape and orientation of a fracture that is used in the following simulations. In these simulations the half-length of a fracture is simulated to observe the impact of the stresses induced by this fracture on its surroundings.

3.3.1.1 Time dependent mechanical stress interference

No fluid flow calculations were done in this simulation. Only mechanical closure was performed. The initial fracture width at the well was ascribed a value of 1 cm. After attaining mechanical equilibrium at the prescribed width, the fracture is allowed to close as the fluid leaks off. The fracture pressure and rock displacement (**u**) are solved for and iterated on until convergence is achieved. The procedure is continued until the calculated width reduces to less than 0.1 mm.

In Figure 3.11 the results of the closure of a fracture with a 5:1 length to height ratio (500 ft : 100 ft) are presented. Figure 3.11a-f show the change in minimum principal stress at distances away from the fractured well as a function of the dimensionless distance away from the fracture. Figure 3.11a and Figure 3.11b do not show much influence of the tip of fracture. The tip effects only become important near the tip as shown in Figure 3.11c and Figure 3.11d. Further away from the fractured well the effect of both the tip and the fracture profile become insignificant as shown in Figure 3.11e and Figure 3.11f.

Clearly, the mechanical closure of the fracture causes a decrease in stress perturbation with time. This change in stress perturbation is more evident near the wellbore. At a distance further away from the wellbore the effect of time becomes less significant. For the case of multi-well pads, wells may be spaced anywhere from 330 ft to

1200 ft away from each other. From Figure 3.11d-Figure 3.11f it is obvious that stresses at such large distances do not change significantly during fracture opening or closure.

3.3.1.2 Time dependent poro-elastic stress interference

The results shown in Figure 3.11 depict the influence of the mechanical opening of the fracture but neglect fluid leak-off and changes in the pore pressure in the formation. In order to couple fluid flow with mechanical effects the following simulation was run. The treatment pumping time was assumed to be about 2 hours. For the first 30 minutes the fluid pressure inside the fracture and the stress on the fracture faces was ramped up to a value of pressure given by Eq. (3-2) in small time steps. Thereafter, the value of pressure inside the fracture and stress on the fracture face were iterated over several time steps to attain a width of 1 cm for the remaining treatment time. This procedure was not an attempt to capture what goes on in the field. This was a numerical exercise to enable a reasonable comparison between the simulation results presented in Figure 3.11, Figure 3.12, and Figure 3.13. If we apply a constant pressure during the entire treatment time, the width of the fracture at the end of the treatment time might be very different from 1 cm. Thus, maintaining the width to be equal for the different cases compared eliminates the changes in mechanical stress interference. After attaining the initial width, the closure equations are invoked and the fracture width is calculated as a function of time.

$$p_f = \sigma_{hmin} - \frac{w_{max} E}{4h_f(1-\upsilon^2)} \tag{3-2}$$

Figure 3.12 shows the variation of minimum principal stress in a 10 μD formation (with poro-elastic effects included). This could be considered a representative value of permeability for a rock formation that has been stimulated by hydraulic fracturing or

other means and that may contain high permeability streaks in the form local heterogeneities such as natural fractures, fissures, weak planes etc. Figure 3.12 like Figure 3.11 shows the variation in the minimum principal stress as a function of distance away from the fractured well and time during which the fracture closes.

Comparing Figure 3.12 and Figure 3.11 it is very evident that the poro-elastic effects may exaggerate the stresses observed at any distance from the crack. For example, if we make a 50 psi change because of fracture closure as a benchmark for significant amount of stress shadow, then for the case with no poro-elastic effects, stress shadow effects become insignificant beyond about 3.2 times the fracture half-height. However, for the case with poro-elastic effects, the stress shadow effects become insignificant beyond about 4 times the fracture half-height.

It is important to justify the high value of permeability and leak-off coefficient used in the above simulation. In unconventional shale oil and gas formations, local heterogeneities such as natural fractures, fissure openings, and planes of weaknesses are very evident. A hydraulic fracture can propagate and interact with these networks of *in-situ* fractures and high permeability zones. This intersection of the hydraulic fracture with the local heterogeneities causes the effective area of fluid leak-off to increase several fold. Since we do not explicitly model the network of fractures or planes of weaknesses in the formation, we use a higher estimate of the permeability and leak-off coefficient of the system to simulate this effect.

Figure 3.13 in contrast with Figure 3.12, shows the variation of minimum principal stress for a much tighter formation. The permeability of the formation considered in Figure 3.13 is 100 nD and hence the leak-off coefficient is reduced to 10^{-4} ft/min$^{0.5}$. These values of leak-off coefficient are within the limits of leak-off coefficients reported in other sources (Bai et al. 2005). A decrease in leak-off coefficient by a factor

of 10 implies that the permeability has been reduced by a factor of 100 (because the leak off coefficient is a function of the square root of the permeability, Schechter 1992). This decrease in leak-off coefficient causes the closure time to increase by a factor of 100. Comparing Figure 3.12 and Figure 3.13, the main difference is in the amount of time it requires to close the fracture. The simulation results presented in Figure 3.13 are representative of a tight formation with little or no high permeability streaks/heterogeneities.

It is important to note here that even after including poro-elastic effects and fluid flow in our system of equations and simulations, the variation in the stress perturbation with time is insignificant at distances larger than 600 ft away from the wellbore. For both low and high permeability, the stress perturbation seen in Figure 3.12d, e, f and Figure 3.13d, e, f does not vary with time. Also the stress perturbation at larger distances from the well remains negligible from the time of creation of the hydraulic fracture till the time of closure. On the other hand, as was discussed in Chapter 2, the stress interference adjacent to the fracture undergoes a significant change (Figure 3.11a, Figure 3.12a, Figure 3.13a). Increasing the time between adjacent fractures in the same well will reduce the stress shadow from one fracture to the next in the same well. Thus, in order to effectively stimulate pad wells more time should be allowed between immediately adjacent fractures in the same well by using zipper fracturing between two or more wells. More details on this are discussed later in this chapter.

3.3.2 Effect of Long-Term Production: Parametric analysis

The impact of long-term production and pore pressure depletion on the stresses can be studied using our geomechanical simulator. An example input data set that can be considered representative of field conditions is used. Table 3.1 shows the layer properties

that were used in the simulations. The numerical simulations conducted for this analysis assumed a single phase fluid. Multi-phase fluid data, viscosity and fluid bulk modulus were represented as functions of pressure to explicitly alter single phase fluid properties in the reservoir. An example curve is shown in Figure 3.14. Similarly, an example data set to model the fluid pressure during production was modelled. This trend is shown in Figure 3.15.

The numerical simulations were conducted on a large reservoir scale grid with multiple identical transverse fractures simulated along the length of horizontal wells (Figure 3.16). Fracture half-length of 310 ft and fracture height of 300 ft were assumed for all the simulated fractures. The wellbore was assumed to be at a depth of XX825 ft. The fracture gradient was assumed to be 0.85 psi/ft and the reservoir pressure gradient was assumed to be 0.835 psi/ft. The horizontal stress contrast at the depth of interest was assumed to be 100 psi. An SRV region along the horizontal well with an enhanced permeability was assumed.

3.3.2.1 Impact of SRV and horizontal well production

In order to understand the impact of a SRV in the vicinity of a horizontal fractured well, we model an enhanced region of permeability around the fractures as shown in Figure 3.17. This enhanced region of permeability around the fractured well has a significant impact on the production from the horizontal well and on the induced poro-elastic stresses. Figure 3.18 compares the changes in the minimum principal stress in the presence and absence of an enhanced permeability SRV region around the horizontal well. This qualitative contour plot shows that the poro-elastic stresses induced during the production from a horizontal fractured well are magnified in the presence of a SRV region around the horizontal well. Figure 3.19 depicts the pressure changes in the vicinity

of the produced horizontal well. Clear differences are observed in the extent of the pore pressure depletion contours away from the horizontal well. For the case of no SRV the pore pressure changes are not significant beyond 400 ft away from the producing horizontal wellbore. However, in the case with the simulated SRV the pore pressure changes as far as 1200 ft away from the horizontal well. The contour chart shows that the extent of the low stress region in the vicinity of the horizontal well is larger for the case with a SRV region. In this current case, where the production of the horizontal well was simulated according to the pressure trend shown in Figure 3.15 the stress contours were observed at the location of other potential locations of the wells in the pad. This was observed more prominently in the presence of the SRV region. An SRV is very likely to be present in low permeability heterogeneous reservoirs as discussed in the previous chapter. Thus it is highly probable that long-term production from a fractured horizontal well in such reservoirs will create poro-elastic stresses that may alter the stresses in the neighborhood of other wells in the pad. These altered stresses can affect the fracture propagation direction in the other pad wells. For example, this can lead to fracture hits from neighboring pad wells into producing well because of the region of low stress in the vicinity of the producing well. Figure 3.20 shows the changes in the minimum principal stresses and the intermediate principal stresses. As observed in the previous figure, the poro-elastic stress interference effect is observed far away (several hundred feet) from the producing horizontal well.

3.3.2.2 Stress interference between horizontal wells

A number of sensitivities were run to understand the impact of well spacing, fracture spacing and fracture sequencing on infill well fracturing strategies. To assess the impact of fracture spacing and well spacing, the chosen values were normalized by the

fracture half-length and fracture height respectively. For example, for a fracture half-length of 300 ft and well spacing of 330 ft, the normalized well spacing is 1.1. For a fracture height of 300 ft and fracture spacing of 200 ft, the normalized well spacing will be 0.67. The normalized well spacing represents the distance between an existing well and the infill well. The normalized well spacing and the normalized fracture spacing will be abbreviated as NWS and NFS for the rest of this document. The normalized outer well spacing will be abbreviated as NOWS.

Figure 3.21 shows a schematic of the multiple well pad with a few fractures shown in two wells. The objective of this exercise is to analyze the impact of well spacing and fracture spacing on the stresses between the fractured horizontal wells before producing the reservoir and after producing the reservoir.

Figure 3.22, Figure 3.23, Figure 3.24, and Figure 3.25 show contour diagrams of the impact of stress interference between fractured horizontal wells. Each figure shows the impact of increasing well spacing on the stress interference. From top to bottom the normalized well spacing increases for each figure. In these figures, the left column shows the contours of changing pore pressure in the reservoir and the right column shows the contours of the horizontal stress contrast. The vertical white lines in the plots depict the location of the fractures in the outer wells. The horizontal white line through the center of the contours depicts the location of the middle infill well. The black dashes represent the direction of intermediate principal stress. The stress interference caused by the fractures in the outer wells changes the stresses in the reservoir and hence changes the direction of the intermediate principal stress. The stress direction can be used as a surrogate to identify the direction of propagation of fractures in the middle well as shown in the previous chapter. The horizontal stress contrast can act as a guide to identify regions of potential fracture complexity as shown in the previous chapter.

The fracture spacing and the fracture height are equal for these cases. Figure 3.22 and Figure 3.23 show the simulation results for NFS = 1. From the figures in the left column of Figure 3.22 we see that immediately after fracturing, the pressure changes are insignificant in the vicinity of the fractured horizontal wells. The mechanical interference caused by the presence of fractures causes the stresses to reorient as seen from the black dashes in the figure. The horizontal stress contrast plots also depict this stress interference. For the smallest well spacing case, the stresses are completely reoriented around the middle horizontal well. Any fractures created in the middle well would potentially be longitudinal or have high complexity in the vicinity of the wellbore. These fractures are expected to be shorter and more complex (more branching). As noted earlier, the effect of mechanical stress reorientation does not affect the adjacent well since it is spatially limited. For the case of NWS = 1.42, the stresses are reoriented, however there is a potential for fractures created at the staggered locations in the middle well to be long with minimal fracture complexity. For the largest normalized well spacing case, the stresses have not been reoriented at the location of the middle well. The stress contrast has decreased in the staggered locations around the middle well. These low stress contrast regions around the middle well are likely to have complex fractures. For this example it seems viable to have fractures in staggered locations of the middle well for the case with the highest well spacing.

Comparing Figure 3.23 with Figure 3.22 we can clearly see the changes in the stresses caused by poro-elastic effects induced by production. In the left column of Figure 3.23 we see some evidence of depletion of reservoir fluids because of the decrease in the pressure in the vicinity of the reservoir fluids for the different cases of varying NWS. This depletion can induce stress changes in the reservoir because of poro-elastic stress changes. This is evidenced in the direction of the intermediate principal stress as well as

the horizontal stress contrast contours. For NWS = 1.06, the stress directions have reoriented to suggest non-longitudinal growth of fractures from the middle well. Similarly for the case of NWS = 1.42, the stress directions are reoriented at the staggered locations in the middle well. The case of NWS = 2.13 shows the most interesting change. There are regions in the staggered locations of the middle well that have complete stress reversal when compared to the corresponding case of Figure 3.22. However, the horizontal stress contrast has been decreased uniformly along the length of the middle well to a value less than 50 psi. This is a very low value of horizontal stress contrast that may induce fracture complexity for any fractures that are created in the middle well.

Figure 3.24 and Figure 3.25 show simulation results for cases similar to Figure 3.22 and Figure 3.23 respectively, but have a different NFS. In Figure 3.24 and Figure 3.25 we discuss cases where the fracture spacing to fracture height ratio is chosen to be 0.67. Figure 3.24 shows the impact of fracturing the outer wells before production is started. The change in pore pressure is negligible immediately after fracturing. The impact of fracture opening on the stresses is significant. This can be seen from the horizontal stress contrast contours and the intermediate principal stress vectors. The intermediate principal stress is completely reoriented in the smallest NWS case everywhere in the reservoir. It is reoriented only around the middle well in the middle NWS case. The NWS = 1.06 case suggests longitudinal fracture growth from the middle well. The NWS = 1.42 case also suggests longitudinal fracture growth. The NWS = 2.13 case suggests complex fracture growth away from the middle well.

Stress reorientation caused by production in this case of smaller NFS is significant. The left column in Figure 3.25 shows the impact of depletion on the pressures around the fractures. There is potential for non-longitudinal fractures in the smallest

NWS case. The other two NWS cases suggest that all the fractures created from the middle well will probably grow longitudinally.

Based on the above analysis using the horizontal stress contrast contours and the intermediate principal stress directions we see that well spacing, fracture length, fracture spacing, fracture height and depletion trends are all very important in determining the changes in stresses in the reservoir.

Shear failure contour diagrams were generated to assess the impact of stress interference on shear failure. Figure 3.9 shows a schematic of how to do this. For comparison purposes we plot the surface plot in Figure 3.26 to understand the stress state in the reservoir before any fractures are introduced in the system. The *in-situ* reservoir state suggests that heterogeneities in the rock that have cohesion and friction angle pairs in the red region will be highly likely to fail in shear.

Figure 3.27 and Figure 3.28 show the probability of shear failure contours for various values of cohesion (0 – 2000 psi on the Y axis of each contour plot) and various values of friction angle (20 – 40 degrees on the X axis for each contour plot). The colors represent the probability of shear failure in the region in consideration for each cohesion and friction angle pair. The figures show the impact of well spacing and production for NFS = 1 (Figure 3.27) and NFS = 0.67 (Figure 3.28). Both figures suggests that both well spacing and poro-elastic stress interference cause changes in the potential of shear failure near the middle well.

These contour plots have been quantified as a single number in the bar charts shown in Figure 3.29 and Figure 3.30. Both NFS cases show that the probability of shear failure radically improves in the middle NWS case, while showing gradual trends for the low and high NWS cases. This seems to suggest that there is an optimal value of NWS for which the probability of shear failure will be highest.

A careful analysis of these effects can help in understanding the implications of mechanical and poro-elastic stress interference on the potential of fracturing infill and pad drilled wells. Such an analysis can be summarized as traffic light charts as shown in Figure 3.31 and Figure 3.32 and can be directly used to make decisions regarding well spacing and fracture design in infill wells.

3.3.3 Case Study

The analysis done so far is now applied to an Eagle Ford pad. This Eagle Ford data set provided by Shell from a 4 well pad consists of completion, production and diagnostic data (microseismic, radioactive tracer, pressure and flow data). It was used to make observations about the impact of fracture spacing, sequencing and design on fracture performance. Three dimensional geomechanics simulations were conducted to understand and explain the diagnostic observations in the field. In this case study we demonstrated the value of the application of our geomechanics model to field scenarios. Fracture spacing, well spacing and the time between adjacent fractures were shown to be crucial parameters when fracturing horizontal wells.

In consecutive fracturing, fractures are created one-after-the-other sequentially in the same well. The time between these fractures was of the order of 3–4 hours; sleeve systems may have a much shorter cycle time. When, two horizontal wells in the same pad are zipper fractured, the time between consecutive fractures in the same well increases. In this pad scenario the time between adjacent fractures was increased to about 6–7 hours. The actual time can be a function of the number of zipper fractured wells and simultaneous operations associated with typical pump down systems. Using field data and the models developed we show that this increase in time between fractures created in the same well decreases the impact of stress shadowing. The extra time allows for the

partial closure of both the main hydraulic fracture and the induced, unpropped (IU) fractures created in the reservoir during the fracturing process (as discussed in Chapter 2). The decrease in the width of the fractures directly affects the stress interference caused by each fracture. The IU fractures can be created by either tensile opening of reservoir discontinuities (such as natural fractures) or shear slip events in the reservoir. These shear events could be activated by a change in the stress field. The microseismic events observed during a fracturing job can be considered to be a reasonable location of the shear induced IU fracture networks and can be used to draw conclusions on the interaction between IU fracture networks of multiple stages.

3.3.3.1 Field data

The field case study was based on a pad in the condensate window of the Eagle Ford shale. The field is located approximately 15 miles from the Mexico border. The Eagle Ford formation is approximately 8,000 to 9,500 ft true vertical depth (TVD) with a thickness of 200 to 300 ft. Table 3.2 includes a summary of all typical reservoir properties.

This 4 well pad had a uniform well spacing of 880 ft. This pad had a dual purpose as a research pad in which multiple completion strategies were assessed (stage spacing, cluster spacing, number of clusters, rate per cluster, and proppant volume per cluster). Diagnostic data in the form of microseismic data, radioactive tracer data, and treatment pressures were recorded and analyzed. Table 3.3 includes some of the relevant data for each of the wells. As can be seen from the table, the landing depths, lateral lengths and stimulation design per stage are all within a small window of 'operational variation'. The C and A wells were completed as single wells, Well C first followed by Well A. While, the B and D wells were zipper fractured for operational efficiency. Zipper fracturing

means that a treatment in a stage in Well B was followed by the treatment of a stage in Well D. This sequence was followed till all the stages were fractured in both the wells.

The microseismic data was collected with a combination of vertical and/or horizontal arrays. Figure 3.33 depicts the layout of the pad with the vertical well (and array) placed between the B and C wells. The horizontal arrays were placed in unstimulated offsets utilizing tractors to place the array across the offset well's stimulated interval. Radioactive tracer was pumped during the stimulation of each stage in the B, C, and D wells. All stages in Well B used Iridium tracers, all stages in Well C used Scandium tracers, and all stages in Well D used Antimony tracer. Distributing tracers in each well independently helped in understanding the potential interaction between the different wells.

3.3.3.2 Field observations and questions

The key observations that were made using the large dataset obtained for the pad are given below:

- The treatment pressure data and the different stage spacings in Wells A and C helped in identifying trends that were presented using simulation results in the previous chapter.
- The radioactive tracer data enlightened us about the communication between the wells (Figure 3.33)
- Microseismic data suggested the scale of interaction between the IU fracture networks (Figure 3.35)
- Both treatment pressure data and microseismic data together helped in diagnosing the impact of fracture sequencing.

Figure 3.36 depicts the clear trend in the Initial Shut-In Pressure (ISIP) values for the four wells in the pad. Figure 3.37 shows the stage by stage trend of the ISIP values for the four wells in the pad. The mean ISIP values of the four wells show the following trend (Table 3.3),

$$ISIP_C < ISIP_D < ISIP_B < ISIP_A$$

Also, notice how the standard deviation of ISIP values in wells A and C is much larger than the standard deviation of the zipper fractured wells B and D. This suggests greater variability in the ISIP values in the consecutively fractured wells compared to the zipper fractured wells.

Figure 3.38 depicts the ascending order of the Average Treatment Pressure (ATP) values for the four wells in the pad. Figure 3.39 shows the stage-by-stage trend of the ATP value for the four wells in the pad. The mean ATP values of the four wells show the following trend (Table 3.3),

$$ATP_C < ATP_D < ATP_A < ATP_B$$

Note that the standard deviation of ATP values is larger for wells A and C than wells B and D. Again suggesting more variability in the recorded pressures in the consecutively fractured wells compared to the zipper fractured wells.

A look at the radioactive data (Table 3.4) shows that many stages in well B are in communication with well D (as indicated by tracer response). However, surprisingly, the same stages in well D do not seem to be connected to well B. The tracer analysis also shows that the radioactive tracer from either well B or well D does not show up in well C (the well between well B and well D). One possible explanation for this is system contamination during the execution of the zippered stages. If the tracer system is not completely flushed some small volume of the tracer from Well B may be injected into Well D and vice versa. Such a thorough flushing of the surface system is not typical

during the execution of these jobs. However, a review of similar field data where wells are treated with a zippering sequence (typically direct offsets) indicate less frequent occurrences and more random occurrences between wells. Given this cursory review of field data, in this analysis we will assume that these observations are not a result of contamination and further explanations will be investigated.

The microseismic maps show a variety of trends for the different fracture stages in the wells (Figure 3.35). The spatial extent of the microseismic events suggests the existence of complex fracture networks and the presence of induced but potentially unpropped (IU) fractures. When we look at this microseismic data in detail we see certain trends. We observed that in some fracture stages (especially in well C), microseismic events were more pronounced towards the previously created fractures in the same well (Figure 3.40). Clearly the green events from stage 3 seem to be in the vicinity of the perforations from stage 2 and the red events from stage 2 are in the vicinity of the perforations of stage 1. We also observed that this spatial overlap in the microseismic event locations was less prominent in the zipper fractured wells B and D (Figure 3.41 and Figure 3.42). As is evident from the results, the microseismic scatter maps tend to stay confined within their respective stage dimensions. Another interesting observation with the microseismic data was the spatial extent of the microseismic data showing overlap between wells B and D (Figure 3.43).

Table 3.3 contains the average microseismic dimensions of the stages mapped in each well. The MS arrays provide biased estimates of the fracture lengths because of vertical and horizontal array placement around any given well. To overcome this location bias we use the length-width ratio of the microseismic extent of the fractures from the biased side (directionally toward the array) to compare the dimensions of the stimulated rock volume. Comparing the length-width ratio for the various wells we observe that well

A has the highest ratio, followed by well C, well B and well D in that order. We observe that the microseismic events of most stages in well B are very dense and are not observed far away from the well (Figure 3.35). Also, the MS maps of well B and well D show minimal overlap and hence lead to greater fracture lengths as depicted in Table 3.3.

In an attempt to better understand these observations we conducted geomechanical simulations of the fracturing operations in the pad. A discussion of the effect of some of the most important parameters in the fracture design (fracture spacing, number of clusters, fracture size etc.) by combining field observations with the simulation results leads to some very interesting conclusions.

In our analysis we assume that the fractures are planar. By using planar models, the conservation equations lead to longer than usual fractures. The microseismic data does not indicate simple, planar networks. It does indicate overlap between the microseismic events between wells. Therefore, this increase in the fracture length is not critical to causing well to well interactions. Also, we assume a single dominant fracture per stage. The inefficiencies associated with multi-cluster stimulations have been discussed in Molenaar et al. (2012).

3.3.3.3 Impact of stage spacing and number of clusters per stage

A distinct signature of stage spacing and the number of clusters per stage is observed in the pressure values recorded in the wells during fracturing and in the microseismic events observed. Both the pressures observed in the field and the MS events recorded are affected by the fracture sequencing.

The numerical simulation results in the previous chapter suggest that decreasing the stage spacing causes the fracture closure pressure values to show an up-and-down trend caused by fracture interference. Since fracture closure pressures were not recorded

in the current data set we use the ISIP as a surrogate for fracture closure pressures. From the field data set we observed that the well with the smallest stage spacing (well A) also had the highest average ISIP and the highest standard deviation in the ISIP values. As expected the mean ISIP of the fractures in well B, well C and well D is lower than the mean ISIP of the fractures in well A. The stage-by-stage trend of the ISIP values in Figure 3.37 suggests greater variation in the consecutively fractured wells and lesser variation in the zipper fractured wells. This suggests that there is greater stage-to-stage stress interference in well A and well C in comparison to well B and well D. There are exceptions caused by reservoir heterogeneity and other local effects that sometimes cause trends to exhibit anomalous behavior such as the high value of ISIP for the first stage in well A. We will ignore these exceptions for now.

The variation in the number of clusters per stage and cluster spacing may also have an effect on the pressures recorded. It is impossible to fully isolate this affect because of the limitations of the data set in this 4 well pad. Well C has 4 clusters per stage with a uniform stage spacing of 300 ft along the length of the well. Well A on the other hand has 1 cluster per stage with a uniform stage spacing of 200 ft along the length of the well. It is highly probable that all of the stages in well A create one fracture. However, for well C it is not easy to justify the non-existence of more than one fracture per stage. Thus a direct comparison of fracture spacing is not possible.

The impact of the number of clusters per stage is reflected in the treatment pressure values. Comparing fracturing treatments in a single cluster per stage well vs. multiple clusters per stage well, for everything else remaining the same, the single cluster per stage well will have a higher average treatment pressure value caused by a higher perforation friction drop. This is evident when comparing the ATP values of wells C, D

and A where well C has the lowest mean ATP value and well A has the highest mean ATP value.

Cluster spacing in a well can also affect the treatment pressure values. Assuming a single propped fracture per stage, IU fracture network created by the first propped fracture in a well can be assumed to be similar in lateral extent in both the single cluster per stage well and multiple cluster per stage well. This assumption of similar IU fracture extent is valid because we assume a single propped fracture per stage. This single fracture per stage forms the primary source of fracture fluid and stress interference in the vicinity of the fracture and hence should lead to similar IU fracture lateral extent. In this scenario, decreasing the cluster spacing while maintaining the same stage spacing can increase overlap of the fracture network and the locations of the clusters of the next stage. This overlap will lead to an increase in the fluid loss from the successive stages into the existing open IU fracture network. Thus smaller cluster spacing between successive fractures in a well could decrease the observed treatment pressure values. This again aligns with the observed trend of treatment pressure values for wells C, D and A. One thing worth noting here is that such trends will be more noticeable in an open-hole completion. However, in a cased-hole completion this effect will be noticed if the created IU network of fractures exists in the vicinity of the perforation clusters of the successive stage. This will allow communication of the fracturing fluid from this new stage to the branched fracture network created by the previous stage thus allowing a high permeability flow conduit and hence reducing the treatment pressure.

With a larger number of clusters per stage overlap between fracture networks can become more probable. We speculate that increasing the number of clusters leads to more overlap of the microseismic events observed for each stage. Microseismic events of the

n+1 stage have a greater tendency to overlap with the previous stage, stage n in the wells. This trend should be more probable in well C than in well A.

Figure 3.46 shows the contour map for the horizontal stress contrast for (a) a single fracture in a horizontal well and, (b) a case of three fractures in a horizontal well. The second case of three fractures is simulated to represent the field scenario of multiple clusters per stage. Here we chose to keep the same amount of proppant in the two simulations and we chose the outer fractures to have longer lengths than the middle fracture in the three fracture case. Further we assume that all the fractures are propped and thus the geometries are fixed. Figure 3.46 clearly depicts an increase in the spatial extent of the stress shadow in the case of three fractures in comparison to the case of a single fracture. From this simulation result it is easy to predict that if multiple propped fractures are created in a stage then the region of stress interference extends further along the well.

Well A has one cluster per stage while well C has 4 clusters per stage. From the simulation results it is evident that if more fractures are activated in a stage, the stress shadow will extend further along the well. Also, the length of the fractures would be expected to be smaller when there are a greater number of clusters per stage. Table 3.3 shows that well A, which has only one cluster per stage has relatively long fractures but the fractures do not have as wide a stimulated fracture network. This is consistent with the results obtained from the simulations (Figure 3.46). Comparing the values, and using the knowledge that Well A has only one cluster when compared with Well C's 4 clusters, one may expect the length of fractures in Well A to be longer than depicted by the numbers in Table 3.3. However, the network width value for well A depicts a much greater lateral overlap as well. This is probable because of the closer stage spacing and hence easier access to the induced unpropped fractures created in the previous stages.

This leads to greater lateral widths. We suspect that if the stage spacing were increased while having only one cluster per stage the length-width ratio would be much higher for Well A.

A relatively greater width of the fracture network for well C implies that there could be significant overlap between the fracture networks induced by consecutive stages in well C. This is also supported by the fact that the cluster spacing in well C is much lower than in well A (75 ft vs. 200 ft.). Figure 3.40 supports this hypothesis and depicts the overlap in the microseismic envelopes of the first three stages of well C.

3.3.3.4 Impact of poro-elastic effects

Figure 3.44 shows the variation in the minimum principal stress value because of the mechanical interference caused by transverse fractures. It is important to note that the stress interference caused by a fracture does not travel too far away from the well. The peaks in the figure represent the location of the fractures in the fractured well and the different curves in the figure are at various distances from the fractured well. The wells on the pad are 880 ft apart from each other. According to the simulation results shown in Figure 3.44 negligible stress interference is observed beyond 880 ft away from the fractured well. This suggests that fractures in Well C will not induce stress changes in Well A which is 1760 ft away from well C. Thus the inter-well stress interference is not sufficient to explain the higher average treatment pressures in Well A.

The simulation results are based on a predefined fracture geometry for all the fractures in the well. For the simulation model we assumed that fractures have 300 ft half-length, 200 ft height and are propped open using 500,000 lbs of proppant. If these geometry specifications are altered the stress interference will also be altered. Thus if the fractured well had 400 ft long fractures then it is possible that the stress interference from

this fractured well interfered with the fractures in the adjacent well. The field results show that the average ISIP value observed for the fractures in Well B is larger than the corresponding value of well D. One possible explanation for this could be the fracturing sequence. Well B was fractured after Well A and Well C were fractured. The fractures in well B could be in a stress caged environment created by the propped fractures in wells A and C. This can lead to higher ISIP values for Well B than Well D. This stress caged environment can also lead to high treatment pressure values for Well B. The cumulative stress interference effect of the fractures in Wells A and C at the location of Well B is not apparent from this figure but as discussed above a change in the simulation parameters can cause greater stress interference at the location of Well B

So far we have shown that the inter-well mechanical stress interference effects are not significant for the current case of 880 ft well spacing. We now show that poro-elastic effects at the fracturing time scale are not able to explain the unique observations on this pad with special reference to the differences between zipper fracturing and consecutive fracturing sequences either. These poro-elastic effects are introduced because of the injection of treatment fluid during the fracturing operation. Figure 2.10 and Figure 2.11 show the mechanical and poro-elastic effects induced by a propped fracture. The simulations used to produce the results presented in Figure 2.10 have a modeled permeability of 1 mD while the results presented in Figure 2.11 use a modeled permeability of 1 μD. In this model, a propped fracture is simulated with 500,000 lbs of proppant. The initial pressure inside the fracture is assumed to be the average treatment pressure. In this simulation the fracture treatment time is 2 hours and for the duration of the treatment time the fluid calculations in the matrix are done with fixed fracture geometry and a constant pressure equivalent to the fracture treatment pressure inside the fracture. Thereafter, the pressure inside the fracture is allowed to dissipate into the

reservoir in time as the pressure inside the fracture is greater than the reservoir pressure. This allows us to simulate fluid leak-off from the fracture into the reservoir. This fluid leak-off increases the pressure in the vicinity of the fracture over time, thus giving rise to poro-elastic effects and hence changing the stresses in the reservoir (Zhai and Sharma 2007). As seen in the figure, a significant decrease in the minimum principal stress is observed in the immediate vicinity of the fracture over time. However, this variation in the minimal principal stress reduces very quickly away from the propped fracture.

Figure 3.45 depicts the influence of both poro-elastic effects and mechanical effects in a pad. The propped fracture half-lengths chosen in the simulations are 300 feet. Thus the 440 ft curve in the two figures is 140 ft away from the tip of the fractures in the fractured well and the peaks on the curve correspond to the location of the fractures. On moving further away from the fractured well the influence of individual fractures on the minimum principal stress diminishes. About 880 ft away from the fractured well, at the location of the adjacent well, the influence of the fractured well is reduced considerably. Both Figure 3.44 and Figure 3.45 show identical trends with negligible influence of poro-elasticity on the stresses far away from the fractured well. This leads us to conclude that poro-elastic effects are insignificant in unconventional shale oil and gas reservoirs at the fracturing time scale.

In summary, these results indicate that the stress shadow effect of the individual fractures (including both mechanical and poro-elastic effects) may be limited to around the mechanically propped region. These stress interference effects do not extend to the adjacent wells. Therefore, it is not possible to explain the performance of zipper fracs on the basis of stress shadow effects of propped fractures if they do not extend appreciably from one well to another. Also, we observed in tracer data that the radioactive tracer pumped in well D shows up in well B. This cannot be explained based on mechanical

interference data alone. As shown above, the mechanical interference effects caused by planar fractures lose their influence at inter-well distances. Other data obtained on the pad revealed that there is a trend observed in the ISIP data, the average treatment pressure data as well as the averaged microseismic extents. However, this data did not guide us in understanding the tracer results observed.

3.3.3.5 Impact of fracture sequencing

Two primary fracture-sequencing techniques were used in this pad (i) consecutive fracturing and (ii) zipper fracturing. Well A and well C were consecutively fractured while well B and well D were zipper fractured. Zipper fractured wells are often considered to create more complex fracture networks. In this case not only was there a characteristic signature of zipper fracturing on the microseismic maps, the production data showed that well B had a better hydrocarbon production response than well C (similar completion strategies). We ran several simulations to identify the possible reasons for the variation in the production response of fractures in a zipper fracturing sequence in comparison to the fractures in a consecutive fracturing sequence. We performed inter-well mechanical interference simulations to understand the influence of fractures in one well on the fractures in another well in the same pad. However, none of those simulations conducted are able to explain the observed trends in the pad. Further analysis suggests that fracture sequencing analysis coupled with fracture closure analysis can help answer most of the unanswered questions on the pad.

Figure 3.49 presents a case where the wells are zipper fractured and hence the time between adjacent fractures in the same well is increased. Figure 3.49a shows the stimulated area at the time pumping is stopped for the 1st stage of fracturing. Figure 3.49b shows the stimulated area of the corresponding zipper fracture at the end of pumping.

Note that we have again used Δt to suggest the time between successive fractures in a well. Generally, the delay time between two consecutive fractures on the pad is smaller in the case of zipper wells but for simplicity we keep it the same as before. At this time the stimulated area of the first frac has also considerably reduced. Based on our schematics, the delay time for the 2nd fracture in the same well for consecutive fracturing is Δt, however, the effective delay time for the 2nd fracture in the same well for zipper fracturing is $t_p + 2\Delta t$. Thus we have increased the effective delay time for the same well by $t_p + \Delta t$! This increase allows the fracture network of the previous stage to close significantly and hence reduces fracture interference and reduces the wastage of fluid and proppant into existing fracture networks as illustrated in Figure 3.49d.

We hypothesize that the time between successive stages in well C was not long enough to allow the opened fracture networks to close completely. We showed in the previous chapter that the stress interference caused by IU fractures will be considerably less than the stress interference caused by the main hydraulic fracture. Thus the IU fracture network of well C does not impose a significant stress shadow. This assumption is supported by the fact that the average ISIP values as well as the average treatment pressure values of the stages in well C are the lowest (Table 3.3). These open fracture networks for the previous stages act as passages for flow when the current stage is treated. Thus the resistance to flow is decreased because of the availability of conductive flow paths in the formation and hence the treatment pressures are decreased. Such an observation is highly likely when the number of clusters per stage is high and the spacing between the clusters and stages is low. This conclusion is depicted in Figure 3.39 which shows the trend of average treatment pressures recorded for the various stages in the wells. The trends suggest that the average treatment pressure in well C is considerably smaller than the average treatment pressure in well A; hence supporting the above

argument. The radioactive tracer data indicates communication between wells B and D. One explanation is one-way propagation of the tracer from well D to B. This indicates that IU fractures may exist and are open during the fracture treatment in well D. This channel for communication shuts down as the fractures close soon after the fracture treatment is complete. Limited communication is observed from B to D (as indicated by tracer breakthrough).

In our simulation model, the fracture is created by assuming an average treatment pressure value (~10,000 psi). This average treatment pressure is higher than the pressure required to prop-open a fracture to the propped fracture width. Thus the fracture is opened to a greater width than before because of the excess fluid pressure. As this fluid pressure decreases inside the fracture because of fluid leak-off, the fracture tries to close until it attains the final propped fracture width. The fracture treatment time was assumed to be 2 hours. During this time the pressure inside the fracture was maintained at the average treatment pressure. In this simulation the fracture closed from its initial width to the final propped width in about 200 minutes. The *in-situ* reservoir conditions are S_{hmin} = 7372 psi, S_{hmax} = 7472 psi, reservoir pressure = 6000 psi, reservoir permeability = 1 μD, reservoir porosity = 5%. (Figure 3.50). A good explanation of the time of closure and its dependence on various factors such as reservoir permeability, existing fracture networks etc. had been discussed in the previous chapter. This time of closure in the simulation is not representative of the values observed in the field because of several reasons. The permeability assumed here is greater than the permeability of the reservoir matrix. The effective surface area of fracture contact with the reservoir is not correctly modeled in this simulation since the presence of a network of fractures connected to the main hydraulic fracture is not modeled. This network of fractures can be very efficient in driving the fluid away from the main hydraulic fracture. However, the closure time has a

similar order of magnitude as the fracture closure times observed in the field in mini-frac and DFIT tests. The closure times in our simulations have not been calibrated against field data and only provide a possible impact of leak-off and fracture closure on the stress interference. In direct comparison between the simulation results and the field results we need to include a lot of other factors, such as, the amount of fluid pumped in the field test, the effect of fluid rheology and including the actual treatment data in the simulations.

We have shown the impact of fracture closure using simulation results. In this section we try to tie those results to the field observations. Well A and well C had consecutive fracturing sequences while well B and well D were zippered. Thus the time between the consecutive fractures in well C and well A were smaller than the time between the consecutive fractures in well B and well D (Figure 3.51). This extra time in well B and well D allowed for the stimulated natural fractures to close and reduce the stress shadow in their vicinity. However, the induced unpropped fractures in well A and well C probably do not close when the next stage is stimulated. Therefore the fracture networks and stress shadows in well A and well C may end up overlapping depending on the influence of the multi-cluster completion strategy. The overlap is evident from the MS maps of the C well. The MS maps of well B and well D show minimal overlap and hence lead to greater fracture lengths as depicted in Table 3.3. This is also depicted in Figure 3.41 and Figure 3.42 where we show the microseismic maps of stages 4, 5 and 6 in wells B and D. As is evident from the results, the microseismic scatter maps tend to stay confined within their respective stage dimensions in comparison to the patterns observed in Figure 3.41. We choose to show only 3 stages in wells B and D to depict the general trend of the microseismic maps observed in the wells. These three stages were chosen to help illustrate the hypothesis. An overall picture can be seen in Figure 3.35.

Another effect of the increase in time between consecutive fractures in well B and well D is the ISIP signature (Figure 3.37). As discussed above the stress shadow greatly impacts the closure pressure observed in consecutive stages in a horizontal well. Since well B and well D were zippered, the time between consecutive stages in both these wells was increased. Thus any open fracture networks in the individual stages of these wells were allowed more time to close. Thus the effect of the stress shadow of the open fracture networks was lost when the consecutive stage in the either well was treated. This reduction in stress shadow leads to a reduction in the general ISIP value and also decreases the oscillation in the ISIP values. Well C on the other hand had less time between consecutive fractures and hence shows a characteristically high and oscillating ISIP trend.

The time between fractures and the closure of fracture networks can be used to explain the tracer results on the pad. As depicted in Table 3, many stages in well B show that they are connected to well D however surprisingly so, the same stages in well D do not seem to be connected to well B. This can be explained by analyzing the microseismic maps of respective stages in the two wells. In Figure 3.43, we discuss one such scenario where we compare the microseismic maps of stage 3 in well B and well D. Stage 3 in well B is stimulated before stage 3 in well D. Thus, at the time of end of treatment of stage 3 in well B a fracture network has been created that is possibly not connected to the well D. However, immediately after stage 3 in well B is completed the treatment of stage 3 in well D is started. At this time the unpropped fracture network of stage 3 in well B is presumably still open. Also, the induced unpropped fracture network of the corresponding stages in well C is most probably closed (since well C was the first well to be fractured and well B and well D were zipper fractured a few days after the completion of well C). Thus, the fracture from well D intersects this pre-existing fracture network of

well B and under a favorable pressure gradient transports the tracer from well D to B. This is further explained by Figure 3.51 where we show the delay time between the corresponding fractures of wells B and D. Other than a few outliers the time between the end of pumping into a fracture in one well and the start of pumping into a fracture in the other well is generally less than 100 mins. We can compare this to the intra-stage average delay time in well C and well A (~4 hours). As shown above we have microseismic evidence of overlapping fracture networks between the respective stages of wells A and C. Since we see overlap in networks for a delay time of about 4 hours, it is highly likely that at the delay time of less than 100 minutes (for the zippered wells) there will be overlap in the fracture networks. If the time between the two stages discussed had been larger (allowing the IU fractures to close), there is a possibility that no tracer communication would have been observed. Thus the tracer data also leads us to believe that there exist some induced unpropped pathways for fluid migration.

3.3.3.6 Strategies to increase time between successive fracture stages

So far we have shown that increasing the time between adjacent fractures in a horizontal well creates more efficient and effective fracture networks and hence can enhance the productivity of the well. However, increasing the delay time between immediate fractures in a single well will lead to lost rig and frac-crew time and may not be economically justified unless the total rig and frac-crew time can be kept the same. Figure 3.51 shows four strategies to enhance the effectiveness of the hydraulic fracturing treatments by increasing the time between immediate fractures in a horizontal well while maintaining the rig time and the frac-crew time less than or equal to the time required to hydraulically fracture a single well.

Figure 3.52a shows the scenario of alternate fracturing (Roussel and Sharma 2011a) where all the bookend fractures are treated before the middle fractures are treated. As shown in Table 3.5 this allows the bookend fractures to be created without any significant interference from the previous stage because of the larger stage spacing. Also, this increases the delay time for the middle fractures several-fold. Thus it is highly likely that when the middle fractures are stimulated, they will have a much smaller overlap with the stimulated volume of the bookend fractures. Figure 3.52b and Table 3.6 depict the case of two zipper fractured wells. As discussed in Figure 3.49, zipper fracturing causes the delay time between the adjacent fractures in the same well to increase from Δt to $t_p + 2\Delta t$. Figure 3.52c and Figure 3.52d depict staggered zipper fracturing strategies. These pad scale strategies can be highly useful in optimizing the stimulated reservoir volumes for each stage in each well in the pad. As shown in Table 3.7 and Table 3.8 the delay time between the immediate fractures in the same well is increased from Δt in the case of consecutive fracturing to $2t_p + 3\Delta t$ and $3t_p + 4\Delta t$ for the three well and four well scenarios respectively. In addition to that deploying staggered fracturing in these multi-zipper-well scenarios can aid in more effectively stimulating the reservoir (Roussel and Sharma 2011b; Rafiee et al. 2012)

The strategies discussed above do not cause any wasted rig time or any wasted frac crew time. For the alternate fracture treatment the time required for the whole process will be comparable to the time required for a conventional fracturing treatment. For all the other cases of zippered wells discussed, with the use of manifolds in the field, the time required to stimulate two or more horizontal wells will be less than or equal to stimulate the same number of wells using the conventional (toe-to-heel single-well) fracturing sequence. The oil and gas industry currently has working technology to apply systems to achieve all the strategies discussed in Figure 3.52.

3.4 CONCLUSIONS

In this chapter we have shown that inter-well stress interference effects are important to consider when designing pad scale fracturing strategies. We showed that the poro-elastic stress interference induced by a fractured horizontal well that was produced for a period of time can induce a gradient of minimal principal stress moving away from the produced horizontal well. This stress change near the produced horizontal well can act as a sink for fractures from nearby wells. Thus fractures from the neighboring wells have an easier time propagating towards a reduced pressure region. This biased fracture propagation can cause fracture hits.

A parametric analysis was conducted to show the impact of several parameters on stress interference in well pads. The impact of this stress interference on factors that affect well productivity are significant. Fracture complexity and small reservoir depletion (availability of hydrocarbon resources) are clearly good for production. Pore pressure contours can be used to check on the viability of an infill well. To predict the likelihood of fracture complexity, a reduced horizontal stress contrast signature and a high probability of shear failure can be used as surrogates.

Using the above knowledge, charts can be drawn to help a completions engineer to design a pad scale fracturing operation. A balance between fracture length and fracture complexity can be sought for efficient reservoir drainage. Fractures can be designed by selecting sand volumes, injection rates, and injection sequence to achieve a certain degree of fracture complexity. An example of such an exercise was presented in this chapter. Traffic light charts were designed based on the analysis presented in 3.3.2.2. (Figure 3.31 and Figure 3.32) to help select well spacing and stage spacing. Figure 3.31 shows the conclusions from the analysis for cases of no production while Figure 3.32 shows the conclusions from the analysis for cases with 365 days of production. Thus, Figure 3.31

should be used when designing pad scale completion strategies while Figure 3.32 should be used when designing infill well strategies. These figures represent a concise way of summarizing analysis done to optimize well spacing, fracture spacing, fracture sequencing for most pad operations.

A field data set from a pad consisting of 4 wells and a complete set of diagnostic data (microseismic, radioactive tracer, pressure and flow data) has been used to make observations about the impact of fracture spacing, sequencing and design on fracture performance. A geo-mechanical simulator was used to calibrate our model and to understand the importance of time between fractures in a hydraulic fracturing treatment design. We demonstrate that the time between adjacent fractures is a crucial parameter when fracturing horizontal wells. In consecutive fracturing, fractures are created one after the other sequentially in the same well. The time between these fractures is generally of the order of 3–4 hours caused by the execution of pump down operations; sleeve systems may have a much shorter cycle time. When, two horizontal wells in the same pad are zipper fractured, the time between consecutive fractures in the same well increases to about 6–7 hours. The actual time is a function of the number of zipper fractured wells and simultaneous operations associated with typical pump down systems. In this work we show that this increase in time between fractures created in the same well decreases the impact of stress shadowing. The extra time allows for the partial closure of both the main hydraulic fracture and the induced, unpropped (IU) fractures created in the reservoir during the fracturing process. The decrease in the width of the fractures directly affects the stress interference caused by each fracture. The IU fractures can be created by either tensile opening of reservoir discontinuities (such as natural fractures) or shear slip events in the reservoir. These shear events could be activated by a change in the stress field. The

microseismic events observed during a fracturing job can be considered to be a reasonable location of the shear induced IU fracture networks.

The case study presented discussed demonstrates the use of the analysis techniques to real field situations. Following conclusions can be made from the case study analysis:

- The creation of propped fractures leads to the formation of induced, unpropped (IU) fractures during the fracturing process.
- The presence of IU fractures is demonstrated both by microseismic data and tracer data (breakthrough of tracer being observed well beyond the propped fracture length). The presence of IU fractures can significantly increase the spatial extent of the microseismic volume (rock volume from which MS events are recorded).
- The time required for some of the IU fractures to close is estimated in this analysis to be of the order of several hours after pumping is ceased. For lower leak-off rates, the time for closure may be of the order of days.
- Interference between fractures in a given wellbore has been shown to depend on the stress shadow created by both the propped fracture and the induced unpropped (IU) fractures.
- The spatial extent of the stress shadow region is much larger when the IU fractures are open and reduced significantly with time as the IU fractures close as the fluid leaks off. This is shown by our simulations and is also seen in the field data presented in this analysis.
- The extent of stress interference between fractures is time dependent. More fracture interference is expected to occur if the time between successive fractures in a single wellbore is small, which may lead to poorer fracture performance as a result of re-stimulation of previously stimulated portions of the reservoir.

- Conversely, if the time between successive fractures in a wellbore is increased long enough for the IU fractures to partially close, the stress shadow region shrinks leading to less interference between fractures and better performing fractures. These effects are clearly shown to be significant through our geomechanical simulations.
- The time dependent closure of IU fractures also clearly explains why zipper fracs work better than consecutive fracturing in many applications. The time between successive fractures is approximately doubled in a zipper frac sequence of fracturing compared to the conventional consecutive fracturing. This allows the IU fractures to close and the stress shadow region to shrink over time leading to less fracture interference (in a given well) when zipper fracs are used.
- The IU fractures can extend in a large region around the treated stage. Increase in time between adjacent stages in a well can induce closure of the IU fractures in the vicinity of the new stage. Thus the fracture treatment in this current/new stage can stimulate unstimulated reservoir volume and hence increase the fracture complexity while reducing the loss of fluid and proppant into existing stimulated regions.
- The simulations presented in this analysis clearly show that fracture interference (or stress shadow effects) between fractures in adjacent wells cannot possibly explain the observations associated with zipper fracs. These observations include, ISIP trends, microseismic trends as well as production trends observed in the field.
- The analysis shows, for the first time, that the time interval between adjacent fractures in a wellbore can have a significant effect on the production performance and geometry of fractures in a horizontal wellbore. This clearly has

implications in the planning, sequencing and execution of multiple fracture treatments in multiple wellbores in pad drilling and fracturing.

3.4.1 Limitations of Current Work

So far we have addressed the issue of optimization of pad scale fracturing using static fractures. A fracture trajectory algorithm has been discussed that helps in capturing the impact of stress interference on the trajectory of subsequent fractures. There are several limitations of such an algorithm:

- Simulation of static fractures requires the use of predefined fracture geometries. Thus, the impact of the stress interference of a fracture on its own propagation direction is lost.
- Horizontal wells are fractured in stages with multiple fractures propagating simultaneously and competing for fluid and proppant. This is not possible to model using a static fracture model.
- Asymmetric growth of fractures that can be observed in cases of fractures growing in the vicinity of depleted wells cannot be captured using static fractures.
- Interaction of fractures with existing natural fractures and other heterogeneities that may alter the propagation direction of these fractures can also not be modeled.

These issues render the current model inadequate and requires the use of a fracture propagation code. In the next chapter we discuss the implementation of a hydraulic fracturing propagation code that can address the above mentioned limitations.

3.5 NOMENCLATURE

c	= Cohesion	$ML^{-1}T^{2}$, psi
Δs	= stage spacing	L, ft
Δt	= delay time between current pad stage and next pad stage	T, min
E	= Young's modulus	$ML^{-1}T^{2}$, psi
f^s	= failure state	dimensionless
ϕ	= friction angle	degrees
h_f	= fracture half-height	L, ft
H_f	= fracture height	L, ft
l_f	= fracture half-length	L, ft
L_f	= fracture length	L, ft
υ	= Poisson's ratio	dimensionless
p_f	= bottom-hole fracture pressure	$ML^{-1}T^{2}$, psi
σ_{hmin}	= minimum principal stress	$ML^{-1}T^{2}$, psi
σ_1	= maximum effective principal stress	$ML^{-1}T^{2}$, psi
σ_3	= minimum effective principal stress	$ML^{-1}T^{2}$, psi
t_p	= treatment pumping time	T, min
w_{max}	= maximum fracture width	L, m

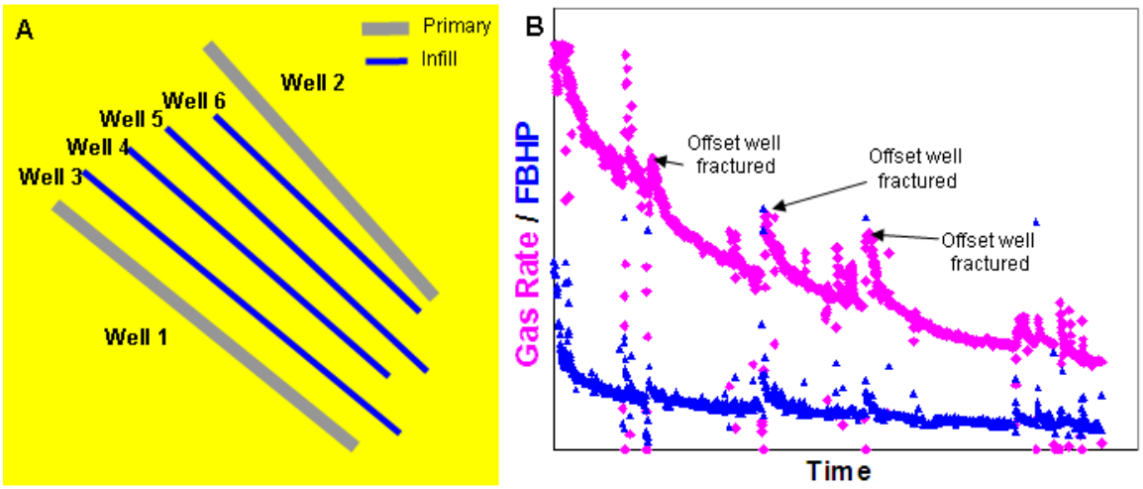

Figure 3.1 (A) Primary and infill wells for the pad, (B) production data for well 1 showing pressure spikes when some offset wells were fractured. This pressure signature suggests some communication between the wells (Gupta et al. 2012).

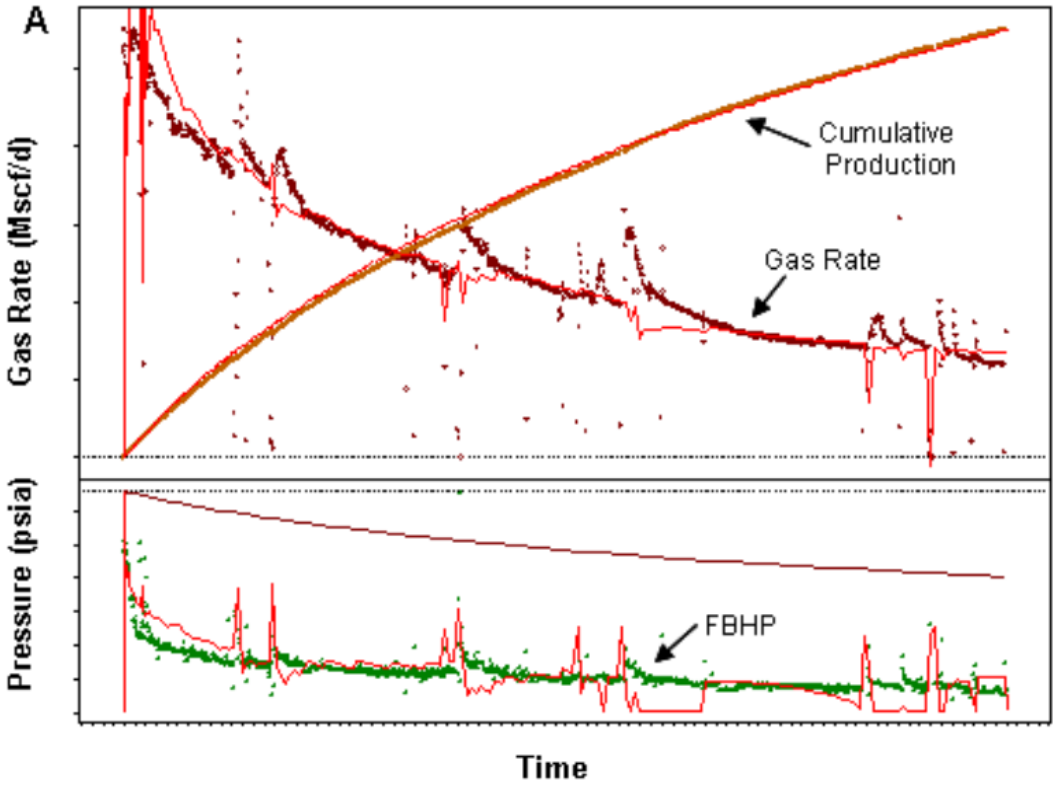

Figure 3.2 History matched Well 1 production data for pad shown in Figure 3.1 (Gupta et al. 2012).

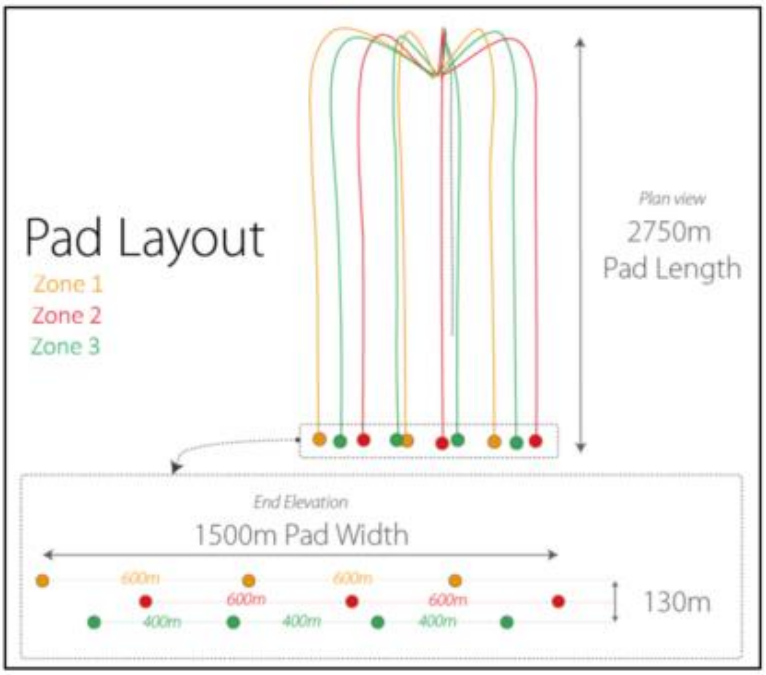

Figure 3.3 Horn River pad layout to test for inter-well pressure communication. (Sardinha et al. 2014)

Percentage of Hits Delivered (By Distance)

Frac Well	Frac Well Zone	0-200m	200m-400m	400m-600m	>600m
Well 1	Zone 1	9	80	27	1
Well 2	Zone 3	91	64	23	8
Well 3	Zone 2	92	90	54	8
Well 4	Zone 3	87	78	100	27
Well 5	Zone 1	38	48	48	2
Well 6	Zone 2	77	73	37	10
Well 7	Zone 3	95	75	53	8
Well 8	Zone 1	21	59	57	11
Well 9	Zone 3	100	86	15	4
Well 10	Zone 2	91	67	14	5

Figure 3.4 Percentage of hits delivered by wells (by distance). (Sardinha et al. 2014)

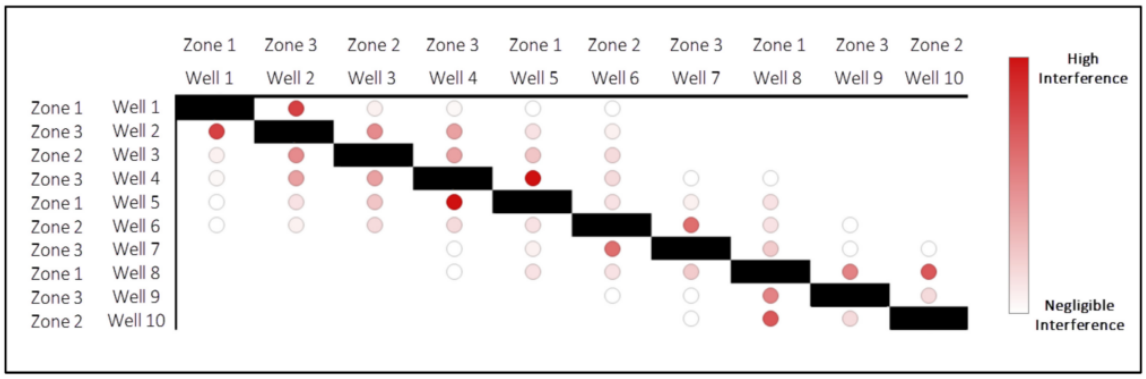

Figure 3.5 Initial flowback production interference. (Sardinha et al. 2014)

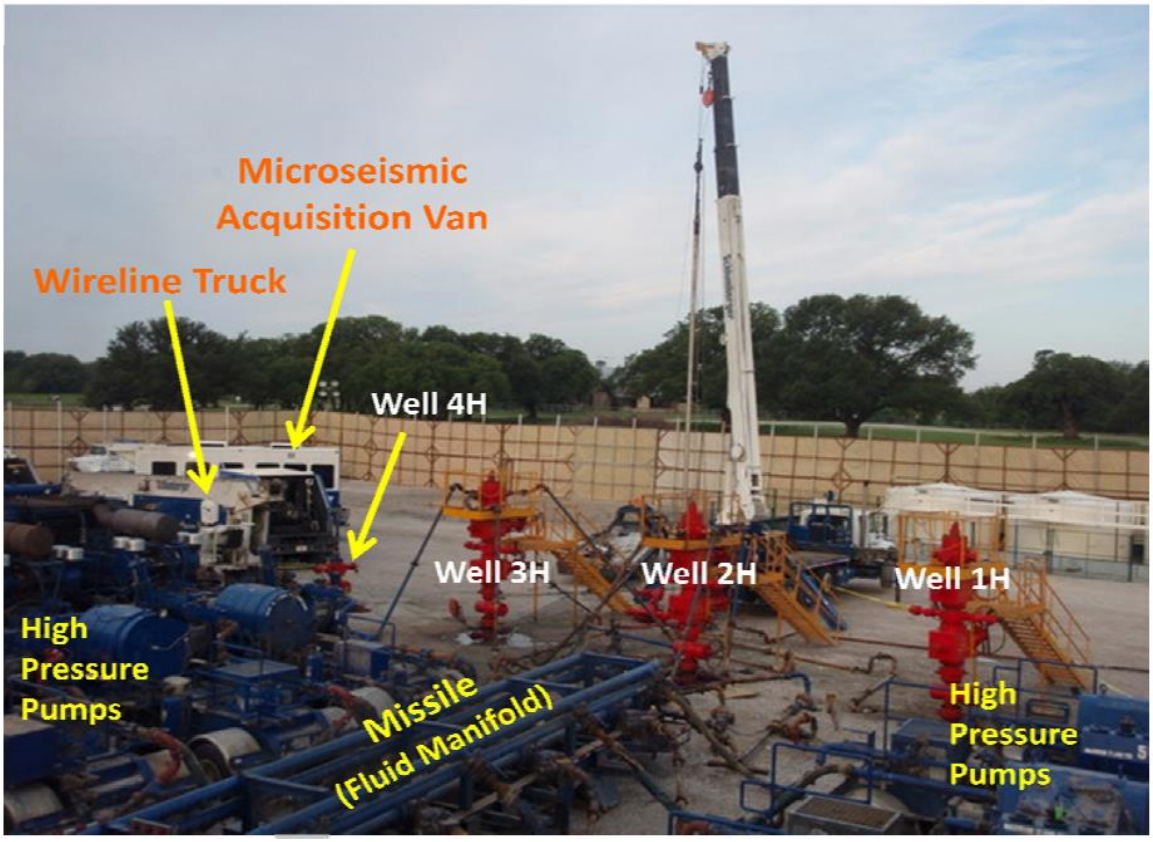

Figure 3.6 Surface wellhead locations of four lateral wells drilled from the same pad and stimulated using the zipper fracturing technique (Ramakrishnan et al. 2011).

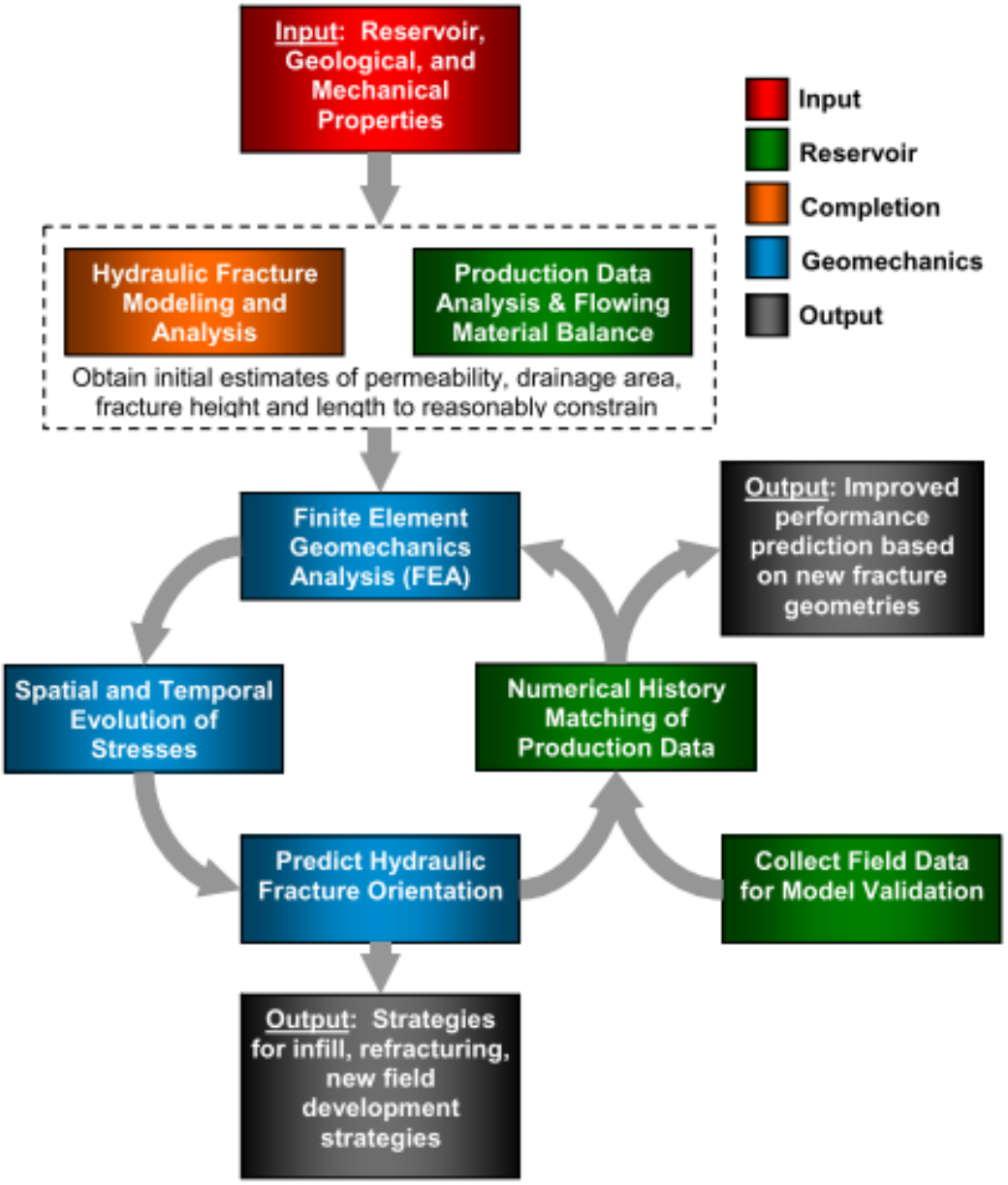

Figure 3.7 Integrated methodology to predict spatial and temporal evolution of stresses and strategies for potential application in refracturing, pad scale fracture design and infill optimization (Gupta et al. 2012).

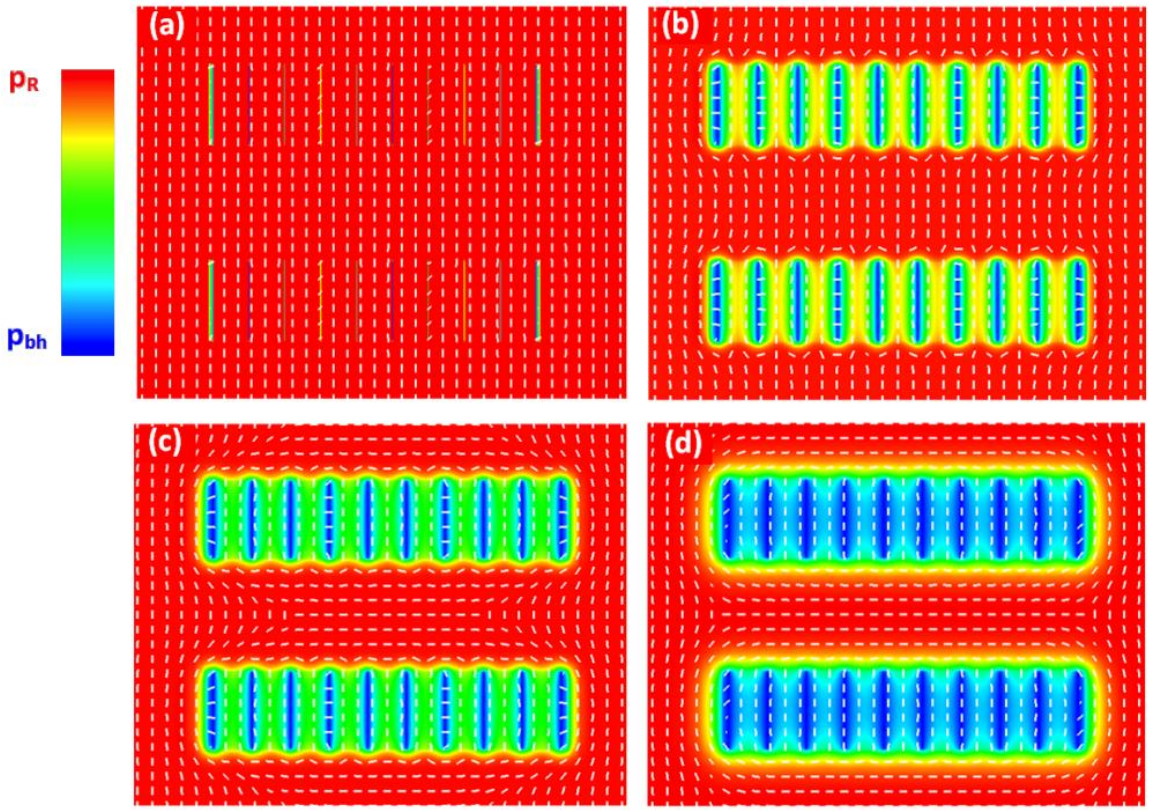

Figure 3.8 Pressure and stress reorientation between producing fractured horizontal wells at different t = (a) 0, (b) 6 months, (c) 1.25 years, and (d) 5 years. (Roussel et al. 2013)

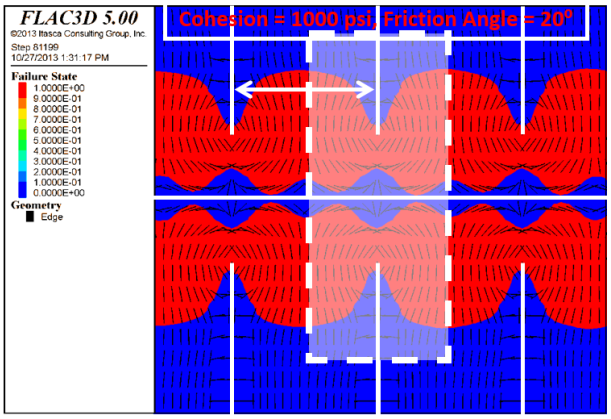

Step 1.

Compute stress state for each case of well spacing and fracture spacing. Extract the stress data in the marked region. The marked region is chosen to have a height equal to the chosen fracture height.

For each stress state calculate the failure state for each grid block in the middle region marked above for different values of cohesion and friction angle.

$$f^s = \sigma_1 - \sigma_3 N_\phi - 2c\sqrt{N_\phi}$$

$$N_\phi = \frac{1+\sin\phi}{1-\sin\phi}$$

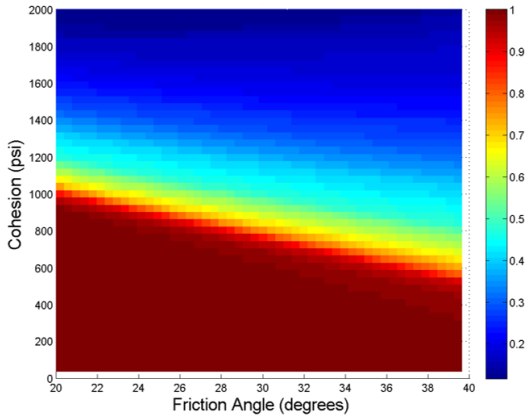

Step 2.

Find the average failure value for each chosen cohesion value and plot on the contour diagram.

$$\overline{f^s} = \frac{\iiint f^s(x,y,z)dxdydz}{\iiint dxdydz}$$

Probability of Failure = 60 %

Step 3.

Compute an average probability of failure for the N_c cases of cohesion and N_{fa} friction angle.

$$\text{Probability} = \frac{\sum_{i=1}^{N_c}\sum_{j=1}^{N_{fa}}\overline{f_{ij}^s}}{N_c N_{fa}}$$

Figure 3.9 Schematic to obtain probability of shear failure estimates in regions of the reservoir impacted by stress interference.

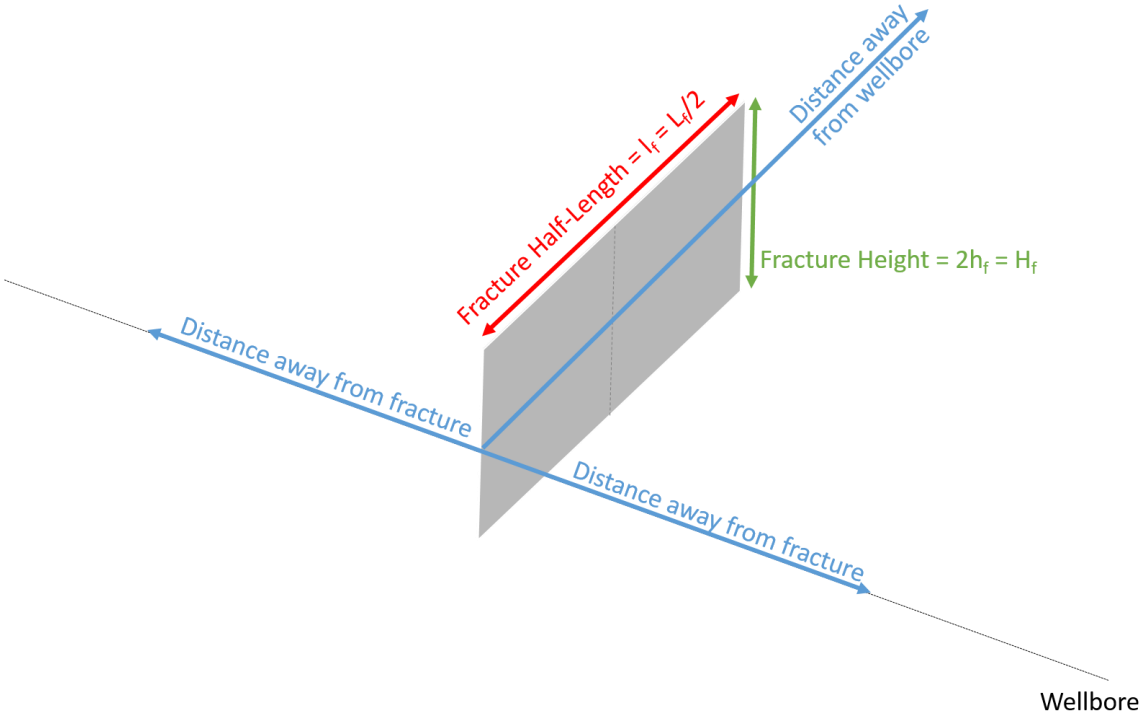

Figure 3.10 Schematic showing half-fracture used in the simulations.

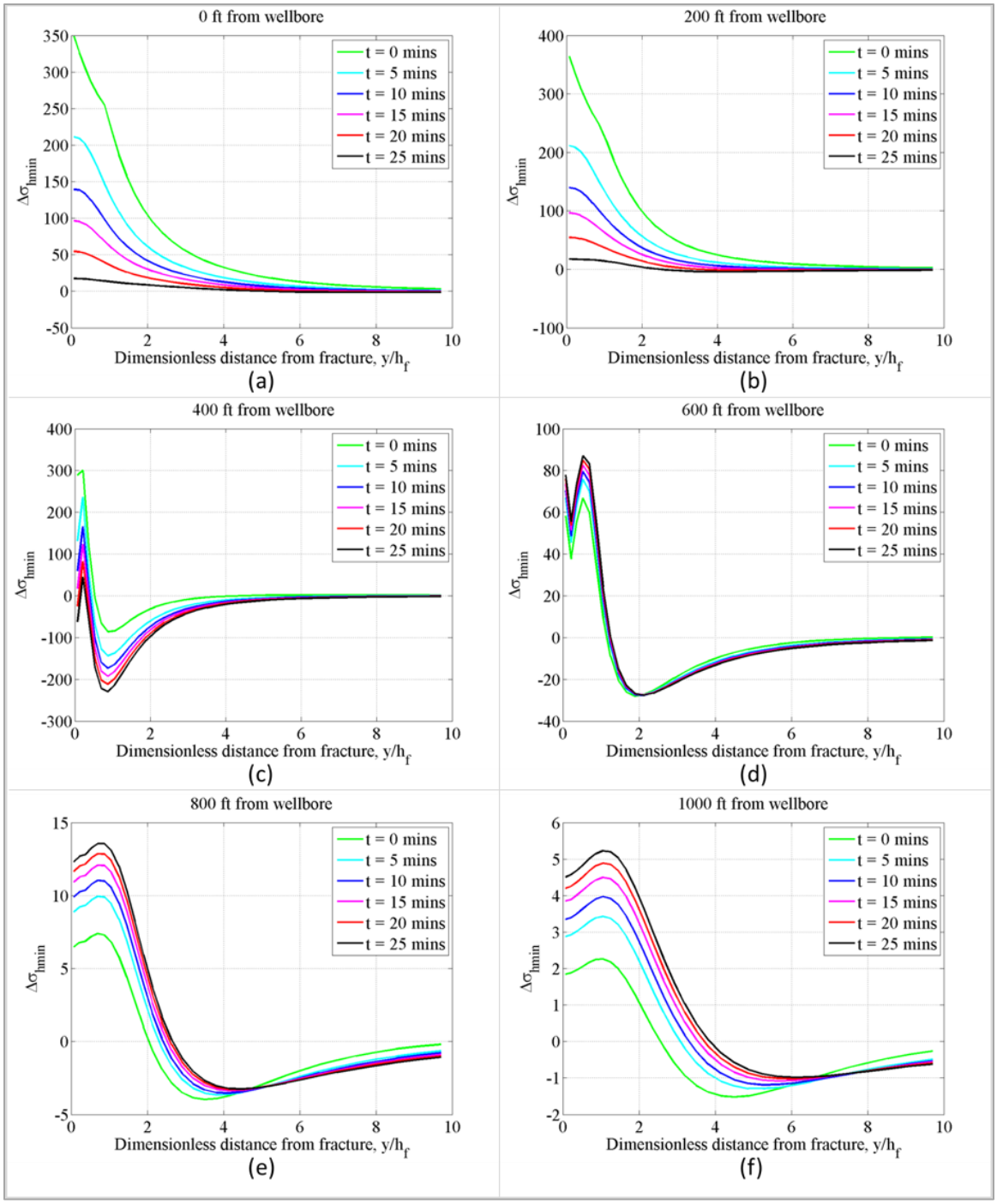

Figure 3.11 Change in minimum principal stress around a fracture caused by only mechanical closure of the fracture. (a)-(f) in order of increasing distance away from wellbore.

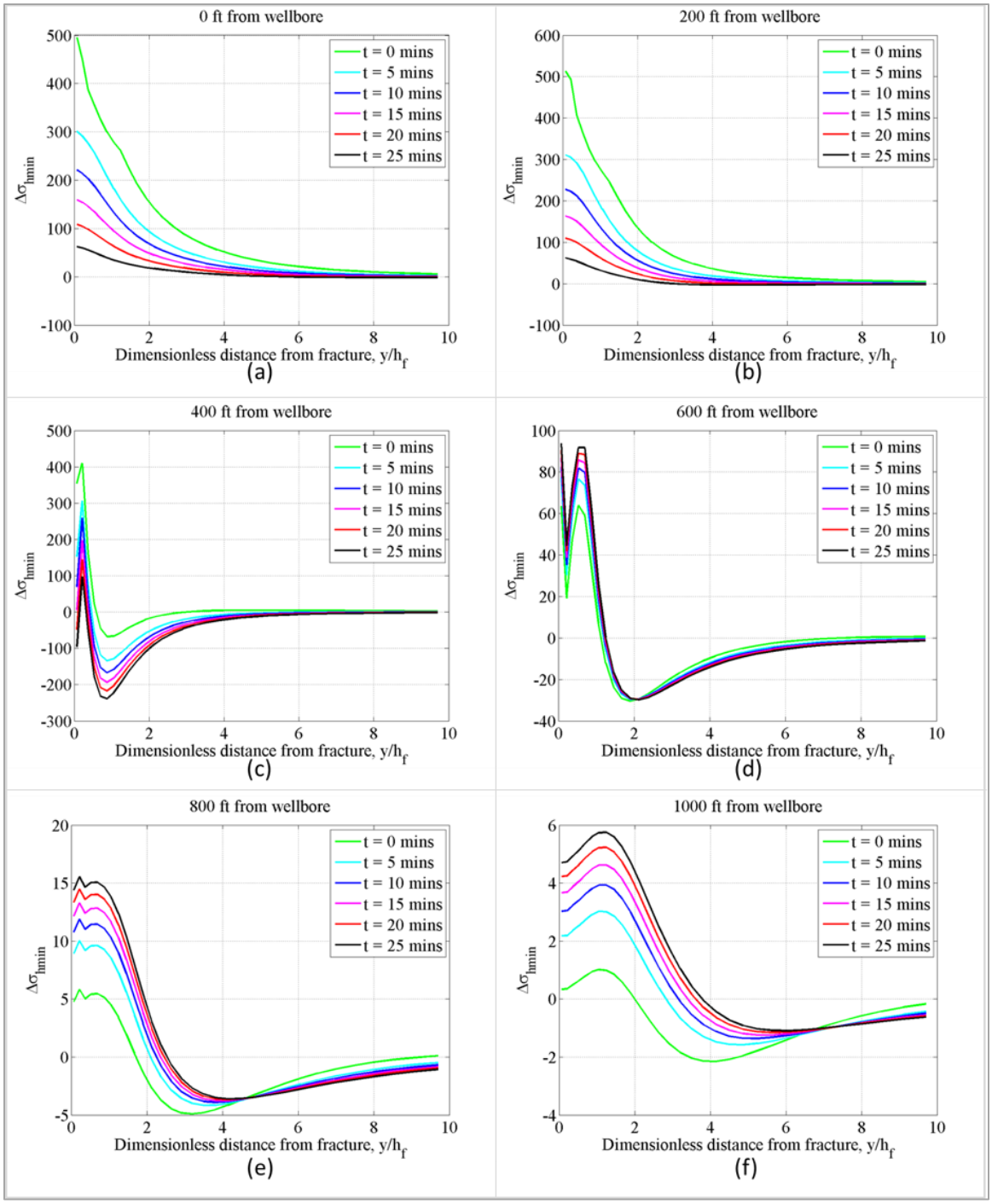

Figure 3.12 Change in minimum principal stress around a fracture caused by poro-elastic closure of the fracture for a 10 μD reservoir permeability. (a)-(f) in order of increasing distance away from wellbore.

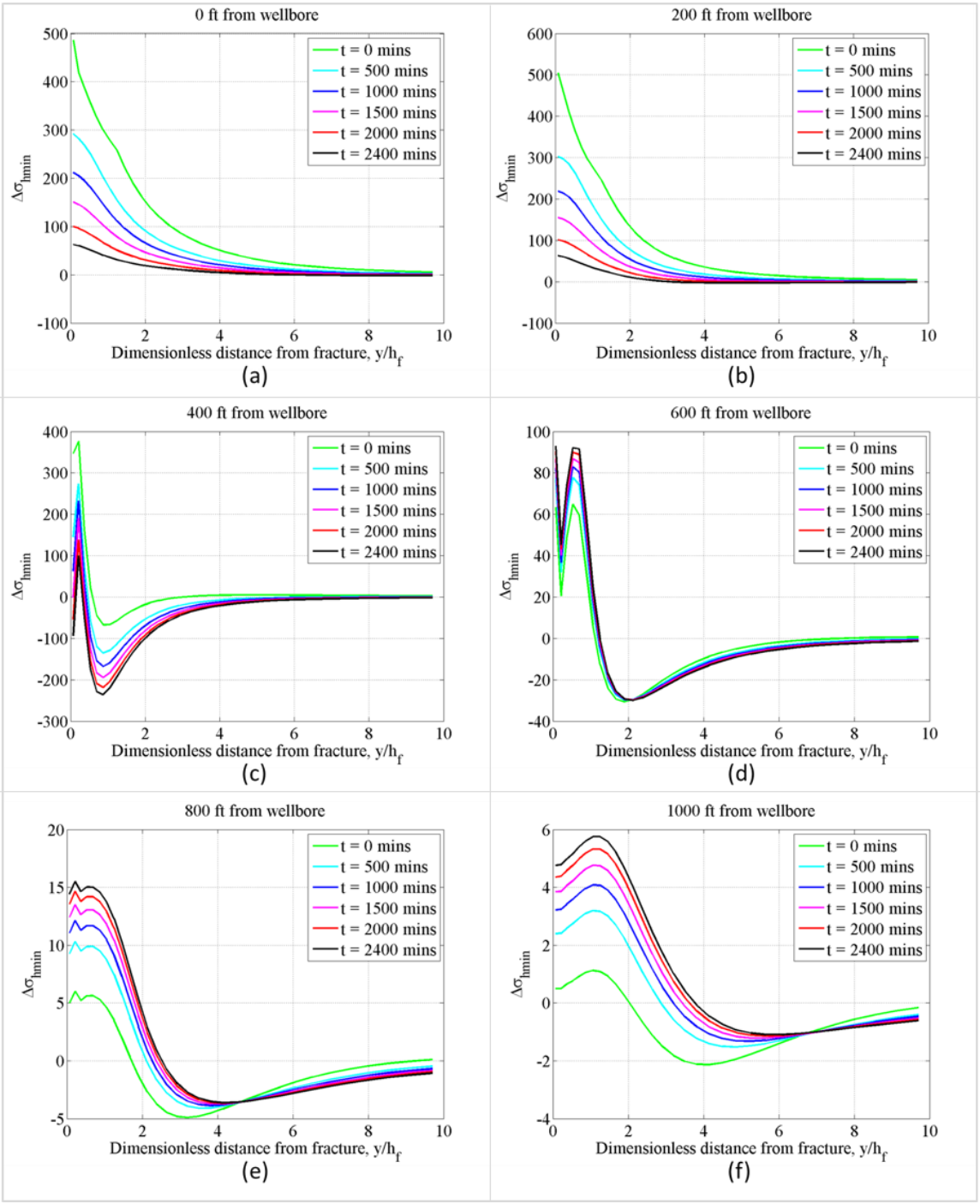

Figure 3.13 Change in minimum principal stress around a fracture caused by poro-elastic closure of the fracture for a 100 nD reservoir permeability. (a)-(f) in order of increasing distance away from wellbore.

Layer #	Top Depth (ft)	Thickness (ft)	Poisson's Ratio	Young's Modulus (MMpsi)	Permeability (nD)	Porosity (%)
1	XX200	500	0.31	5	5	2
2	XX700	54	0.28	3.75	600	9
3	XX754	27	0.28	2.25	825	6
4	XX781	30	0.26	2.5	1950	9
5	XX811	22	0.26	2.5	2875	10.5
6	XX833	30	0.26	2.75	2375	11.5
7	XX863	31	0.27	2.5	1275	10.25
8	XX894	30	0.31	2	925	8
9	XX924	500	0.30	6	5	2

Table 3.1 Example layer properties used as input for the simulations to capture the stress interference between fractured horizontal wells.

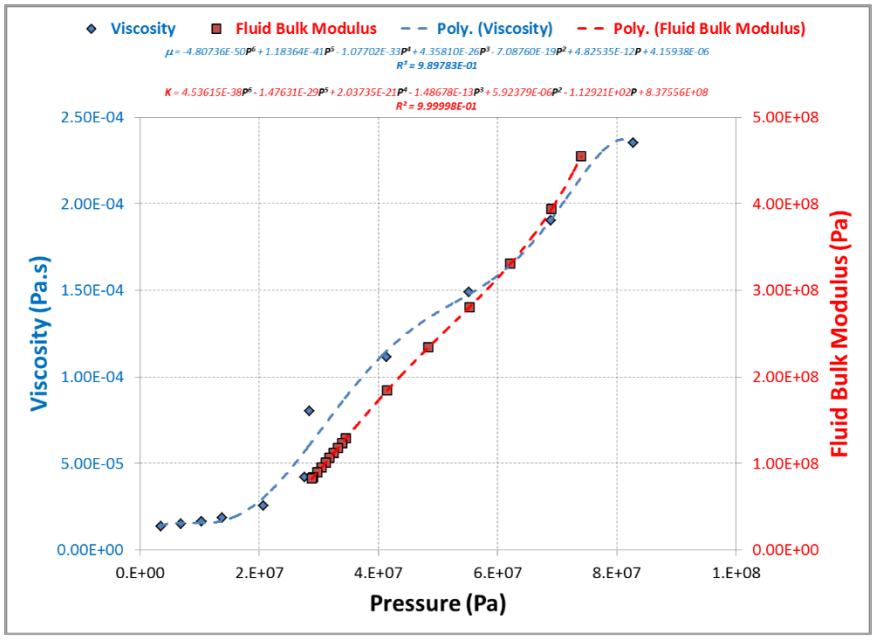

Figure 3.14 Example fluid property data for single phase simulation of reservoir fluids. These empirical trends were extracted from example fluid data.

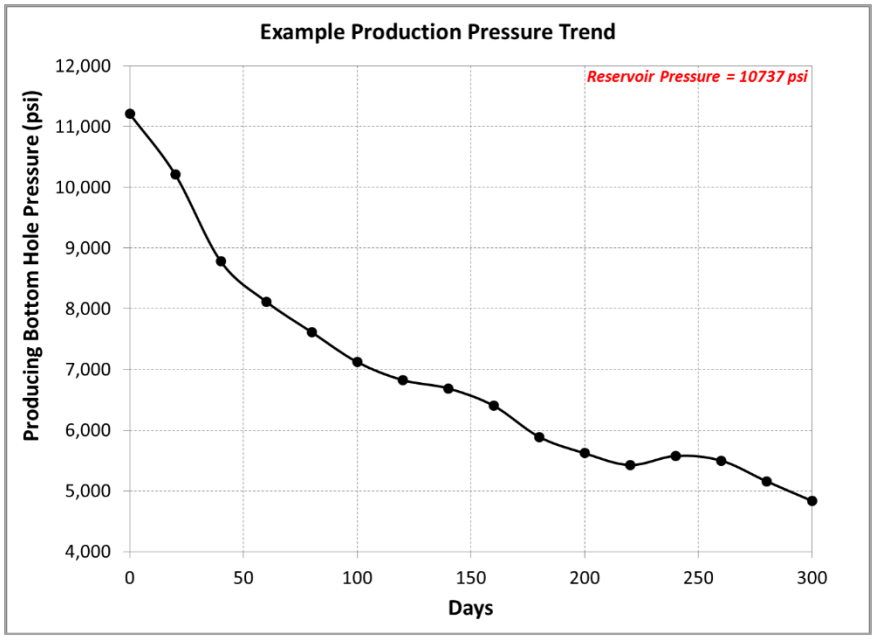

Figure 3.15 Example bottom hole production pressure trend. This trend was input into the simulation as input to simulate production.

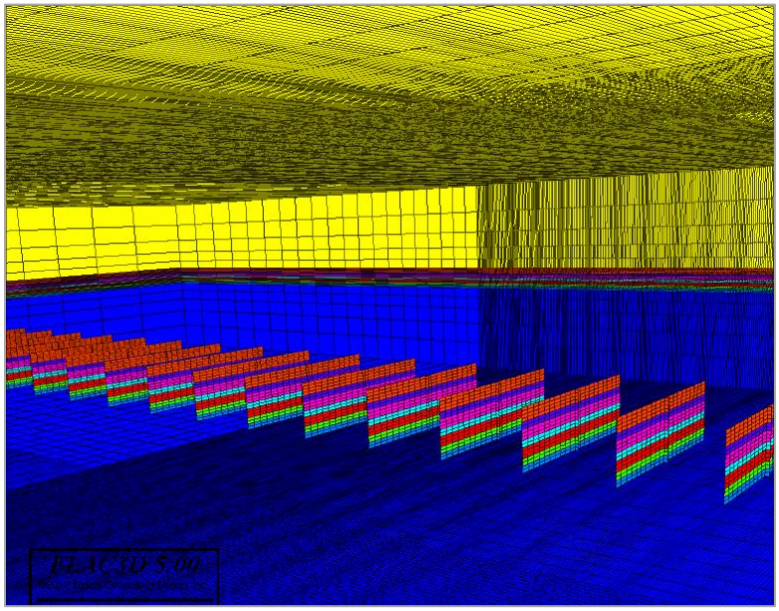

Figure 3.16 Simulation schematic showing multiple fractures in a single well going through multiple layers of the reservoir. The colors in the figure represent the different Young's modulus values shown in Table 3.1.

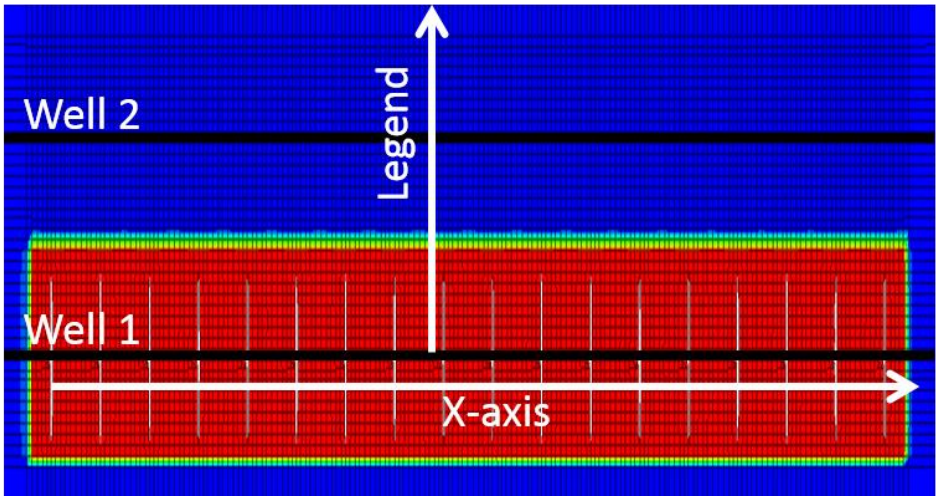

Figure 3.17 Multi-well simulation schematic to visualize results. The red region in the above plot represents the enhanced permeability SRV region around the fractured horizontal well.

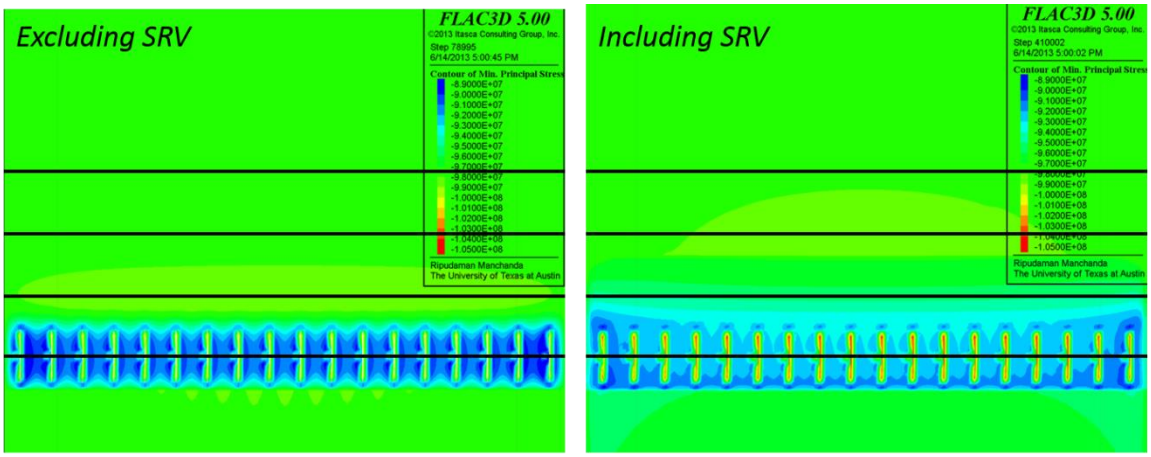

Figure 3.18 S_{hmin} changes caused by poro-elastic stress interference. (a) excludes a SRV, (b) includes a SRV. The production period was 180 days using the pressure trend presented in Figure 3.15.

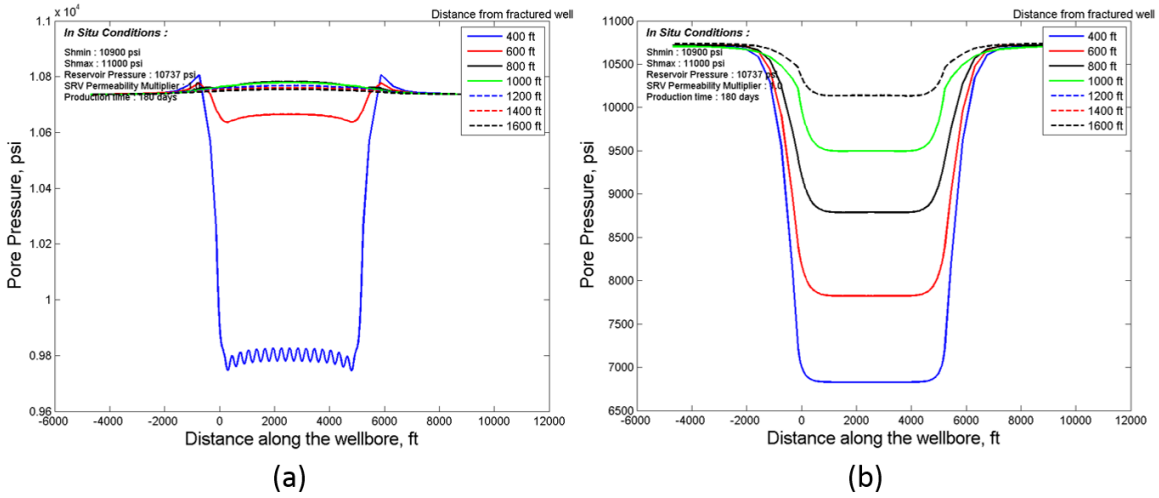

Figure 3.19 Pore pressure changes after 180 days of production simulation. (a) excludes SRV, (b) includes SRV. The lines of different colors show the pore pressure at various distances away from the fractured horizontal wellbore. The impact of the SRV region is very evident.

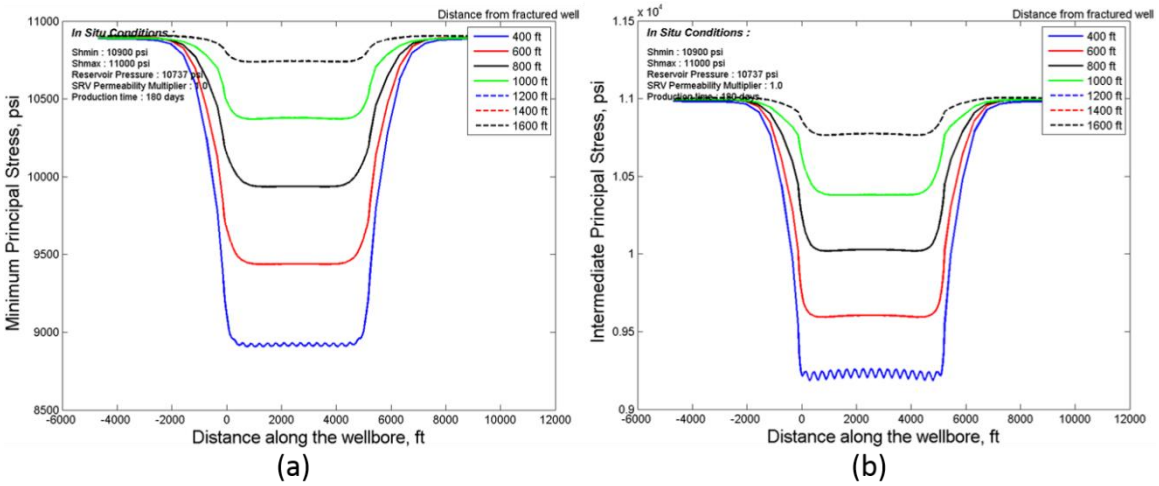

Figure 3.20 Reservoir stress changes after 180 days of production simulation in the presence of an enhanced permeability SRV region around the fractured horizontal well. The lines of different colors show (a) the minimum principal stress and (b) the intermediate principal stress, at various distances away from the fractured horizontal wellbore.

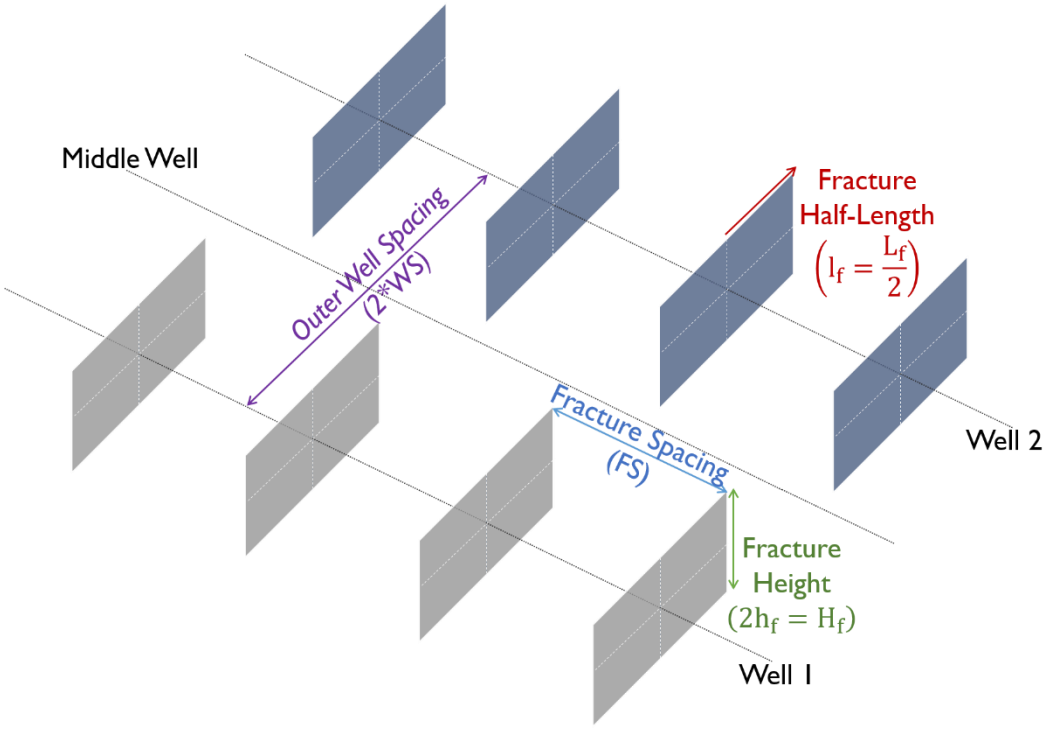

Figure 3.21 Multi-well schematic to represent the position of the fractures for the multi-well simulations.

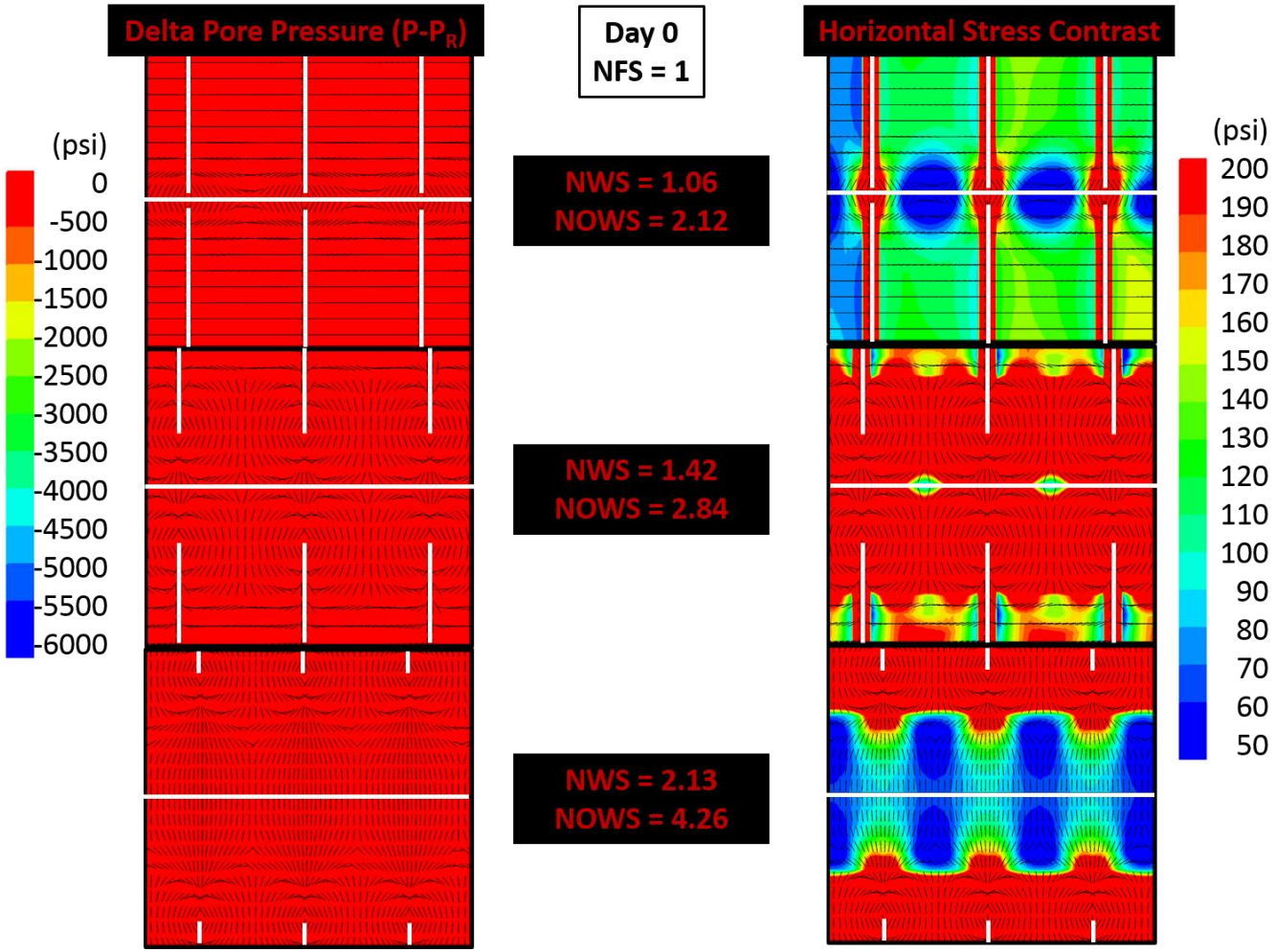

Figure 3.22 Pore pressure and horizontal stress contrast changes for stresses between two hydraulically fractured wells for various well spacings before any production. The fracture spacing to fracture height ratio is 1.

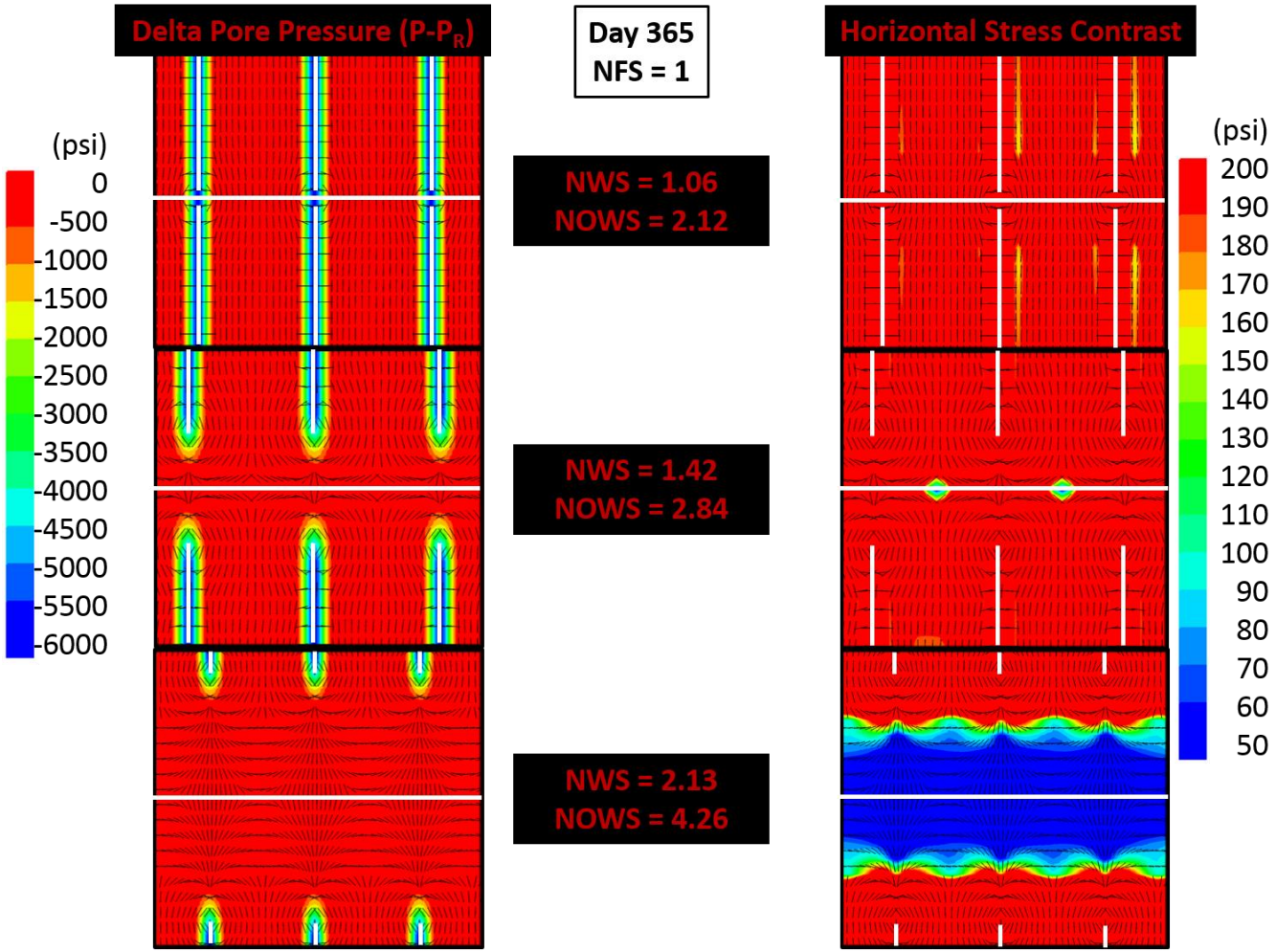

Figure 3.23 Pore pressure and horizontal stress contrast changes for stresses between two hydraulically fractured wells for various well spacings after 365 days of production. The fracture spacing to fracture height ratio is 1.

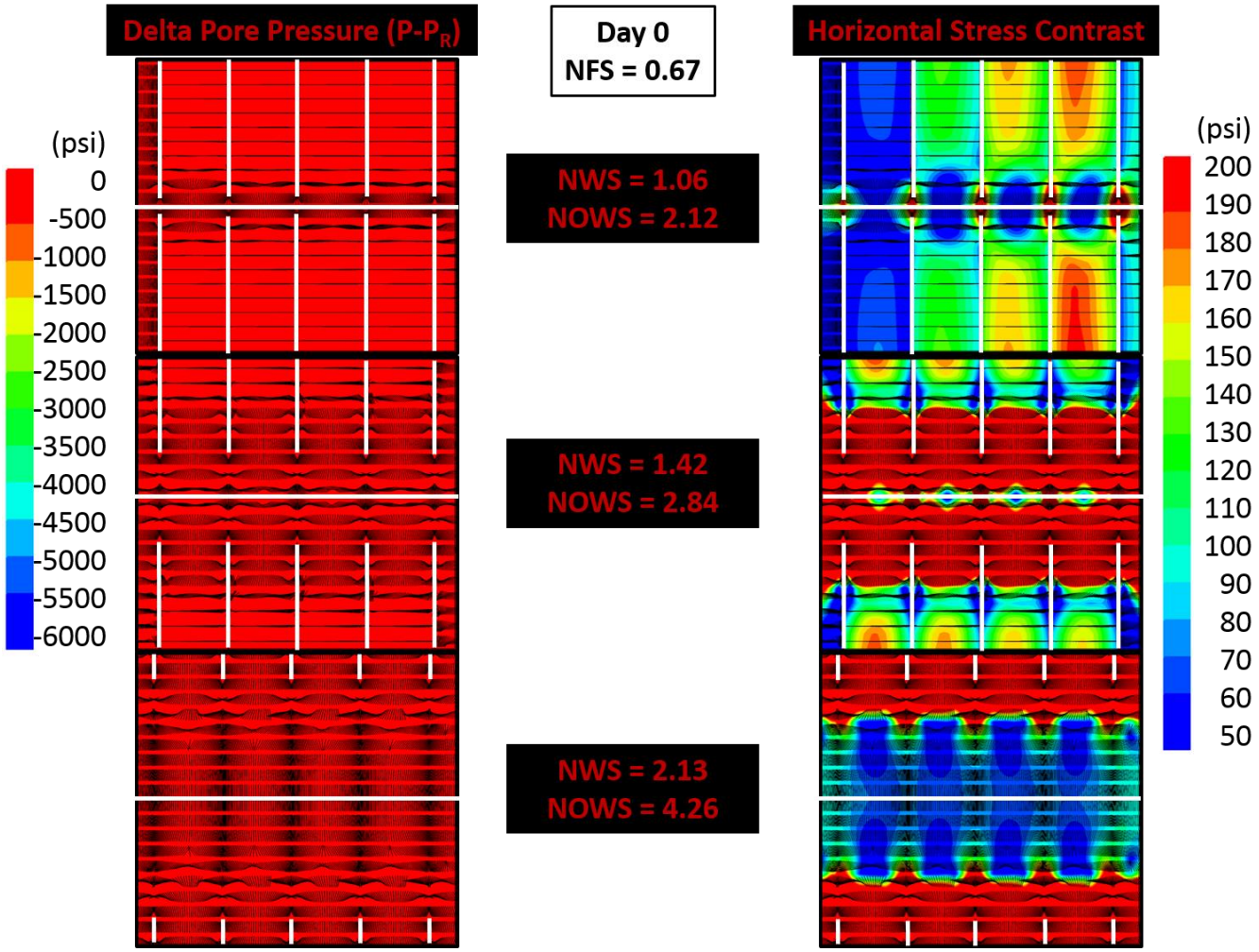

Figure 3.24 Pore pressure and horizontal stress contrast changes for stresses between two hydraulically fractured wells for various well spacings before any production. The fracture spacing to fracture height ratio is 0.67.

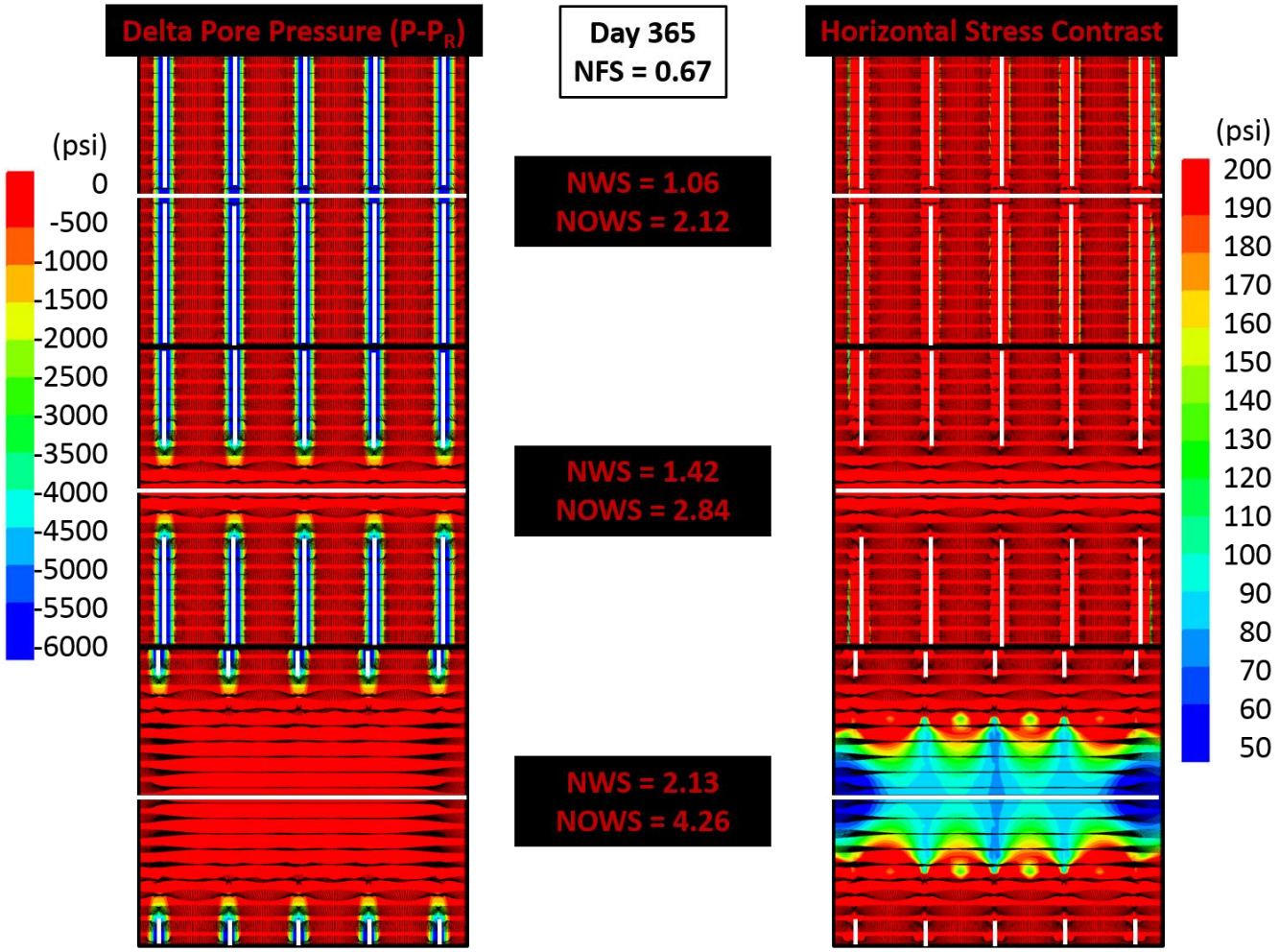

Figure 3.25 Pore pressure and horizontal stress contrast changes for stresses between two hydraulically fractured wells for various well spacings after 365 days of production. The fracture spacing to fracture height ratio is 0.67

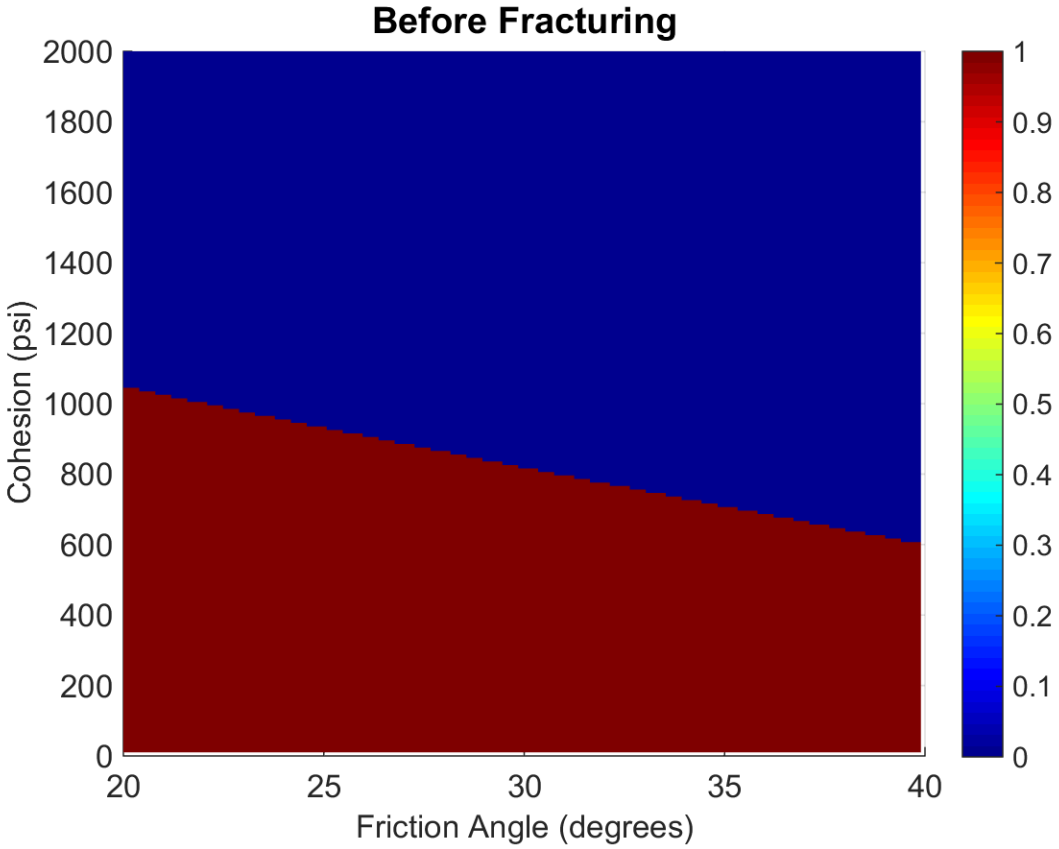

Figure 3.26 Contour chart showing the probability of shear failure for different cohesion and friction angle values for *in-situ* conditions.

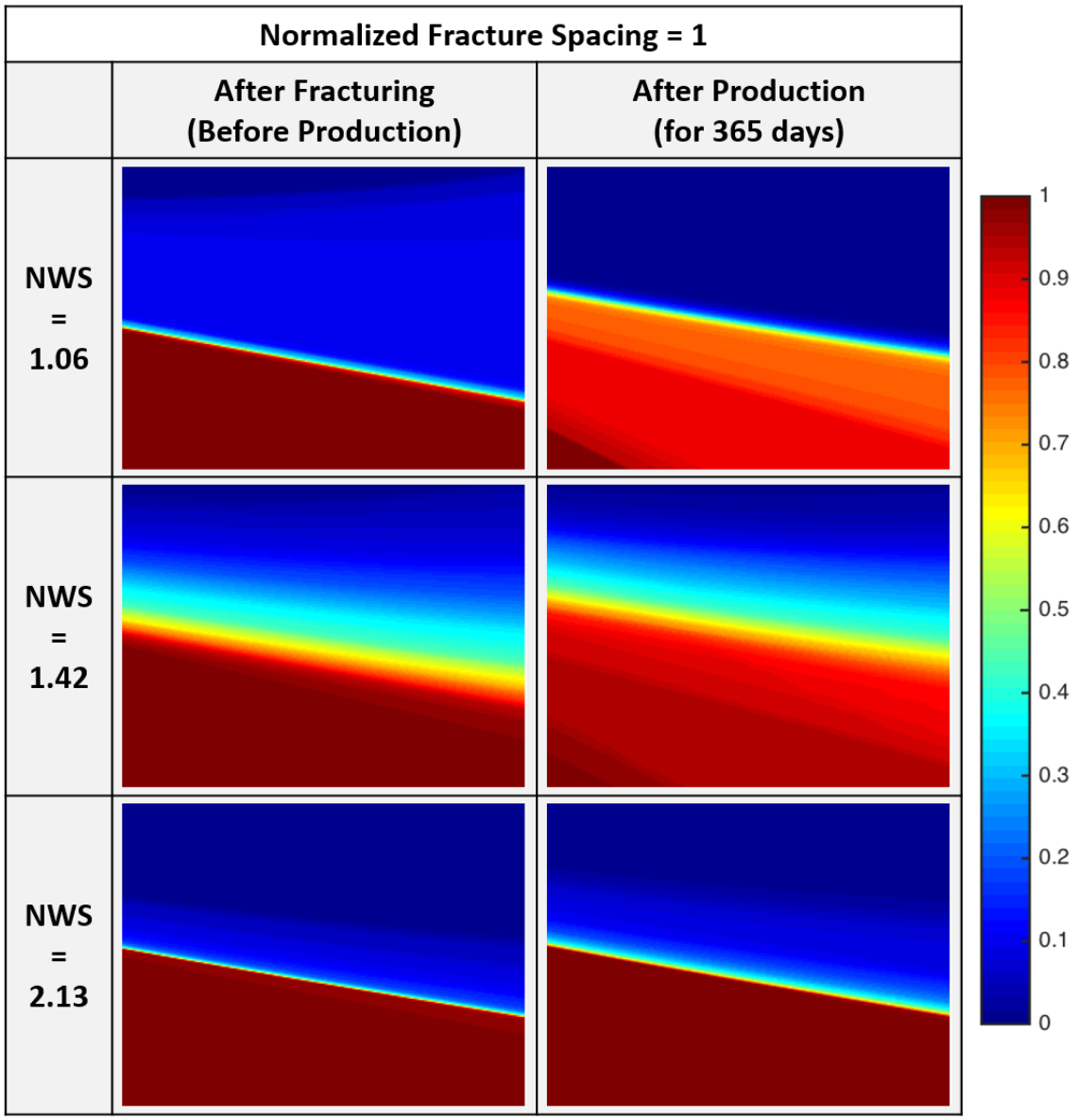

Figure 3.27 Impact of well spacing and poro-elastic stresses caused by production on the possibility of shear failure in the middle of the outer producing wells for normalized fracture spacing = 1.

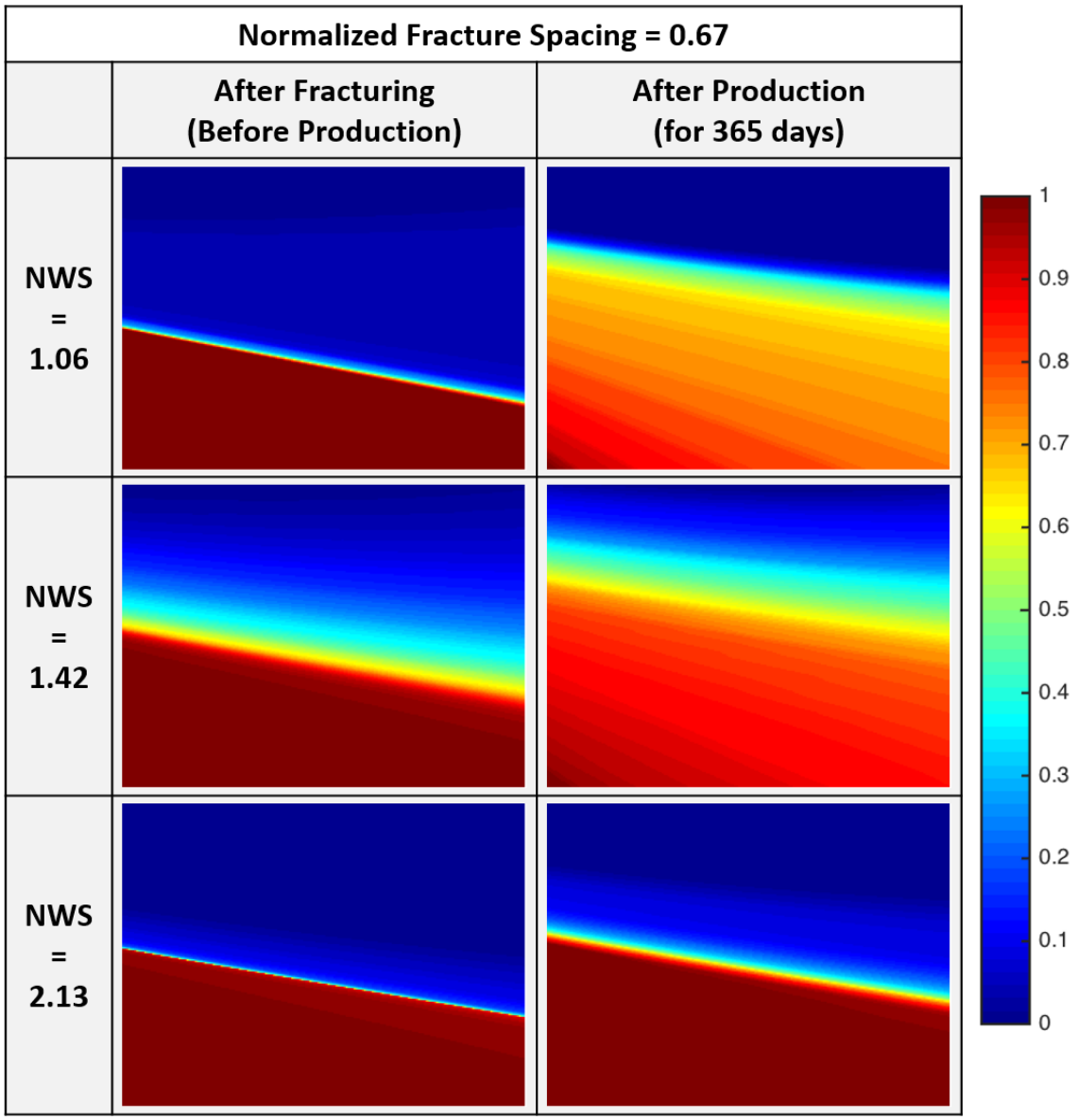

Figure 3.28 Impact of well spacing and poro-elastic stresses caused by production on the possibility of shear failure in the middle of the outer producing wells for normalized fracture spacing = 0.67.

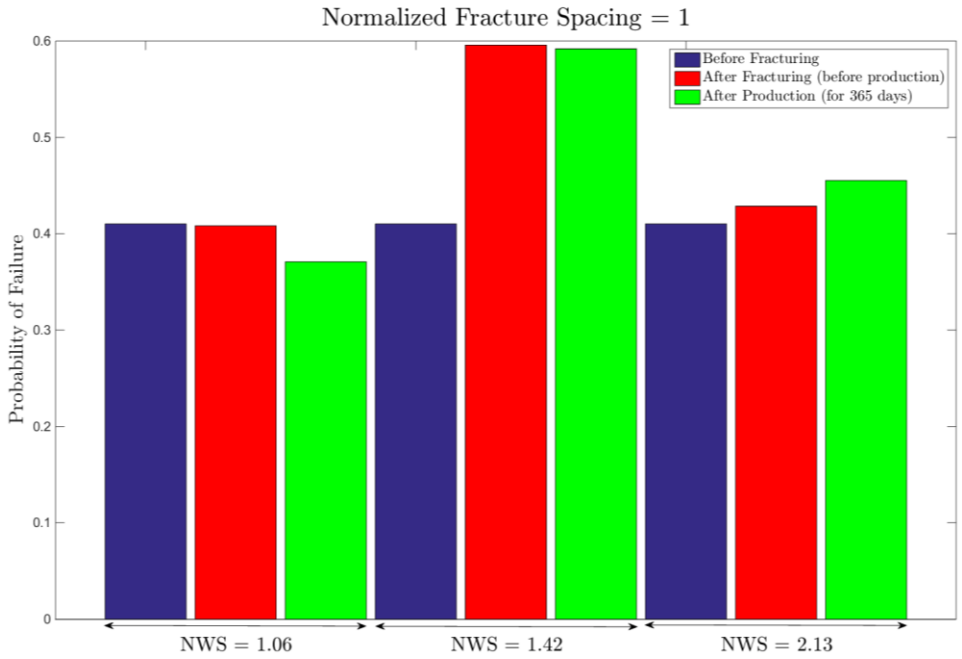

Figure 3.29 Bar chart to characterize the probability of shear failure for regions between wells with normalized fracture spacing = 1.

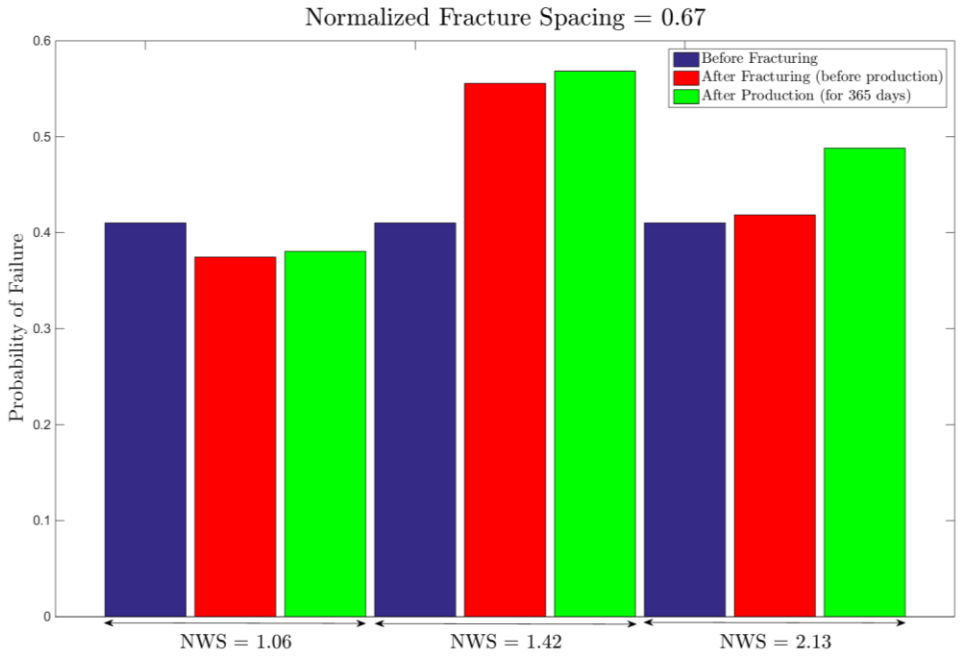

Figure 3.30 Bar chart to characterize the probability of shear failure for regions between wells with normalized fracture spacing = 0.67

Day 0 (No Production)	Normalized Fracture Spacing = 0.67	Normalized Fracture Spacing = 1
NWS = 1.07 NOWS = 2.14	• Low Δs_H ➔propped complexity • Near Well Stimulation • Possibility of Fracture Interference with Other Wells • Low probability of shear failure	• Low Δs_H ➔propped complexity • Near Well Stimulation • Possibility of Fracture Interference with Other Wells • Low probability of shear failure
NWS = 1.42 NOWS = 2.84	• High Δs_H ➔long planar fracs • Longitudinal growth near well • Staggered locations only • High probability of shear failure	• High Δs_H ➔long planar fracs • Staggered locations only • High probability of shear failure
NWS = 2.13 NOWS = 4.26	• High Δs_H at corresponding frac locations ➔long planar fracs • Low Δs_H at staggered frac locations ➔planar frac close to well with complexity deep in the reservoir. • High probability of shear failure	• Low Δs_H at staggered frac locations ➔planar frac close to well with complexity deep in the reservoir. • Near Well Stimulation • High probability of shear failure

Risky, Longitudinal Fracs etc. | No specific advantage | High chance of fracture complexity

Figure 3.31 Traffic light chart usable as a guide by a completions engineer to design fracture treatments in pad treatments.

Day 365 (1 Year of Prod.)	Normalized Fracture Spacing = 0.67	Normalized Fracture Spacing = 1
NWS = 1.07 NOWS = 2.14	• High Δs_H ➔ long planar fracs at staggered locations. • No Complexity • Low probability of shear failure	• High Δs_H ➔ long planar fracs at staggered locations. • No Complexity
NWS = 1.42 NOWS = 2.84	• High Δs_H • No Complexity • Longitudinal Fractures • High probability of shear failure	• High Δs_H ➔ long planar fracs at staggered locations. • No Complexity • Possibility of longitudinal fractures near well • High probability of shear failure
NWS = 2.13 NOWS = 4.26	• Longitudinal fractures with some propped complexity • Almost in situ Δs_H • High probability of shear failure	• Low Δs_H ➔propped complexity • Near Well Stimulation • Staggered fracs recommended to avoid frac hits • High probability of shear failure

Risky, Longitudinal Fracs etc. | No specific advantage | High chance of fracture complexity

Figure 3.32 Traffic light chart usable as a guide by a completions engineer to design fracture treatments in infill wells.

Top Depth (ft)	Thickness (ft)	Young's Modulus (MMpsi)	Poisson's Ratio
7691	342.5	8.449	0.278
8034	68.0	6.000	0.229
8102	52.0	6.000	0.229
8154	77.0	5.148	0.240
8231	14.0	5.156	0.186
8245	16.0	3.913	0.280
8261	33.0	4.404	0.219
8294	37.0	3.760	0.221
8331	18.0	6.000	0.229
8349	342.5	8.449	0.278

Table 3.2 Layer and mechanical property data used in the simulations for the pad scale case study.

	Well	A	B	C	D
Frac Design	Landing Depth (all at T/ Lower EF)	-10 ft, +40 ft	-5 ft, +40 ft	-5 ft, +60 ft	-20 ft, +60 ft
	Stage Spacing, ft	200	300	300	300
	Stages	26	17	16	16
	Clusters	1	4	4	2
Frac Data	Proppant/Stage, k-lbm	477	495	496	496
	Fluid/Stage, k-gals	205	196	205	203
	Average Rate, bbls/min	51	50	50	51
	Average Treating Pressure ± Standard Deviation, psi	6,809 ± 578	6,933 ± 265	6,388 ± 391	6,646 ± 311
	Average ISIP ± Standard Deviation, psi	5,403 ± 921	5,195 ± 204	4,969 ± 449	5,060 ± 168
	Average Intra-Stage Time, hrs	3.90	6.40	4.10	6.50
MSM Data	Fracture half-length, ft	833	669	533	749
	Network width, ft	596	566	402	652
	Height, ft	277	440	347	402
	Length/Width	2.80	2.36	2.65	2.30

Table 3.3 Pad completion, fracturing, and microseismic data.

Well	A	B	C	D
Completion Order	2	Zippered with D	1	Zippered with B
First Stage	12/18/11 9:54 AM	12/29/11 9:55 PM	12/14/11 5:50 PM	12/30/11 1:18 AM
Last Stage	12/28/11 8:29 AM	1/4/12 1:38 PM	12/18/11 4:16 PM	1/4/12 10:15 AM
Logging Date	Not Logged	2/3/12	2/5/12	2/7/12
Tracers Used	None	**Ir** (all stages)	**Sc** (all stages)	**Sb** (all stages)
Stage	**Tracers Detected**			
1	X	**Sb**	None	None
2	X	**Sb**	None	None
3	X	**Sb**	None	None
4	X	**Sb**	None	None
5	X	**Sb**	None	None
6	X	**Sb**	None	None
7	X	**Sb**	None	None
8	X	**Sb**	None	None
9	X	**Sb**	None	None
10	X	**Sb**	None	None
11	X	**Sb**	None	None
12	X	**Sb**	None	None
13	X	**Sb**	None	**Ir**
14	X	None	None	**Ir**
15	X	None	None	None
16	X	None	None	None
17	X			None
18	X			
19	X			
20	X			
21	X			
22	X			
23	X			
24	X			
25	X			
26	X			

Table 3.4 Radioactive tracer analysis results for the pad.

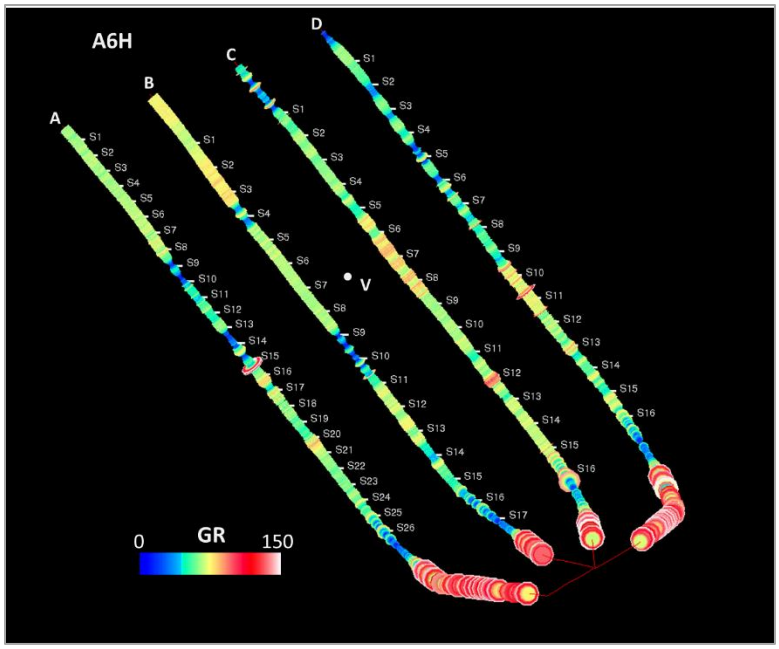

Figure 3.33 Aerial view of 4 well pad with borehole image of gamma ray variation.

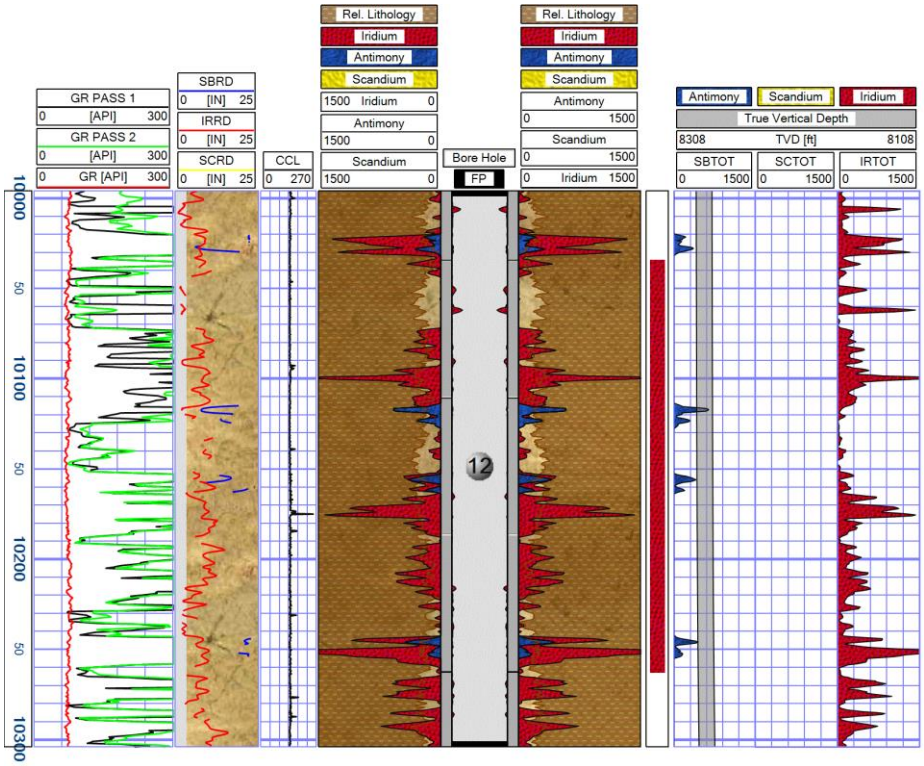

Figure 3.34 Radioactive tracer log data for Stage 12 in well B.

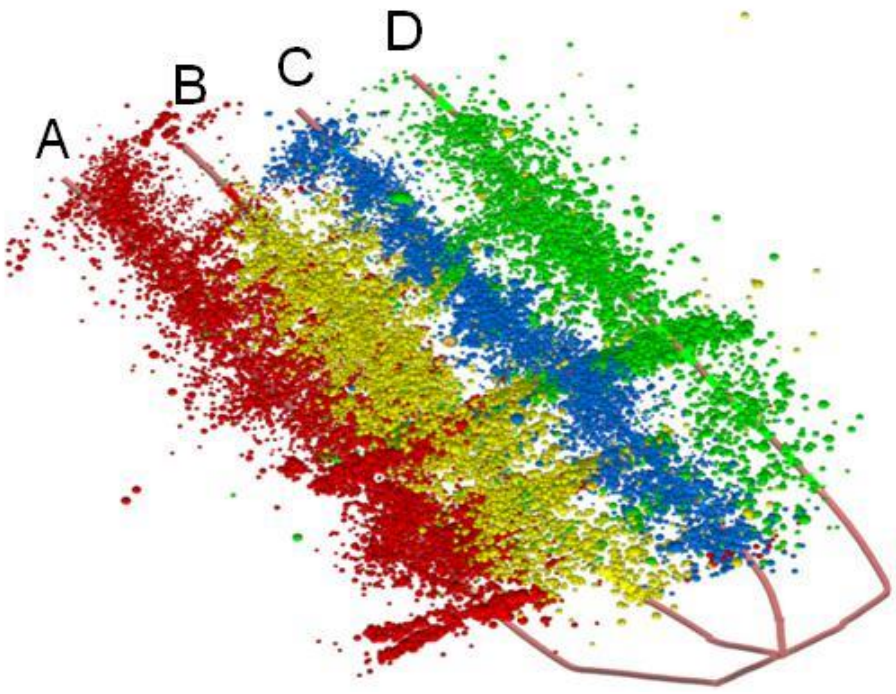

Figure 3.35 Microseismic events recorded during fracturing in the four-well pad.

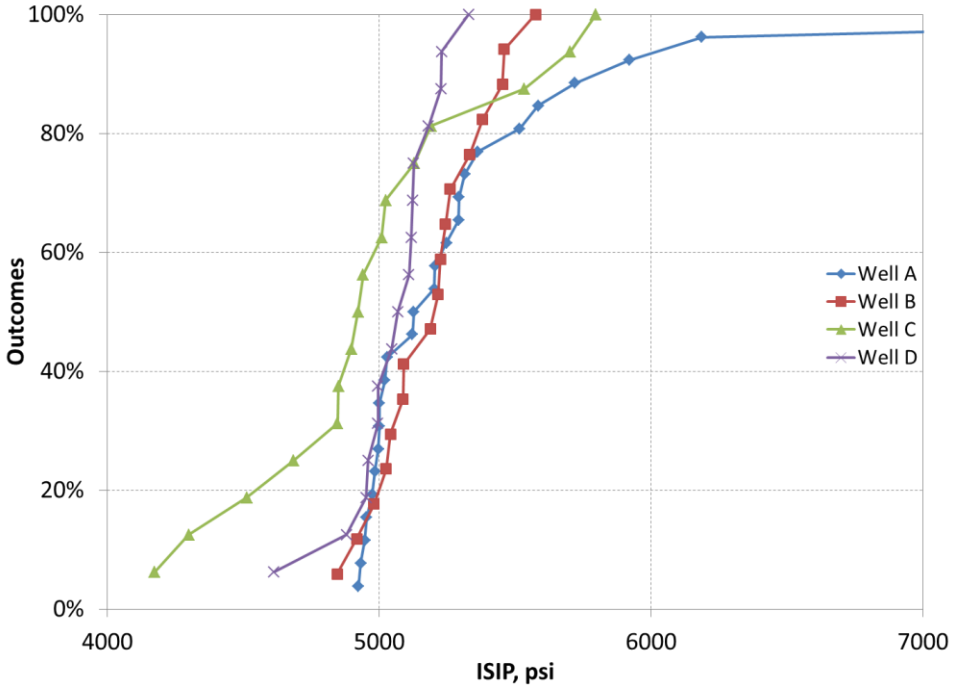

Figure 3.36 Ascending order of Initial Shut-In Pressures (ISIPs) for pad wells.

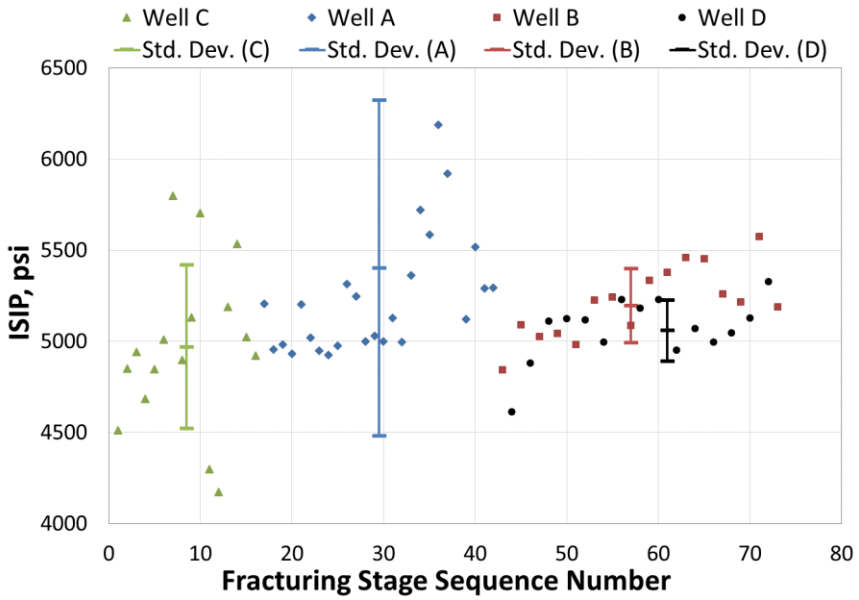

Figure 3.37 The trend of ISIP values of each stage in each well in the pad. The solid vertical line shows the range of one standard deviation of the ISIP values for each well and the horizontal lines in the middle of the vertical lines show the average ISIP value for each well.

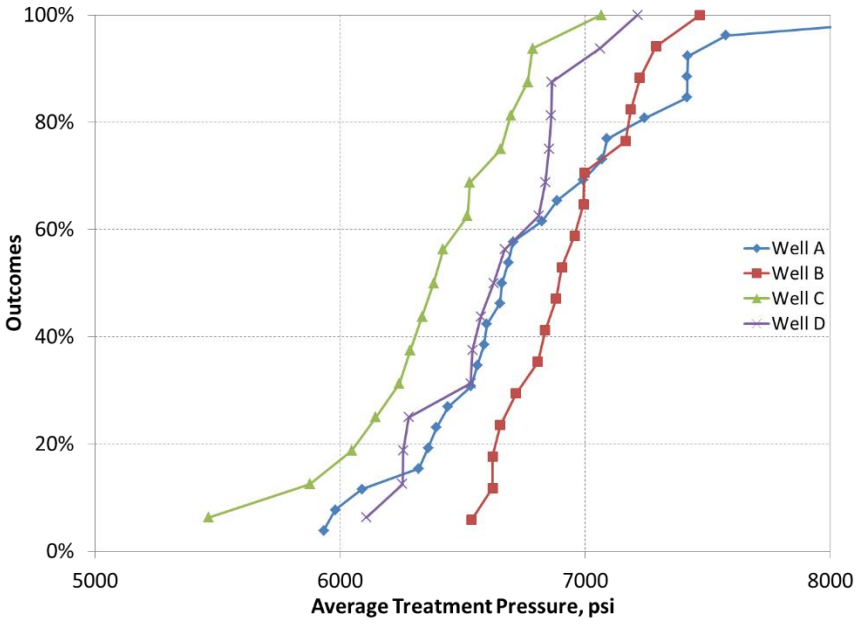

Figure 3.38 Ascending order of average treatment pressures for pad wells.

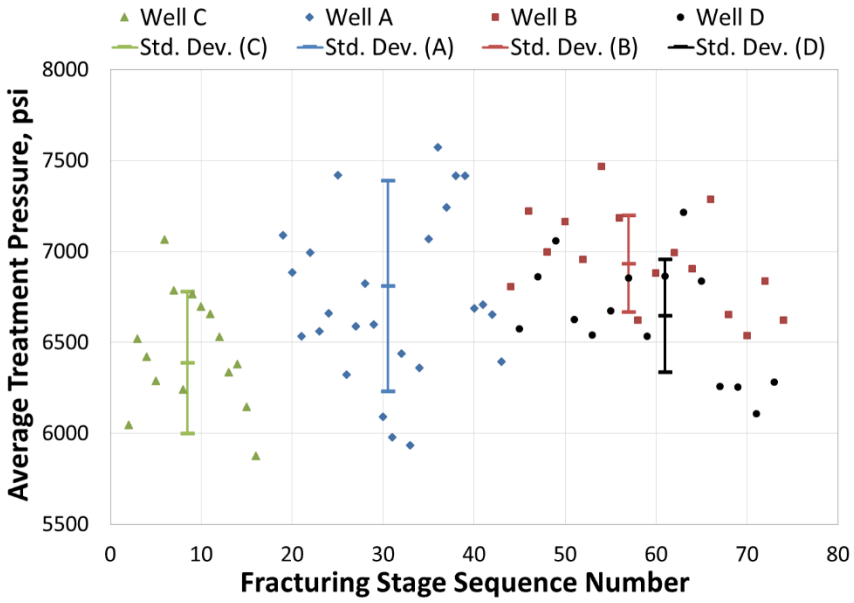

Figure 3.39 The trend of ATP values of each stage in each well in the pad. The solid vertical line shows the range of one standard deviation of the ATP values for each well and the horizontal lines in the middle of the vertical lines show the average ATP value for each well.

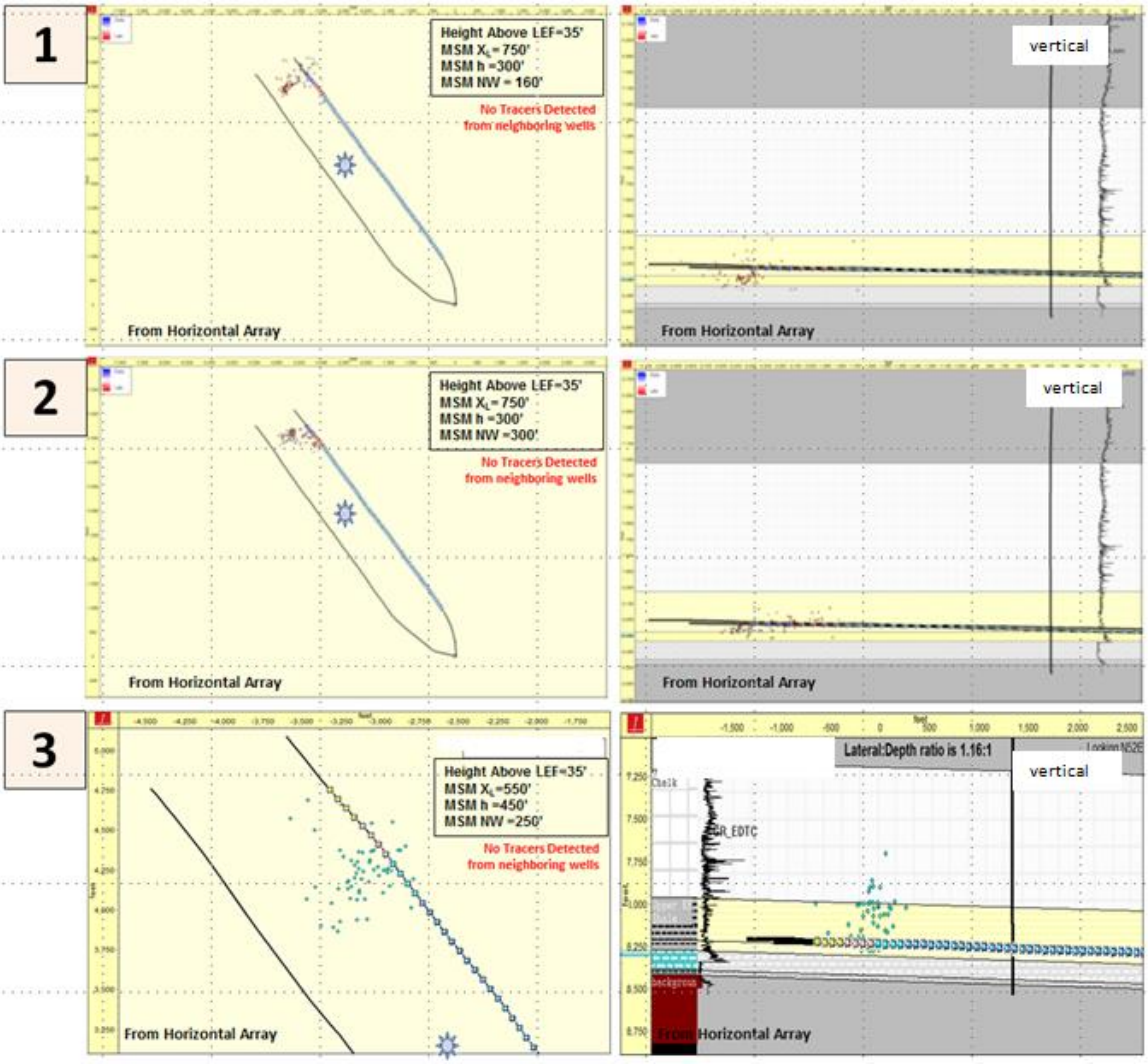

Figure 3.40 Microseismic maps of the first three stages of well C. The locations of the perforations should be used as a reference of scale in the pictures.

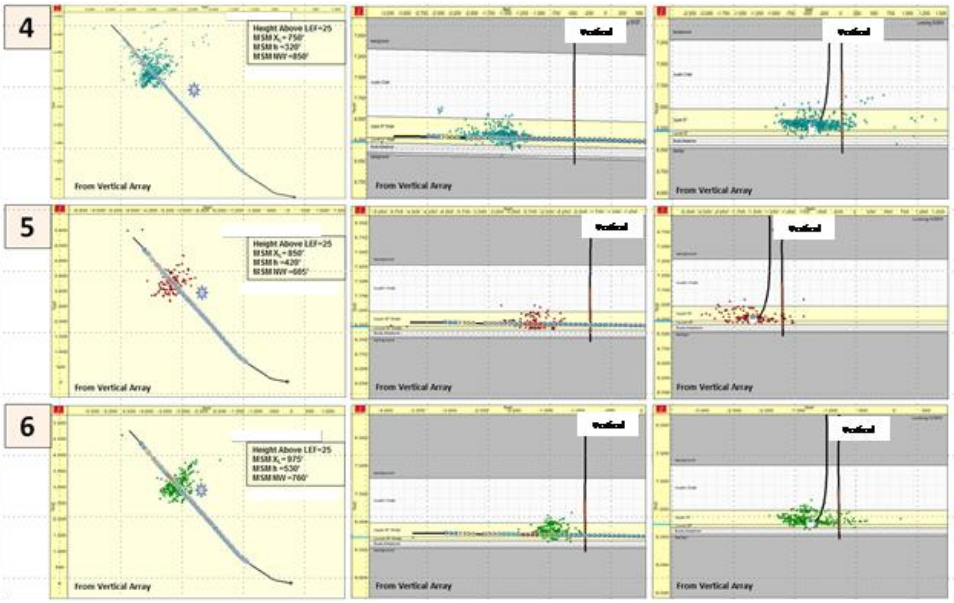

Figure 3.41 Microseismic maps for stages 4, 5 and 6 for well B.

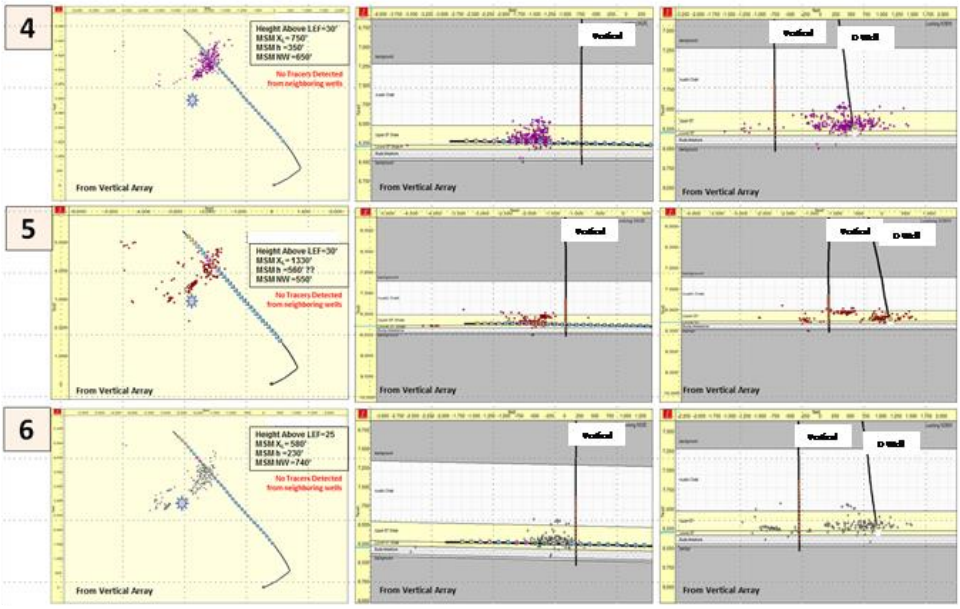

Figure 3.42 Microseismic maps for stages 4, 5 and 6 for well D.

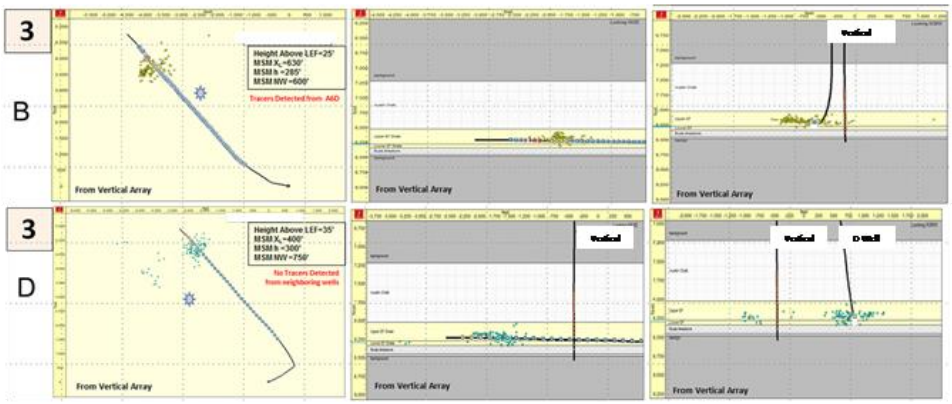

Figure 3.43 Microseismic maps of stage 3 in well B and stage 3 in well D.

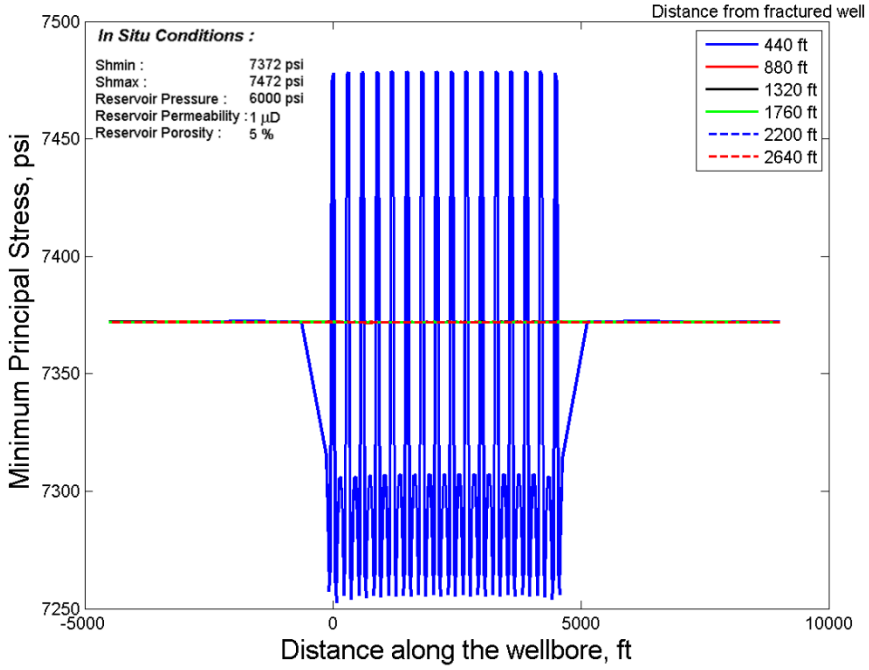

Figure 3.44 Variation in local minimum principal stress because of mechanical interference of fractures at a transverse distance away from the well. For reference, the wells in the pad were spaced 880 ft apart from each other.

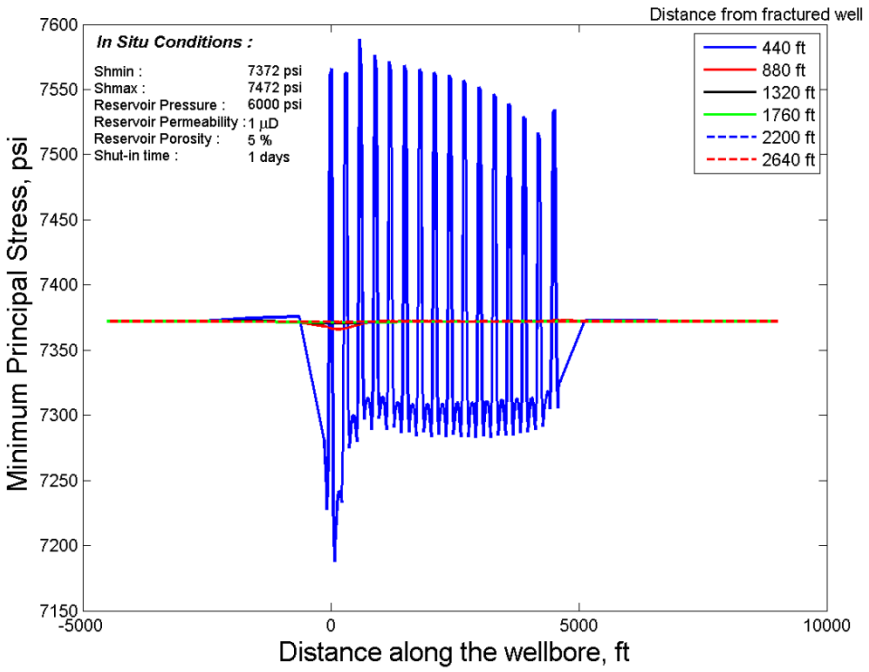

Figure 3.45 Variation in local minimum principal stress because of both mechanical and poro-elastic interference of fractures at a transverse distance away from the well. For reference, the wells in the pad were spaced 880 ft apart from each other

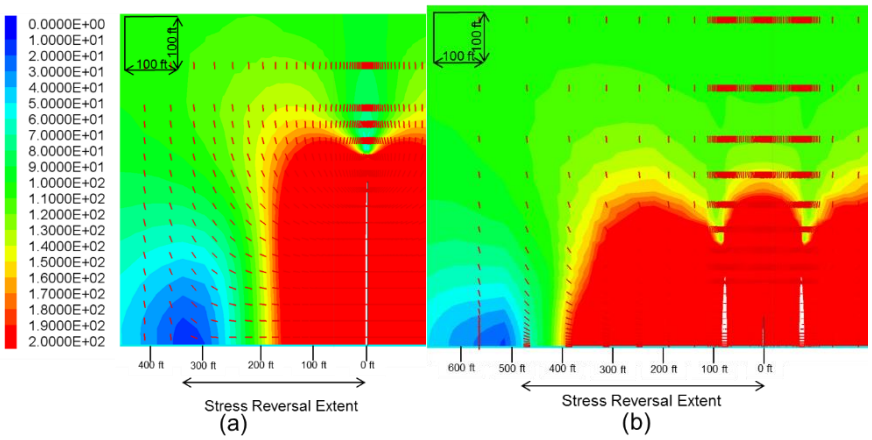

Figure 3.46 Contour of horizontal stress contrast depicting the impact of multiple clusters per stage. (a) One fracture, (b) Three fractures spaced 75 ft apart. The distances shown along the bottom boundary of the figures represent the distance from the single fracture in (a) and the middle fracture in (b).

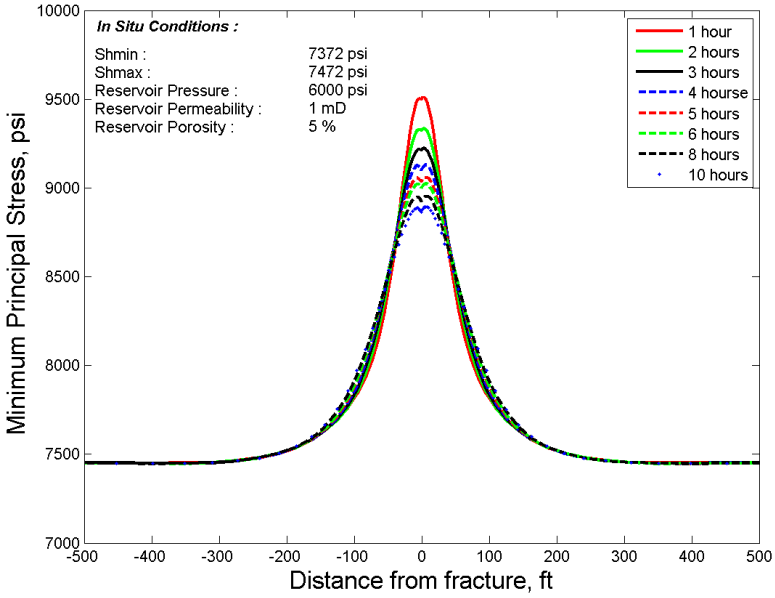

Figure 3.47 Changes in the local reservoir minimum principal stress caused by pressure depletion of a propped fracture. The permeability of the case here is 1 mD permeability.

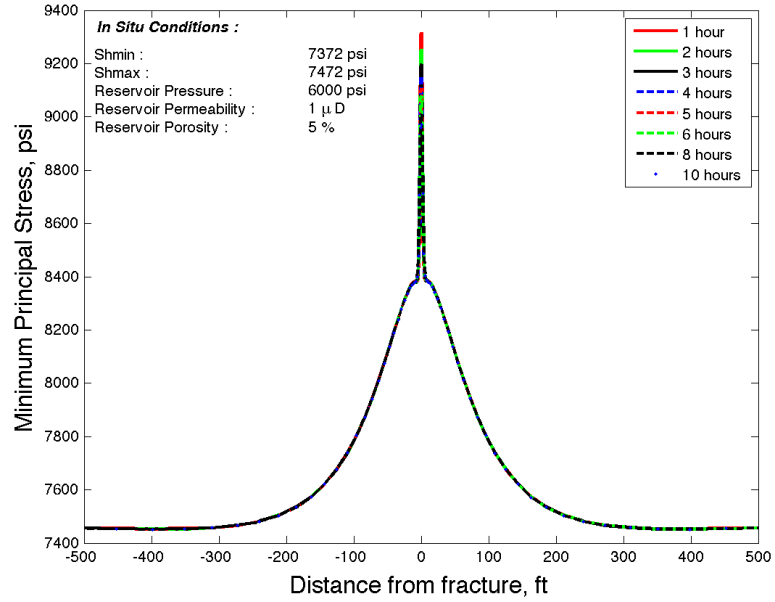

Figure 3.48 Changes in the local reservoir minimum principal stress caused by pressure depletion of a propped fracture with a permeability of 1 μD permeability.

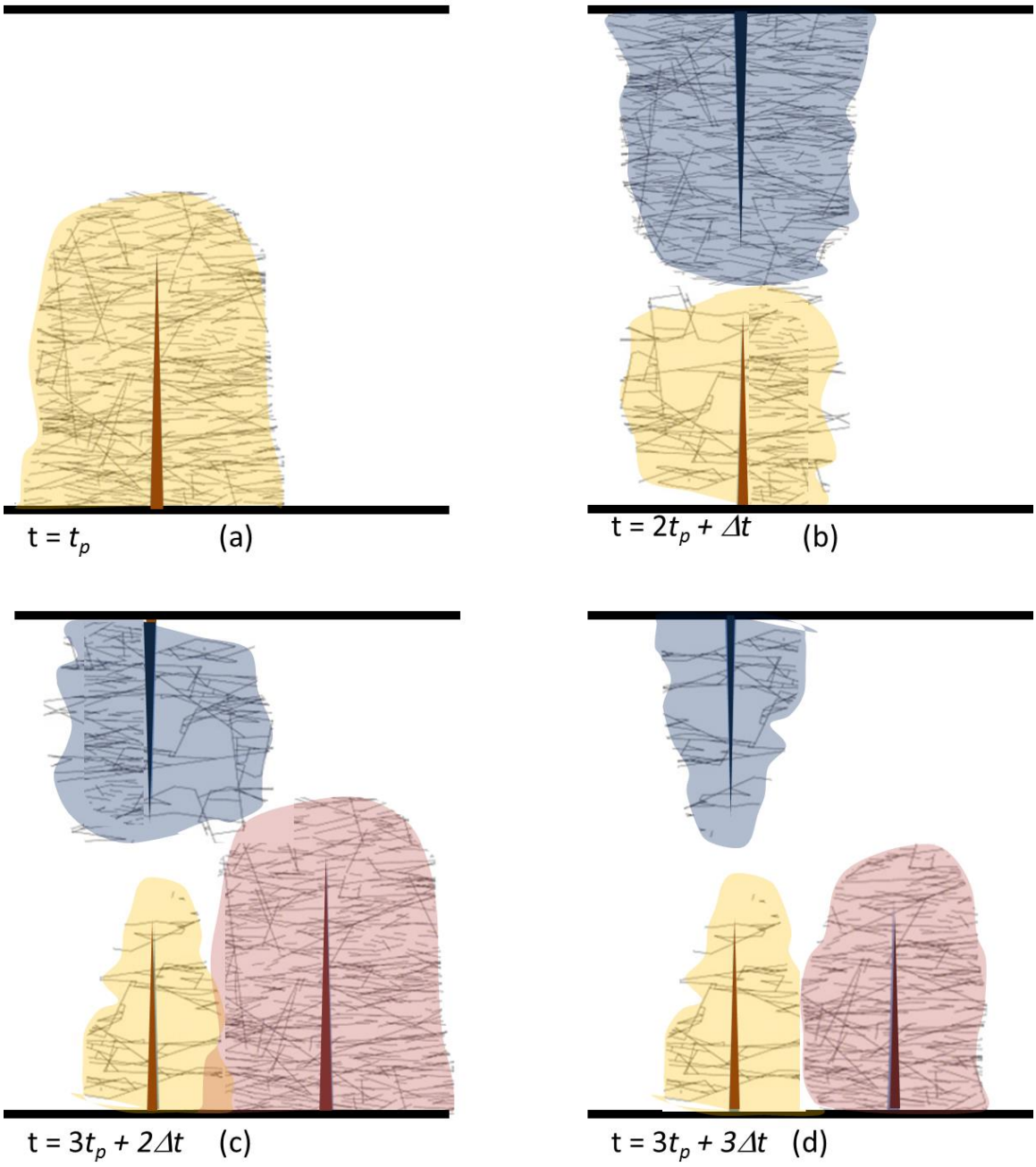

Figure 3.49 Fracture networks after various treatments in zipper wells, (a) Fracture network stimulated at the end the 1st hydraulic fracture treatment, (b) Fracture network at the end of the 2nd hydraulic fracture treatment on the pad, (c) Stimulated fracture networks at the end of the 3rd hydraulic fracture treatment on the pad (2nd frac treatment in the 1st well), (d) Existing fracture network at the start of the 4th hydraulic fracture treatment on the pad (2nd frac treatment in the 2nd well).

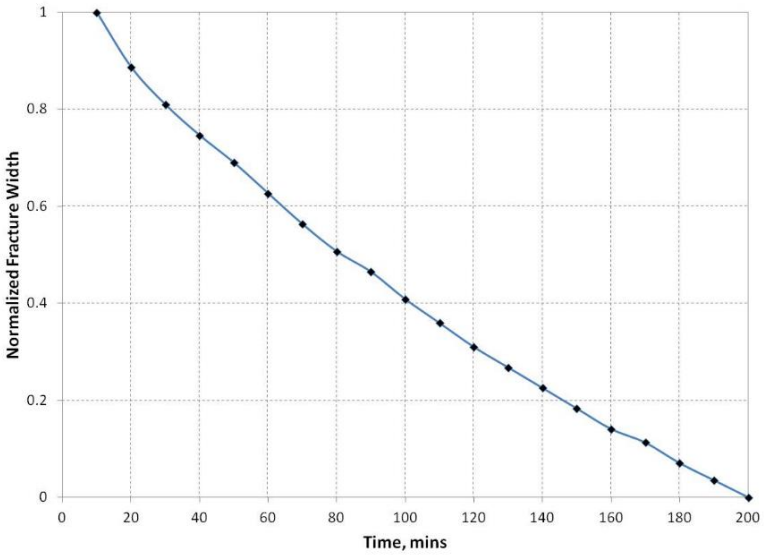

Figure 3.50 Change in the normalized fracture width because of fracture closure. The normalized fracture width is defined as the ratio of the difference between the current width and the final width and the difference between the initial width and the final width.

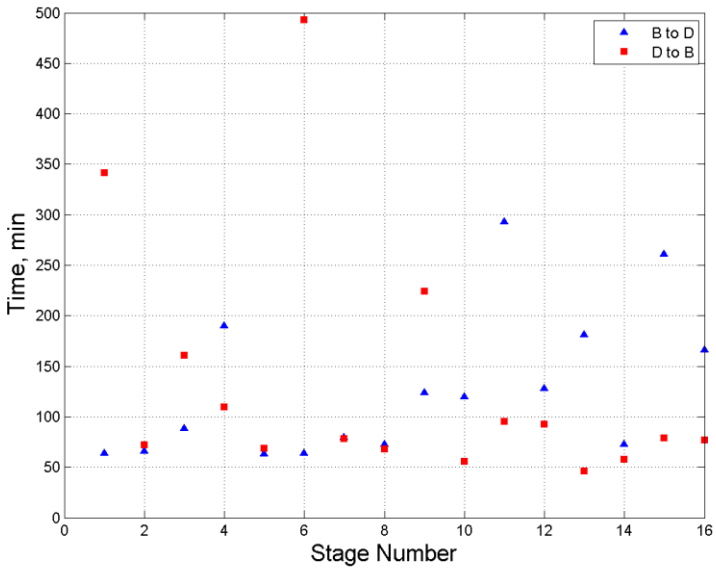

Figure 3.51 Delay time between the corresponding stages of the zipper fractured wells. B to D signifies the time between the end of pumping in the n^{th} fracture of well B and the start of pumping in the n^{th} fracture of well D. D to B signifies the time between the end of pumping in the n^{th} fracture of well D and the start of pumping in the $(n+1)^{th}$ fracture of well B.

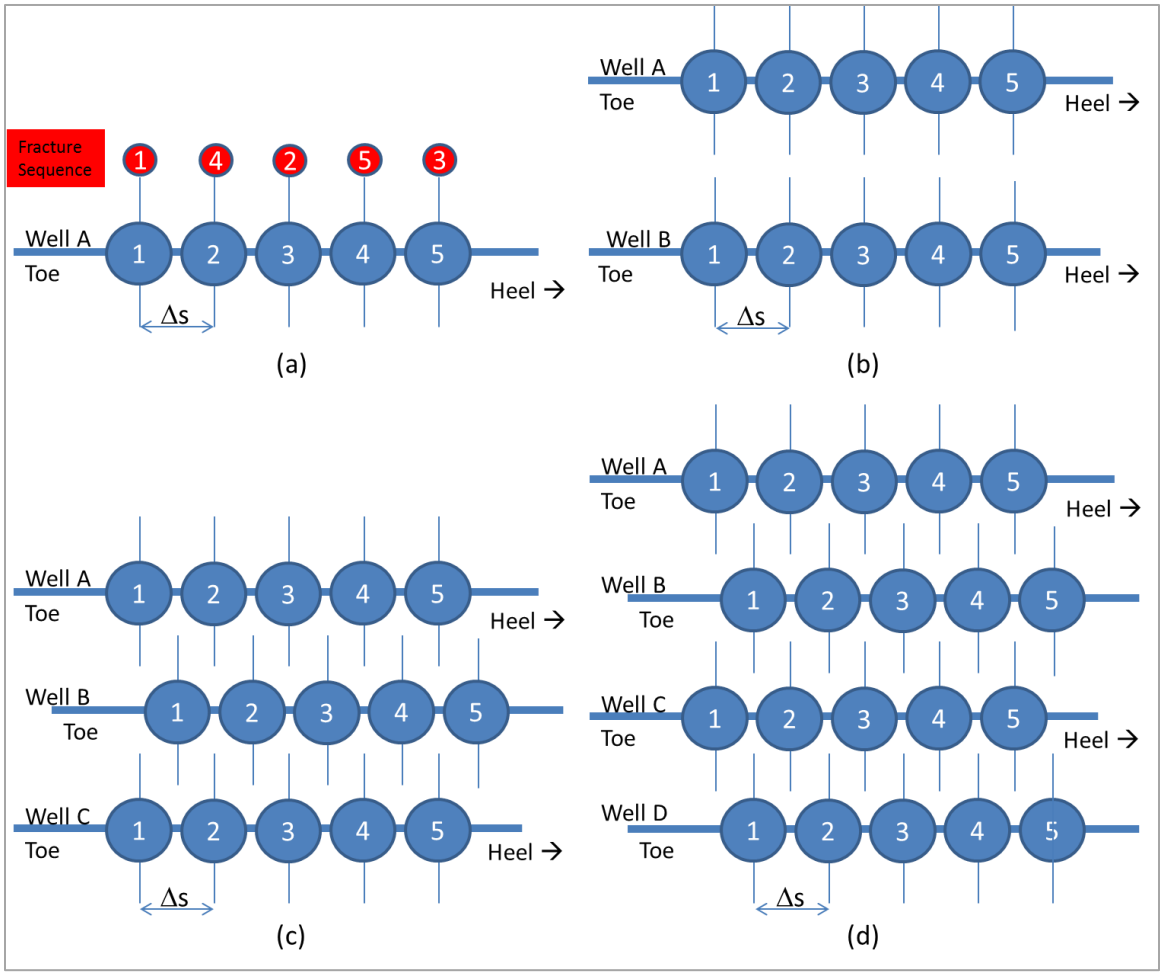

Figure 3.52 Schematics for the strategies to increase the time between consecutive fractures in the same well. (a) Alternate Fracturing, (b) Two well zipper fracturing, (c) Three well staggered zipper fracturing, (4) Four well staggered zipper fracturing. The fracture sequencing strategies are depicted in Table 3.5 - Table 3.8. Δs represents the distance between two consecutive fractures in the same well.

Fracture Location	Treatment Start Time	Treatment End Time	Start Time After Recent Nearest Fracture (Delay Time)	Distance From Previous Nearest Fracture
1	0	t_p	∞	∞
3	$t_p + \Delta t$	$2t_p + \Delta t$	Δt	$2\Delta s$
5	$2(t_p + \Delta t)$	$3t_p + 2\Delta t$	Δt	$2\Delta s$
7	$3(t_p + \Delta t)$	$4t_p + 3\Delta t$	Δt	$2\Delta s$
2	$4(t_p + \Delta t)$	$5t_p + 4\Delta t$	$2t_p + 3\Delta t$	Δs
4	$5(t_p + \Delta t)$	$6t_p + 5\Delta t$	$2t_p + 3\Delta t$	Δs
6	$6(t_p + \Delta t)$	$7t_p + 6\Delta t$	$2t_p + 3\Delta t$	Δs
8	$7(t_p + \Delta t)$	$8t_p + 7\Delta t$	$3t_p + 4\Delta t$	Δs

Table 3.5 Fracture sequencing strategy for two-well staggered zipper fracturing. Corresponds to the scheme shown in Figure 3.52a.

Fracture Location	Treatment Start Time	Treatment End Time	Start Time After Recent Nearest Fracture (Delay Time)	Distance From Previous Nearest Fracture (in same well)
A_1	0	t_p	∞	∞
B_1	$t_p + \Delta t$	$2t_p + \Delta t$	∞	∞
A_2	$2(t_p + \Delta t)$	$3t_p + 2\Delta t$	$t_p + 2\Delta t$	Δs
B_2	$3(t_p + \Delta t)$	$4t_p + 3\Delta t$	$t_p + 2\Delta t$	Δs
A_3	$4(t_p + \Delta t)$	$5t_p + 4\Delta t$	$t_p + 2\Delta t$	Δs
B_3	$5(t_p + \Delta t)$	$6t_p + 5\Delta t$	$t_p + 2\Delta t$	Δs
A_4	$6(t_p + \Delta t)$	$7t_p + 6\Delta t$	$t_p + 2\Delta t$	Δs
B_4	$7(t_p + \Delta t)$	$8t_p + 7\Delta t$	$t_p + 2\Delta t$	Δs

Table 3.6 Fracture sequencing strategy for two-well staggered zipper fracturing. Corresponds to the scheme shown in Figure 3.52b.

Fracture Location	Treatment Start Time	Treatment End Time	Start Time After Recent Nearest Fracture (Delay Time)	Distance From Previous Nearest Fracture (in same well)
A_1	0	t_p	∞	∞
C_1	$t_p + \Delta t$	$2t_p + \Delta t$	∞	∞
B_1	$2(t_p + \Delta t)$	$3t_p + 2\Delta t$	∞	∞
A_2	$3(t_p + \Delta t)$	$4t_p + 3\Delta t$	$2t_p + 3\Delta t$	Δs
C_2	$4(t_p + \Delta t)$	$5t_p + 4\Delta t$	$2t_p + 3\Delta t$	Δs
B_2	$5(t_p + \Delta t)$	$6t_p + 5\Delta t$	$2t_p + 3\Delta t$	Δs
A_3	$6(t_p + \Delta t)$	$7t_p + 6\Delta t$	$2t_p + 3\Delta t$	Δs
C_3	$7(t_p + \Delta t)$	$8t_p + 7\Delta t$	$2t_p + 3\Delta t$	Δs
B_3	$8(t_p + \Delta t)$	$9t_p + 8\Delta t$	$2t_p + 3\Delta t$	Δs

Table 3.7 Fracture sequencing strategy for three-well staggered zipper fracturing. Corresponds to the scheme shown in Figure 3.52c.

Fracture Location	Treatment Start Time	Treatment End Time	Start Time After Recent Nearest Fracture (Delay Time)	Distance From Previous Nearest Fracture (in same well)
B_1	0	t_p	∞	∞
D_1	$t_p + \Delta t$	$2t_p + \Delta t$	∞	∞
A_1	$2(t_p + \Delta t)$	$3t_p + 2\Delta t$	∞	∞
C_1	$3(t_p + \Delta t)$	$4t_p + 3\Delta t$	∞	∞
B_2	$4(t_p + \Delta t)$	$5t_p + 4\Delta t$	$3t_p + 4\Delta t$	Δs
D_2	$5(t_p + \Delta t)$	$6t_p + 5\Delta t$	$3t_p + 4\Delta t$	Δs
A_2	$6(t_p + \Delta t)$	$7t_p + 6\Delta t$	$3t_p + 4\Delta t$	Δs
C_2	$7(t_p + \Delta t)$	$8t_p + 7\Delta t$	$3t_p + 4\Delta t$	Δs
B_3	$8(t_p + \Delta t)$	$9t_p + 8\Delta t$	$3t_p + 4\Delta t$	Δs
D_3	$9(t_p + \Delta t)$	$10t_p + 9\Delta t$	$3t_p + 4\Delta t$	Δs
A_3	$10(t_p + \Delta t)$	$11t_p + 10\Delta t$	$3t_p + 4\Delta t$	Δs
C_3	$11(t_p + \Delta t)$	$12t_p + 11\Delta t$	$3t_p + 4\Delta t$	Δs

Table 3.8 Fracture sequencing strategy for four-well staggered zipper fracturing. Corresponds to the scheme shown in Figure 3.52d.

Chapter 4: Fracture Propagation using Finite Volume Discretization: Model Formulation and Verification

In the previous chapters we discussed the influence of hydraulic fractures on stresses in their vicinity. This initial development has been discussed in papers published over the last 5 years (Roussel and Sharma 2011a, 2011b; Manchanda and Sharma 2012, 2013, 2014; Manchanda et al. 2012, 2013, 2014; Roussel et al. 2012). The preceding work was done using the Itasca software FLAC3D® (Itasca Consulting Group 2012) and it was shown that the creation of hydraulic fractures leads to changes in stresses around the fracture and this change in stresses can lead to stress reorientation in the vicinity of the fracture. This model was extended to create a workflow for pad scale fracturing simulations as was discussed in the previous chapters.

There are some inherent limitations of the FLAC3D® model that restrict further development work:

- The gridding and meshing in FLAC3D® is time consuming and inefficient
- FLAC3D® imposes restrictions on gridding turning fractures dynamically.
- FLAC3D® can only use a single computer for the computation and parallelization on super-computers is not possible. The scale of the questions we want to answer require the simulation of a pad of hydraulic fractures that could entail simulating more than 10 fractures. Doing this on a single computer is not efficient and in most cases computationally intractable using FLAC3D®.
- For the pad fracturing simulations the fracture geometry in FLAC3D® needs to be predetermined. The propagation of turning fractures cannot be dynamically modelled in FLAC3D®.

In order to meet the goals of this project advanced gridding and efficient solvers are necessary. This is primarily because of the computational time required to run a

reservoir scale problem where one is interested in both the near fracture effects as well as the far-field effects. This vast range in resolution of the problem requires advanced gridding to capture the nuances of the problem at all scales.

In this chapter we develop an advanced object oriented software that can help in circumventing the issues presented by FLAC3D®. First a review of the Finite Volume Method (FVM) for the problem at hand is presented. Thereafter, the model formulation with the new discretization for both static fractures and propagating fractures is presented. Then the developed model is verified by comparing the simulation results with analytical mechanical and poro-elastic models. We end the chapter with some analysis of the numerical features of the developed model.

4.1 LITERATURE REVIEW

A review of the available methods to solve geomechanics problems is presented here. We review the implementation of a control volume based discretization in contrast with the more popular Finite Element (FE) discretization and Finite Difference (FD) discretization used by other researchers. We introduce the use of fluid-structure-interaction physics to model the fracture-reservoir system using a finite volume discretization.

4.1.1 Finite Volume Method (FVM) and Solid Mechanics

Reservoir scale geomechanics modeling is typically done using finite element software such as ABAQUS (Systemes n.d.) or finite difference software such as FLAC3D® (Itasca Consulting Group 2012). Both categories of models are reliable and have been validated for various poro-elastic, and poro-plastic formulations of partial differential equations. In this work however, we attempt to address the reservoir scale geomechanics questions using FVM. Other researchers' contributions have been

reviewed below to show that FVM can be used to solve solid mechanics equations and generate comparable results when compared with Finite Element Method (FEM) and Finite Difference Method (FDM). The FVM is found to be simpler and better suited for our multi-physics applications.

The FV strategy to solve the stress-strain equations involves the conservation of the force components over a control volume followed by discretization and integration to obtain a coupled system of linear equations for the displacement components. Fryer et al. (1991) were amongst the first to explain the discretization of the elastic stress-strain equations for unstructured meshes using FVM. They compared the use of FVM with FEM to solve three simple problems, a cantilever beam problem, a temperature induced strain problem, and an irregular geometry multi-material problem. For all the above problems, their work showed comparable results for both FVM and FEM. They concluded that FVM could have an important advantage over FEM for problems with nonlinear boundary conditions as well as for cases where the displacement variable is coupled with thermal and pressure variables. In these cases the authors suggested the importance of an iterative scheme using FVM. Fallah et al. (2000) compared the results from FEM and FVM for non-linear stress analysis. They consider FVM to be a special case of the FEM with a unit weighting function and show that the FVM can be a viable method for solving solid-mechanics-based problems. FVM also provides the opportunity to solve multi-physics phenomena such as fluid-structure interaction using a single modeling formulation. On the contrary, FEM proves to be difficult to use for multi-physics problems like fluid flow problems coupled with solid deformation (Demirdžić and Martinović 1993). Solving the geomechanics equations is one such multi-physics problem that involves coupling of both solid mechanics and fluid mechanics.

Demirdžić and Muzaferija (1995) showed the application of FV numerical methods to simultaneously couple the solid body and fluid mechanics equations. They solved the integral form of the mass, energy and momentum conservation equations using an unstructured finite volume approach. They showed that the governing equations are elliptical and follow the same structure with different coefficients for most of the multi-physics phenomena that we want to simulate. They successfully applied the method to analyze the fluid flow and stress analysis of an air-cooled internal combustion engine.

A detailed description of the FV discretization has been provided by several researchers (Demirdžić and Martinović 1993; Demirdzic and Muzaferija 1994; Demirdžić and Muzaferija 1995; Demirdžić et al. 2000). A very useful review of the FV stress analysis methods and their various forms is also given by Tuković, Ivanković, and Karač (2013). They focused on the implementation of FV stress analysis methods for multi-material calculations. An implementation and extension of this multi-material interface design method has been used in this research and was presented recently (Bryant et al. 2015). It is important to address the multi-material discretization for reservoir scale geomechanics applications to account for variation in layer properties and to include heterogeneous structures such as faults, natural fractures, and joints in the discretized domain.

Jasak and Weller (2000) discussed the FV discretization of the linear elastic equations and implemented the equations in OpenFOAM (OpenFOAM Foundation 2013). They noted the simplicity of FVM when compared to FEM for complex domains involving fluid flow to be the main reason for preferring the use of FVM for linear elastic models. They further illustrated improvement in solution efficiency using parallelization and recommend using parallel multigrid methods to improve the efficiency further.

Tang (2013) used the OpenFOAM (OpenFOAM Foundation 2013) libraries to implement the small strain poro-elasto-plastic system of equations. A qualitative analysis of the convergence of the system of equations used to describe poro-elasto-plastic media has been discussed (Tang et al. 2015). This work explains step-by-step the method of implementation of the geomechanics equations in the OpenFOAM environment.

Thus, there is sufficient past work that demonstrates the advantage of using a FV discretization in unstructured parallelized domains for reservoir scale geomechanics applications. In the current work, we extend the methods developed by Tang (2013) to solve the poro-elastic reservoir domain equations coupled with fracture propagation.

4.1.2 Crack Propagation using Finite Volume Discretization

Numerical simulations of dynamic fracture propagation are conventionally done using finite difference, finite element and boundary element formulations. Finite difference methods and finite element methods can be used when discretization of the reservoir is important while boundary element method is used when the reservoir domain heterogeneity can be ignored. With the above justification for using FVM for solid mechanics problems, it is imperative to understand the implementation of dynamic fracture propagation in a reservoir domain using FV discretization.

Ivankovic et al. (1994) first studied and implemented a FV rapid crack propagation code for dynamic fracture propagation. The development of the dynamic fracturing model was implemented both as a node release technique (V Stylianou and Ivankovic 2002) and a cohesive zone model (V. Stylianou and Ivankovic 2002). The cohesive zone implementation has been shown to physically describe crack initiation and propagation (Barenblatt 1959, 1962). Experimental measurements can be used to derive

traction-separation curves and have been used in simulation models to study rapid crack propagation (Ivankovic et al. 1997, 2004).

Conventional fracture propagation methods ignore interference between fractures and assume a predetermined crack path trajectory. Evidence of non-planar fracture growth has been presented using laboratory experiments (Olson 1993; Ispas et al. 2012), field tests (Warpinski and Teufel 1987; Warpinski and Branagan 1989; Warpinski et al. 1990; Cipolla et al. 2000) and numerical simulation models (Olson 1993; Weijers et al. 2005; Dahi-Taleghani and Olson 2011; McClure and Horne 2013; Roussel et al. 2013; Wu and Olson 2013; McClure et al. 2015). Arbitrary fracture growth occurs because of reservoir heterogeneity and stress interference between fractures. Thus, it is important to address and allow simulated fractures to propagate and follow the path of least resistance in a numerical model and not predetermine the crack path.

Limited work has been done to allow arbitrary crack propagation procedures using FVM (Carolan et al. 2013). Carolan et al. (2013) used the cohesive zone model and implemented the method developed by Tuković, Ivanković, and Karač (2013) to estimate the tractions at all the mesh faces. These traction values can be used to define propagation criteria to implement the arbitrary turning of fractures. An effective traction criteria was discussed by Bryant, Hwang, and Sharma (2015) for hydraulic fracturing applications. The estimation of tractions at the interface of multiple solid materials can be used to characterize the stress around heterogeneities using FVM and help the simulated fractures to propagate along the direction of least resistance. Carolan et al.'s (2013) method was extended to include the impact of multi-material heterogeneities more common-place for oil and gas applications (Bryant et al. 2015). In this work the implementation presented by Bryant, Hwang, and Sharma (2015) is extended to hydraulic fracturing applications.

This includes not only single fracture propagation but also includes the propagation of simultaneous competitive multiple fracture propagation.

4.1.3 Simultaneous Multiple Fracture Propagation

Horizontal wells are completed in stages with each stage having clusters of perforations that serve as initiation points of fractures. Each stage is fractured with the hope of creating fractures from each cluster. However diagnostic data in the field has shown that in most cases all clusters do not create dominant fractures (Fisher et al. 2004; Miller et al. 2011). It has been discussed that about 30% of the clusters might not contribute to production. The increase in the compressive stresses in the vicinity of the fracture can inhibit fracture growth from nearby perforation clusters (Fisher et al. 2004). Some researchers have also concluded that if the perforation clusters were kept very close to each other then there is a possibility of fracture coalescence or longitudinal growth of fractures (Daneshy 2011; Wong et al. 2013).

Some experimental work has been reported that shows that the perforation cluster spacing has an effect on the fracture growth pattern. When closely spaced multiple fractures were propagated simultaneously, some fractures were much larger than others (El-rabaa 1982; Abass et al. 2002). In some cases one fracture could become the dominant fracture propagating amongst the clusters.

There has been some analytical work done to understand the implications of competitive fracture propagation. Bunger, Zhang, and Jeffrey (2012) performed a dimensional analysis to understand the most important parameters that need to be addressed when optimizing multiple fracture growth problems. They look into the deflection patterns that are generated due to interaction of the fractures with existing fractures. They applied their model to a 2-D fracture growth simulator. In a later paper

their model was used to understand the impact of viscosity and toughness dominated regimes on multiple fracture propagation (Ames and Bunger 2015). They use a mathematical model to couple the contribution of fluid flow, rock breakage and perforation pressure drop to the total power requirement for the growth of multiple hydraulic fractures. Their model predicts that when the stage spacing is less than the fracture height, the probability of multiple fracture growth is small. The fundamental understanding their model provides can be very useful in explaining observations from numerical models, however, it lacks the rigor of a model that can address the heterogeneity observed at the field scale.

Several researchers have attempted to numerically simulate fluid distribution and interaction between simultaneous propagating multiple fractures. Like all numerical models, certain simplifying assumptions have been made to enable rapid calculations.

Some wire mesh models have also been developed where an orthogonal mesh is used to represent the fracture system with predetermined fracture spacing and fracture orientation (Xu et al. 2010; Meyer and Bazan 2011). In these methods the explicit treatment of individual fracture propagation with the propagation path is ignored. These methods are semi-analytic and are not accurate in explaining the physical processes of interacting fractures.

Many researchers have attempted to use the displacement discontinuity method to model the stress interference created by hydraulic fractures. Using this method researchers have attempted to analyze the impact of simultaneous multiple fracture growth (Yamamoto et al. 2004; Min and Ghassemi 2012; Wong et al. 2013; Lecampion and Desroches 2015; Wu and Olson 2015). Several of these methods have been extended to allow for interaction with heterogeneities in the reservoir (Weng et al. 2011; Sesetty and Ghassemi 2012; McClure and Horne 2013; Wu and Olson 2013; McClure et al.

2015). The existing formulation of the displacement discontinuity method (DDM) used does not require a complete description of the reservoir domain and is not able to capture the heterogeneity in material properties. In addition, poroelastic effects are neglected. These details can be important when comparing the observed simulation trends to field observations.

Castonguay et al. (2013) developed a boundary element method for modeling the competitive growth of cracks in an elastic domain. Their model was based on a single fracture model developed earlier (Rungamornrat et al. 2005) and was able to generate three dimensional growth of competing fractures. However, as with the DDM models, the reservoir domain was not discretized.

The finite element method (FEM) can be used as an alternative when the discretization of the reservoir domain to account for heterogeneity is important. Dahi-Taleghani and Olson (2011) have used the extended finite element method (XFEM) for 2-D fracture propagation and interaction with existing flaws. Shin and Sharma (2014) also used XFEM to analyze the impact of various factors controlling the simultaneous propagation of multiple competing fractures. Haddad and Sepehrnoori (2014) have also used a similar method coupled with a cohesive zone model to look at the propagation of 3-D competing fractures. The authors showed competitive growth with fracture curving in another publication (Haddad and Sepehrnoori 2015). These models grid the entire reservoir domain and hence are computationally expensive but have the potential of including reservoir heterogeneity. Numerical enhancements and efficiency upgrades are necessary for practical simulations.

In this work we look at an alternative of FEM methods and use FVM to model competitive multiple fracture propagation. As shown above, the reservoir domain can be discretized using a finite volume approach and heterogeneity can be included using multi-

material methods. Two approaches for the fracture domain discretization are considered. In one approach the fracture domain, the wellbore and the perforation pressure drop are considered as single blocks and average pressures and pressure drops are estimated without discretizing each individual block. In the second domain the fracture domain is discretized using FVM. In this second approach the fracture domain and the reservoir domain are coupled using fluid structure interaction (FSI) methods.

4.1.4 Fluid Structure Interaction (FSI)

In all FSI applications a fluid domain and a solid domain interact at an interface. The fluid flow can cause changes in the solid geometry and deformation of the solid can impact the fluid flow around it. Nature is full of examples of FSI. A leaf falling on the ground is an example. The air currents caused by the rotation of fan blades is another example. FSI has applications in aeronautics, blood flow, bridges, turbines, musical instruments, naval and offshore engineering etc. The list is very long. FSI in general has applications in problems where multi-physics problems (a different set of partial differential equations being solved in different coupled domains) are involved.

Finite volume implementations of FSI methods are becoming popular because of the versatility of FVM to handle complex multi-physics problems in a modular manner. Kanyanta, Ivankovic, and Karac (2009) and Ivankovic et al. (2002) used an FSI algorithm to model arterial blood flow. They modelled the transient flow through flexible conduits such as arteries using their FSI procedure. They then used an iterative partitioned scheme to couple the fluid domain and solid domain and get an implicit result. Their algorithm was developed using the OpenFOAM libraries. Others have developed more capabilities and libraries in OpenFOAM to handle FSI problems such as dynamic moving meshes

(Jasak and Tukovic 2010). Others have used different FV libraries and methods to model FSI systems using unstructured moving meshes (Slone et al. 2002; Tsui et al. 2013).

Limited work has been done in the use of FSI methods in the oil and gas industry. Most of the work done has been in the field of facilities and offshore engineering. Fluids interact with structures in a variety of upstream oil and gas applications. Some examples are fluid flow in a wellbore, sand production, proppant transport, and hydraulic fracture propagation. In some cases such as wellbore fluid flow, the solid medium (the casing or the rock in case of open-hole) can be considered as static boundary conditions. Fracture propagation, sand production and proppant transport are more dynamic processes, in which a solution of both the fluid domain and the solid domain is essential to have a complete understanding of the problem.

Bai and Lin (2014) presented a tightly coupled FSI implementation of hydraulic fracturing for a 2-D fracturing code using XFEM. They extended their work to develop a code for multiple competitive fracture propagation (Bai and Lin 2014b). They used a partitioned approach to solve the fluid-solid domain coupling. They used analytical methods to estimate the fluid domain calculations and coupled the calculations with an FEM method to calculate the solid domain linear elastic deformations.

There are two choices to couple the fluid and solid domains (1) a monolithic approach, and (2) a partitioned approach (Degroote et al. 2009). In the monolithic approach the fluid flow calculations and the solid domain calculations are solved simultaneously using a single solver. On the other hand, in the partitioned approach, the fluid domain and solid domain are solved separately using two distinct solvers. The code development for the monolithic approach is very specific with respect to matrix construction, and inclusion of physics. However, the monolithic approach is implicit and can have very limited convergence related problems. The partitioned approach, on the

other hand, requires software modularity to couple the fluid domain and solid domain solvers in an iterative manner. In the partitioned approach optimized individual domain solvers can be coupled with ease, however, the coupling algorithm needs to be accurate and convergent. Degroote, Bathe, and Vierendeels (2009) and Degroote et al. (2010) compare the development of an adaptive under-relaxation procedure for the FSI methodology and compare its efficiency with the monolithic approach for solving FSI problems. In the spirit of the finite volume iterative scheme developments, we use the partitioned approach to couple the fracture and solid domains in this work. The fluid domain calculations are coupled with the solid domain calculations using an adaptive under-relaxation scheme to achieve a stable convergent solution.

4.2 MODEL FORMULATION

In the current work, a new model is developed that uses advanced meshing libraries and computationally efficient solvers to capture stress interference effects and poro-elastic effects for pad-scale simulations.

We use Biot's poro-elastic framework to model the mechanical behavior of a fluid filled porous material. The conceptual model has a solid skeleton with pore fluid that is allowed to freely move with both the solid and fluid phases fully connected (Detournay and Cheng 1993; Coussy 2004). The displacement of the solid skeleton and the pressure changes in the fluid help track the movement of the porous solid and the fluid respectively.

4.2.1 Poro-elastic deformation

For the reservoir calculations, we solve the momentum balance in the form of Cauchy's equation of motion as shown in Eq. (4-1)

$$\frac{\partial^2(\rho \mathbf{u})}{\partial t^2} = \nabla . \boldsymbol{\sigma} + \rho \mathbf{f} \tag{4-1}$$

In the stress analysis formulation the inertial time derivative term is considered negligible and steady state calculations are performed to calculate stress as a function of the spatial coordinates.

The solid matrix strain tensor, $\boldsymbol{\varepsilon}$ is defined in terms of the displacement vector, $\mathbf{u}$ as shown in Eq. (4-2).

$$\boldsymbol{\varepsilon} = \frac{1}{2}[\nabla \mathbf{u} + (\nabla \mathbf{u})^T] \tag{4-2}$$

4.2.1.1 Constitutive model

The constitutive equation defines the relation between stress and strain tensors for the solid matrix. We use the assumption of linearized poro-elasticity for the skeleton (Coussy 2004) (Eq. (4-3)).

$$\boldsymbol{\sigma} = 2G\boldsymbol{\varepsilon} + \lambda \varepsilon_v \mathbf{I} - \alpha p \mathbf{I} \tag{4-3}$$

For this work compressive stresses are considered as negative and a decrease in volume leads to negative volumetric strain. The model described is a pure elastic model, however, the constitutive equation between stress and strain can be modified to include plastic behavior. This would involve using an incremental displacement and an incremental stress formulation. The details of the elasto-plastic formulation will not be discussed in this work.

4.2.2 Fluid Flow Formulation[3]

Continuity equation for the fluid components is given by Eq. (4-4)

$$\frac{\partial \zeta}{\partial t} + \nabla . \mathbf{q} = 0 \tag{4-4}$$

Darcy's law can be used to describe the fluid flow through the rock.

$$\mathbf{q} = -\frac{k}{\mu}\nabla p \tag{4-5}$$

The constitutive equation for pore pressure is given in Eq. (4-6)

$$p = M(\zeta - \alpha \varepsilon_v) \tag{4-6}$$

Equations (4-4), (4-5) and (4-6) can be combined to model the coupled deformation-diffusion processes. Thus using the combination of the continuity equation for fluid, Biot's theory of consolidation, and single-phase Darcy flow of a slightly compressible fluid in a porous medium we can derive Eq. (4-7).

$$\frac{kM}{\mu}\nabla^2 p = \frac{\partial p}{\partial t} + \alpha M \frac{\partial \varepsilon_V}{\partial t} \tag{4-7}$$

The definition of Biot's modulus and Biot's coefficient for the poro-elastic medium is given by,

$$\frac{1}{M} = \frac{\alpha - \phi}{K_s} + \frac{\phi}{K_f}$$
$$\alpha = 1 - \frac{K}{K_s} \tag{4-8}$$

[3] Detailed derivation of the fluid flow formulation can be found in several sources (Jaeger et al. 1979; Detournay and Cheng 1993; Coussy 2004)

The Biot's coefficient compares the material deformation with the deformation of the solid matrix i.e. the grains that compose the material. For a special case of an incompressible solid, Biot's coefficient takes a value of 1.

4.2.3 Coupled System of Equations

Combining Eqs.(4-1), (4-2), (4-3) and assuming no effect of inertial terms, the equations can be combined into Eq. (2-6)

$$\nabla.[G\nabla\mathbf{u} + G(\nabla\mathbf{u})^T + \lambda\mathbf{I}tr(\nabla\boldsymbol{u})] - \alpha\nabla p\mathbf{I} + \rho\mathbf{f} = 0 \tag{4-9}$$

The above equation can be solved for displacement which can then be converted to strain and stress explicitly.

The volumetric strain in Eq. (4-7) can be written as the divergence of displacement

$$\nabla.\left(\frac{kM}{\mu}\nabla p\right) = \frac{\partial p}{\partial t} + \alpha M\frac{\partial}{\partial t}(\nabla.\mathbf{u}) \tag{4-10}$$

Eq. (2-6) and Eq. (4-10) can be solved in an iteratively explicit manner to a desired tolerance. This procedure was successfully implemented by Tang (2013) and is shown in Figure 4.3.

4.2.4 Boundary Conditions

In this formulation Dirichlet and/or Neumann boundary conditions are allowed. Thus, one can specify displacement and/or stress (gradient of displacement) as a boundary condition. The implementation of the stress boundary involves converting the traction force at the boundary to a displacement gradient boundary (Eq. (4-11)).

$$(\nabla \mathbf{u}).\mathbf{n} = \frac{\mathbf{T} - [G(\nabla \mathbf{u})^{\mathrm{T}} + \lambda \mathbf{I} tr(\nabla \mathbf{u})].\mathbf{n}}{G} \tag{4-11}$$

The initial stresses in the system can be explicitly described and then the fracture opening pressure can be modeled as a traction boundary on the fracture surface.

The boundary condition for the pressure equation can similarly be described as a gradient of pressure or a fixed pressure depending on the application. For example, to simulate Darcy flow through a boundary the pressure boundary condition can be described as shown in Eq. (4-12).

$$\nabla p = -\frac{\mu \mathbf{q}}{(\mathbf{k}.\mathbf{n}).\mathbf{n}} \tag{4-12}$$

4.2.5 Finite Volume Discretization

We have used open source CFD libraries (OpenFOAM – Open Source Field Operation And Manipulation) to solve the problems at hand as desired (OpenFOAM Foundation 2013). OpenFOAM is a C++ toolbox for the development of the customized numerical solvers, and pre-post-processing utilities for the solution of continuum mechanics problems. This FV code is predominantly a CFD code. OpenFOAM has the library of functions and solvers available that can be used to develop stress analysis solvers that can be adapted to unstructured and advanced meshes (Jasak and Weller 2000; Hrvoje Jasak et al. 2007; Jasak et al. 2007). This work can be extended into the plastic domain and has been coupled with fluid pressure equations to form the base structure of a fully coupled geo-mechanics solver (Tang 2013; Tang et al. 2015).

There are several advantages of using a library or toolbox of C++ solvers and utilities for multi-physics applications (Jasak et al. 2007). The following advantages justify our choice of using OpenFOAM to model geomechanics systems:

- Such a library provides the ability to model partial differential equations with relative ease. Since the method of incorporation of different kinds of partial differential equations has been abstracted, users can incorporate several different equations and can rely on the discretization of the system of equations by the software.
- OpenFOAM is widely developed and used for computational fluid dynamics (CFD) simulations. CFD applications require the ability to model complex domains. The object oriented nature of the software allows us to use the meshing developments (such as unstructured meshes) done for CFD problems in our stress analysis problems.
- The open source nature of the software enables extensive collaborations and incorporation of multiple physics.
- The object oriented structure of the software also helps in collaboration, with the added benefit of reduced copied-and-pasted code.
- OpenFOAM has abstracted parallelization. This level of abstraction enables new developments to be parallelized with relative ease. This reduces the need to interact with the computer architecture.
- Preliminary work has shown the usability of OpenFOAM for stress analysis.
- OpenFOAM libraries are open source and freely available.

We discretize the governing equations for the problem at hand using the Finite Volume (FV) method. OpenFOAM includes a library of solvers that are predominantly used for CFD calculations and is compatible with the FV discretization. These solvers can be adapted to perform mechanics calculations as well (Jasak and Weller 2000). The above mentioned equations Eq. (2-6) and Eq. (4-10) can be discretized using FVM (Demirdžić and Martinović 1993; Demirdžić and Muzaferija 1995). In FVM the values of

the variables are stored at the centers of cells and are interpolated to the faces and the vertices of the cells. In this work the distribution of the displacement and pressure variables is considered to a have a linear distribution within a cell. The FV discretization of Eq. (2-6) for a cell centered at P is presented in Eq. (4-13) (ignoring the body forces here).

$$\int_{V_P} \nabla.[G\nabla\mathbf{u} + G(\nabla\mathbf{u})^T + \lambda\mathbf{I}tr(\nabla\mathbf{u})]dV - \int_{V_P} \alpha\nabla p\mathbf{I}dV = 0 \tag{4-13}$$

Using Gauss' theorem Eq. (4-13) becomes Eq. (4-14).

$$\oint_{\partial V_P} d\mathbf{s}.[G\nabla\mathbf{u} + G(\nabla\mathbf{u})^T + \lambda\mathbf{I}tr(\nabla\mathbf{u})] = \oint_{\partial V_P} \alpha p d\mathbf{s} \tag{4-14}$$

The surface integrals in Eq. (4-14) are split into the sum of integrals over the cell faces.

$$\oint_{V_P} d\mathbf{s}.(G\nabla\mathbf{u}) = \sum_f G_f \mathbf{s}.(\nabla\mathbf{u})_f$$

and (4-15)

$$\oint_{V_P} d\mathbf{s}(\alpha p) = \sum_f \mathbf{s}(\alpha p)_f$$

Where, the subscript *f* refers to the corresponding value at the face between the two cells. In the above discretization (Eq. (4-15)) only the $\mathbf{s}.(G\nabla\mathbf{u})$ term can be treated implicitly. All the other terms need to be treated explicitly. This is because the implicit term does not depend on the other components of displacement while the explicit terms comprise of inter-component coupling.

4.2.5.1 Implicit discretization (Jasak and Weller 2000)

Eq. (4-16) shows the discretization when the face area normal and the vector joining the centers of the neighboring cells are parallel. The subscript P refers to the value at the current cell while N refers to the value at the neighboring cell in consideration. The vector PN is the line joining the centers of the two cells. For non-parallel normal and cell center vectors a 'non-orthogonal correction' can also be added (Jasak 1996) for the gradient calculation.

$$\mathbf{s}.(\nabla\mathbf{u})_f = |\mathbf{s}|\frac{\mathbf{u}_N - \mathbf{u}_P}{|\mathbf{PN}|} \tag{4-16}$$

Thus, the value represented by the sum of Eq. (4-16) over all the faces around a control volume can be expressed in terms of the values in P and the nearest neighbors of P (Ns) and an algebraic equation of the form Eq. (4-17) can be obtained.

$$\sum_f G_f \mathbf{s}.(\nabla\mathbf{u})_f = a_P\mathbf{u}_P + \sum_N a_N\mathbf{u}_N$$

where, (4-17)

$$a_N = G_f\frac{|\mathbf{s}|}{|\mathbf{PN}|} \; and \; a_P = \sum_N a_N\mathbf{u}_N$$

4.2.5.2 Explicit discretization (Jasak and Weller 2000)

For the terms $G(\nabla\mathbf{u})^T$ and $\lambda\mathbf{I}tr(\nabla\mathbf{u})$ explicit discretization is required. Here, the various terms are explicitly interpolated to the face adjoining the cells with centers P and N as shown in Eq. (4-18) and Figure 4.4.

$$(\nabla\mathbf{u})_f = f_x(\nabla\mathbf{u})_P + (1 - f_x)(\nabla\mathbf{u})_N \tag{4-18}$$

where,

$$f_x = \frac{|\mathbf{fN}|}{|\mathbf{PN}|}$$

Various approaches can be used to estimate the gradient values at the control volume centers. These approaches should be selected with consideration of the mesh quality. Skew-correction is recommended for non-orthogonal meshes (Jasak and Weller 2000).

4.2.5.3 Displacement equation discretization

Eq. (4-13) can be reduced to the algebraic form of Eq. (4-19) for each control volume where the $\mathbf{b}_p$ term contains the explicit terms, and the boundary condition terms.

$$a_P \mathbf{u}_P + \sum_N a_N \mathbf{u}_N = \mathbf{b}_P \tag{4-19}$$

Thus a system of algebraic equations is created (Eq (4-20))

$$\mathbf{A}\mathbf{u} = \mathbf{b} \tag{4-20}$$

Here **A** is the sparse matrix with coefficients a_p on the diagonal and **u** is the vector of the displacement vector of all the cells in the domain. The diagonal dominance of **A** is beneficial for the solution algorithm.

The system of equations in consideration above requires under-relaxation algorithms to attain efficient convergence. This is because the explicit terms contain more information than the implicit sparse matrix (Jasak and Weller 2000). An alternate way is to add $(G + \lambda)\nabla\mathbf{u}$ to the implicit part and subtract the same amount from the explicit part. This converts the steady state form of Eq. (2-6) to Eq. (4-21).

$$\underbrace{\nabla.[(2G + \lambda)\nabla\mathbf{u}]}_{implicit} = \underbrace{-\nabla.[G(\nabla\mathbf{u})^T + \lambda\mathbf{I}tr(\nabla\boldsymbol{u}) - (G + \lambda)\nabla\mathbf{u}]}_{inter-component\ coupling,explicit} + \underbrace{\alpha\nabla p}_{p-coupling,explicit} \tag{4-21}$$

This new system of equations is discretized in the same way as before. This new over-relaxed system along with multi-grid acceleration techniques and domain decomposition parallelization algorithms makes a very fast solver with impressive convergence (Jasak and Weller 2000). Similarly the pressure equation can be discretized as shown in Eq. (4-22) (Jasak 1996).

$$\underbrace{\frac{kM}{\mu}\nabla^2 p}_{implicit} = \underbrace{\frac{\partial \mathrm{p}}{\partial \mathrm{t}}}_{implicit} + \underbrace{\alpha M \frac{\partial}{\partial t}(\nabla . \mathbf{u})}_{\mathbf{u}-coupling,explicit} \tag{4-22}$$

4.2.5.4 Solution algorithm

The system of equations is non-linear in nature. A segregated algorithm is used to solve the system of equations presented above where each component of displacement is solved separately with inter-component explicit coupling (Eq. (4-21)) (Jasak and Weller 2000; Tang 2013). The system of equations is considered to be converged when the residual value becomes less than the user prescribed convergence tolerance. Various solvers can be used to solve the system of equations (Demirdzic and Muzaferija 1994; Jasak and Weller 2000; Tang 2013; Tang et al. 2015).

We solve Eq. (4-21) and Eq. (4-22) iteratively to couple the stress calculation procedure and the pore pressure equations (Figure 4.3). This explicit coupling algorithm should help faster convergence. Since the reservoirs of interest for this project are reservoirs with low permeability, the custom coupling allows the flexibility to not solve the steady state displacement equations every time step.

4.3 WORKFLOW FOR PAD SCALE FRACTURE MODELING

In this section we discuss the implementation of a pad fracturing workflow in the new finite volume discretization. This workflow is designed for static fractures.

4.3.1 Modeling Fracture Treatment in a Pad Using Static Fractures

Work shown in the previous chapter suggests that the most important parameters that influence the stress reorientation due to a created fracture are the geometry of the fracture (width, height and length), fracture surface area (representative of leak-off area), and fracture orientation. In this section we reproduce the work done using FLAC3D® and incorporate a workflow to use OpenFOAM for modelling pad scale fracture treatments.

4.3.1.1 Fracture creation

In a field treatment, a hydraulic fracture is opened by the pressure acting on its surface by the fluid pumped into the fracture. We model this by imposing two boundary conditions on the fracture face, a traction boundary condition for the mechanical opening and a fluid pressure boundary condition for the poro-elastic coupling. One way of incorporating any arbitrary shaped fracture in the mesh is by using a STL file of the fracture dimensions (Figure 4.5). A mesh can be created around the surface described by this STL file and the boundary conditions can be applied on the fracture surfaces.

4.3.1.2 Fracture trajectory estimation

In Chapter 2 we discussed a fracture trajectory estimation algorithm that could capture the impact of stress shadow and could be used to model the trajectory of successive fractures in a horizontal well. That algorithm is reused here to develop a similar fracture trajectory estimation procedure.

4.3.1.3 Fracture SRV

In hydraulic fracturing treatments, it is assumed that along with planar hydraulic fractures a network of fractures is also created. Instead of capturing the entire network of fractures created several researchers have attempted to model the stimulated region with

an enhanced permeability. This enhanced permeability region in the rock is sometimes known as the Stimulated Rock Volume (SRV).

We try to estimate the permeability of this stimulated region by performing a volume balance on the fluid injected during the fracture treatment. The main assumptions in this procedure are:

- We use pre-defined fracture and SRV dimensions.
- The SRV extent along the wellbore is assumed to be half of the distance between the fractures in most cases. In those cases we essentially assume a SRV all along the horizontal wellbore.
- We assume a constant permeability in the entire SRV. The SRV permeability should vary with the density of the induced network of fractures. However, here we try to predict an average estimate of the density of the induced network of fractures.
- In most cases we assume that the treatment pressure is constant during the treatment duration. This simplifies the algorithm further.

The amount of fluid injected should be equal to the sum of the amount of fluid in the fracture and the amount of fluid that leaks off. Assuming that the fluid injected is incompressible, this mass balance can be treated as a volume balance. The fluid volume in the fracture can be given by Eq. (4-23).

$$V_{fracFluid} = \phi_{frac} w_{avg} L_f H_f \tag{4-23}$$

Since the boundary condition we apply on the fracture surface is a pressure boundary condition instead of a rate boundary condition, the leak-off from the fracture surface is different for different values of SRV permeability as shown in Eq. (4-24)

$$V_{leakOff} = -\frac{k_{SRV}}{\mu_{fluid}}(2L_f H_f)\nabla p|_{frac} \quad (4\text{-}24)$$

The algorithm used to estimate the SRV permeability is shown in Figure 4.6

4.3.1.4 Fracture closure

The fracture closure model used is very similar to the closure model discussed in Chapter 2. Here we follow the steps shown above to open the fracture to an initial fracture width. After this the pressure is allowed to leak-off into the formation. As time passes by, due to fluid leak-off, the fracture should close. As discussed in the previous chapter the maximum width of an open PKN like fracture at any time can be represented using Eq. (2-13)

$$w_t = w_{t-\Delta t} - 6.37C_L\left(\sqrt{t} - \sqrt{t-\Delta t}\right) \quad (4\text{-}25)$$

where, w_t is the maximum width at any particular instant after pumping is stopped, $w_{t-\Delta t}$ is the maximum width of the fracture at the previous time step, C_L is the chosen leak-off coefficient and t is the time after pumping is stopped. We use the above equation to estimate the fracture width at any particular time after pumping is stopped. Using this estimate of fracture width the fracture pressure can be altered to converge for the estimated maximum width. This fracture gradually closes with fluid leak-off till the fracture attains its propped dimensions. The lower limit of the fracture maximum width is represented by Eq. (4-26)

$$w_{propped} = \frac{Proppant\ Mass}{\pi\rho_{proppant} l_f h_f\left(1-\phi_{propped}\right)} \quad (4\text{-}26)$$

where, $\rho_{proppant}$ is the density of the proppant, l_f is the fracture half-length, h_f is the fracture half-height, $\phi_{propped}$ is the porosity of the fracture when it is propped and $w_{propped}$

is the maximum propped width of the fracture. This calculation assumes an elliptical fracture opening.

4.3.2 Modeling Multiple Static Hydraulic Fractures in a Pad

In the previous version of the static fracture simulator a stress superposition technique was used to model multiple fractures in a horizontal well. This was primarily because the meshing in FLAC3D® did not allow mapping of field variables from one topology to another. In the new model this difficulty is overcome by using the advanced utilities that have been developed. Using utilities such as '*mapFields'* and '*snaappyHexMesh'* we are now able to mesh geometries of arbitrary shapes. '*mapFields'* allows to map the values of field variables from one grid to a corresponding grid. The utility interpolates the values between the corresponding grid points and re-interpolates the values to the cell centers. *'snappyHexMesh'* can be used to mesh complicated geometries inside a coarse mesh. This involves using an initial coarse mesh generated using *'blockMesh'* followed by using a STL file of a fracture as input to the *'snappyHexMesh'* utility.

Figure 4.7 depicts a workflow that can be used to model successive fractures in a pad. These hydraulic fractures can be modeled for realistic fracture geometry, spacing and orientation. The workflow is used to create the fractures shown in Figure 4.8. Also, for the various wells in a pad this should enable variable well spacing, orientations and lateral extent (Figure 4.9). This also allows incorporation of custom fracture sequencing in the horizontal wells on the pad (zipper fractures, alternate fractures etc.).

4.3.3 Modeling Fracture Propagation

Initial work on hydraulic fracture propagation using the model presented above has been discussed before (Bryant et al. 2015). The fractures are modeled as a

discontinuity (an internal boundary) within the reservoir mesh. The fracture boundary is dynamically updated during fracture propagation by splitting mesh faces and adding them to the fracture boundary. A schematic of this mechanism is shown in Figure 4.10.

4.3.3.1 Fracture Initiation and Propagation

Crack propagation has been implemented for nodal release methods using finite volume-based stress analysis with materials having varying elastic properties (Carolan et al. 2013). For poro-elastic fracture propagation, the failure criterion should be modified by using the effective stress tensor instead of the total stress tensor (Bryant et al. 2015).

Failure of a face in the mesh is determined by comparing the effective tractions to the effective maximum cohesive strengths. The maximum cohesive strengths, σ_{max} and τ_{max}, are related to effective tensile and shear material strengths. These effective stresses are calculated on all the faces of the mesh. The normalized effective traction is then calculated using Eq. (4-27) on all the internal faces of the mesh.

$$\left(\frac{|t^{\parallel}|}{\sigma_{max}}\right)^2 + \left(\frac{|t^{\perp}|}{\tau_{max}}\right)^2 \begin{matrix} \geq 1 \rightarrow \quad failed \\ < 1 \rightarrow not\ failed \end{matrix} \tag{4-27}$$

The internal faces with normalized effective traction within a predefined tolerance of the maximum normalized effective traction value are chosen to create the fracture. Generally a 1% value is used. Thus, all the internal faces with normalized effective traction within 1% of the maximum normalized effective traction are considered to be part of the fracture. A nodal release method is used to detach the chosen faces and the fracture is propagated. These faces are turned into boundary faces that are connected to the fracture.

The faces on the fracture can belong to two categories: (1) damaged, or (2) cracked. According the cohesive zone method, failed faces within the cohesive volume

that are less than a critical separation distance, δ_C, apart are subject to an inward traction resisting further outward displacement. These faces are classified as "damaged" faces. Fracture faces with separation greater than δ_C are considered cracked.

The inward traction applied on the damaged faces is calculated using traction separation laws.

$$t^{\parallel}_{damaged} = \begin{cases} \sigma_{max}(1-\delta/\delta_C) & for\ \delta \le \delta_C \\ 0 & for\ \delta > \delta_C \end{cases}$$
$$t^{\perp}_{damaged} = \begin{cases} \tau_{max}(1-\delta/\delta_C) & for\ \delta \le \delta_C \\ 0 & for\ \delta > \delta_C \end{cases} \quad (4\text{-}28)$$

These traction separation laws help relate the maximum tensile and shear tractions to fracture energy. For example, for a linear traction-separation law, this relationship is,

$$G_c = \frac{1}{2}\sigma_{max}\delta_C \quad (4\text{-}29)$$

This fracture energy can be accumulated for each fracture face by using the current traction and the current displacement increment. Including mode-mixity for both tensile and shear fracture energy, when the fracture damaged region accumulates sufficient energy to satisfy the relation shown in Eq. (4-30), then the corresponding fracture faces move to the cracked category.

$$\left(\frac{G_I}{G_{Ic}}\right)^2 + \left(\frac{G_{II}}{G_{IIc}}\right)^2 \begin{matrix} \ge 1 \rightarrow cracked \\ < 1 \rightarrow damaged \end{matrix} \quad (4\text{-}30)$$

For a hydraulic fracture, the cracked faces should be treated as the fracture boundary and the fluid pressure should be applied on them. This fluid pressure should be

applied as both a normal traction as well as a fluid pressure boundary on the boundary faces of the cracked part of the fracture. Estimation of this fluid pressure inside the hydraulic fracture can be done by either assuming spatially uniform fracture pressure or calculating the spatial variation of the fracture pressure. Both these methods are discussed below.

4.3.3.2 Spatially uniform fracture pressure

A general fracture propagation workflow is shown in Figure 4.11. The boundary conditions and the failure criteria used are shown below. This fracture propagation workflow is only valid for cases in which an assumption of uniform pressure inside each simulated fracture is valid. In this workflow we assume no frictional pressure drop in the wellbore or the fracture. This workflow is adapted for multiple fractures and hence the mass of the injected fluid is conserved. The formulation used is shown below. All the unknowns have been expressed in bold font.

The treatment fluid in the wellbore is assumed to be slightly compressible and accounting for the storage term of the wellbore is important to numerically simulate the physical process of multiple fracture propagation. The bulk modulus of the fluid is defined as shown below,

$$K = -V\frac{dP}{dV} = -V\frac{\Delta P}{\Delta V} \tag{4-31}$$

Wellbore storage can be formulated assuming uniform pressure in the wellbore. Assuming uniform pressure and ignoring frictional pressure drop is a simplifying assumption to avoid discretizing the wellbore. A more rigorous approach is discussed later (4.3.3.3).

$$\Delta V_w = V_{out} - V_{in} = (Q_{out} - Q_{in})\Delta t \tag{4-32}$$

$$\boldsymbol{P_w} - P_w^o - \frac{K_f}{V_w}(Q_{in} - \boldsymbol{Q_{out}})\Delta t = 0 \tag{4-33}$$

The pressure drop through a cluster of cylindrical perforations is given by the following expression,

$$\Delta P_i^{perf} = \boldsymbol{P_w} - \boldsymbol{P_i} = \frac{\overline{\rho}}{2{\alpha_d}^2 {n_{perfs}}^2 (\pi {r_i}^2)^2}\boldsymbol{q_i}^2 = a_i \boldsymbol{q_i}^2$$

Or (4-34)

$$\boldsymbol{P_w} - \boldsymbol{P_i} - a_i \boldsymbol{q_i}|\boldsymbol{q_i}| = 0$$

where,

$n_{perfs} = number\ of\ perforations$,
$\alpha_d = damage\ factor = \sim 0.9$,
$q_i = flow\ rate\ through\ the\ cluster\ of\ perforations$,
$r_i = radius\ of\ each\ perforation$,
$\overline{\rho} = density\ of\ fluid - proppant\ suspension$

The flow distribution from the fluid exiting the bottom of the well through the perforations into the fractures (assuming incompressibility of the fluid) can be expressed as,

$$\boldsymbol{Q_{out}} - \sum_{i=1}^{n} \boldsymbol{q_i} = 0 \tag{4-35}$$

Using the same definition of bulk modulus shown above, the compliance of the fracture can be simulated. The fluid leak-off and the change in volume of the fracture is included in this formulation. V_i^c is a constant initial volume that represents the volume

associated with the storage in the stage and the initial perforations. The change in volume of a fracture is given as,

$$\Delta V_f = \left(q_i - q_{L,i} - q_{V,i}\right)\Delta t \tag{4-36}$$

$$\boldsymbol{P_i} - P_i^o - \frac{K_f}{(V_i^o + V_i^c)}\left(\boldsymbol{q_i} - q_{L,i} - q_{V,i}\right)\Delta t = 0 \tag{4-37}$$

Again, the simplifying assumption of uniform pressure inside each fracture can be avoided by solving for the pressure drop inside the fracture system (4.3.3.3).

This gives us a system of 2n + 2 equations with 2n + 2 variables namely, $\boldsymbol{P_w}$, $\boldsymbol{Q_{out}}$, $\boldsymbol{P_i}$ and $\boldsymbol{q_i}$. $\boldsymbol{P_i}$ can be eliminated from the equations,

$$\boldsymbol{P_w} - a_i\boldsymbol{q_i}^2 - P_i^o - \frac{K_f\left(\boldsymbol{q_i} - q_{L,i} - q_{V,i}\right)\Delta t}{(V_i^o + V_i^c)} = 0 \tag{4-38}$$

Similarly $\boldsymbol{P_w}$ can be eliminated

$$P_w^o + \frac{K_f}{V_w}(Q_{in} - \boldsymbol{Q_{out}})\Delta t - a_i\boldsymbol{q_i}^2 - P_i^o - \frac{K_f}{(V_i^o + V_i^c)}\left(\boldsymbol{q_i} - q_{L,i} - q_{V,i}\right)\Delta t = 0 \tag{4-39}$$

And $\boldsymbol{Q_{out}}$ can also be eliminated,

$$f_i(q_1, q_2, \dots) = P_w^o + \frac{K_f}{V_w}\left(Q_{in} - \sum \boldsymbol{q_i}\right)\Delta t - a_i\boldsymbol{q_i}^2 - P_i^o - \frac{K_f}{(V_i^o + V_i^c)}\left(\boldsymbol{q_i} - q_{L,i} - q_{V,i}\right)\Delta t = 0 \tag{4-40}$$

This is a system of $\boldsymbol{n}$ equations with $\boldsymbol{n}$ unknowns. In order to solve this system of equations the Newton Raphson method can be used. In order to do so, the Jacobian matrix for the above functional representation needs to be calculated:

For $n = 2$,

$$J = \begin{bmatrix} \frac{\partial f_1(q_1,q_2)}{\partial q_1} & \frac{\partial f_1(q_1,q_2)}{\partial q_2} \\ \frac{\partial f_2(q_1,q_2)}{\partial q_1} & \frac{\partial f_2(q_1,q_2)}{\partial q_2} \end{bmatrix} = \begin{bmatrix} -\frac{K_f}{V_w}\Delta t - 2a_1\boldsymbol{q_1} - \frac{K_f}{(V_1^o + V_1^c)}\Delta t & -\frac{K_f}{V_w}\Delta t \\ -\frac{K_f}{V_w}\Delta t & -\frac{K_f}{V_w}\Delta t - 2a_2\boldsymbol{q_2} - \frac{K_f}{(V_2^o + V_2^c)}\Delta t \end{bmatrix}$$

The diagonal terms of the Jacobian matrix are given as

$$J[i][i] = \frac{\partial f_i}{\partial q_i} = -\frac{K_f}{V_w}\Delta t - 2a_i\boldsymbol{q_i} - \frac{K_f}{\left(V_i^o + V_i^c\right)}\Delta t$$

and the off-diagonal terms are

$$J[i][j] = \frac{\partial f_i}{\partial q_j} = -\frac{K_f}{V_w}\Delta t, \forall\ i \neq j$$

Now the system of equations can be solved using a Newton Raphson method as shown below,

$$\overline{Q^{n+1}} = \overline{Q^n} - \overline{\overline{J^{-1}}}.\overline{F(q_1, q_2, \dots q_n)}$$

where,

$$\overline{Q^n} = \begin{bmatrix} q_1 \\ q_2 \\ \vdots \\ q_n \end{bmatrix}, and\ \overline{F(q_1, q_2, \dots q_n)} = \begin{bmatrix} f_1 \\ f_2 \\ \vdots \\ f_n \end{bmatrix}$$

The above matrix equation is solved to a desired solution tolerance to obtain the best estimate of the flow distribution into the individual fractures. This flow distribution can be converted into pressures in the respective fractures using the above system of equations. These pressure values can then be applied to the surfaces of the individual

fractures as a boundary condition for both the displacement equation as well as the fluid pressure equation.

4.3.3.3 Spatially varying fracture pressure

A second more comprehensive approach to simulate fracture propagation involves solving for the fluid flow inside the fracture. In the above method we assumed the fracture to be a single unit and only solved for the storage contribution of the pressure inside the fracture. We ignored the pressure drop inside the fracture. Calculating pressure drop inside the fracture requires discretization of the fracture. In this section we address a finite volume discretization of the fracture domain.

The mass conservation equation is shown in (4-41).

$$\frac{d(\rho V_f)}{dt} + \nabla.(\rho \mathbf{q} V_f) = 0 \tag{4-41}$$

The flow inside the fracture can be simulated using an implementation that looks like Darcy's law (4-42)

$$\mathbf{q} = -\frac{k}{\mu}\nabla p \tag{4-42}$$

In the above expression the permeability can be assumed to vary with the width of the fracture using the expression shown in (4-43) (Schechter 1992; Ehlig-Economides and Economides 2000)

$$k = \frac{w^2}{12} \tag{4-43}$$

Permeability and density are incorporated explicitly in the system of equations. This means that iterations are performed to converge to the correct value of density and permeability. Since the permeability only depends on the width of the fracture, it is

coupled every time the fracture domain is deformed. The density on the other hand depends on the pressure in the fracture (4-45). Thus it makes the system of equations non-linear and needs to be solved till convergence of the system of equations.

$$V_f \frac{d\rho}{dt} + \rho \frac{dV_f}{dt} - \nabla.\left(\frac{\rho k}{\mu} \nabla p_{frac} V_f\right) = 0 \tag{4-44}$$

For a slightly compressible fluid,

$$\rho = \rho^{ref} e^{c_f\left(p_{frac} - p_{frac}^{ref}\right)} \tag{4-45}$$

Thus the equation now becomes

$$c_f \rho V_f \frac{dp_{frac}}{dt} + \rho \frac{dV_f}{dt} - \nabla.\left(\frac{\rho k}{\mu} \nabla p_{frac} V_f\right) = 0 \tag{4-46}$$

We can now convert the above equation to the finite volume discretization form as shown above,

$$\int_{V_f} c_f \rho \frac{dp_{frac}}{dt} dV_f + \int_{V_f} \rho \frac{\left(1 - {V_f^{old}}/{V_f}\right)}{\Delta t} dV_f - \int_{V_f} \nabla.\left(\frac{\rho k}{\mu} \nabla p_{frac}\right) dV_f = 0 \tag{4-47}$$

The above equation is solved using finite-volume principles and an estimate of p_{frac} is obtained. The calculated value of p_{frac} is under-relaxed for stable convergence of the iterative schemes. In the above equation, density of the fracturing fluid is explicitly treated. This makes the system nonlinear and the system is solved using the fixed point iteration scheme. The previous iteration guess of density is used to solve for the current iteration estimate of pressure inside the fracture. The process is continued till convergence.

The boundary conditions for the described fracture domain system of equations are obtained from the reservoir domain. The pressure gradient calculated on the reservoir domain fracture boundary is applied as a pressure gradient for the fluid domain fracture boundary. On the other hand the relaxed pressure calculated from the fluid flow calculations in the fluid domain are applied as pressure boundary condition on the reservoir domain. This enforces the Dirichlet-Neumann coupling. The pressure boundary condition applied on the reservoir domain is applied for both the fluid pressure equation as well as the traction for the displacement equation. This Fluid-Solid-Interaction (FSI) approach is used to couple flow inside the fracture with the displacement and fluid pressure of the reservoir. The general algorithm of the FSI solver is shown in Figure 4.12. The detailed FSI coupling algorithm is described in Figure 4.13.

The fracture domain increases in size over time. This increase in size of the fracture domain is incorporated using the algorithm developed by Philip Cardiff (Cardiff et al. 2015). A schematic of the algorithm is shown in Figure 4.14.

4.4 MODEL VERIFICATION

To test the validity of the models we need to verify the formulation by comparing the results with analytical expressions. The numerical formulation presented above has been verified earlier (Tang 2013; Tang et al. 2015) for cases of linear elastic deformation around a circular cavity, plastic deformation around a circular cavity and plastic 1 D consolidation. Here we attempt to verify the model by comparing with other available analytical models.

4.4.1 Stress shadow

Sneddon (1946) derived analytical expressions of the increase in stresses in the direction perpendicular and parallel to a penny shaped fracture. These stresses as a

function of the normalized distance along the axis of the fracture are given in Eq. (2-15). We compared the results of the analytical solutions by plotting the normalized additional stress in the direction parallel and perpendicular to the fracture for a uniform net pressure inside the fracture. The parameter values used to generate these results are presented in Table 4.1. This comparison is shown in Figure 4.16. This shows that the model formulated is able to simulate the stress shadow accurately.

$$\frac{\Delta\sigma_{xx}}{p_{net}} = -\frac{2}{\pi}\left[\frac{\xi(\xi^2-1)}{(\xi^2+1)^2} - \tan^{-1}\left(\frac{1}{\xi}\right)\right]$$

$$\frac{\Delta\sigma_{yy}}{p_{net}} = -\frac{1}{\pi}\left[\frac{3\xi+\xi^3}{(\xi^2+1)^2} + \frac{2\upsilon\xi}{\xi^2+1} - (1+2\upsilon)\tan^{-1}\left(\frac{1}{\xi}\right)\right] \quad (4\text{-}48)$$

4.4.2 One-Dimensional Consolidation[4]

Stress shadow verification showed the successful implementation of the linear elastic equations of deformation. We now validate the coupling of porous flow and solid mechanics by solving the classic 1D consolidation problem. This verification for the current model has also been discussed elsewhere (Bryant et al. 2015). Consider a saturated layer of soil of finite thickness (H) and large horizontal extent resting on an impermeable base. A constant surface load is applied on the layer under undrained conditions. The boundaries in the x and y directions are constrained to avoid any deformation in the lateral direction. Since no fluid is allowed to escape, the fluid pressure in the soil increases until it becomes uniform everywhere (p_0) based on the Skempton effect. When equilibrium is attained, the top surface is allowed to drain the fluid by setting the pore pressure to be 0 there. Gradually, the pore fluid drains out of the upper surface, and the pore pressure relaxes until it drops down to the boundary pressure. While

[4] The validation of the current poro-elastic model was first presented elsewhere (Bryant et al. 2015)

this occurs, the layer continues to deform vertically upward. Analytical solution to this problem is available (Detournay and Cheng 1993) using the following assumptions:

- Soil matrix is assumed to be homogeneous and fully saturated.
- The water in the pores is incompressible
- The soil skeleton behaves as a linear elastic material
- Individual soil particles making up the soil skeleton are incompressible
- Darcy's law governs the flow of the pore water through the soil skeleton
- Gravitational effects are ignored.

The initial value of pore pressure that is induced from loading can be derived from the fluid constitutive law with the simplification of undrained conditions,

$$\begin{aligned} p_0 &= M(-\alpha\epsilon_{zz}) \\ p_z &= (\lambda + 2G)\epsilon_{zz} - \alpha p \end{aligned} \tag{4-49}$$

Solving the two equations above, we get the initial pore pressure in the system to be,

$$p_0 = \frac{\alpha M}{(\lambda + 2G + \alpha^2)} p_z \tag{4-50}$$

The system can now be setup for the diffusion equation (Eq. (4-51)).

$$\begin{aligned} \frac{\partial p}{\partial t} &= c\frac{\partial^2 p}{\partial z^2} \\ \text{Where, } c &= \frac{k/\mu}{\left(\frac{1}{M} + \frac{\alpha^2}{\lambda+2G}\right)} \end{aligned} \tag{4-51}$$

The boundary conditions for the pressure equation are:

$$p = 0 \text{ @ } z = H; \frac{\partial p}{\partial z} = 0 \text{ @ } z = 0 \tag{4-52}$$

Detournay and Cheng (1993) have solved the equation above and present the following solution for pressure and vertical displacement,

$$\hat{p} = 2\alpha \frac{p_0}{p_z} \sum_{i=0}^{\infty} \frac{sin(a_i \hat{z})}{a_i} e^{-a_i^2 \hat{t}}$$
$$\hat{u}_z = 2\alpha \frac{p_0}{p_z} \left[\sum_{i=0}^{\infty} \frac{cos(a_i \hat{z})}{a_i^2} e^{-a_i^2 \hat{t}} \right] + \hat{z} - 1 \quad (4\text{-}53)$$

Where,

$$\hat{p} = \frac{p}{p_z}, \hat{z} = \frac{H-z}{z}, \hat{t} = \frac{ct}{H^2}, \hat{u}_z = \frac{(\lambda+2G)u_z}{Hp_z}$$

The parameter values used to solve the 1D consolidation problem are shown in Table 4.2. The grid that is used to simulate the 1D consolidation is shown in Figure 4.17. We used one grid block in the x and y directions and 200 grid blocks in the z direction. Each grid block was 0.1 m X 0.1 m X 0.1 m in size. The initial consolidation caused the initial pressure (p_0) to be 36448 Pa. When the top draining was started, the pressure slowly decreased over the entire domain. The pressure contours at various times are shown in Figure 4.18. These contours and grid dimensions have been quantified in Figure 4.19 and Figure 4.20. It can be concluded from the figures that the simulation results are in good agreement with the analytical simulations results.

4.4.3 Single Fracture Propagation[5]

Verification of the fracture propagation model is done by using the classical 2-D KGD model (Geertsma and de Klerk 1969). This single fracture propagation is assumed to be in a homogeneous elastic domain under plane strain conditions. The fluid injected

[5] The validation of single fracture propagation using the current modeling workflow was presented elsewhere (Lee et al. 2015).

in the fracture is assumed to be incompressible. This verification has been presented elsewhere (Lee et al. 2015) and is repeated here for completeness. The parameter values used to describe the material are shown in Table 4.3.

The comparison was made to the analytical model using a similar approach as Ouchi, Katiyar, York, et al. (2015). The analytical solution for fracture pressure, half-length, and maximum fracture width are given in Eq. (4-54) where q is the volumetric injection rate per unit height, $\acute{E}$ is the plane-strain Young's modulus, and t is injection time in seconds.

The initial assumed fracture geometry has a length of 3cm and its aperture and cohesive energy are set to zero to allow the free opening and the fluid injection (Carrier and Granet 2012). The computation domain is illustrated in Figure 4.21. We compare the fracturing pressure response, induced fracture half-length, and the maximum fracture width over the injection duration. Good agreement between the numerical and analytical results can be seen in the original paper. The results have been reproduced here and shown in Figure 4.22.

As discussed in the paper the numerical results deviate from the analytical solution (Eq. (4-54)) because of boundary effects, where the ratio of the crack length to bounding box span becomes large. The total injected fluid volume is however conserved so a shorter but wider fracture than the analytic solution is induced at the end of the simulation.

$$P_{frac} = 1.09\left(\acute{E}^2\mu\right)^{1/3} t^{-1/3}$$

$$x_f = 0.539\left(\frac{q^3\acute{E}}{\mu}\right)^{1/6} t^{2/3}$$

$$w_f = 2.36\left(\frac{q^3\mu}{\acute{E}}\right)^{1/6} t^{1/3} \tag{4-54}$$

$$\acute{E} = \frac{E}{1-\upsilon^2}$$

4.5 NUMERICAL ANALYSIS

In this section we discuss numerical analysis that is done to test various numerical parameters that can increase efficiency, improve accuracy, stabilize simulations, and adaptive methods.

4.5.1 Mesh Dependence

In all mesh based numerical simulation methods, it is important to perform a mesh size sensitivity analysis. We perform a mesh sensitivity analysis to verify the impact of mesh size on both fracture propagation as well as fluid distribution. We model simultaneous propagation of two fractures spaced 10 m apart. The *in-situ* minimum horizontal stress is 50 MPa (~7250 psi) and the *in-situ* maximum horizontal stress is 50.7 MPa (~7350 psi). The *in-situ* reservoir pore pressure is 40 MPa (~5800 psi). The injection rate is chosen to be 0.0212 m^3/s (~48 bpm/ft). The initial well volume is chosen to be 20 m^3 (~125 bbl) and the perforation pressure drop coefficient for both fractures is chosen to be 1e9 $Pa.s^2/m^2$. A refinement box around the initiating points of the fractures is used where the mesh is structured. The size of the refinement box is 40 m in the X direction and 40 m in the Y direction. After creating a Cartesian mesh, additional

diagonal cuts are introduced in these squares in the refinement region to allow more degrees of freedom for the fractures to propagate. Beyond this refinement box the mesh is unstructured. The entire mesh is composed of prisms which means that all the cells in the mesh have 5 faces with 2 faces perpendicular to the Z direction. This restricts the fractures from twisting and having the fracture face normal Z component to be 0. A schematic of this mesh is shown in Figure 4.23. The dimensions of the entire domain are 2010 m in the X direction, 2000 m in the Y direction, and 3 m in the Z direction and is centered at (5, 0, 1.5).

Results from this mesh sensitivity analysis are presented in Figure 4.24. Figure 4.24(a) shows the coarsest mesh in consideration with 5 m square blocks in the center refinement region. Figure 4.24(b) has 1 m square blocks in the center refinement region, Figure 4.24(c) has 0.5 m square blocks in the center refinement region, and Figure 4.24(d) has 0.1 m square blocks in the center refinement region. The results show that for all the cases the fractures grow with rotational symmetry. In all cases the left fracture propagates further in the north direction and the right fracture propagates further in the south direction. The rotational symmetric nature of the fractures is reflected in both the fracture length and fracture width. This rotational symmetric nature of the fractures is potentially caused by the stress interference between the fractures. Here small numerical differences in the mesh cause the stress interference effects to overpower the symmetric tendency of fracture propagation. These simulation results thus show that the multiple fracture propagation case is an unstable case and can be easily dominated by the heterogeneity in a reservoir.

For all the mesh sensitivity cases considered the average trends of the fracture propagation are similar. There is, however, some distinct dependence of the results on the mesh. The results for the finest mesh size considered show that the fractures turn away

from their diagonal trajectories and follow the in-situ stress state within the refinement region. This depicts the mesh dependence of the results.

4.5.2 Simulation Speed Test

The speed of numerical methods depends on the algorithms used to solve the matrices and the input-output methods for the data structures. In this model the matrices being inverted are sparse and diagonally dominant. Hence most available schemes provide quick and efficient results. For the current work, the PCG (Preconditioned Conjugate Gradient) solver with a DIC (Diagonal Incomplete Cholesky) preconditioner is used to solve the displacement equation while the GAMG (Generalized Algebraic Multi Grid) solver is used for the pressure equation. The simulations conducted using the above solvers should scale up linearly with an increase in the number of unknowns in the simulation.

Since these simulations are in 2-D there are three unknowns per cell (U_x, U_y and p). For 3-D cases there are 4 unknowns per cell (U_x, U_y, U_z, and p). In the simulations discussed above, the mesh size in the vicinity of the fracture was varied. In order to assess the speed of the solvers and the input-output operations it is important to have a similar number of fracture cells in the comparison cases. Thus we perform an analysis by varying the boundary domain size as shown in Figure 4.25. In these cases, the middle refinement region is not modified (Figure 4.26). The distance of the boundary from the middle region is varied. The size of the boundary cells is kept the same and the gradient of cell sizes is automatically calculated using the meshing software *GMSH* (Geuzaine and Remacle 2009). If we focus on the time taken for the fracture propagation within the refinement region, then we effectively increase the number of cells in the mesh with limited modification of the fracture trajectory and limited modification of the number of

fracture faces. Thus we can capture the unbiased differences in the speed of simulations for cases with fracture propagation. Figure 4.27 shows the comparison and suggests an almost linear trend for the cases considered. This suggests that the solvers and methods applied in the models are efficient.

4.5.3 Dynamic Mesh Refinement

Dynamic mesh refinement also referred to as adaptive mesh refinement is generally used to minimize error in simulations by adaptively refining local regions of high error. These methods generally involve the estimation of the error for a prescribed refinement, using the simulation results to predict a new refinement for a target accuracy and implementation of the predicted refinement involving mesh regeneration (Zienkiewicz and Zhu 1992). Thus error estimation is an important aspect of choosing the regions of mesh refinement. The superconvergent patch recovery procedure (SPR) is used by several researchers to adaptively refine the meshes in finite-element domains (Khoei et al. 2008; Moslemi and Khoei 2009).

Several researchers have studied adaptive mesh refinement in detail with regards to crack propagation (Rashid 1998; Bouchard et al. 2000, 2003; Khoei et al. 2008; Moslemi and Khoei 2009). Most of this work deals with fracture propagation with nodal release methods using discrete cracks. Since the geometry of the cracked body changes continually during the propagation of the fracture, adaptive remeshing is needed during the crack growth process. This helps in increasing the accuracy and consequently models the crack growth process effectively. The above mentioned SPR technique can help in determining and predicting the local error for various mesh configurations and hence can help in choosing meshes with minimal errors. For example, the tip singularity induced due to LEFM crack propagation can induce large errors in coarse meshes near the tip.

Certain configuration of a refined mesh near the crack tip can help in reducing the error caused by the singularity (Moslemi and Khoei 2009).

All of the above work has been done for adaptive mesh changes in finite-element simulation frameworks. Here we present a simple strategy to introduce more degrees of freedom for the fracture to turn in arbitrary directions based on the stress state in the vicinity of the fracture tip. The local measure of error was ignored in this algorithm. The algorithm has been developed for Cartesian meshes. The inputs required are target minimum volume of cells and radius of refinement. Based on this the following algorithm is developed to refine the mesh in the vicinity of the fracture:

1. Find all the cells immediately adjacent to the existing fracture that have cell volume greater than the input target minimum cell volume and store in *adjacentCellsToRefine*. Store the minimum adjacent cell volume in variable *minCellVolume* and the number of cells in *adjacentCellsToRefine* in *adjacentCellsToRefineSize.*
2. If *minCellVolume* is less than or equal to the target minimum cell volume and *adjacentCellsToRefineSize* is zero then go to step 5.
3. Cut each cell in *adjacentCellsToRefine* first in the X direction and then cut the two obtained cells in the Y direction to form four cells.
4. Go to step 1
5. Find all the cells within the target radius from the fracture surface that have cell volume greater than the input target minimum cell volume and store in *localRadiusCellsToRefine*. Store the minimum cell volume in variable *minCellVolume* and the number of cells in the *localRadiusCellsToRefine* list in *localRadiusCellsToRefineSize.*

6. If *minCellVolume* is less than or equal to the target minimum cell volume and *localRadiusCellsToRefineSize* is zero then go to step 9.
7. Cut each cell in *localRadiusCellsToRefine* first in the X direction and then cut the two obtained cells in the Y direction to form four cells.
8. Go to step 5
9. Go through the entire mesh and refine all the cells in the mesh that have more than 8 faces recursively.
10. Go through the cells within 0.75 times the target radius from the entire fracture surface and find all the cells that have more than 5 faces. Store these cells in *diagonalRefinementCells.*
11. Cut all the *diagonalRefinementCells* using a plane that has normal in the direction (1, 1, 0) and is centered at the center of each cell.
12. Cut each of the two cut cells using a plane that has normal in the direction (-1, 1, 0) and is centered at the center of each cell.
13. Repeat steps 1-12 every failure iteration.

Figure 4.28 depicts the steps described above as an illustration.

This described dynamic mesh refinement method is useful in increasing the number of smaller cells in the vicinity of the fracture. As shown above smaller cells in the vicinity of the fracture help in allowing fracture propagation more accurately. This method can also reduce the errors in the vicinity of the crack tip. This dynamic mesh refinement method helps to increase the efficiency of the simulations. Figure 4.29 shows the comparison between the results of a single fracture propagation in a fine mesh and a dynamically refined mesh. The fine mesh has each cell of size 0.25 m X 0.25 m X 1 m, while the dynamically refined mesh initially has each cell of size 1 m X 1 m X 1m. Thus the fine mesh has 16 times the number of cells in the initial configuration of the

dynamically refined mesh. The target minimum cell volume for the dynamically refined mesh is 0.1 cu-m and the refinement radius is 2 m. These parameters cause the initial coarse cells near the fracture to be refined in the X and Y directions twice thus making the resulting cells 0.25 m X 0.25 m X 1 m in dimension. An additional diagonal cell cutting step is performed that splits smallest refined cells into 4 triangular prisms (Figure 4.30). Thus we obtain more resolution in the vicinity of the fracture than in the fine mesh. In this comparison study the two main observations were that the dynamically refined mesh lead to a faster simulation and that the resulting fracture lengths and widths were very similar from both the cases. The dynamically refined mesh took 40% less time to run when compared to the fine mesh simulation. Thus the dynamically refined mesh simulation was more efficient and had a better resolution.

The algorithm also creates diagonal cuts in the mesh to allow for fracture turning. This helps increase the number of fracture propagation directions at any failure iteration. This increases the chances of turning fractures *in-situ*ations in which turning fractures are more probable. For instance when the principal stresses are rotated, the direction of fracture propagation should be expected to be rotated. Figure 4.31 shows a set of results in which the *in-situ* direction of maximum horizontal stress is rotated. The horizontal stress contrast in these simulations was chosen to be 5 MPa. Clearly the results show that the fracture follows the prescribed *in-situ* stress direction in both the 30 degree and 45 degree rotation cases.

Thus dynamic refinement of mesh with fracture propagation has been shown to be an essential feature in the development of this work. This method has the following advantages:

- Increased efficiency by increasing the speed of the simulation
- Increased number of degrees of freedom for fracture turning

4.5.4 Parallelization

Figure 4.32 shows the domain decomposition for an example 3-D simulation mesh. Traditionally OpenFOAM solvers and methods use distributed parallelization algorithms. The linear matrix solvers are parallelized and pre-packaged utilities such as *"decomposePar"* and *"reconstructParMesh"* help with the pre-processing and post-processing of most OpenFOAM cases. Data structures in OpenFOAM have also been parallelized. This adds another level of abstraction when defining variables and requires minimal attention when parallelizing. There are some situations however that require the parallelization of specific tasks. One example would be in boundary conditions where we may need to integrate over surfaces. In our simulations when the fracture is simulated as a boundary there is an opposite face for each face on the fracture surface. The fracture volume in this scenario is calculated by using the calculated displacement of opposite faces to estimate the width of the fracture at any point on the fracture surface and then the fracture width can be integrated over the entire fracture surface to estimate the fracture volume. However, the fracture boundary can be a part of multiple processor domains. Thus a global integration of fracture width needs to be done to estimate the fracture volume. Fortunately, there are simple methods that allow mathematical and logical operations that are based on the scatter and gather operations that form the foundation of the parallelization of code over multiple processors. These simple mathematical operations (such as *gSum*) can sum up the product of the width of the fracture and the face areas to give the fracture volume.

Most of the parallelization of the fracturing procedure that addressed the implementation of the cohesive zone method and included the topological changes to the mesh were completed by various researchers. Special mention to Philip Cardiff for help with the parallelization of the fracture boundary conditions used in this work.

Parallelization speedup testing was done for a test case. This test case had 179740 mesh cells. The results from the parallelization speedup (Figure 4.33) suggests that the speedup is linear for up to approximately 6000 cells per processor. Beyond this number we still get speedup but it is drastically reduced from the linear trend. This result can be used as a rule of thumb for future large scale simulations.

4.5.5 Impact of Solution Tolerance

In Figure 4.11, Figure 4.12, and Figure 4.13 we discussed the algorithms for fracture propagation used in this work. All numerical schemes depend on a predetermined tolerance value to test for convergence of the calculated numerical solution. The choice of the relaxation factor for certain variables can impact the speed of convergence. A smaller value of the chosen relaxation factor implies slower and steadier convergence, however, a larger value of the relaxation factor may lead to faster convergence but sometimes may cause erratic behavior leading to divergence.

Figure 4.34 shows the impact of displacement tolerance on solution accuracy and simulation speedup. The displacement equation relaxation factor was set to be a low value of 0.01 in this set of results. We analyze the importance of scaling the relative residual tolerance dependent on the value of chosen relaxation factor. The figures shown in the left column show the results for simulations in which the relative residual was not scaled while the figures in the right column show results for simulations in which the relative residual was scaled. The scaling of the relative residual is performed by multiplying the provided relative tolerance value with the relaxation factor. Thus if the displacement relative residual tolerance is provided to be 1e-2 and the relaxation factor is 1e-2, the relative residual tolerance becomes 1e-4. Theoretically this avoids situations in which the relaxed solution for a variable might be within the target residual tolerance

leading to an illusion of convergence. Practically, this is important only when the relaxation factor and the target relative residual tolerance are of similar order. Also, as seen in the figure the results do not change much with and without scaling.

From Figure 4.34 it is clear that for the scaled set of simulations, the displacement variable tolerance less than 1e-4 takes similar simulation times and produces similar results. Tolerance values more than 1e-4 do not impact the results too much and take much longer to run. For instance the simulation results for tolerance value 1e-6 take approximately 2.75 times the time taken for the simulations run with a tolerance value 1e-4. Thus, the simulation speed can be increased by more than 2 times without a loss of accuracy by using smaller tolerance values.

We tested this for a case with competitive growth of two fractures similar to the cases presented in Figure 4.24. In this analysis we compared the impact of the defined displacement equation tolerance value on the simulation results as well as the simulation speed. From Figure 4.35 it is evident that for the two considered cases of tolerance 1e-2 and 1e-6 the results are identical. We get simulation speedup from 720 seconds to 330 sec. This is another validation of the above analysis that suggests that the chosen displacement tolerance can be increased with little impact on results but more than two-fold increase in simulation speed. With this result it is also verified that choosing a higher displacement tolerance does not affect the fluid distribution algorithm.

4.5.6 Adaptive FSI Relaxation

For the FSI models discussed above, the fracture fluid flow calculations and the reservoir displacement and fluid flow calculations are iteratively explicitly coupled using a fixed point iteration scheme. The algorithm for this coupling is shown in Figure 4.13. The pressure calculated in the fluid domain is applied as a boundary condition to the solid

domain and causes changes in the displacement and pressure fields in the solid mesh. However, before application this calculated pressure sometimes needs to be relaxed using a pre-determined factor. Eq. (4-55) shows the equation used to relax the calculated pressure in the fracture domain ($p_{frac}^{boundary}$) before application as a boundary condition to the reservoir domain.

$$p_{reservoir}^{boundary} = \alpha_{FSI} p_{frac}^{boundary} + (1 - \alpha_{FSI}) p_{reservoir}^{boundary} \tag{4-55}$$

For a tightly coupled system such as the one in consideration, it becomes very important to tune this relaxation parameter to ensure convergence. This tuning is dependent on various solution parameters and cannot be generalized for all problems. From several iterations of attempts to tune this factor it was observed that as the fracture length increases this FSI relaxation factor needs to be smaller to ensure convergence. The dependence of the relaxation factor on the propagating fracture geometry suggested the opportunity to make this relaxation factor adaptive. We can change the value of this relaxation factor over successive iterations by tracking the value of calculated FSI residuals. An algorithm was incorporated in the code to implement the adaptive FSI relaxation procedure. This algorithm is shown in Figure 4.36. This algorithm helps in increasing the speed of the simulation by adaptively changing the relaxation factor used for the fluid and solid domain coupling.

Figure 4.37 shows the results for the comparison of the adaptive FSI relaxation procedure with fixed relaxation methods. In this simulation it was hard to obtain convergence for relaxation factors much more than 0.1. The adaptive method starts with a relaxation factor of 0.9 and goes to a relaxation factor of 0.01 using the algorithm shown in Figure 4.36. It is evident from Figure 4.37 that using the adaptive procedure faster simulations can be conducted when compared to the fixed relaxation simulations with

small effect on the results. The smallest relaxation factor discussed shows a much smaller fracture length. The scaling of the FSI tolerance might be necessary for such low relaxation factors as discussed for the displacement tolerance in the section above. Without this scaling it is possible that the simulation continues with a misleading evidence of convergence.

4.6 CONCLUSIONS

In this chapter, we have discussed the model development, verification and validation of a finite volume based numerical geomechanics reservoir scale simulator with arbitrary fracture propagation. The model allows us to model multiple, competing fractures propagating in a heterogeneous medium and oriented in any arbitrary direction (turning). Both mechanical and poroelastic effects are accounted for and modeled in 3-D. Fluid flow in the fracture can also be solved for to obtain the pressure distribution in the fracture and coupled with the poroelastic problem in the matrix using an FSI approach. The model development was done using OpenFOAM's finite volume libraries and discretization methods. The key contributions from this chapter are:

- A finite volume method has been developed that can be used to model non-linear multi-physics problems. The pressure equation in the reservoir and the displacement equation in the reservoir are coupled using a segregated iterative fixed point iteration method.
- The workflow for pad scale fracturing has been adapted to the new finite volume discretization. The model is capable of simulating multiple static fractures in multiple horizontal wells to understand the importance of stress interference in a pad. These fractures can have arbitrary curvatures and the fracture trajectory estimation algorithm can be used to determine the impact of stress shadow on the

fracture trajectory. A fracture closure algorithm has also been introduced in this system. Thus, the workflow discussed in the previous two chapters has been successfully ported to this new discretization method.

- The elastic equations included in the model have been tested and verified. The stress shadow induced by a penny shaped fracture obtained from the model is consistent with analytical solutions.
- The poro-elastic coupling used in the model used in this work has been validated with analytical solutions
- The cohesive zone method used for fracture propagation in this work was described in Bryant et al. (2015). The uniform fracture pressure formulation is used to validate the fracture propagation model (Lee et al. 2015).
- An extensive numerical analysis is performed to improve the numerical efficiency of the developed code.
- The mesh size sensitivity analysis suggested that fracture elements of size less than 5m are able to reproduce similar fracture propagation trends. Fracture interference and simultaneous multiple fracture propagation looks similar for all the sensitivity cases.
- The efficiency of the linear solvers was studied. The time taken for simulations is shown to linearly increase with number of unknowns in the domain.
- An adaptive mesh refinement procedure was developed to model fracture propagation. This dynamic mesh refinement procedure was shown to provide benefit in introducing speed-up of the numerical simulations as well as introducing additional degrees of freedom for the fractures to turn.
- The solvers and methods used in the model have been parallelized and simulations can be performed on multiple computers simultaneously. The model

can be used on high performance computing resources such as Texas Advanced Computing Center's (TACC) High Performance Computing (HPC) resource. The parallelization speed-up was tested and it was shown that the speed-up of the simulations was linear for up to approximately 6000 cells per processor.

- The solution methods use fixed point iteration schemes. The solution is assumed to have converged when the residual meets a pre-determined tolerance criteria. A tighter tolerance criterion is supposed to get more accurate results. It was shown that at tolerance values up to 1e-2, the simulation results showed similar fracture propagation lengths.
- A new scaling was introduced for simulations run with higher values of relaxation factors. This scaling method prevented the illusion of convergence of the iterative scheme because of a low relaxation factor.
- An adaptive FSI relaxation scheme was incorporated that helped in increase the simulation efficiency. The simulation results were shown to be very similar to the simulation results obtained for the fixed relaxation factor comparison cases while reducing run times substantially.

4.6.1 Future Model Development

The model developed above was developed for a linearized poro-elastic framework. Extensions of the model including plasticity have been discussed (Lee et al. 2015; Tang et al. 2015). Inclusion of plasticity may make the solvers slower because of the non-linearity. However, inclusion of plasticity in a robust manner is essential for certain applications such as unconsolidated fracturing, frac-packing and sand production. Bryant et al. (2015) showcased the use of this model for multi-material interfaces and showed the alteration of fracture propagation direction because of simulated

heterogeneities. A combination of plasticity and inclusion of characterized heterogeneities in the system can help in simulating shear failure and reproduce microseismic patterns observed in the field.

The fracture domain calculations can help in estimating proppant flow as shown in Lee et al. (2015). Similar procedures can allow incorporation of diverting agent (Ramakrishnan et al. 2011; Naceur and Touboul 2013) transport and hence model plugging of selective fractures during refracturing.

The simultaneous propagation of multiple fractures methodology was discussed. The same workflow can be repeated for multiple stages in a horizontal well. It can also be extended to multiple wells in the same way and help in understanding the flow distribution between fractures in multiple wells in various pad scale scenarios such as simul-fracs and zipper-fracs (Vermylen and Zoback 2011; Roussel et al. 2013; Manchanda et al. 2014).

In this work, the 3-D mesh used is structured in the region of fracture propagation. This structured nature of the mesh makes fracture twisting a difficult possibility. In order to capture 3-D fracture propagation with twisting as shown by other researchers (Rungamornrat et al. 2005; Castonguay et al. 2013) (using boundary element methods), efficient 3-D meshes can be generated and used for the current finite volume discretization schemes. Additional mode III failure criteria will need to be considered.

The intended application of the described model is in realistic pad scale fracturing scenarios. The large scale of the simulations requires the method to be efficient. Several additional efforts can be made to make the iterative scheme more numerically efficient for practical use. Some of the proposed developments are listed below:

- In the current implementation of the adaptive mesh refinement procedure the mesh is refined in the vicinity of the entire fracture. In the future implementations

of dynamic mesh refinement we propose to dynamically coarsen the mesh away from the fracture tip.

- Error driven dynamic refinement of the mesh. This will cause the regions in the mesh that do not have large error in the calculation to be unrefined and hence save computational time.
- Parallelization of the dynamic refinement framework will further increase the efficiency of the solution. Research on load-balancing between multiple parallel processors using dynamic refinement has been conducted elsewhere (Menon et al. 2015) and can be used in the current model.
- The dynamic refinement models currently only work for 2-D cases. Development of these methods for 3-D cases is essential.
- The parallelization of the numerical methods can be made more efficient by making the Input/Output (IO) methods used more efficient. Currently, the solvers run in parallel by creating individual processor domain folders and writing field calculations to files in these individual processor directories every time step. This increases the number of files written per time step and can be made more efficient using advanced IO methods (Lofstead et al. 2008).
- The parallelization of the FSI method in use is necessary to conduct large scale fracture propagation simulations.
- The FSI algorithm can be improved to have better fluid-structure coupling. The current algorithm relaxes the pressure calculations from the fluid domain and then the relaxed pressure is applied to the solid domain. An alternative method will be to relax the displacements obtained from the solid domain to define the deformation of the fluid domain. This may lead to better convergence efficiency.

- The FSI algorithm implemented in this work is 2-D and has been extended to 3-D. Verification of the 3-D FSI procedure using a PKN fracture case will be essential to ensure validity of the developed model.
- An alternate FSI algorithm is presented in Figure 4.38 to showcase the potential changes possible in the numerical algorithms. This algorithm was used for the example cases discussed in Figure 4.37. For the case with relaxation factor 0.1, this new algorithm took 285 sec to run the simulation and gave the exact same results. This suggests an increase in the simulation speed by 54%. This modified scheme is similar to having the fracture pressure being evaluated in a boundary condition for the solid domain. The fracture domain is updated and solved every time the solid domain equation matrices are solved. This tight coupling may cause divergence hence, a thorough analysis of this scheme is essential. Further testing of such methods will ensure the development of a stable and efficient scheme.
- The adaptive FSI relaxation method used can also be further developed to increase the numerical efficiency of the code. Mathematical analysis of the relaxation schemes can enable the incorporation of better adaptive relaxation schemes that can make the numerical simulator more efficient (Degroote et al. 2009, 2010).

In the next chapter we apply the model developed here to several realistic field scale scenarios to understand the impact of various operational variables on the propagation and fluid distribution between multiple fractures.

4.7 NOMENCLATURE

α	= Biot's coefficient of effective stress	dimensionless
α_d	= damage factor for perforation press drop	dimensionless
c_f	= fracture fluid compressibility	$M^{-1}LT^{-2}$, Pa^{-1}
C_L	= leak-off coefficient	$LT^{-1/2}$, $m/s^{1/2}$
$\boldsymbol{\varepsilon}$	= solid matrix elastic strain	dimensionless
ε_V	= trace of the strain tensor	dimensionless
E	= Young's modulus	$ML^{-1}T^2$, Pa
$\acute{E}$	= Plane strain Young's modulus	$ML^{-1}T^2$, Pa
$\mathbf{f}$	= force vector	MLT^{-2}, N
G	= shear modulus of rock	$ML^{-1}T^2$, Pa
ϕ	= porosity	dimensionless
ϕ_{frac}	= fracture porosity	dimensionless
$\phi_{propped}$	= propped fracture porosity	dimensionless
h_f	= fracture half-height	L, m
H_f	= fracture height	L, m
k	= permeability	L^2, m^2
k_{SRV}	= permeability of SRV region	L^2, m^2
$\mathbf{k}$	= permeability tensor	L^2, m^2
K	= macroscopic bulk modulus	$ML^{-1}T^2$, Pa
K_f	= fluid bulk modulus	$ML^{-1}T^2$, Pa
K_s	= solid bulk modulus	$ML^{-1}T^2$, Pa
λ	= Lame's parameter	$ML^{-1}T^2$, Pa
l_f	= fracture half-length	L, m
L_f	= fracture length	L, m
$\mathbf{n}$	= normal vector	dimensionless
n_{perfs}	= number of perforations	dimensionless
μ	= fluid viscosity	$ML^{-1}T$, Pa.s
μ_{fluid}	= frac fluid viscosity	$ML^{-1}T$, Pa.s
M	= Biot's modulus	$ML^{-1}T^2$, Pa
υ	= Poisson's ratio	dimensionless
p	= pressure field	$ML^{-1}T^2$, Pa
p_{frac}	= fracture pressure field	$ML^{-1}T^2$, Pa
p_{net}	= fracture net pressure	$ML^{-1}T^2$, Pa
P_i	= pressure in the i^{th} fracture	$ML^{-1}T^2$, Pa
P_w	= wellbore pressure	$ML^{-1}T^2$, Pa
P_w^o	= old wellbore pressure	$ML^{-1}T^2$, Pa
$\mathbf{q}$	= fluid flux	LT^{-1}, m/s
q_i	= flow per fracture	L^3T^{-1}, m^3/s
$q_{L,i}$	= leak-off rate from each fracture	L^3T^{-1}, m^3/s
$q_{V,i}$	= volume change rate for each fracture	L^3T^{-1}, m^3/s
Q_{in}	= volumetric flowrate into a well	L^3T^{-1}, m^3/s

Q_{out}	= volumetric flowrate out of a well	L^3T^{-1}, m^3/s
ρ	= bulk density	ML^{-3}, kg/m^3
$\rho_{proppant}$	= density of proppant	ML^{-3}, kg/m^3
$\bar{\rho}$	= average slurry density	ML^{-3}, kg/m^3
r_i	= perforation radius	L, m
$\boldsymbol{\sigma}$	= effective stress tensor	$ML^{-1}T^2$, Pa
σ_{xx}	= stress in x direction	$ML^{-1}T^2$, psi
σ_{yy}	= stress in y direction	$ML^{-1}T^2$, psi
t	= time	T, sec
$\mathbf{T}$	= traction vector	MLT^{-2}, N
$\mathbf{u}$	= displacement vector field	L, m
V_f	= fracture volume	L^3, m^3
$V_{fracFluid}$	= volume of fluid in fracture	L^3, m^3
V_i^c	= current fracture volume	L^3, m^3
V_i^0	= initial fracture volume	L^3, m^3
$V_{leakOff}$	= volume of fluid leaking off from fracture	L^3, m^3
V_w	= volume of wellbore	L^3, m^3
w	= fracture width field	L, m
w_t	= maximum fracture width at time t	L, m
$w_{propped}$	= maximum propped width of fracture	L, m
ξ	= dimensionless distance from fracture	dimensionless
x_f	= fracture half-length	L, m
ζ	= pore fluid content	dimensionless

Young's modulus (E)	5 MMpsi
Poisson's ratio (ν)	0.2
Crack radius (h_f)	100 ft
P_{net}	2000 psi
S_{hmin}	10000 psi
S_{hmax}	11000 psi
S_v	15000 psi

Table 4.1 Parameter values used to simulate penny shaped fracture stress shadow verification test case (elastic model was used).

Young's modulus (E)	1 GPa
Poisson's ratio (ν)	0.2
Permeability (k)	1.5e-14 m^2
Viscosity (μ)	0.001 Pa.s
Biot's coefficient (α)	0.6
Porosity (ϕ)	0.2
Fluid Bulk Modulus (K_f)	2.3 GPa
Top load (p_z)	1e5 Pa

Table 4.2 Parameter values used to simulate the consolidation problem (poro-elastic model was used).

Domain size	20 m X 32 m
S_{hmax}	12 MPa
S_{hmin}	8 MPa
Young's modulus	60 GPa
Poisson's ratio	0.25
Injection rate	1.25e-5 m_3/m/s
Critical tensile normal stress	0 MPa
Mode I energy release rate	1e-6 Pa.m

Table 4.3 Parameter values used to simulate KGD fracture propagation (elastic model was used) (Lee et al. 2015).

```
fvVectorMatrix UEqn
(
    rho*fvm::d2dt2(U)
 == fvm::laplacian(twoMuLambdaf, U, "laplacian(DU,U)")
  + fvc::div
    (
        (
            mesh.Sf() &
            (
                - (muf + lambdaf)*gradUf
                + muf*gradUf.T() + lambdaf*(I*tr(gradUf))
                + sigma0f
            )
        ) - biotf*pf*mesh.Sf()
    )
);
```

Figure 4.1 Example partial differential equation input for OpenFOAM

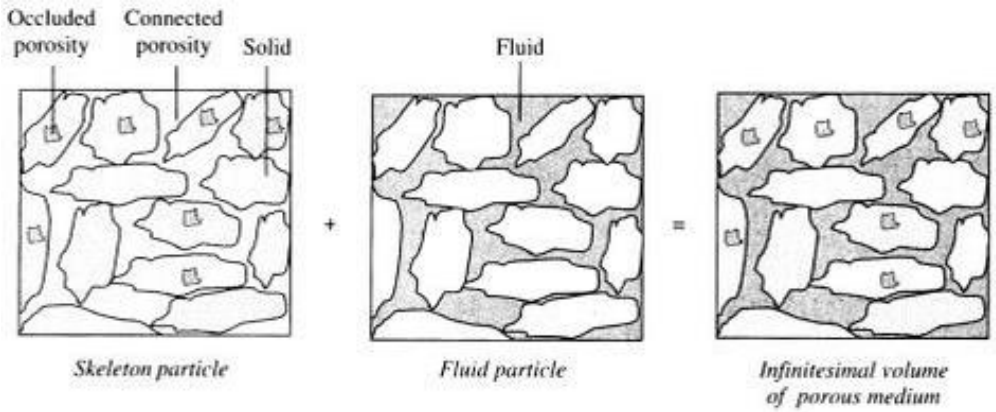

Figure 4.2 Representation of porous media with a solid skeleton and fluid in the pore space (Coussy 2004).

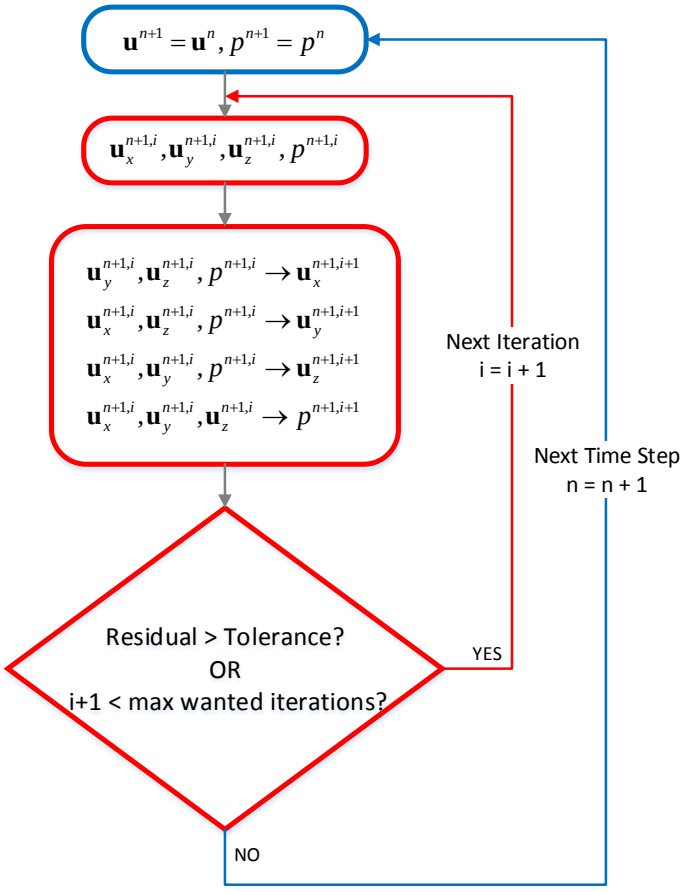

Figure 4.3 Segregated solution procedure to solve the displacement and pressure equations.

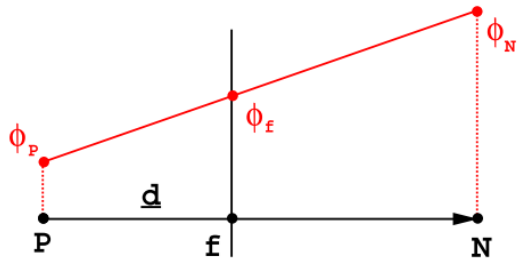

Figure 4.4 Face interpolation (Jasak 1996)

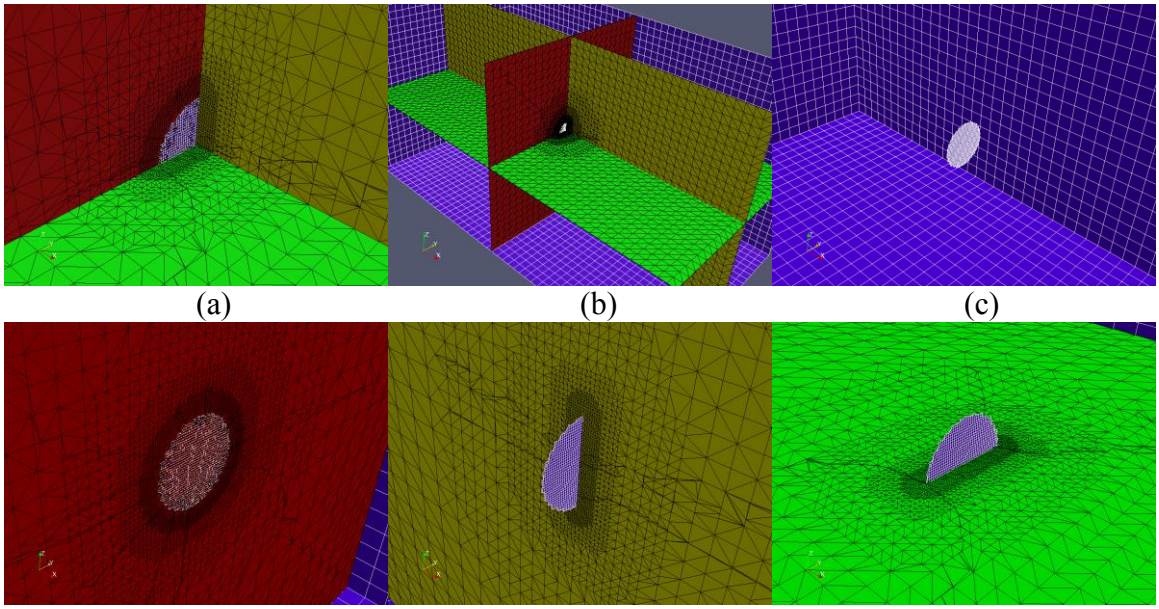

Figure 4.5 Meshing of a penny-shaped fracture in the YZ plane and centered at origin (a) Close-in view of a quarter penny-shaped fracture with X, Y and Z planes passing through the origin for reference, (b) Zoomed out view of (a), (c) The penny-shaped fracture in the reservoir domain, (d) X=0 plane view, (e) Y=0 plane view, (f) Z=0 plane view.

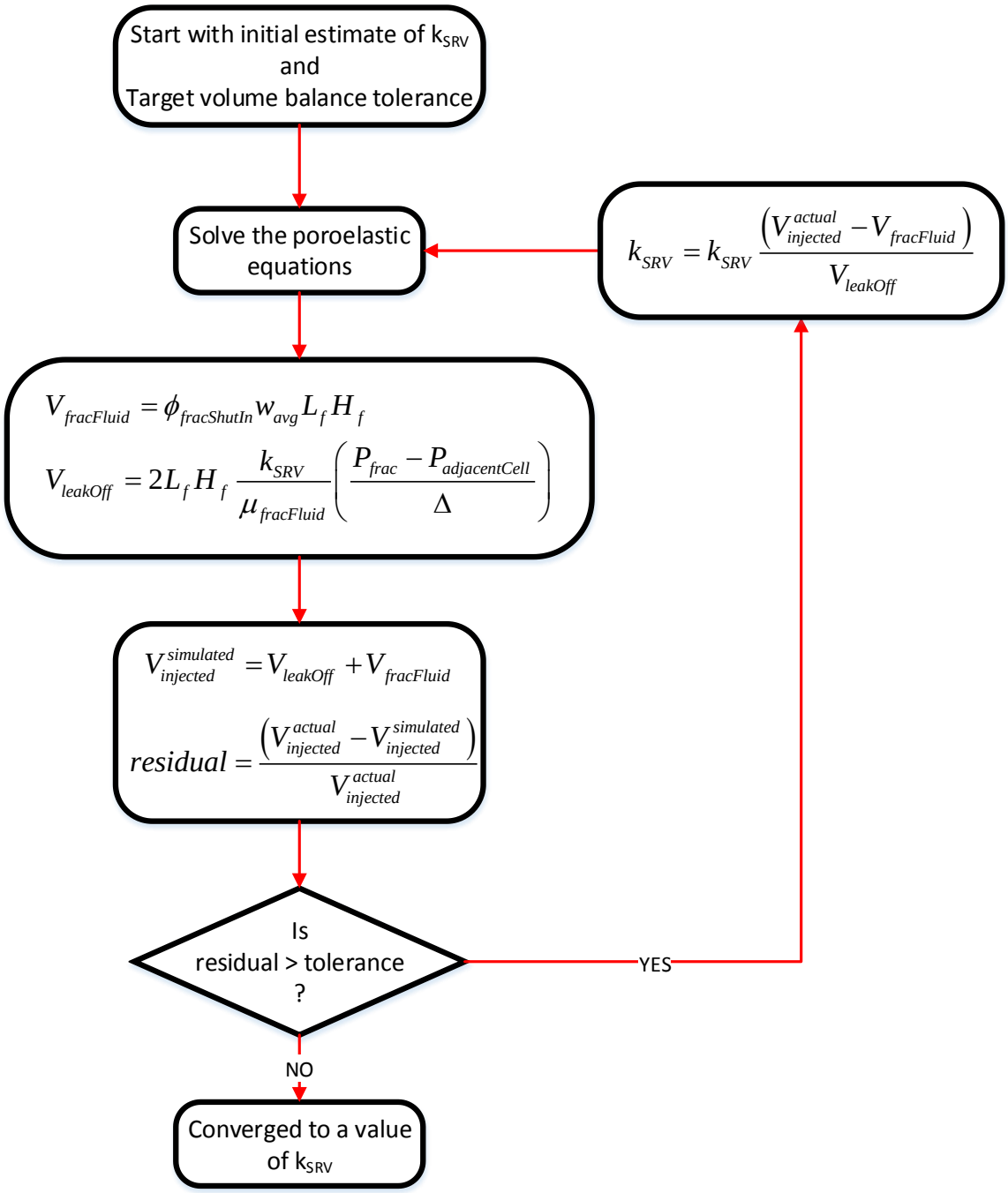

Figure 4.6 Algorithm for estimation of stimulated rock volume permeability

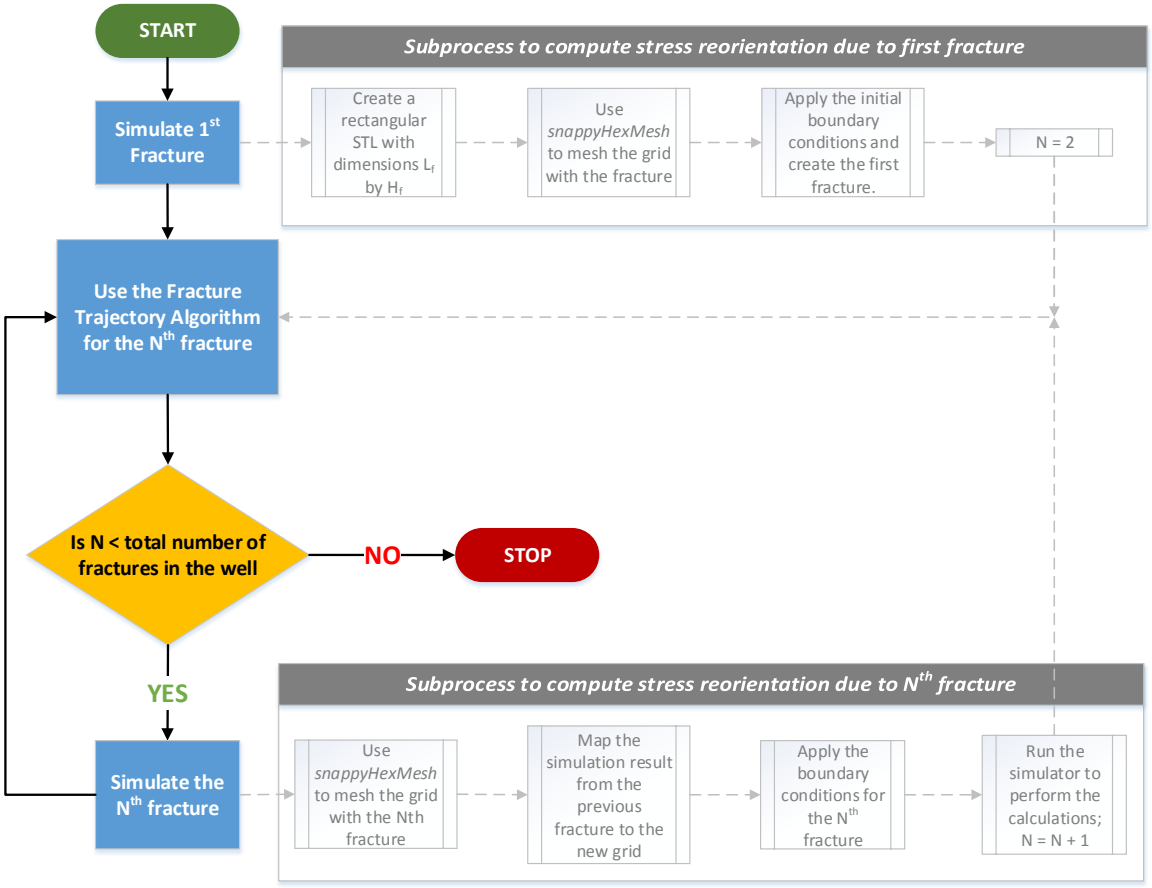

Figure 4.7 Flow diagram describing the process of simulating multiple successive fractures in the same well.

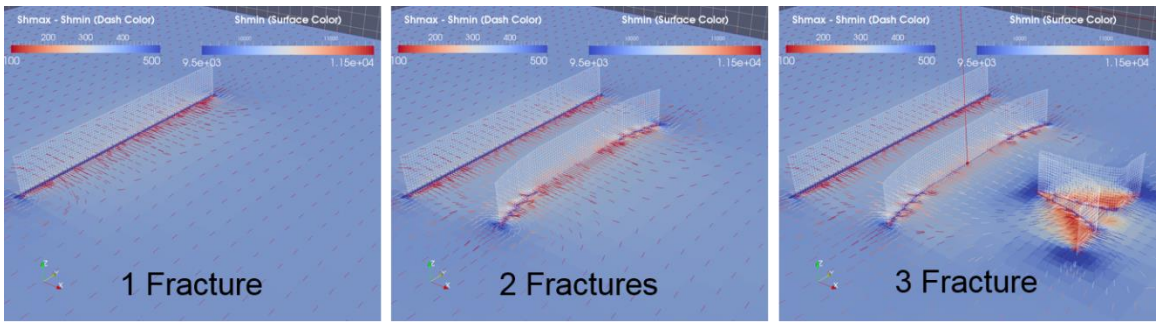

Figure 4.8 Implementation of flow diagram shown in Figure 4.7 to create multiple fractures sequentially in a horizontal well.

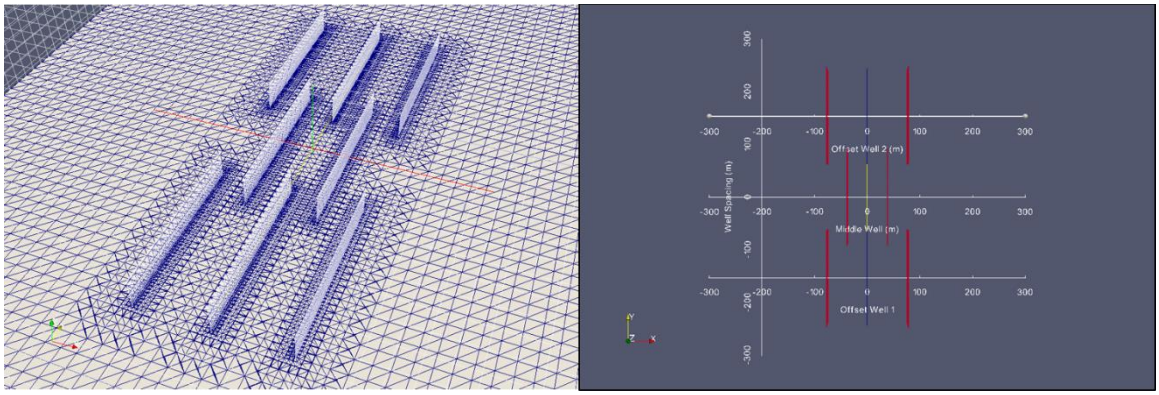

Figure 4.9 Simulating multiple transverse fractures in multiple horizontal wells. Transverse fractures in multiple wells are shown in (a) the reservoir grid, (b) plan view.

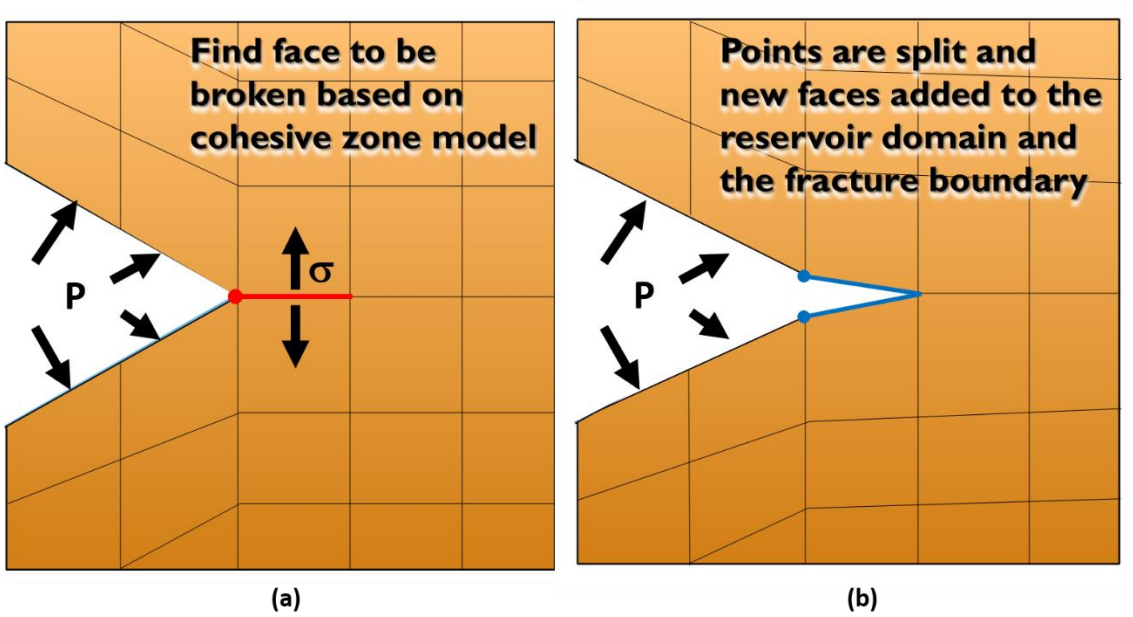

Figure 4.10 Schematic showing the procedure for adding new faces to the fracture boundary.

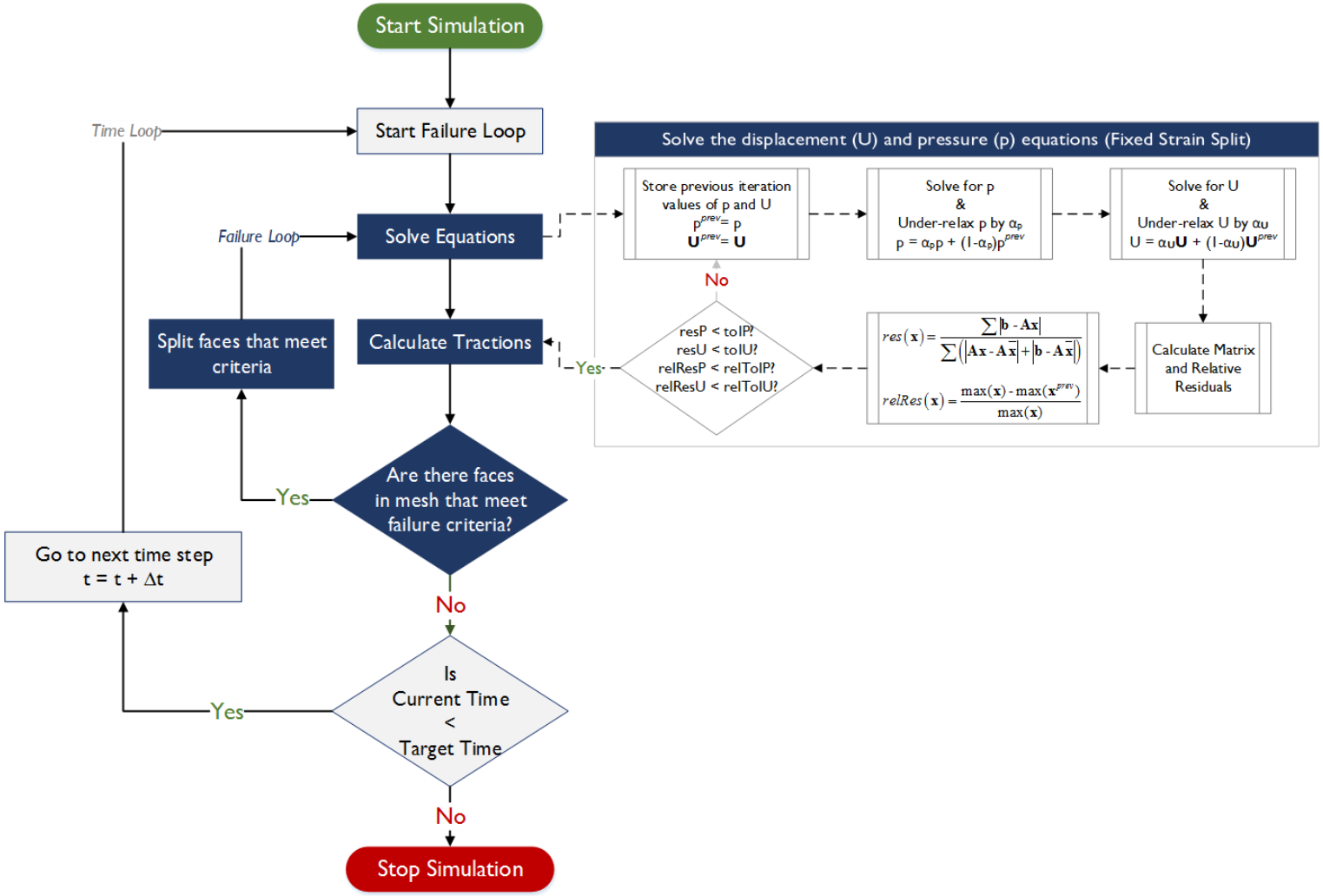

Figure 4.11 Algorithm to simulate fracture propagation with uniform pressure inside each fracture.

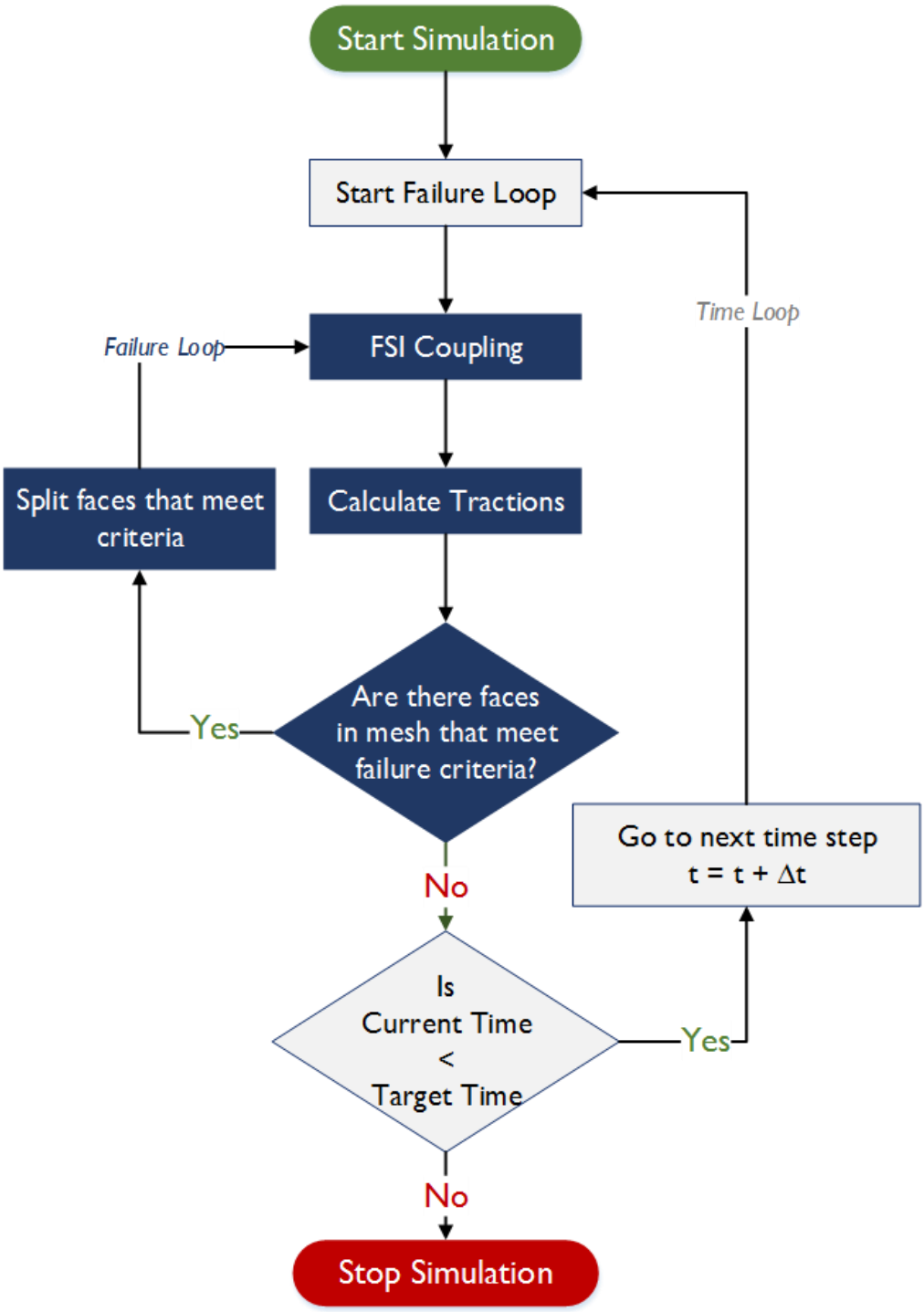

Figure 4.12 Algorithm to simulate fracture propagation with spatially varying pressure inside each fracture.

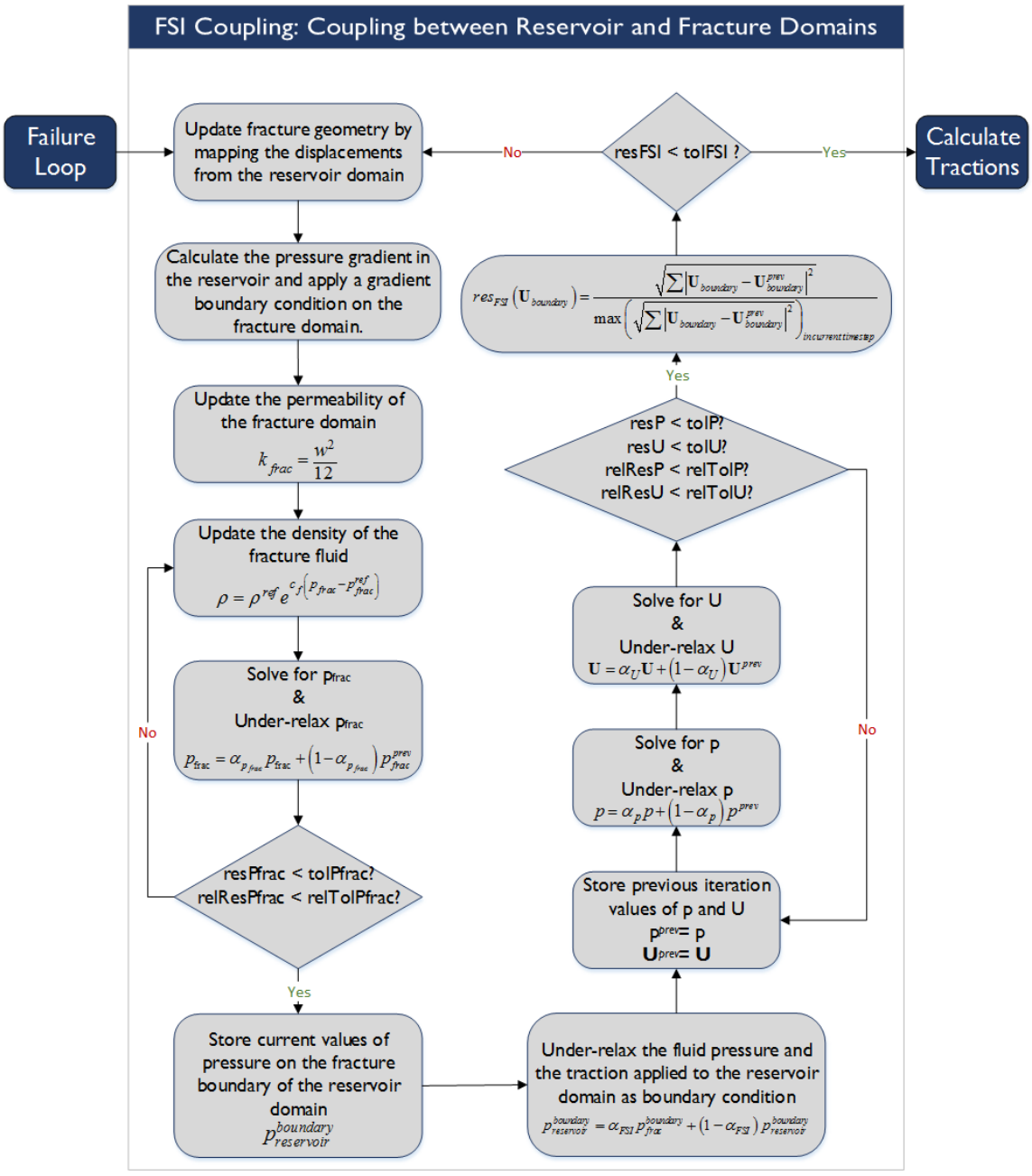

Figure 4.13 Algorithm for the FSI coupling. This algorithm replaces the block named "FSI coupling" in Figure 4.12.

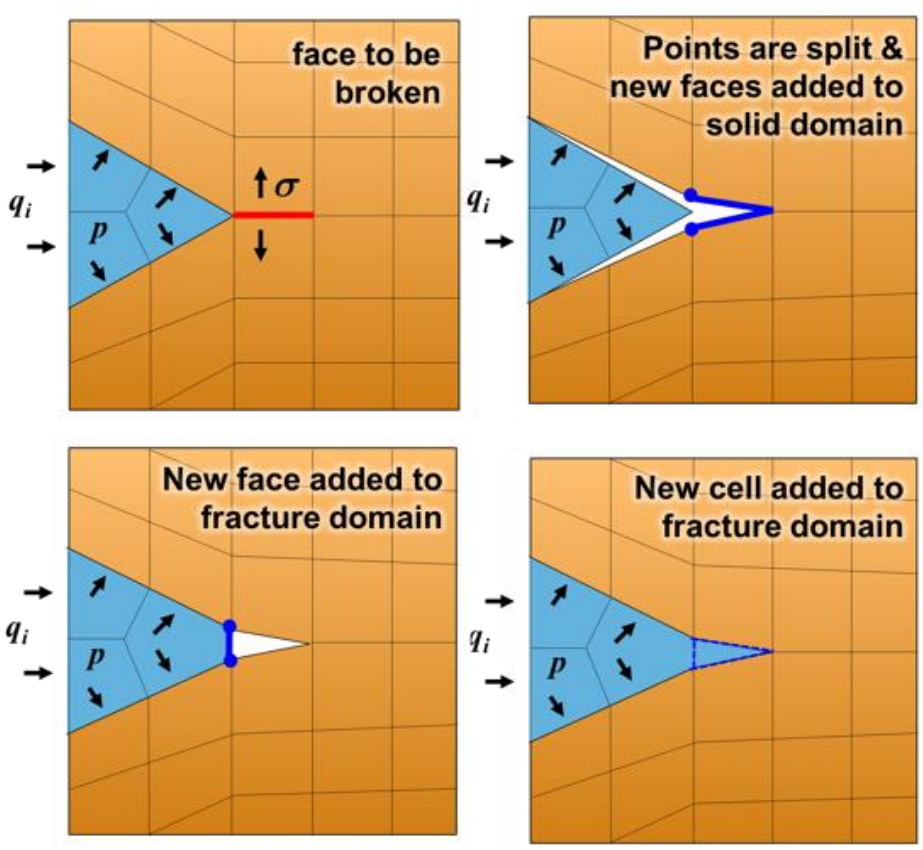

Figure 4.14 Schematic illustrating the extension of the fracture domain

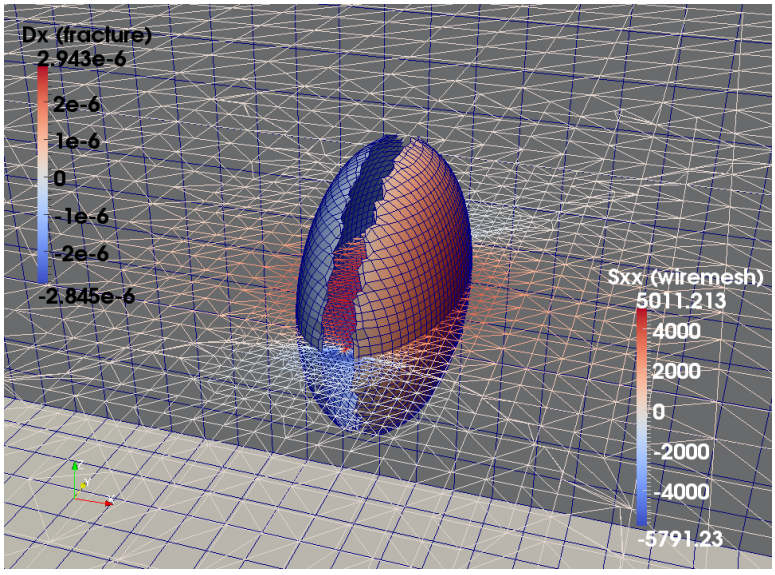

Figure 4.15 Opening of a penny shaped fracture.

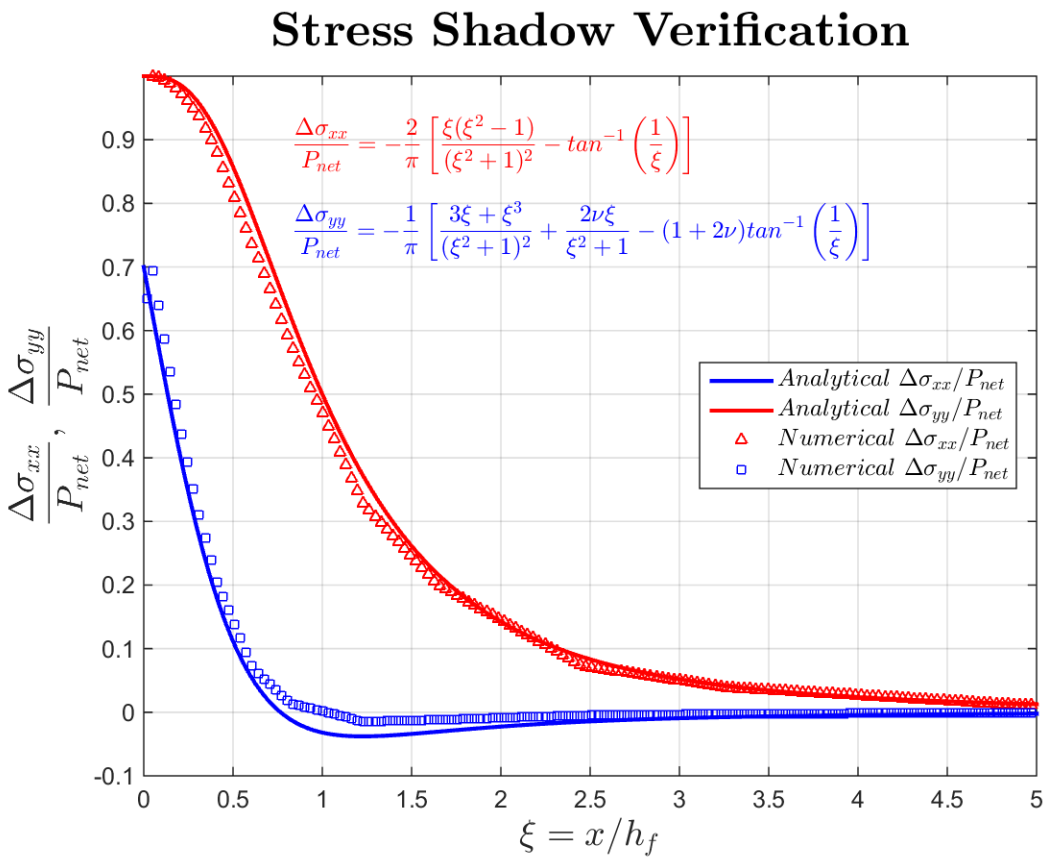

Figure 4.16 Comparison of analytical and numerical additional stresses along a normal (y=z=0) to a penny-shaped fracture.

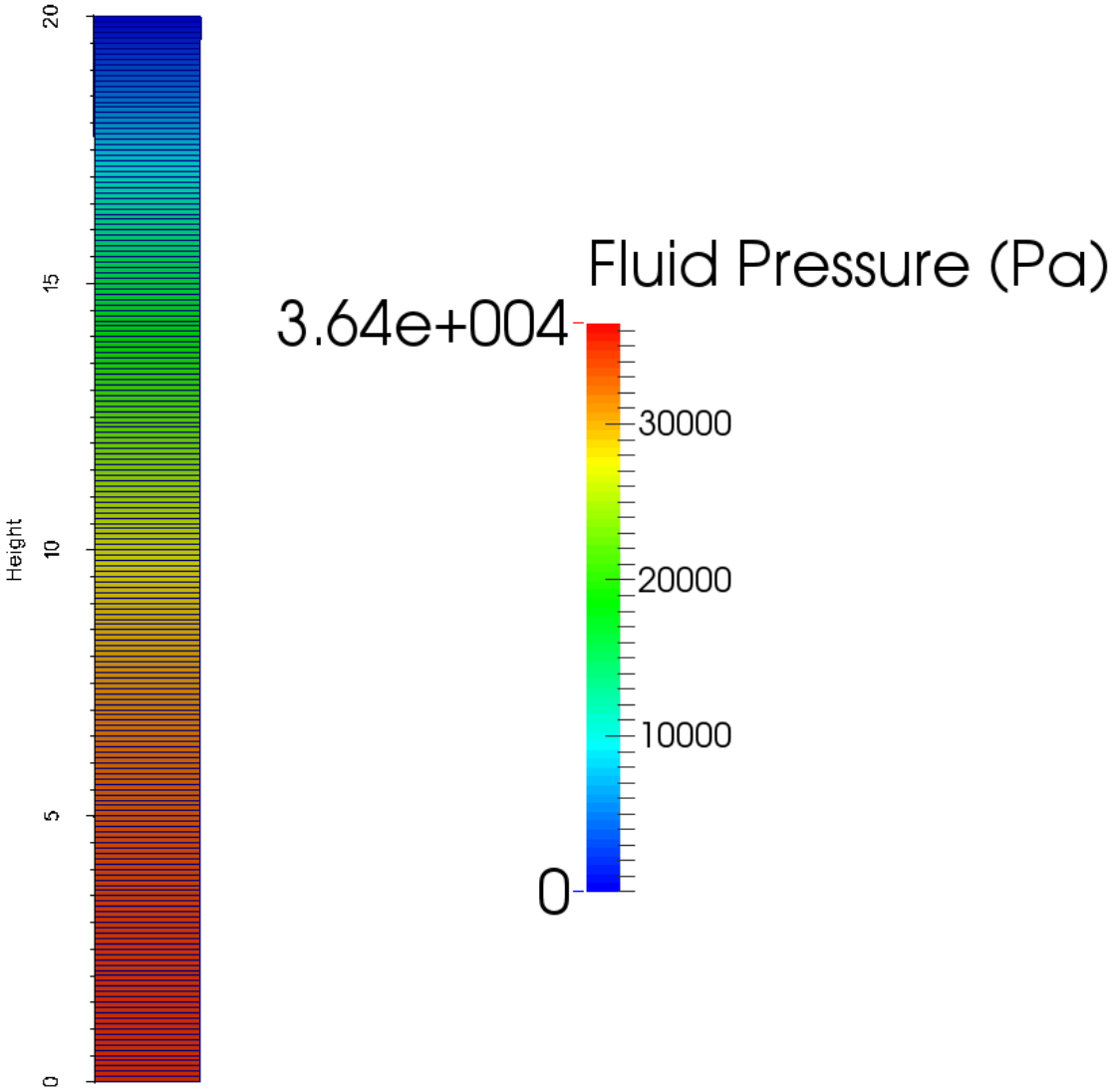

Figure 4.17 Schematic of the grid used to solve the 1D consolidation problem. The grid has been scaled 20 times it's original dimension in the X and Y directions.

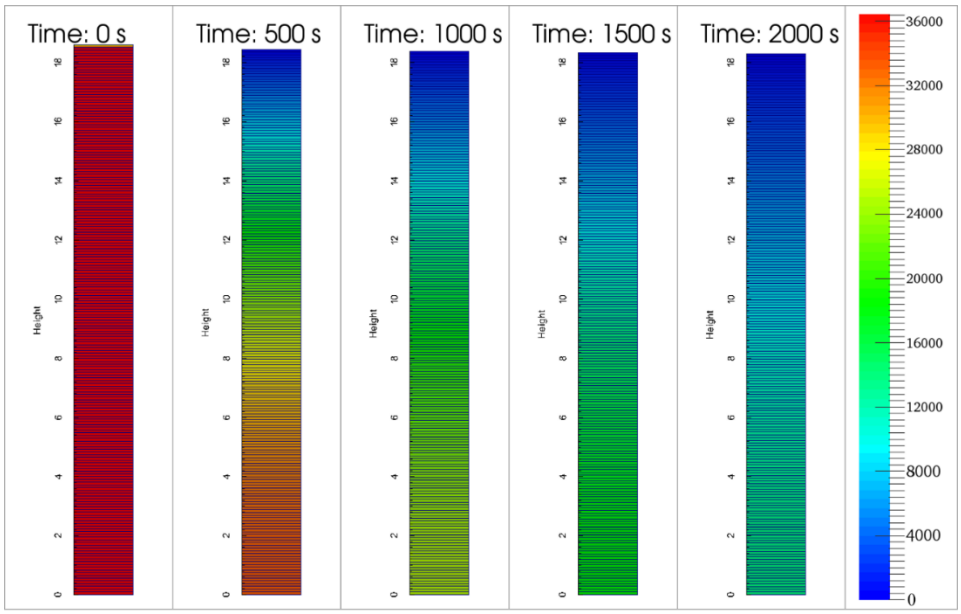

Figure 4.18 Pore pressure contours for the consolidation verification case at various times. Each grid has been transformed by a 20 x 20 x 1 scale in the x, y, z and the displacement vector has been scaled by 10^4 for better visualization.

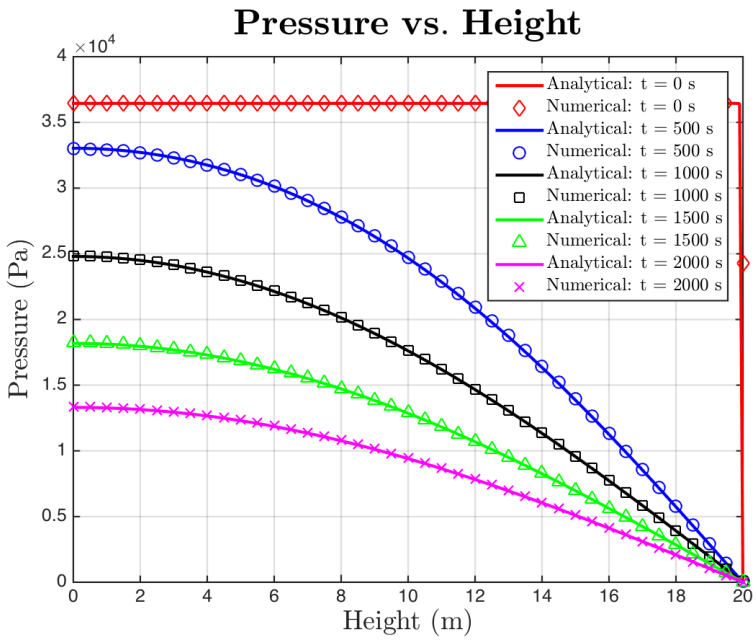

Figure 4.19 Comparison between analytical and numerical 1D consolidation solutions. Pressure vs. Height.

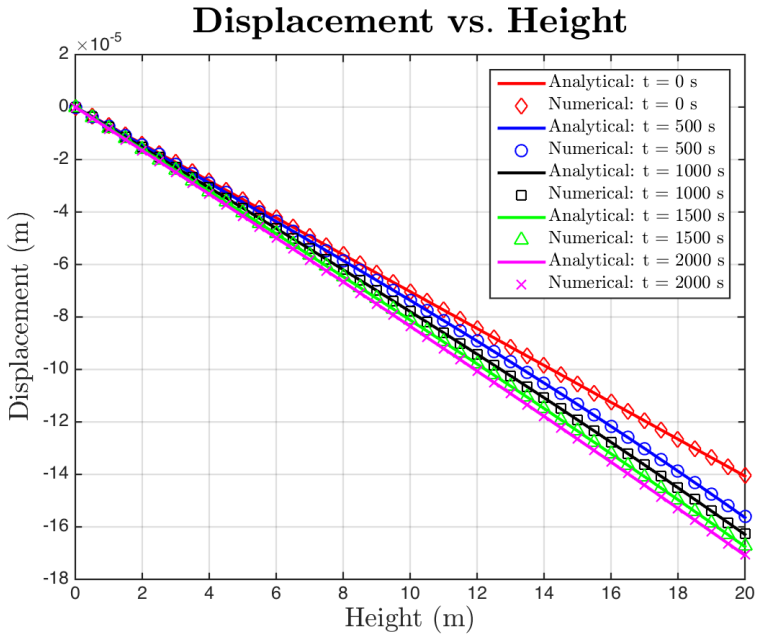

Figure 4.20 Comparison between analytical and numerical 1D consolidation solutions. Displacement vs. Height.

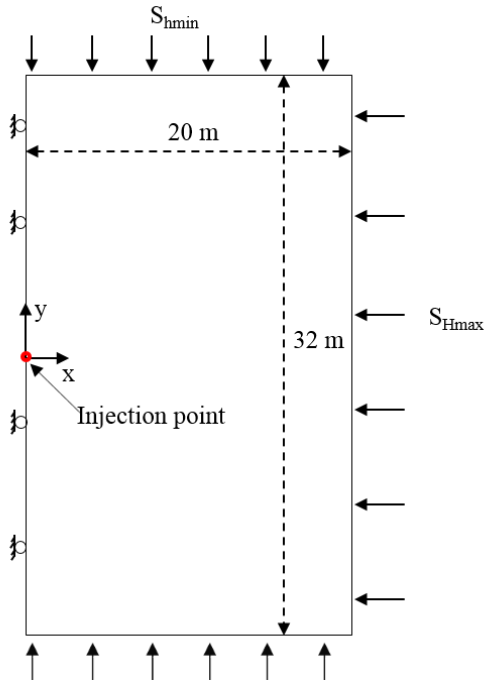

Figure 4.21 Schematic of the 2-D computation domain used for validating single 2-D fracture propagation (Lee et al. 2015).

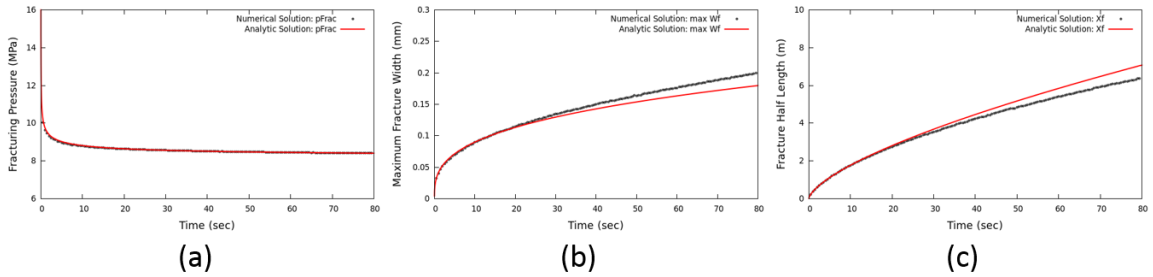

Figure 4.22 Comparison of numerical and analytical results for single fracture propagation (Lee et al. 2015).

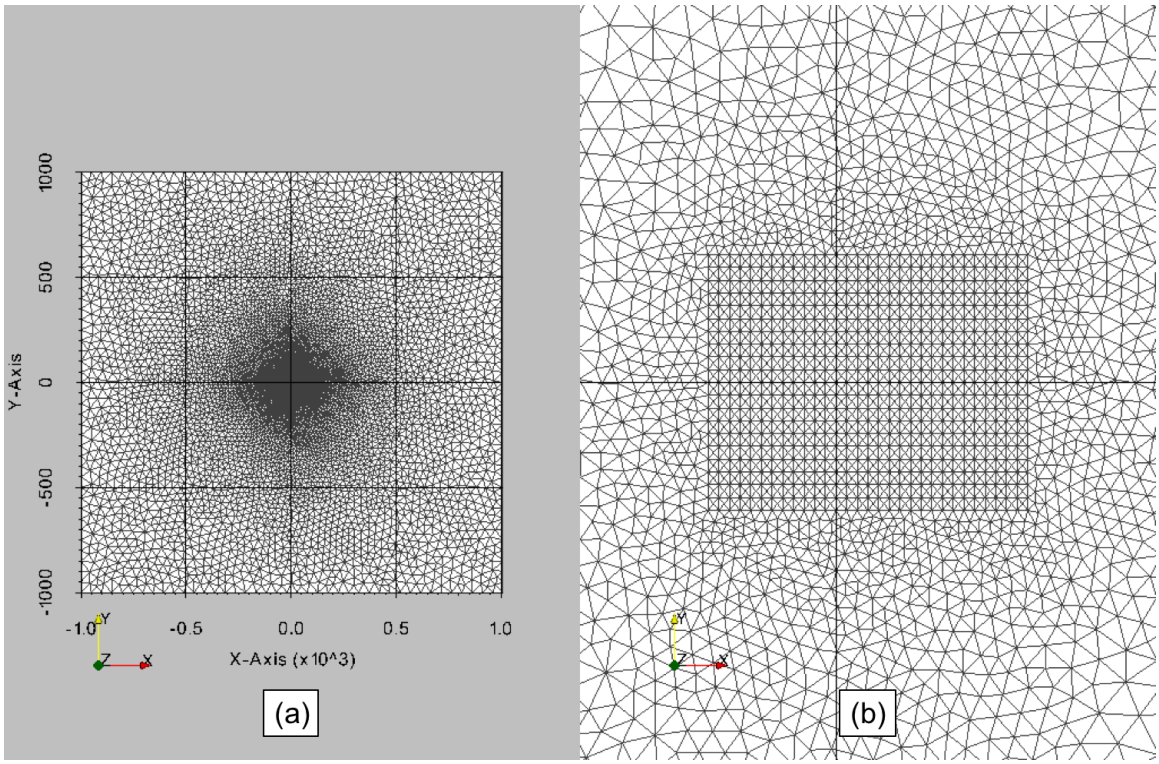

Figure 4.23 Top view of the mesh used to test for the mesh sensitivity. (a) entire mesh, (b) close-up look at the center refined region of the mesh.

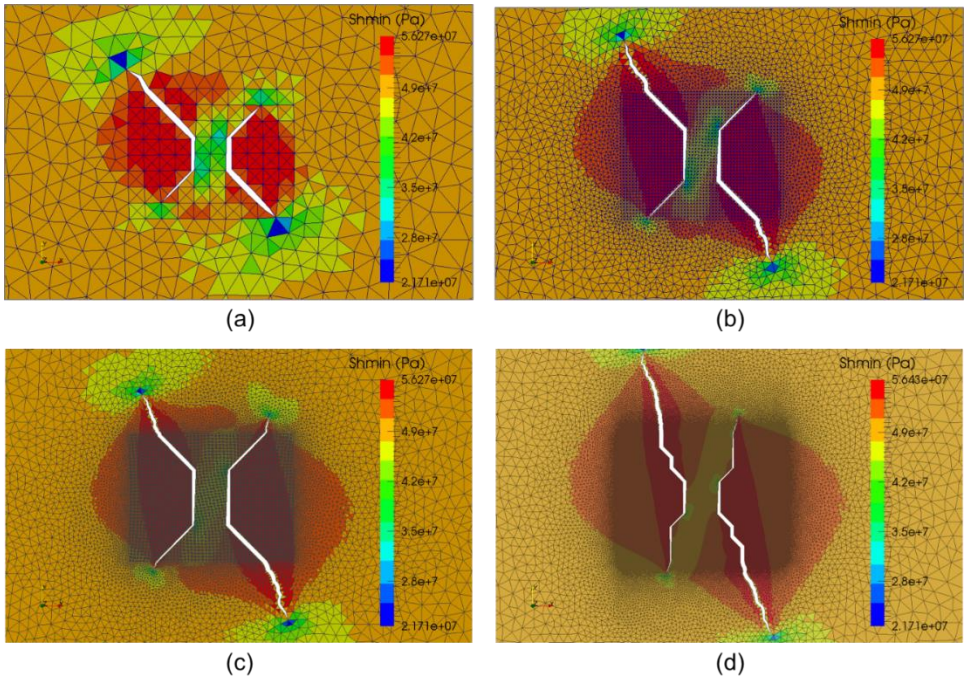

Figure 4.24 Mesh sensitivity analysis. Refinement region in the mesh has squares of side length (a) 5 m, (b) 1 m, (c) 0.5 m, and (d) 0.1 m.

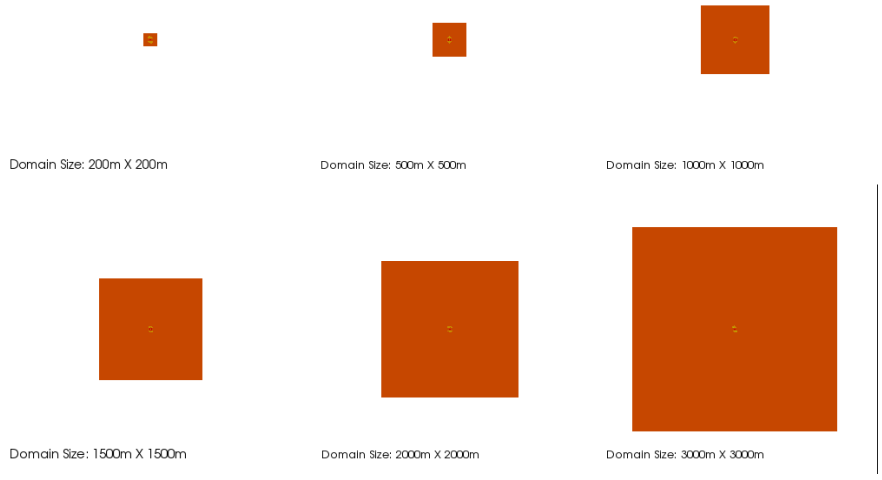

Figure 4.25 Simulations conducted on domains of various sizes to capture the impact of number of cells in the mesh on simulation speed.

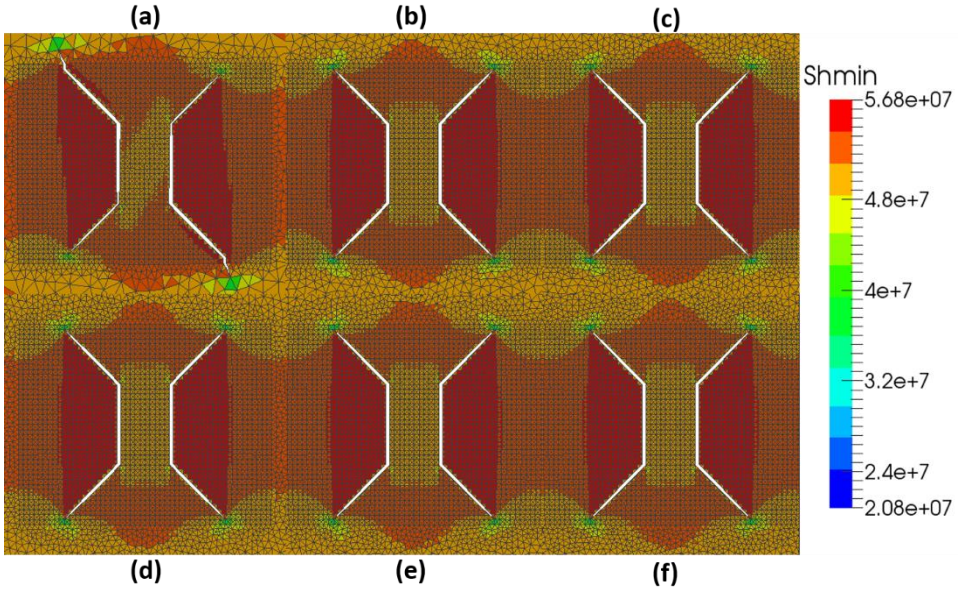

Figure 4.26 Fracture propagation for the different domain sizes (a) 200m X 200m, (b) 500m X 500m, (c) 1000m X 1000m, (d) 1500m X 1500m, (e) 2000m X 2000m and (f) 3000m X 3000m. Contour colors depict the minimum principal stress value.

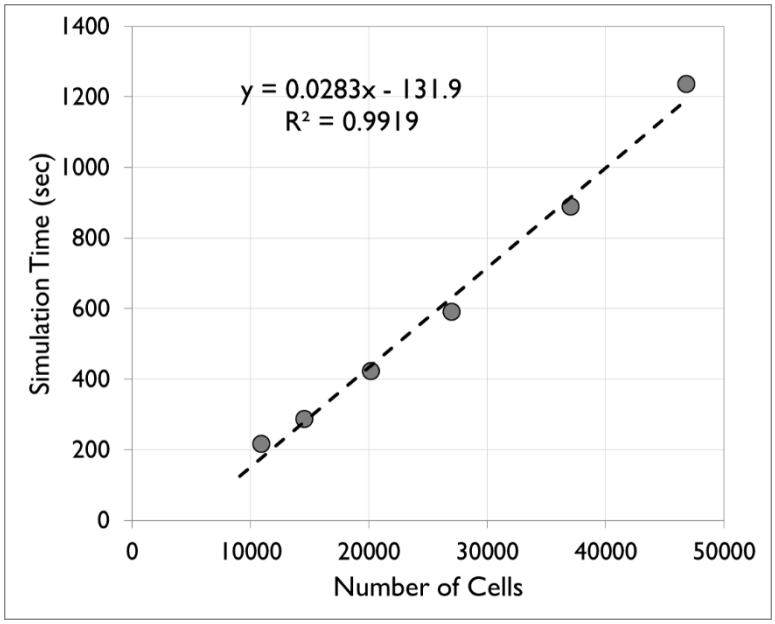

Figure 4.27 Comparison of simulation speed for similar cases run with varying number of cells in the mesh.

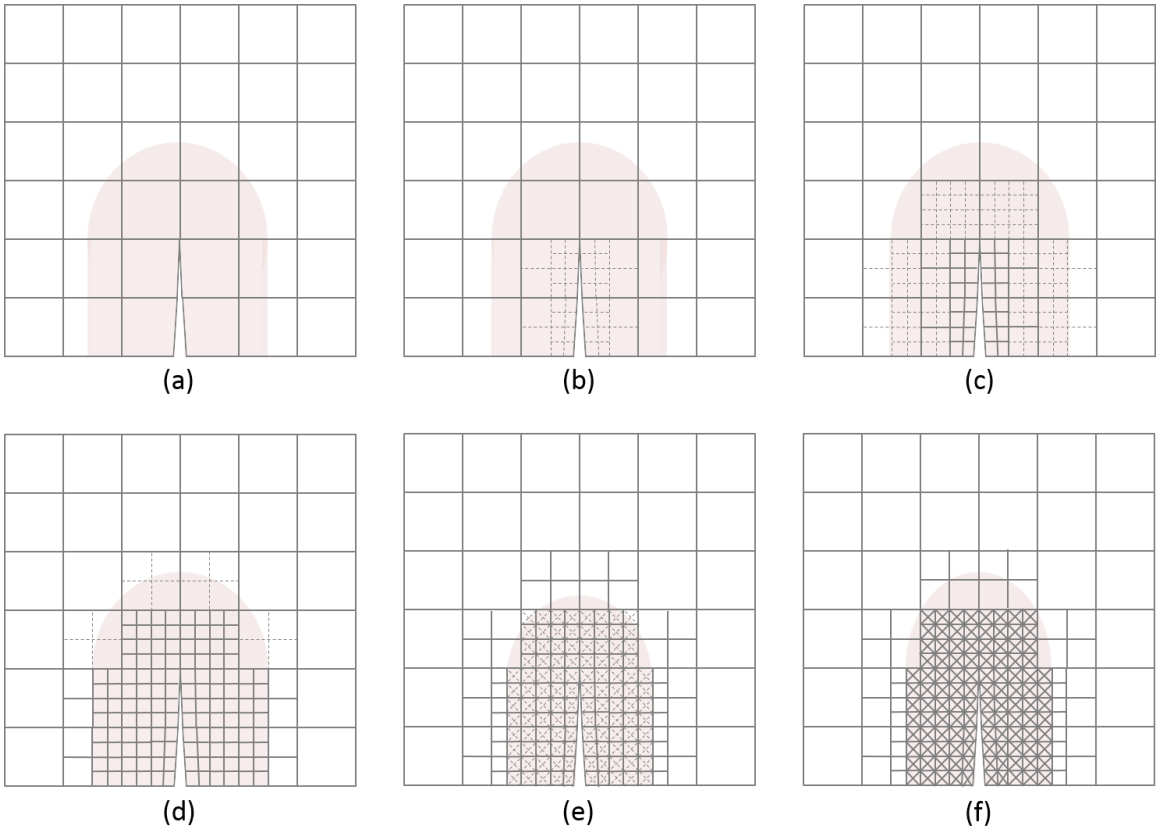

Figure 4.28 Schematic showing the steps involved in the adaptive mesh refinement algorithm. (a) specify target refinement region and find all cells in the refinement region, (b) refine the cells adjacent to the fracture, (c) refine all the cells within the target refinement region, (d) refine generated polyhedral cells with more than 8 faces, (e) make diagonal cuts in the refinement region, and (f) final mesh on which computations are performed.

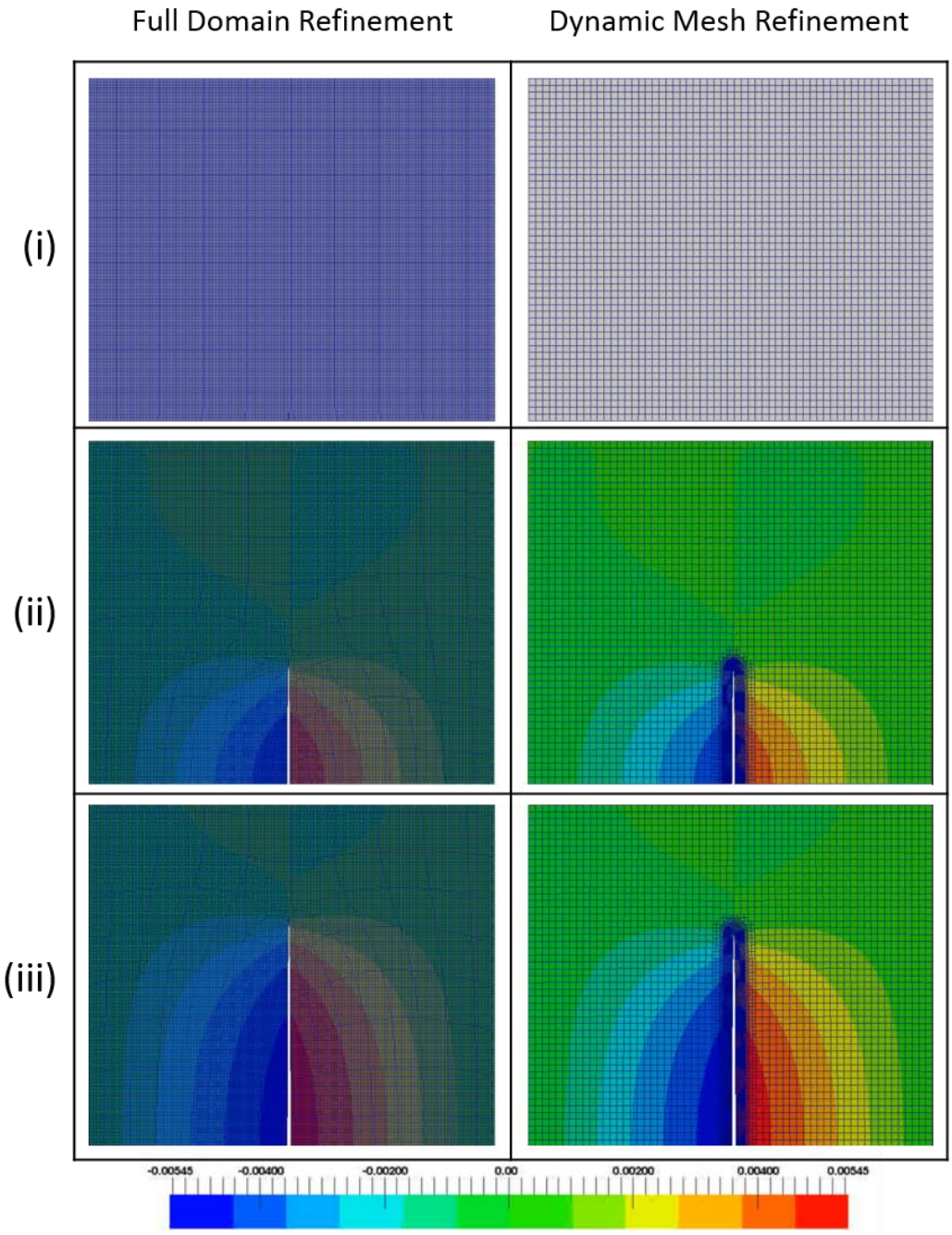

Figure 4.29 Impact of dynamic mesh refinement on results. Uniformly gridded fine mesh (left column) vs. uniformly gridded coarse mesh with dynamic refinement (right column). (i), (ii), (iii) (in that order) represent increasing time. The colors represent the induced X direction displacement.

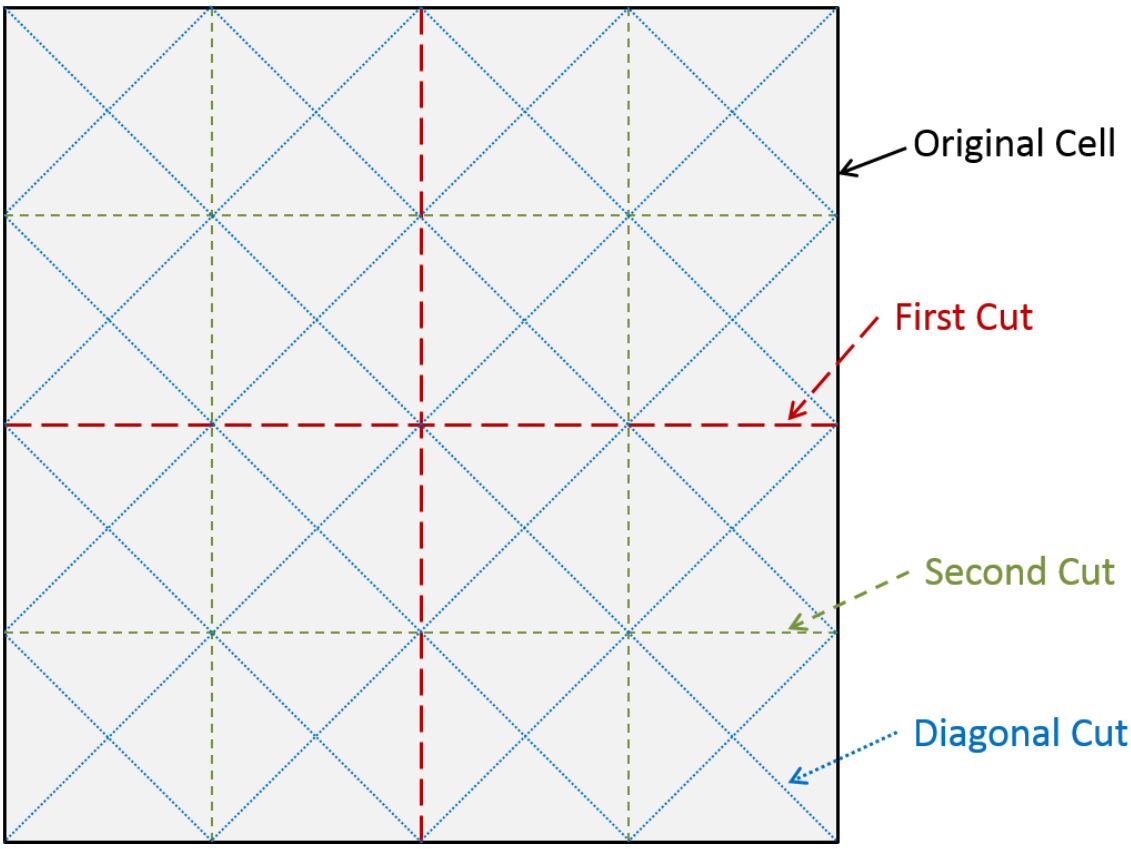

Figure 4.30 Schematic showing the order of cuts for a coarse cell in the vicinity of the fracture.

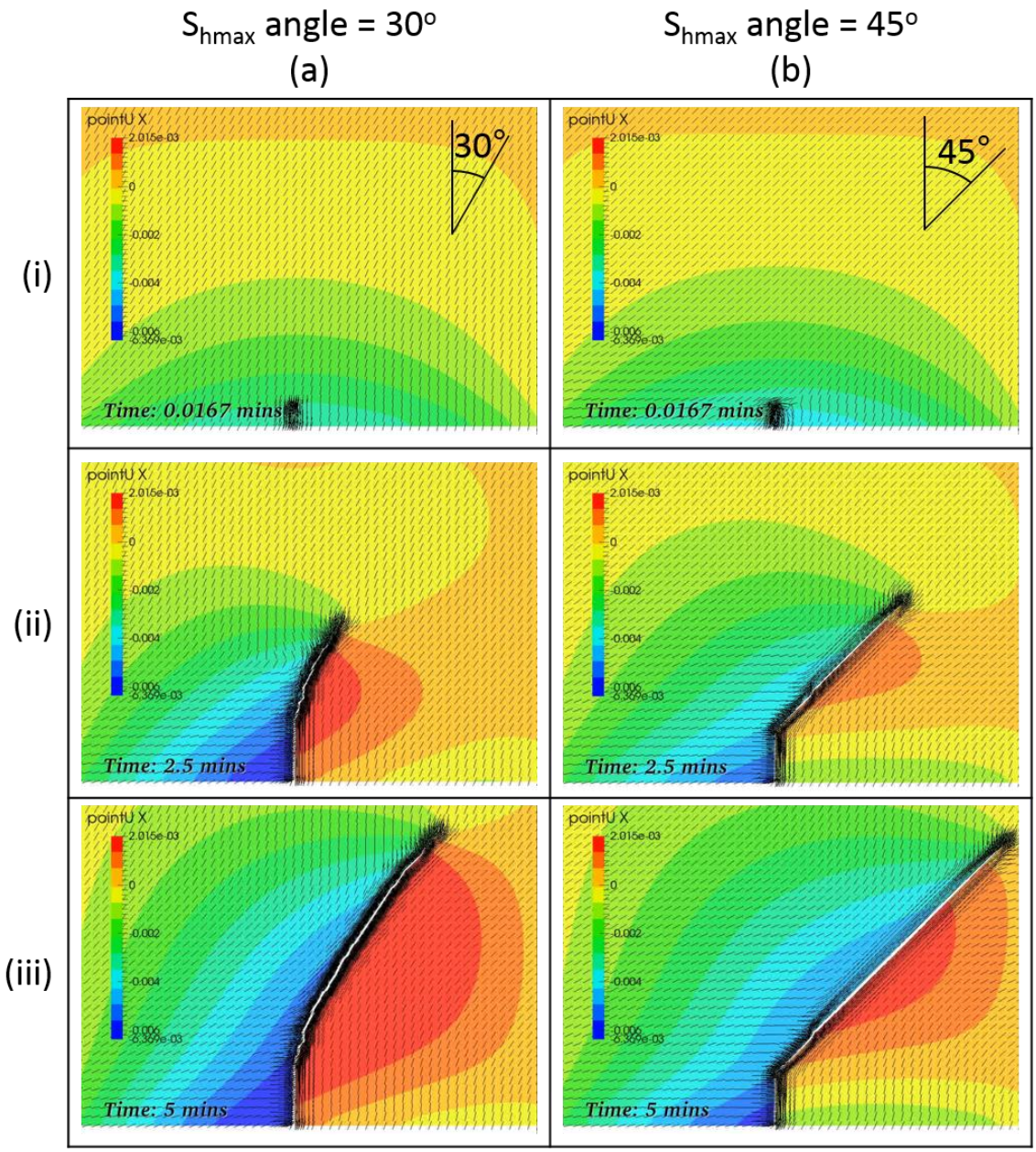

Figure 4.31 Fracture turning induced by a rotation of *in-situ* stress directions. The rows represents results at the (i) beginning, (ii) middle, and (iii) end of the simulation. The colors represent the induced X direction displacement. The dashes in the figures depict the S_{hmax} direction.

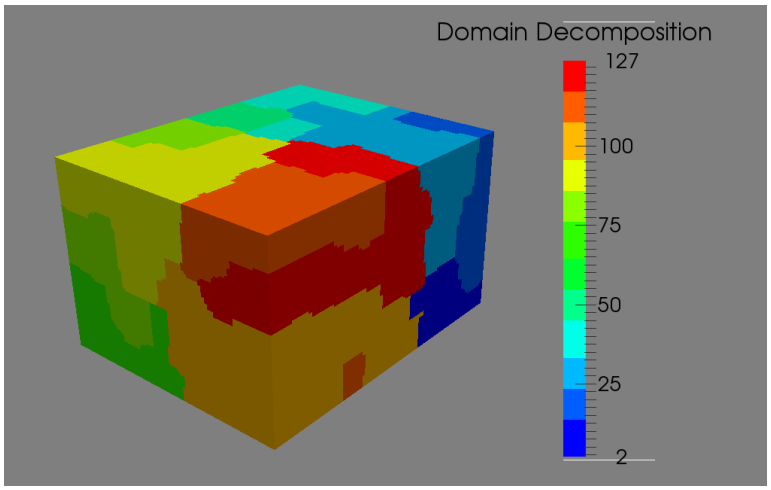

Figure 4.32 Example domain decomposition using metis algorithm. This mesh is decomposed into 128 domains.

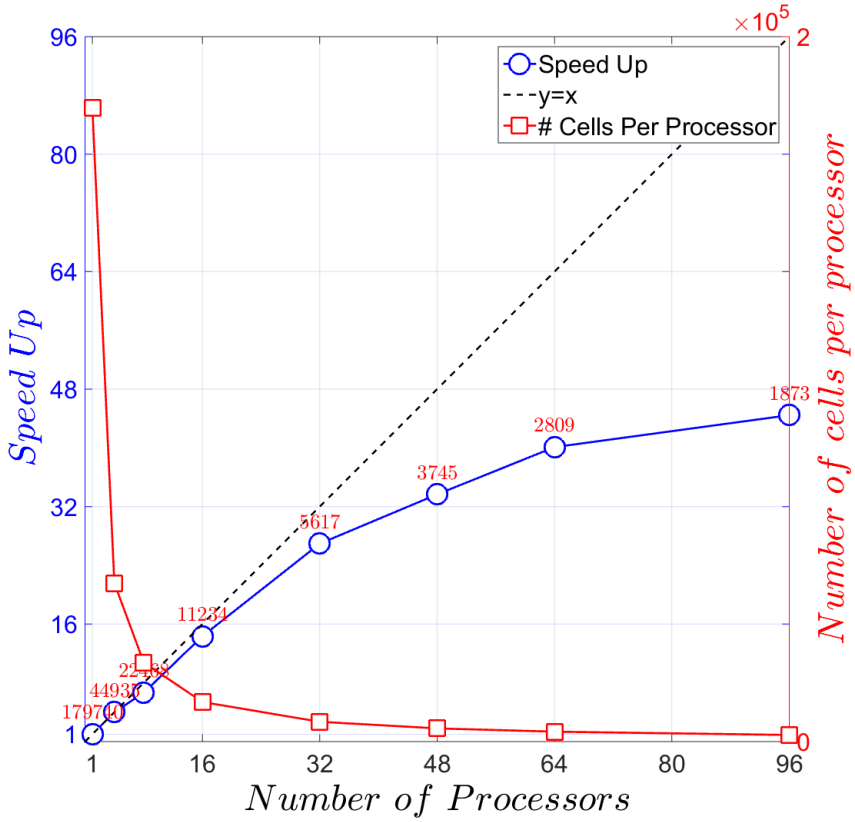

Figure 4.33 Parallelization speed up. The numbers on the speed-up curve represent the average number of cells per processor.

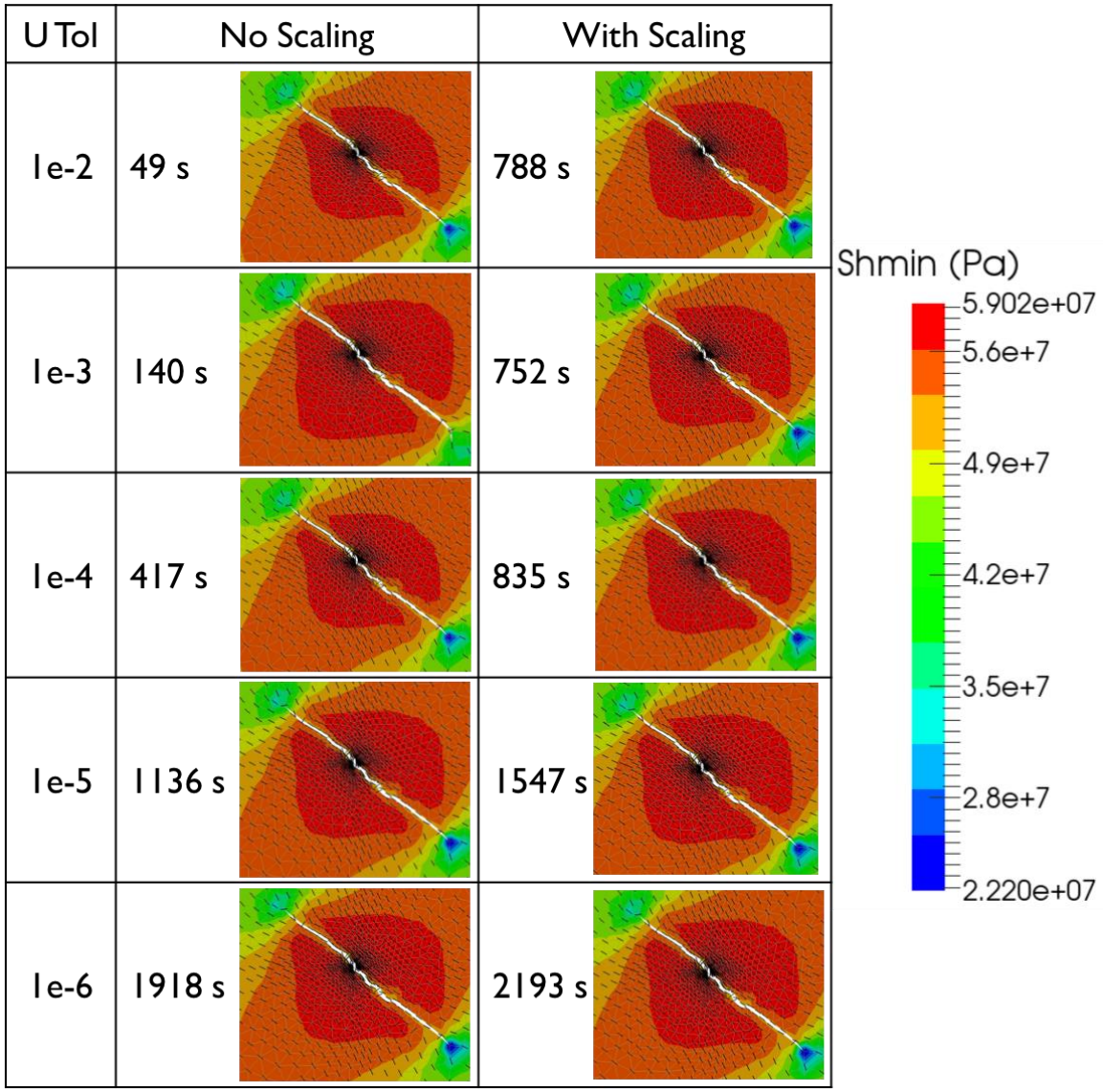

Figure 4.34 Impact of displacement tolerance for a low relaxation factor for the displacement variable with (right column) and without (left column) scaling for the relative tolerance for displacement. The relaxation factor used in these results is 0.01.

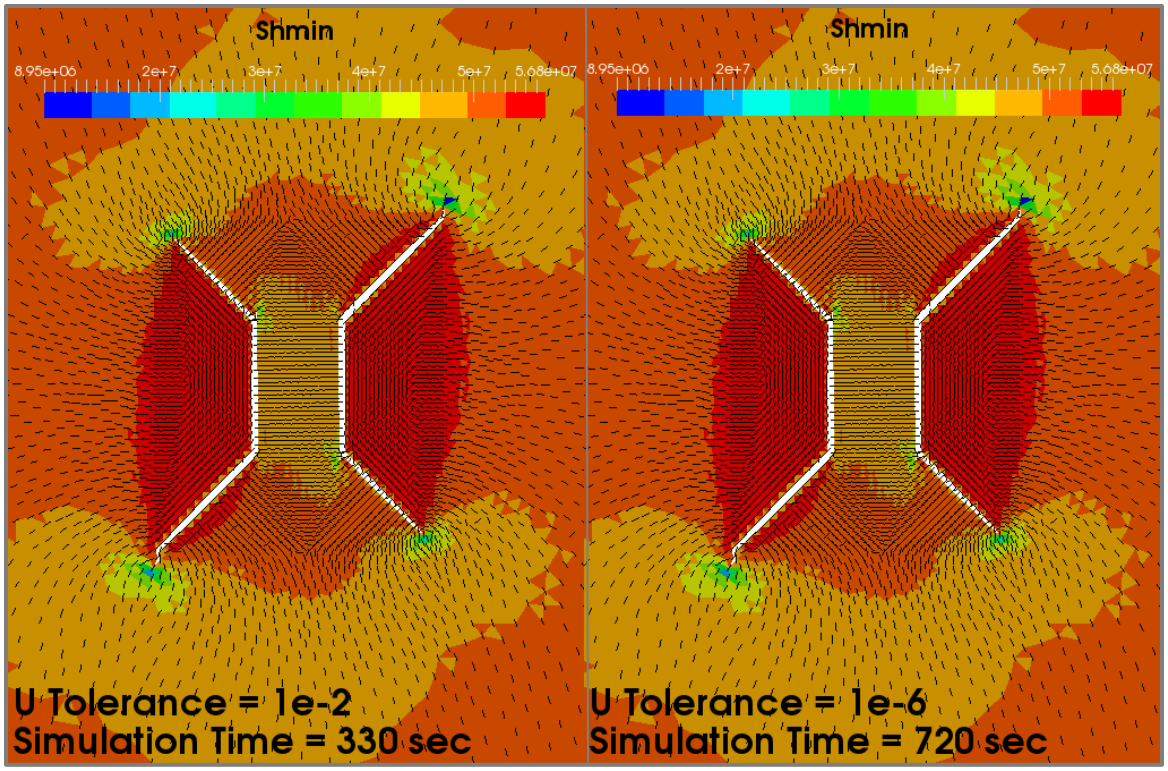

Figure 4.35 Impact of displacement equation tolerance on simulation time and the resulting fracture trajectories.

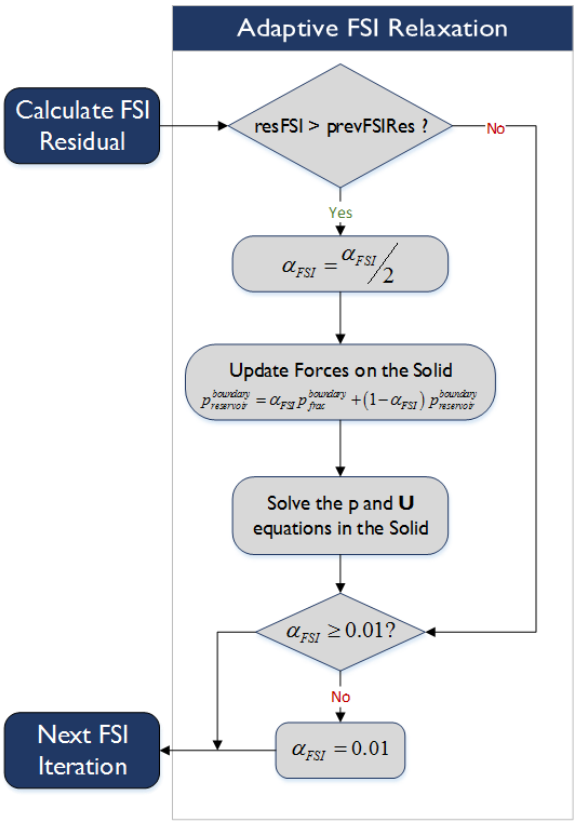

Figure 4.36 Adaptive FSI Relaxation procedure

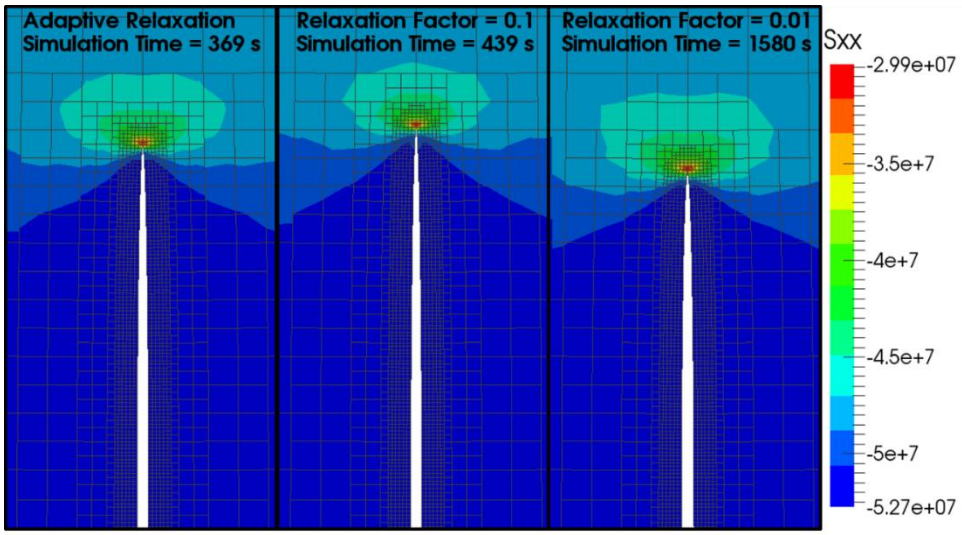

Figure 4.37 Comparison in simulation results for fracture propagation with adaptive FSI relaxation and fixed relaxation techniques.

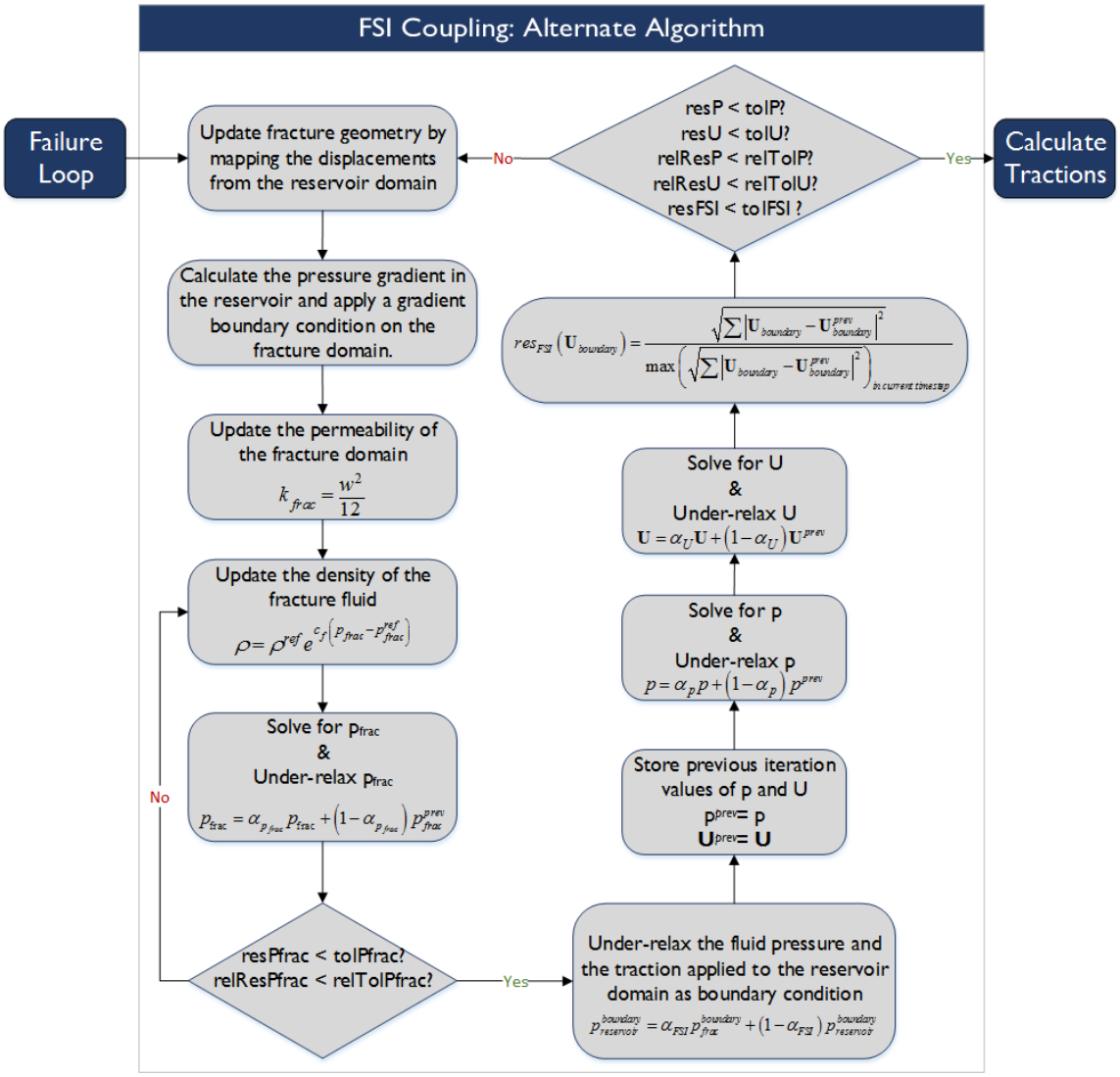

Figure 4.38 Alternate FSI coupling algorithm that increases simulation efficiency for an example test case.

Chapter 5: Multiple Fracture Propagation using Finite Volume Discretization

In this chapter we discuss the application of the finite volume geomechanics simulator discussed in Chapter 4 to pad-scale fracturing operations. There are various pad-scale fracturing scenarios that require the use of a poro-elastic simulator. The poro-elastic simulator developed in this work is used to model multi-cluster hydraulic fracturing stimulation scenarios along a horizontal well. We also show that the developed simulator can simulate infill well stimulation, re-fracturing, mini-frac tests, and fracture propagation in heterogeneous reservoirs.

5.1 Propagation of Single Fractures: Comparison with Other Models

In order to verify that the developed simulation model generates physically reasonable results a parametric analysis was performed. Injection fluid viscosity, matrix permeability and injection rate were varied to understand their impact on the simulated fracture geometry. This analysis was performed using the two dimensional (2-D) Fluid Solid Interaction (FSI) algorithm discussed in section 4.3.3.3.

Eq. (5-1) shows the analytical expressions that define the half-length (l_f) and the maximum width (w_f) of a propagating fracture as a function of injection flow rate and fluid viscosity (Geertsma and de Klerk 1969; Lee et al. 2015).

$$l_f = 0.539\left(\frac{q^3\acute{E}}{\mu}\right)^{1/6} t^{2/3}$$

$$w_f = 2.36\left(\frac{q^3\mu}{\acute{E}}\right)^{1/6} t^{1/3} \tag{5-1}$$

$$\acute{E} = \frac{E}{1-\upsilon^2}$$

Figure 5.1 shows the impact of treatment fluid viscosity on the rate of fracture propagation. After 5 minutes of injection at approximately 80 bpm per 100 m of fracture height, the case with lower treatment fluid viscosity yields a longer thinner fracture while the case with higher treatment fluid viscosity yields a shorter stouter fracture. This is in agreement with Eq. (5-1).

Figure 5.2 shows the impact of treatment injection rate on the propagation of a single hydraulic fracture. Higher injection rate suggests a longer fracture. This is primarily because a higher injection rate increases the volume of fluid injected in comparison with a lower injection rate scenario for the same duration of injection. It also leads to larger widths because of increased pressure drop and larger fracture pressure (Nordgren 1972; Schechter 1992). This result is also in agreement with Eq. (5-1).

Both results qualitatively agree with the equations presented in (5-1). A quantitative comparison is not performed here because the analytical model has an assumption of zero pressure drop inside a hydraulic fracture while the simulation FSI model simulates the pressure drop inside the fracture. The quantitative comparison of the uniform pressure formulation was shown in section 4.4.3.

Figure 5.3 shows the pressure around a fracture for the cases of low and high reservoir permeability. Fracture in the lower permeability case are shown to be longer than the fracture in the higher permeability case. Larger reservoir permeability induces greater fluid leak-off. Greater fluid leak-off in the higher permeability case induces higher pressure in the vicinity of the fracture. Since the volume of fluid injected is the same in both cases, more leak-off in the higher permeability case induces smaller fracture volume. This decrease in fracture volume decreases both the length and the width of the fracture.

Since the models used in this work discretize the poro-elastic reservoir domain, there is no need for semi-analytical estimates of fluid leak-off using Carter's leak-off type expressions (Ehlig-Economides and Economides 2000).

5.2 Spatially Uniform Fracture Pressure Vs. Spatially Varying Fracture Pressure

In Chapter 4 we discussed two models to calculate the fracture pressure in a propagating hydraulic fracture. In one method uniform pressure was assumed inside each fracture (4.3.3.2). This method models the fracture domain – reservoir domain interface as a boundary condition and is efficiently parallelized. Also, this approach can be used for 3-D simulation as well. Other researchers have also used the assumption of uniform pressure inside a hydraulic fracture to simplify the simulation of hydraulic fracturing (Dong and de Pater 2001; Olson 2008; Cheng 2009; Roussel 2011).

In the second method, a FSI algorithm was used to couple the fracture domain fluid pressure with the reservoir domain displacement and pressure (4.3.3.3). The fracture domain was discretized using the finite volume discretization method in the FSI implementation. The FSI algorithm was developed for 2-D plane strain methods. Development of a 2-D plane strain FSI algorithm was considered as a stepping stone before the development of a corresponding 3-D method was pursued. Multiple hydraulic fracture propagation is a 3-D process because the stress shadow impacted by a hydraulic fracture is dependent on the dimensions of the hydraulic fracture. Thus incorporation of a 2-D plane strain algorithm for 3-D representation of hydraulic fractures is not suitable. Additionally, the FSI algorithm has not been parallelized. 3-D field-scale hydraulic fracturing simulations require the code to be efficiently parallelized. Thus, the FSI methods need to be further developed to efficiently simulate large scale fracture propagation simulations.

Simulations conducted using the FSI implementation, and calculations performed using simplified analytical expressions of fluid pressure drop inside fractures (Eq. (5-2)) have shown that the pressure drop from the wellbore to the tip of a hydraulic fracture is negligible compared to the pressure in the hydraulic fractures near the wellbore (Perkins and Gonzalez 1985).

$$\Delta P_f = 1.784 \left[\frac{q\mu l_f E^3}{(1-\nu^2)^3 H_f^4} \right]^{0.25} \tag{5-2}$$

Thus, we implement the uniform fracture pressure approach to simulate pad-scale fracture propagation scenarios because of the following reasons:

1. Inadequate development of the FSI approach,
2. Relatively minimal fracture pressure drop,
3. Efficient procedures developed for the uniform fracture pressure approach, and
4. Capability to perform 3-D simulations with the uniform fracture pressure approach

5.3 Parametric Analysis of Multiple Fracture Propagation

In 5.1 a small parametric analysis for single fracture propagation was discussed. In the current section we discuss a more thorough parametric analysis and analyze the impact on simultaneous multiple fracture propagation. We used a base case for comparison. The base case parameters and the respective sensitivity case parameters are shown in Table 5.1. The entire mesh domain is shown in Figure 5.4. The domain dimensions were large enough to have minimal boundary effects on the geometry and nature of the fractures.

Figure 5.5 shows a close-up view of the region in the vicinity of the fracturing stage. The mesh is created with triangular cuts between the square grids of the structured

refinement region. Three clusters were modelled as starter fractures to simulate simultaneous propagation of multiple fractures. Figure 5.6 shows the results from the injection of fluid into this three cluster stage. The results for the base case simulation show that the outer fractures propagate symmetrically. The stress shadow caused by the propagating outer fractures inhibits the growth of the middle fracture. Sharp turns observed in the fracture geometry are primarily caused by the coarseness of the mesh. Figure 5.7 shows the impact of a finer mesh on the propagation of the fractures. The fractures still turn away from each other however they propagate in a planar manner away from the well for a larger distance. This suggests that a coarser mesh over-estimates the stress interference between the fractures.

Figure 5.8 and Figure 5.9 quantify the field observations for the created fractures in the base case considered above. Figure 5.8(a) depicts the flow distribution between the three clusters. The plot shows symmetric distribution of flow between cluster 1 and cluster 3, with cluster 2 getting negligible fluid. This suggests that the stress interference between the clusters is evident from the beginning of the treatment. This can potentially be ascribed to the large size of the initial cluster. Also, this could be potentially ascribed to the tight tolerance chosen for fracture propagation. In the current algorithm, fracture surface is created when the effective tractions in the faces adjacent to the fracture in the reservoir mesh are greater than the chosen tensile strength. All the faces within a pre-defined percentage of the maximum effective traction are thereafter included as a part of the fracture. Here this tolerance percentage was chosen to be 1%. Thus, in this procedure it is possible that the reservoir mesh faces that have effective traction greater than the prescribed tensile strength of the material are not broken in a given failure iteration. The coupled approach of fracture propagation used in this work ensures a very numerically stable result as shown by other researchers (Shin and Sharma 2014, Profit et al. 2015).

This algorithm may need to be modified to produce results similar to other numerical models (Wu and Olson 2013, Pierce and Bunger 2015).

Figure 5.8(b) shows the pressures calculated for the three clusters and the wellbore. The wellbore pressure and the pressure in the middle cluster are higher than the pressure in the outer fractures. This pressure difference is because of the perforation pressure drop. The estimated perforation pressure drop is a function of the flow rate through the perforations and hence decreases the fracture pressure for the outer fractures that take most of the fluid. The middle cluster has negligible flow into it and hence has pressure very similar to the wellbore pressure because of negligible pressure drop. Figure 5.8(c) and (d) show the area and the length of the respective fractures. The middle fracture does not grow in area or length while the outer fractures continue propagating. Since these simulations are performed in a 3-D domain, the fracture area is a better estimate of the dimension of the fracture than fracture length. This is because fracture area also contains information about the propagating fracture's height. For the following parametric analysis, only fracture area plots are considered.

The variation of fracture average width versus time is shown in Figure 5.9(a). The trend suggests increasing width of the outer fractures. Comparing the fracture area plot and the fracture width plot, it can be inferred that the fracture grows longer at a higher rate than it grows wider. This is qualitatively in agreement with the expressions shown in Eq. (5-1) which show that length of the fracture increases as a function of $t^{2/3}$ while the width increases as a function of $t^{1/3}$. Figure 5.9(b) quantifies the perforation pressure drop inferred from Figure 5.8(b). The chosen perforation pressure drop coefficient suggests an approximately 900 psi pressure drop at the perforations of the outer fractures. The perforation pressure drop can be estimated using Eq. (5-3)

$$\Delta P_i^{perf} = \frac{\overline{\rho}}{2{\alpha_d}^2 {n_{perfs}}^2 (\pi {r_i}^2)^2} \boldsymbol{q_i}^2 = a_i \boldsymbol{q_i}^2 \quad (5\text{-}3)$$

In the current poro-elastic model the leak-off from the fracture is calculated by coupling the pressure calculation in the fracture with the pressure calculation in the reservoir. Thus empirical models such as a Carter's leak-off model are not needed to predict the fluid leak-off from the fracture. This however also suggests that the simulated fluid leak-off depends on the mesh in the vicinity of the fracture. The calculated leak-off rate and the cumulative volume of leak-off are shown in Figure 5.9(c) and Figure 5.9(d). Both the leak-off rate and the cumulative volume of leak-off increase with time. The increase in fracture area with time increases the leak-off rate with time. Increasing leak-off rate induces a concave upwards trend in the cumulative leak-off from the fracture.

The results presented were simulated on the Stampede cluster of the TACC supercomputer. Most of the simulations were conducted in parallel on 96 processors with approximately 6000 cells per processor. The finer mesh case was run on 400 processors while maintaining approximately 6000 cells per processor.

The finer mesh results have been further quantified in Figure 5.10, Figure 5.11, and Figure 5.12. For the base case we saw that the middle cluster does not lead to fracture propagation. Also, the outer fractures created symmetric fractures. From here on, we study the variation in the parameters to understand their effect on the symmetric outer fractures and the corresponding properties. Figure 5.10(a) shows a larger fracture area for the finer mesh and Figure 5.10(b) shows a smaller average fracture width for the finer mesh case. This suggests that a coarser mesh under-estimates the length of the fracture while over-estimating the width of the fracture. This over-estimation of width leads to a larger stress shadow and increases the stress interference between the competitively

growing fractures. This is the primary reason why the fractures in the base case turn away from each other sooner than the fractures do in the finer mesh case.

Figure 5.11(a) shows the total leak-off from the outer fracture and Figure 5.11(b) shows the fracture volume versus time. Clearly, the finer mesh causes a greater volume of leak-off. The smaller mesh adjacent to the fracture increases the pressure gradient and leads to a larger amount of leak-off. Also, the increased fracture area for the finer mesh case induces larger leak-off. Even though the relative increase in the volume of leak-off is large, the absolute values are very low compared to the fracture volume. At the chosen reservoir permeability 0.6% of the injected fluid leaked off in the simulation.

Figure 5.12(a) shows the impact of mesh refinement on the injection rate into the outer fractures and Figure 5.12(b) shows the impact of mesh refinement on the calculated wellbore pressures. The mesh refinement does not impact the fluid distribution between the two outer fractures in this symmetric scenario. However, the finer mesh does indicate lower estimates of wellbore pressures and consequently reduces the observed width of the fracture.

Comparing the fracture trajectories obtained in the base case simulation (Figure 5.6) and the finer mesh simulation (Figure 5.7) it becomes clear that the simulation results are sensitive to the mesh. A finer mesh size is recommended for these numerical simulations (for more accuracy), however, that would imply use of larger amounts of computational resources and longer computation times because of an effective increase in the number of unknowns. We here used the coarser mesh to perform a parametric analysis to relatively understand the impact of various parameters on multiple fracture propagation. More accurate estimation of simultaneous multiple fracture propagation behavior can be done with incorporation of dynamic mesh refinement procedures and other efficiency procedures discussed in Chapter 4.

5.3.1 Impact of Operationally Controllable Variables

Operators in the field are limited by the geology and the rock quality they are operating in. Hence, it becomes important to look at the impact of the treatment and completion variables to understand their impact on the multiple fractures created per stage.

5.3.1.1 Impact of injection rate

Figure 5.13 shows the impact of the treatment injection rate on the fracture trajectories observed. For the case with a higher injection rate, larger volume of fluid is injected which hence causes the propagated fractures to be larger in volume. The created fracture area and the average width of one of the outer fractures is shown to be larger for the higher injection rate case (Figure 5.14). Correspondingly, the wellbore pressure is also shown to be higher for the higher injection rate case (Figure 5.15). The symmetric distribution of fluid is illustrated in Figure 5.15(a). Higher injection rate, higher wellbore pressure, larger fracture area, and larger fracture width consequently increase the cumulative volume of leak-off, increase the fracture volume generated, and increase the perforation pressure drop.

5.3.1.2 Impact of number of clusters

Figure 5.17 shows the impact of the number of clusters on the fracture trajectories observed. In this case the cluster spacing was the same as the base-case cluster spacing, however the number of clusters in the stage were increased from 3 to 5. Thus, the outer clusters were 40 m away from each other compared to the base case where the outer clusters were 20 m away from each other. In the base case the fractures diverted away from each other because of the close proximity and high stress interference. Once the fractures started propagating away from each other the fracture length increased rapidly

hence causing a reduction in the fracture width. The increased distance between the outer fractures caused a reduction in the stress shadow induced by the outer fractures on each other. In contrast to the base case considered we observe the outer fractures to propagate symmetrically and transversely away from the wellbore for the larger number of clusters case. Parallel propagation of the fractures increased the stress interference. This increase in stress interference was not enough to make the fractures turn away from each other. Thus, no relaxation in the stresses between the fractures was observed as illustrated in Figure 5.18.

Another observation from Figure 5.19 is that for the 5 clusters per stage case the middle cluster also propagates a small fracture. The increased stress interference induced by the surrounding bigger fractures inhibits further growth of this middle fracture.

Figure 5.20 depicts the impact of number of clusters per stage on fracture area and fracture width versus time of injection. As shown in Figure 5.18, the fractures start deviating from the transverse trajectory for the base case after approximately 5 minutes of injection. Differences in the fracture area and fracture width trends are more noticeable beyond this 5 minute mark. The outer fractures seem to be inhibited in their growth in the 5 clusters per stage case because of competitive growth. Figure 5.21 shows the observed wellbore pressure versus time for the cases considered. An increase in the wellbore pressure can increase the simulated fracture width as seen in Figure 5.20(b).

5.3.1.3 Impact of cluster spacing

Figure 5.22 shows the impact of cluster spacing on fracture trajectories. In this case the cluster spacing was assumed to be 15 m (~ 50 ft) versus the base case cluster spacing of 10 m (~35 ft). As above larger distance between clusters cause the created fractures to have reduced stress interference. Thus the outer fractures propagate

transversely away from the wellbore in the higher cluster spacing case. The explanation of increased stress interference is very similar to the discussion in the section above.

Figure 5.23 shows the variation in fracture area and fracture width as a function of time of injection for the cases considered here. Similar to the case of 5 clusters per stage, this case also shows a relative increase in the fracture length for the turning fracture base case compared to the planar transverse fracture growth case for the larger cluster spacing. Figure 5.24 shows the impact of cluster spacing on the wellbore pressure versus time. The results shown in Figure 5.23 and Figure 5.24 are very similar to the results shown in Figure 5.20 and Figure 5.21. The impact of increasing the number of clusters per stage is very similar to the impact of increasing the cluster spacing. In both cases two dominant fractures propagate and inhibit the growth of fractures from the other clusters.

The inhibition of the outer fractures in both the cases discussed in section 0 and section 0 is potentially a mesh dependent issue. A simulation conducted using a coarse mesh restricts fracture turning. Thus, in the cases considered it is possible that the large mesh size used inhibited the fracture from turning because of inaccurate traction calculations.

5.3.1.4 Impact of perforation parameters

As discussed in Eq. (5-3) there are various parameters that control the perforation pressure drop. At the high injection rates used in the fracturing operation, perforation parameters can lead to a large amount of perforation pressure drop. The base case perforation pressure drop coefficient was chosen to be 1e9. This is equivalent to a cluster with 12 active perforations, 1 cm perforation diameter, 0.9 damage factor, and 1500 kg/m^3 slurry density. The comparison case perforation pressure drop coefficient was

chosen to be 4e9. Which can be obtained by reducing the active number of perforations to 6 or decreasing the perforation diameter to 0.707 cm.

Figure 5.25 shows the impact of perforation coefficient on the observed pressure trends. Figure 5.25(a) clearly shows the wellbore pressure to be higher for the case of larger perforation coefficient. Figure 5.25(b) shows that the perforation pressure drop for the larger perforation coefficient case is approximately 4 times the perforation pressure drop observed for the smaller perforation coefficient case.

The perforation variables can thus be varied for the various clusters in a stage to potentially promote multiple fracture growth.

5.3.2 Impact of Formation Properties

Operators can optimize their completion strategies by varying the controllable parameters. Reservoir parameters are domain specific parameters that cannot be modified. However, based on the diagnostic information about some of these reservoir parameters, the completion design can be optimized to efficiently stimulate a fracture stage. Some of the important formation properties that can impact the fracture propagation in a horizontal well stage are discussed here.

5.3.2.1 Impact of matrix permeability

Figure 5.26 shows the interesting impact of the increase in matrix permeability on the trajectory of fracture propagation and the induced pore pressure changes in the vicinity of the fractures. For the comparison case the permeability in the reservoir matrix was increased from 1 microDarcy to 1 milliDarcy. This increases the volume of leak-off from the fractures hence leading to a higher pressure in the vicinity of the fractures as shown in Figure 5.26. Figure 5.27 shows the impact of fracture propagation in the two cases considered and the impact on the developed stresses in the X direction.

Figure 5.28 shows the evolution of fracture area and fracture width and Figure 5.29 shows the evolution of cumulative leak-off volume and fracture volume for this comparison analysis. The primary impact of higher permeability is an increase in fluid leak-off. This increase in fluid leak-off causes the fracture volume. The decrease in fracture volume consequently reduces the fracture area and the fracture width.

The secondary impact of higher reservoir permeability is the increase in the poro-elastic impact because of fluid leak-off. The poro-elastic impact on fracture propagation has been discussed using analytical models (Detournay et al. 1989; Boone and Detournay 1990; Detournay and Cheng 1993; Berchenko and Detournay 1997). Here we use our numerical model to understand the impact of poro-elasticity on fracture interference. The pressure equation calculation (Eq. (4-7)) is a function of the volumetric strain induced in the matrix. The displacement vector calculation is dependent on the gradient of the pressure in the matrix. Thus the two equations form a tightly coupled system of equations.

Greater leak-off causes the pressure in the vicinity of the fracture to increase in the high permeability case. The poro-elastic impact of increased pressure in the reservoir increases the compressive stresses on the fracture surface. This thus decreases the width of the fracture (Figure 5.28(b)). The fractures turn away from each other after approximately 4 minutes of injection. At that time the fracture average widths are approximately 0.8 inches for the base case and 0.7 inches for the comparison-high-permeability case. The reduced stress interference induced by this smaller fracture width can prevent fracture turning. Thus, the stresses are not relaxed between the fractures and that further inhibits fracture propagation as discussed above and induces smaller fracture area in the higher permeability case.

The poro-elastic impact of the fluid leaking off also impacts the fracture trajectories. Figure 5.30 shows the pressure contours in the vicinity of the fracture after 4 minutes of injection. We focus on the region near the fracture tip of the left fracture in the two permeability cases. In Figure 5.31 and Figure 5.32 the pressure contours and the pressure gradient vectors before fracture turning and after fracture turning are shown. The pressure contours show that after 4 minutes of fluid injection the pressure ahead of the fracture tip is smaller in the low matrix permeability case than in the high matrix permeability case. Lower pressure does not however explain the turning fracture trajectory. In Chapter 4 we discussed the poro-elastic equations where we showed that fluid pressure can act as a body force on the solid skeleton (Eq. 4-9). The figures here show the pore pressure gradient directions and the magnitude of the pore pressure gradient. One clear distinction between the low and high permeability cases is the direction of pore pressure gradient calculated at the faces adjacent of the fracture tips. This is especially observable at the faces that create a fracture in the next time step shown in Figure 5.32. This alteration in gradient direction can also impact the fracture trajectory and cause it to turn in the low permeability case.

Care needs to be taken in the presented analysis here to realize that the gradient calculations can be very dependent on the mesh coarseness near the fracture tip. For a low permeability case the fluid does not travel too far from the fracture. A large cell next to the fracture can underestimate the pressure gradient calculations for the low permeability case. A refined mesh region in the vicinity of the fracture tip can more accurately estimate the pressure, pressure gradient and stress calculations and potentially provide a more concrete understanding of the fracture tip processes. Refined mesh calculations were not performed using the current methods. Dynamic mesh refinement

methods are considered necessary to increase the efficiency of the simulations and perform a more accurate analysis.

5.3.2.2 Impact of in-situ horizontal stress contrast

Hydraulic fractures are presumed to propagate in the direction of least resistance. Thus the fracture propagation direction is generally perpendicular to the minimum principal stress. The change in stress in the direction perpendicular to a hydraulic fracture is less than the change in stress in the direction parallel to a hydraulic fracture in the vicinity of the hydraulic fracture (Manchanda and Sharma 2014). Hydraulic fracturing can reorient the stresses to change the direction of the intermediate principal stresses. Under conditions of small horizontal stress contrast the stresses can be reoriented with more ease (Dahi-Taleghani and Olson 2011). We illustrate this effect by comparing the propagation of hydraulic fractures in a high stress contrast environment and a low stress contrast environment (Figure 5.33). As expected the fractures turned away from each other in the low horizontal stress contrast case but didn't turn in the high stress contrast case.

Figure 5.34 shows the impact of stress contrast on fracture area evolution and fracture width evolution. Similar to the previously discussed trends, the turning fractures have lower stress interference and generate fractures with larger area and smaller widths. Figure 5.35 shows the impact of stress contrast on the observed wellbore pressure. The pressures observed and the widths observed are consistent as the higher pressures observed in the high stress contrast case reflect wider fractures. These wider fractures are also a consequence of the inhibited growth of the fractures.

5.3.2.3 Impact of Young's modulus

Oil and gas reservoirs have large variability in the rock mechanical properties. Here we look at the impact of Young's modulus on the observed fracture geometries. When compared with the base case the higher Young's modulus case discussed here shows that the stresses in the vicinity of the fracture increase however the increase is not enough to show variation in the fracture trajectory. The fracture dimensions however were observed to be different (Figure 5.36). The fracture area in the high Young's modulus case is observed to be larger than the small Young's modulus case. The fracture width however shows the opposite trend hence conserving the volume of fluid injected. These trends qualitatively agree with the trends presented by the analytical expressions discussed in Eq. (5-1).

5.3.2.4 Impact of Poisson's ratio

Poisson's ratio has limited variability in the rock properties. Poisson's ratio generally varies between 0.2 and 0.35 in rocks. In this comparison analysis we see that the Poisson's ratio does not significantly impact the fracture propagation and fracture interference (Figure 5.37) when Poisson's ratio is increased from 0.2 to 0.3.

5.3.2.5 Impact of vertical heterogeneity

Geological deposition can induce vertical heterogeneity in reservoir properties. These geological bedding planes can be of varying sizes and can affect the height growth of fractures. A schematic simulation depicting the impact of these heterogeneous layers was performed by fracturing in the middle of an intermediate (40 GPa) Young's modulus layer which was bounded by small (5 GPa) and high (70 GPa) Young's modulus layers. The results from this simulation are shown in Figure 5.38. The top layer was chosen to be

the high Young's modulus layer while the bottom layer was chosen to be the low Young's modulus layer.

Fracture propagation begins from the center of the middle layer. The fracture initially propagates downwards to the low Young's modulus layer. For a propagating fracture the stress ahead of a fracture tip is a function of the mechanical properties of the rock in the vicinity of the fracture tip. The impact of reservoir heterogeneity can thus be integrated in a non-local manner. In the current case, the pressure in the fracture induces strain in the matrix. The variation in the layer properties cause the induced strain is to be asymmetric. For the same traction at the fracture face, the reservoir deforms more in the low Young's modulus layer. The strain in the low Young's modulus layer is felt further away from the layer interface. This reduces the compressive stresses in the downward direction. Thus, the fracture initially propagates downwards till it reaches the interface between the intermediate Young's modulus layer and the small Young's modulus layer. When the presence of the material boundary is felt at the propagating tip of the fracture, the traction calculations at the tip automatically guide the fracture along the path of least resistance.

The fracture does not propagate into the bottom layer because of the impact of Young's modulus on fracture width (Eq. (5-4), Schechter 1992). The equation suggests that the fracture width in the low Young's modulus region will have to be 8 times the fracture width in the intermediate Young's modulus region for the same value of net pressure. This is an improbable possibility in a continuum model since the displacements have to be continuous at the interface. Thus the fracture does not propagate into the low Young's modulus layer.

$$w(z,t) = \frac{2(1-v^2)}{E}\sqrt{(h^2 - z^2)}P_{net}(t) \quad (5\text{-}4)$$

After coming into contact with the bottom layer the fracture starts propagating radially upwards. The fracture propagates less rapidly towards the high Young's modulus layer. But when it reaches the interface, the fracture is relatively easily able to break through the interface and propagate further into the stiffer material because of the criteria specified above. The propagation rate is faster in the high Young's modulus layer because the obtained widths in the layer are smaller and because the effective tractions calculated are higher. The vertical cross-section of the fracture after it propagates into the high Young's modulus layer is shown in Figure 5.39. The continuity of displacement at the layer interface is observed and the pinching of the fracture in the high Young's modulus layer in accordance with the above equation is also evident.

In the above simulation, the Young's modulus was varied in the three layers however the stresses in the three layers were chosen to be the same value. This allowed us in isolating the impact of Young's modulus. The distance of the boundaries from the fracture location was chosen to be far enough and negligible impact of fracture propagation was observed for both cases of zero-displacement boundary conditions as well as constant-stress boundary conditions.

Figure 5.40 shows the impact of reservoir stresses and Poisson's ratio on fracture containment. The top and the bottom layers were initialized with a high *in-situ* minimum principal stress value (7250 psi) while the middle layer was initialized with a lower *in-situ* minimum principal stress value (5500 psi). The Poisson's ratio was also correspondingly varied in the layers – 0.3 in the top and bottom layers; and 0.2 in the

middle layer. The propagating fracture is shown to be contained in the low stress and low Poisson's ratio layer, as expected.

The above simulation results show that the vertical layer heterogeneity can be decisive in altering the fracture growth pattern and it is important to include the reservoir characterization in the simulations conducted.

5.3.2.6 Impact of lateral heterogeneity

Fractures in vertical wells are generally targeted to deplete a single pay zone. Horizontal wells are drilled in their target pay zone, however, out-of-zone drilling and reservoir heterogeneity can introduce variable lateral heterogeneity along the horizontal well. Thus multi-cluster fracturing operations can be strongly affected by the heterogeneity observed in the mechanical properties in the vicinity of the horizontal well. Heterogeneity along the horizontal well is actively used to stimulate the wells by choosing regions of high "fracability" (Mullen and Enderlin 2012; Fang and Amro 2014; Jahandideh and Jafarpour 2014; Jin et al. 2014, 2015; Su et al. 2014). Different researchers pose different ways to determine the fracability of the reservoir in the vicinity of horizontal well stages. Sometimes brittleness is taken as a surrogate for fracability. Several models to calculate brittleness exist (Kias et al. 2015). New logging techniques are enabling engineered completion design to get away from geometric spacing between fracturing clusters and have more customized fracture placement (Dahl, Samaripa, J. Spaid, et al. 2015; Dahl, Samaripa, J.S. Spaid, et al. 2015). This allows operators to reduce the number of fracturing treatments in a well and hence enable better economics. Operators have started using pin-point methods of fracturing that have shown to reduce water use, increase productivity of wells and create efficient fracture networks (Lane et

al. 2013; Carrasco et al. 2014). These completion methods could also be used to stimulate selected regions along a well based on the petrophysical analysis.

The question we address here is the following: How big a role does formation heterogeneity play relative to stress shadowing in controlling the competitive growth of fractures? The formation properties of the red and blue regions in FIGURE were chosen as follows: Young's modulus (blue-20 GPa, red-25 GPa), Poisson's ratio (blue-0.2, red-0.3), porosity (blue-0.10, red-0.20), permeability (blue-1 microDarcy, red-10 microDarcy), Biot's coefficient (blue-0.7, red-0.8). Five simulations were run to address the impact of each property separately. Fluid injection at 60 bpm into the stage with two clusters spaced 10 m apart is simulated. The horizontal stress contrast chosen for the simulations is 100 psi. Figure 5.41 shows the results from the simulation analysis. In all the cases the properties chosen in the red region favored fracture propagation.

Similar pressures in the clusters but difference mechanical properties cause the displacements to be different in the two domains. The tensile strength criterion is met in the high modulus region and a fracture is initiated in this region. According to linear elastic fracture mechanics (LEFM), the energy required to propagate a fracture in a higher Young's modulus material is smaller. After fracture initiation in the high modulus region, the initiated fracture continues propagating and prevents the propagation of a fracture from the other cluster. This happens primarily because of the heterogeneity in the properties of the rock matrix and the induced stress shadow caused by the propagating fracture. Relatively small changes (5-10%) in the elastic moduli of the rock can lead to changes in stresses that are comparable in magnitude to the stress shadow induced stresses. This implies that the effects of rock heterogeneity will be superimposed on the stress shadow and poroelastic effects presented earlier and in some instances can play a dominant role in determining how many fractures are effectively stimulated.

In order to understand the impact of porosity we consider the definition of the hydraulic diffusivity generally used in reservoir engineering (Eq. (5-5)). A decrease in hydraulic diffusivity induces a slower pressure change in the system. From the simulations conducted we have observed that the fracturing process reduces the pressure ahead of a fracture tip to a low value. A smaller change in this pressure for the high porosity case suggests that the pressure ahead of the fracture tip is closer to the reservoir pore pressure. A higher pressure ahead of the fracture tip leads to a higher tensile effective stress. The calculated traction will then meet the criteria of fracture propagation earlier in the high porosity case and this will lead to faster fracture propagation.

$$Diffusivity = \frac{k}{\phi \mu c} \tag{5-5}$$

Finally, a larger Biot's coefficient value suggested preferential fracture propagation. A greater Biot's coefficient value increases the impact of fluid pressure on the reservoir stresses. Thus, for greater Biot's coefficient the effective tensile strength in the region in front of the tip is greater and hence induces preferential fracture propagation.

Thus, it has been shown that poro-elastic stresses can cause changes in fluid distribution and fracture propagation in multi-cluster stages. Estimates of porosity can be obtained from density, neutron and sonic logs. Permeability estimates can be obtained from core analysis. These estimates can then be included in the simulation model to analyze their impact of fracture propagation.

Figure 5.42(a) shows the impact of Young's modulus and Figure 5.42(b) shows the impact of Poisson's ratio on the propagation of multi-cluster fracture propagation with 5 clusters. The blue region in all the cases considered had 20 GPa Young's modulus

and 0.2 Poisson's ratio. 15 m cluster spacing was used for the simulation of this 5 cluster stage. A red band of heterogeneity was introduced in these simulations. For the two cases of Young's modulus considered the red band in the top figure of Figure 5.42(a) had a Young's modulus that was 5% larger than the Young's modulus in the surrounding region, while the Young's modulus was increased by 25% in the bottom figure. It is observed that a 5% change in the material heterogeneity does not impact the fracture propagation trajectory. Only the outer fractures propagate in this case. When the material property is varied by 25% the heterogeneous band promotes fracture propagation and only one fracture is simulated. Similar observations are made for the case of Poisson's ratio variation in Figure 5.42(b). 5% change in heterogeneity does not induce preferential fracture propagation while 25% change introduces preferential fracture propagation from the middle cluster. Thus, there is a critical variability in heterogeneity above which the stress shadow effect becomes insignificant and heterogeneity governs the simulated fracture trajectories.

Performing petrophysical and geomechanical analysis can help in identifying reservoir properties. Such analyses can then help in populating the simulation model and hence model fracture propagation in heterogeneous media. In the simulations shown in this section a relatively coarse grid was used. A finer mesh should be used to perform a more quantitative analysis.

5.4 Stress Shadow Effects in Multi-Stage Hydraulic Fracturing

Hydraulic fracturing treatments in horizontal wells are generally performed from the toe to the heel of the well. Each hydraulic fracture treatment is performed in a stage that comprises of several clusters of perforations. In the section above we discussed the impact of various reservoir and treatment parameters on the fracture evolution from

clusters in one such stage in a horizontal well. In this section we look at the impact of the fractures created in a horizontal well stage on the fractures formed in the next hydraulic fracture stage in the same well.

Two stage fracture treatment simulation was performed to understand the impact of fractures in one stage on the fractures in a subsequent stage. The treatment for the first stage is started with a 5 min ramp of fluid injection to an injection flow rate of 60 bpm. This injection rate is maintained constant for 25 more minutes. Thereafter, injection into the stage is stopped in one minute. The treated stage is shut-in and no fluid is injected into the reservoir for the next 29 minutes after which the same treatment schedule is executed for the next stage. This treatment profile is presented in Figure 5.43.

The simulated fracture patterns are presented in Figure 5.44 and Figure 5.45 at various times during the fracture treatment. Symmetric fractures are observed in the first stage. The clusters in the stages are simulated at a 15 m distance from each other. For the chosen mesh, limited stress interference is observed in the fractures propagating in the first stage as the fractures do not turn away from each other. The stress interference is however enough to prevent the propagation of fractures from the middle cluster in stage 1. After the simulated fluid injection into stage 1 is stopped, the created fractures start closing. Figure 5.44 also shows the stress interference in the reservoir at the beginning of injection into stage 2. For the chosen mesh, the stress shadow from the first stage, prevents more than one fracture to propagate in the next stage. The stress shadow from the fractures created in stage 1 are the least at the location of the furthest cluster in stage 2. Thus, the single propagating fracture from the second stage is created in the cluster furthest from the first stage.

In Chapter 2 and Chapter 3, using static fractures we had discussed the alteration of fracture trajectory in successive stages in a horizontal well. Here however, we see that

the propagation of fractures in successive stages does not depict any fracture turning. This is caused by inadequate meshing. Firstly, in the current method fracture turning is a mesh sensitive process. As we saw earlier, a coarse mesh ahead of the fracture tip inhibits fracture turning. Secondly, the method requires an initial starting fracture. Stress reorientation caused by the fractures in the previous stage would suggest that the fractures would start propagating in a direction that is not perpendicular to the well. In the current method this starter fracture is a plane that is perpendicular to the wellbore. Thus the initial fracture created does not observe the stress re-orientation. This bias can be rectified by positioning the initial fracture at the well location in the local maximum and intermediate principal stress plane. These two effects, in combination prevent the fracture from accurately predicting the fracture trajectory in the presented case.

Figure 5.46 shows the simulated treatment pressures in the two fracture stages. The pressures recorded in Stage 1 show that Frac 1 and Frac 3 are symmetric during the first 60 minutes of treatment. The pressure in Frac 2 and the wellbore was observed to be the same suggesting that there was negligible perforation pressure drop in the middle fracture. Differences in the pressure trends for the fractures in stage 1 appear when the treatment is started in the second stage. Fracture propagation in the second stage induces changes in the pressures recorded in the first stage.

The pressures observed in the well during fracture propagation in stage 2 are much higher than the pressures observed in stage 1. Since all the injected fluid goes through a single cluster (Figure 5.48(b)) the perforation pressure drop is increased for the cluster that creates a fracture in stage 2 (Figure 5.47(b)). This higher perforation pressure drop consequently leads to higher wellbore pressure because for the case of larger pressure drop the wellbore pressure needs to be much higher to have a high enough fracture pressure to propagate the fracture.

Figure 5.48 shows the fluid injection rate into the clusters of the two stages. The trends observed seem very similar to the trends presented in Figure 5.43. There are some blips that occur in the Figure 5.48(a) from 60 to 90 minutes. These changes in injection rate represent the changes in fracture dimensions of the fractures in stage 1 during the fracture propagation in stage 2. The two fractures in stage 1 remain in hydraulic connection when the fractures in stage 2 are created. This induces exchange of fluid between the fractures in stage 1 and induces the trends observed in Figure 5.48.

The fracture geometries are represented in Figure 5.49, Figure 5.50, and Figure 5.51. These curves present a very clear picture of the observations from the previous analysis. For the first 30 minutes, fluid is injected into stage 1. This causes an increase in the fracture width for the fractures formed from cluster 1 and cluster 3. During this period the area and the volume of the fractures in stage 1 linearly increases. From time 30 minutes to 60 minutes, the fracture width and fracture volume slowly decrease because of leak-off while the fracture area remains constant. During this period no fluid is injected into any of the clusters and hence during this period the created fractures close. Injection of fluid into stage 2 is started at 60 mins. The third cluster in stage 2 starts propagating a fracture within a minute after starting the treatment. The impact of this fracture's stress shadow is observed in the fractures in the previous stage. The width of fracture 3 in stage 1 decreases more than the width of fracture 1 because stress interference is larger on the fracture closer to stage 2. This decrease in width compresses the fluid in the existing fractures and increases the pressure inside the fractures hence causing fracture 3 in stage 1 to propagate. This increase in fracture area decreases the fracture width. Increase in the third fracture's area impacts the first fracture's area by decreasing its width. This decrease in width of the first fracture redistributes the fluid to the third fracture and allows for further fracture propagation.

The above described workflow can now be applied to simulate multi-stage multi-cluster fracturing in horizontal well pads. Heterogeneity in reservoir properties can be included in this model to predict competitive growth and interaction between hydraulic fractures. This can help in identifying the number of active clusters per stage in a horizontal well. Such an analysis can help in reducing costs by helping optimize the spacing between clusters and helping optimize the number of clusters per stage while taking into consideration impact of reservoir mechanical and porous properties, treatment variables, and completion variables.

5.5 INFILL WELL HYDRAULIC FRACTURING

Poro-elastic stress reorientation with emphasis on hydraulic fracture propagation trajectory has been studied very comprehensively using field analysis (Warpinski and Branagan 1989; Weng and Siebrits 2007; Fischer et al. 2009; Dahm et al. 2010; Ajani and Kelkar 2012), lab experiments (Bruno and Nakagawa 1991), analytical estimations (Berchenko and Detournay 1997) and numerical simulations (Weng and Siebrits 2007; Singh et al. 2008; Roussel 2011; Gupta et al. 2012; Roussel et al. 2013).

In Chapter 3 using numerical simulations of producing hydraulic fractures in horizontal wells we discussed the impact of reservoir depletion, well spacing and fracture spacing on the hydraulic fracture complexity in a potential infill well. We showed that the poro-elastic impact of reservoir depletion causes stress reorientation in the reservoir and can induce altered stress trajectories as well as hydraulic fracture complexity in the infill wells. In this section we simulated hydraulic fracture propagation from an infill horizontal well in a pad with multiple fractured wells that had been on production for two years. Figure 5.52 shows reservoir depletion caused by the production of the pad horizontal wells. As shown in the top left section of Figure 5.52(a) and Figure 5.52(b),

the outer purple wells are simulated with 8 fractures each of dimension 30 m X 75 m and spaced 20 m apart from each other. The outer purple wells are positioned 300 m apart from each other and are in a horizontal plane that is 60 m above the infill well. The pad wells are simulated in the X direction with the fractures in the outer wells simulated in the YZ plane. The top right section in Figure 5.52(a) and (b) show the view of the pad in the Y direction. This view shows the location of the outer wells in different horizontal planes. The plane with the pressure contour is a vertical plane through the infill well in the middle of the outer wells. The bottom right section shows the view of the pad in the X direction. The fractures in the outer wells and the location of the cluster in the infill well is visible. The plane showing the pressure contours is in the YZ plane through the location of the infill well cluster. The bottom left section shows the plan view of the horizontal plane through the infill well.

Figure 5.52(a) shows the pore pressure contours after 1 week of depletion and Figure 5.52(b) shows the pore pressure contours after 2 years of depletion. Exaggerated depletion trends were simulated by applying a 0 pressure boundary condition on the outer fractures for 2 years. *In-situ* reservoir pore pressure is simulated to be approximately 5800 psi and the *in-situ* horizontal stress contrast is simulated to be 1000 psi. The pressure contours show extensive depletion in the reservoir at a matrix permeability of 100 microDarcy. A decreasing pressure trend is observed from the infill well to the producing wells after 2 years of production.

A single fracture is simulated in the infill well at the location shown in Figure 5.52(b). The reservoir depletion induces poro-elastic stress changes in the reservoir hence causing asymmetric fracture propagation from the infill well as shown in Figure 5.53. The figure shows that the fracture propagates towards the infill wells. The variation in the stresses also induces the fracture width to vary in the Z direction i.e. the along the height

of the fracture. Pressure reduction makes the total stress less compressive following Eq. (5-6). A decrease in pressure for constant effective stress causes the total stress to be less compressive.

$$\mathbf{S} = \boldsymbol{\sigma} - \alpha P \mathbf{I} \tag{5-6}$$

Depletion of pore pressure in the vicinity of the producing fractured wells also induces the effective stress to be less compressive. There are two coupled reasons for this. Firstly, a decrease in pressure in a system causes the volumetric strain to decrease. In a continuum system, the decrease in volumetric strain introduces tensile stresses and subsequently makes the effective stress less compressive. Secondly, local pressure reduction induces a pressure gradient in the reservoir. The pressure gradient acts as a body force on the matrix and an outward pressure gradient introduces tensile forces on the matrix thus making the effective stress less compressive.

The pressure gradient in this case acts mostly in the vertical direction and decreases the compressive effective stress in the depleted region of the rock matrix. This induces a change in the fracture width profile. For a uniform pressure along the height of a fracture, lower rock stresses induce larger fracture width and higher rock stresses induces smaller fracture width in the Z direction as shown in Figure 5.54.

This example simulation suggests that the model can be used to simulate complex pad-scale scenarios with multiple wells. Using a similar methodology, zipper fracturing, frac wave (Sardinha et al. 2014) and other innovative fracture sequencing strategies can also be simulated. Fracture closure is also automatically handled in the formulation. Thus stress shadow reduction in the vicinity of closing fractures can be modelled and methodologies that involve variation in times between fractures can be simulated. These

simulations have been shown to include the impact of reservoir heterogeneity and thus can be performed for a customized per-pad analysis.

5.6 OTHER MODEL APPLICATIONS

We have shown the capabilities of the developed simulation framework for simulating a few pad scale scenarios such as fracturing of multiple stages in multiple wells in a pad and fracturing of infill wells in a depleted pad. The simulation framework provides a comprehensive structure that can serve as a base structure to simulate several other complicated oil field operations.

5.6.1 Re-fracturing

Re-fracturing operations are used to recover oil and gas resources from un-depleted reservoir regions. Re-fracturing can be an essential strategy in situations where a horizontal well is not stimulated efficiently and hence requires re-stimulation. This re-stimulation of the well is generally done after putting the well on production for a certain period of time. Sometimes, the re-fracturing process is done to re-stimulate existing fractures and sometimes new clusters of perforations are shot to enable new potential fractures.

We simulated reservoir depletion using static fractures of uneven lengths and uneven spacing in the developed geomechanics reservoir simulator. Figure 5.55 shows the impact of production from existing fractures on the minimum principal stress, the pore pressure and the horizontal stress contrast along the length of the horizontal well. The production induced changes in stresses in the vicinity of the fractures and the horizontal well. Non-uniform depletion and regions of low and high minimum principal stress are exhibited in the results. The un-depleted regions are the regions with high

pressure. This illustration suggests that new fractures can potentially be created in these regions and more oil and gas resources can be recovered.

The developed poro-elastic framework can be used for simulating the re-fracturing process. Further development is necessary to model the flow and distribution of diverting agents (Hill et al. 1978; Allison et al. 2011; Cortez and Reddy 2013) in the wellbore. This would entail both experimental work with regards to modelling of the reduction in permeability induced by diverting agent plugging as well as simulation development to incorporate transport equations for the flow of diverting agents (Yi and Sharma 2015). Fluid flow simulation and pressure drop simulation inside the fracture will also be necessary to effectively simulate the diversion of fluid.

5.6.2 DFIT Analysis

Diagnostic Fracture Injection Testing (DFIT) is performed to estimate minimum principal stress, reservoir permeability and other reservoir parameters. DFIT analysis has in the past been based on a simple model of fluid flow in a fracture and subsequent fracture closure (Fairhurst 1964; Nolte 1979; Barree et al. 2007, 2009). Poro-elasticity has been shown to modify the existing theories by introducing time dependence in the estimation of the *in-situ* stresses (Detournay et al. 1989). Poro-elasticity theory suggests a decrease in fracture width and an increase in fracturing pressure relative to the analogous elastic theory because of the incorporation of pore pressure induced back stress on the fracture. Thus, incorporation of poro-elasticity should decrease closure times depending on the time of injection, reservoir permeability and associated poro-elastic parameters such as Biot's coefficient and Biot's modulus.

There have been some recent developments in DFIT analysis that suggest a more thorough analysis of the fracture flow profile to estimate the time of closure and estimate

the closure stress more accurately by considering variable fracture compliance (McClure et al. 2014). In the current simulation framework, the pressure change in the fracture during closure is tightly coupled with the reservoir pressure and displacement. A compliance equation can be coupled with the fracture flow equation to account for the impact of variable fracture compliance. This can help generate pressure trends during fracture closure which can help in obtaining the flow profiles in the fractures.

The pressure profile for one such fracture closure simulation (constant compliance) is shown in Figure 5.56. This simulation was performed using the 2-D FSI framework. Fluid injection at approximately 0.13 bpm/ft (~10 bpm for a 75 ft tall fracture) was simulated for 100 seconds to create a fracture. Fluid injection was stopped after this and subsequently fracture closure was simulated for 900 more seconds. Figure 5.57 illustrates the fracture width and the consequent displacement induced in the reservoir. Fluid injection is stopped after 100 seconds of injection as shown in Figure 5.57(a). The fracture continues to extend after shut-in for approximately 20 more seconds (Figure 5.57(b)). The fracture closure induces decrease in the fracture width and relaxation in the reservoir displacements as shown in Figure 5.57(c).

Further development is needed to perform accurate fracture closure and DFIT analysis. These include the incorporation of contact laws (Elata and Berryman 1996) to simulate fracture surface contact, variable fracture compliance, and accurate 3-D flow calculations inside the fracture.

5.6.3 Fracture Network Heterogeneity

Bryant et al. (2015) used an initial version of the current model to showcase fracture propagation in a heterogeneous medium. They showed that fracture propagation is affected by the heterogeneity included in the system. Figure 5.58(a) shows a case in

which the material was simulated to be homogeneous and Figure 5.58(b) shows a case in which heterogeneity in the material properties was included.

Bryant et al. (2015) clearly showcased that the simulation framework can be adapted to include Discrete Fracture Networks (DFN) and simulate interaction of the propagating hydraulic fractures with existing planes of weaknesses. They used both mode I and mode II failure criteria to simulate fracture propagation. Further development to simulate fracture network heterogeneity entails inclusion of better meshing protocol to discretize the DFN in the reservoir matrix.

5.7 CONCLUSIONS

In summary, in this chapter we have discussed the application of the poro-elastic reservoir scale hydraulic fracturing simulator to some typical pad-scale fracturing problems. The capability of the model to simulate pad-scale simulations of multi-stage hydraulic fracture treatments, infill-well fracturing, re-fracturing, DFIT analysis and fracture network heterogeneity have been discussed. Detailed conclusions are listed below:

- Qualitative verification of the FSI fracture propagation model was performed for single fractures suggesting physically reasonable results. An increase in treatment fluid viscosity, a decrease in injection rate and an increase in matrix permeability resulted in shorter fractures.
- Parametric analysis of both operationally controllable parameters and formation properties was conducted. Intuitive simulation results were observed for most cases. All the case results showed that the stress shadow between fractures caused some clusters in the fracturing stages to not create fractures.

- Increasing the injection rate induced longer fractures however it increased pressure drop in the perforations.
- Increasing the number of clusters and increasing cluster spacing decreased the stress interference between the propagating fractures and prevented the fractures from turning away from each other.
- Simulation of multiple fractures turning away from each other decreased the stress interference between the fractures. Parallel propagating fractures depicted larger stress interference and inhibited fracture growth.
- Decreasing the number of perforations in a cluster and/or decreasing the diameter of perforations in a cluster depicted an increase in the fracturing pressure.
- Higher reservoir permeability induced increased pore pressure in the vicinity of the fracture. We observed that the poro-elastic impact of hydraulic fracturing reduced the stress interference between simultaneously propagating fractures and inhibited fracture growth and turning.
- Increased *in-situ* horizontal stress contrast increased the stress interference but prevented fracture turning away from each other.
- Increased Young's modulus induced fracture width reduction which consequently induced an increase in the fracture area.
- Poisson's ratio did not have a significant impact on the simulated fracture dimensions.
- Fracture height growth was shown to be sensitive to reservoir layer heterogeneity. Fracture propagation in a homogeneous material layer propagated preferentially towards a softer material layer. Fracture breakthrough into a soft layer from a harder layer was shown to be less probable. Fracture breakthrough into a harder

layer from a softer layer was shown to be easier. This knowledge can be used when drilling to optimize the position of a well.

- Heterogeneity along the horizontal well in Young's modulus, Poisson's ratio, porosity and permeability was studied. Higher Young's modulus and higher Poisson's ratio induced preferred fracture propagation because of increased tensile effects. Higher porosity and higher permeability induced preferred fracture propagation because of the induced poro-elastic. Incorporation of these trends to the analysis of pad-scale heterogeneous situations is recommended to position clusters in a horizontal well in regions of high fracability. Further analysis should also be done to simulate such behavior for realistic heterogeneity cases.
- A two stage multi-cluster hydraulic fracturing simulation was conducted that showed that the stress shadow impact of fractures in one stage induced stress shadow on the fractures in the subsequent stage and vice versa. This stress shadow limited the number of active clusters in the next stage.
- The multi-stage simulation also showed that fractures in a previous stage extended further because of the stress shadow induced by the fractures propagating in the next stage. This can explain some observations of induced microseismic events observed in stages after fluid injection was stopped in the stage (Fischer et al. 2008).
- The poro-elastic impact of reservoir depletion is observed in the height growth of fractures infill well simulations. Fracture growth was observed to be preferentially oriented towards the depleted regions in the reservoir. Thus, simulations including the impact of reservoir depletion on fracture propagation can also be performed.

- There is potential to develop the model to simulate some other pad-scale fracturing scenarios such as re-fracturing, mini-frac analysis (DFIT) and the propagation of heterogeneous fracture networks.

5.7.1 Future Development

Application of the model to pad-scale scenarios requires large computer resources and long computation times. Efficient simulation algorithms can help in reducing the amount of computational resources required. Simple profiling of the numerical algorithm suggests that the input and output structures being used in the algorithms use a majority of the resources devoted to a simulation. Improved algorithms that can be used were discussed in the previous chapter. Another way of increasing efficiency is to use an efficient dynamic meshing method to improve the resolution of fracture propagation and decrease simulation times as discussed in the previous chapter.

Fracture propagation direction is sensitive to mesh refinement at the fracture tip. Three dimensional simulations are necessary to simulate fracture propagation for pad-scale scenarios. The mesh refinement in three dimensional simulations can increase the number of cells in the mesh significantly. Thus a practical simulation of field scale scenarios requires the incorporation of dynamic meshing methods that refine around a propagating fracture tip.

The pressure drop calculation in the fractures was ignored in the simulation results shown in this chapter. This was considered reasonable for simulations involving small pressure drops in the fractures during propagation. However, fracture pressure drop estimation can be important for certain fracturing scenarios such as high viscosity treatment fluid injection, re-fracturing, and fracture network simulation. The fracture pressure calculation method developed is currently 2-D and not parallelized. Thus it is

important to extend the capabilities of the method to simulate 3-D fracture propagation and parallelize the FSI methods to enable more accurate and efficient hydraulic fracture simulation.

5.8 NOMENCLATURE

α	= Biot's coefficient of effective stress	dimensionless
α_d	= damage factor for perforation press drop	dimensionless
ΔP_i^{perf}	= perforation pressure drop in ith frac	$ML^{-1}T^2$, Pa
ΔP_f	= fracture pressure drop	$ML^{-1}T^2$, Pa
E	= Young's modulus	$ML^{-1}T^2$, Pa
h	= fracture half-height	L, m
H_f	= fracture height	L, m
l_f	= fracture half-length	L, m
μ	= fluid viscosity	$ML^{-1}T$, Pa.s
υ	= Poisson's ratio	dimensionless
P	= pressure field	$ML^{-1}T^2$, Pa
P_{net}	= fracture net pressure	$ML^{-1}T^2$, Pa
q_i	= flow per fracture	L^3T^{-1}, m^3/s
$\bar{\rho}$	= average slurry density	ML^{-3}, kg/m^3
r_i	= perforation radius	L, m
$\boldsymbol{\sigma}$	= effective stress tensor	$ML^{-1}T^2$, Pa
$\mathbf{S}$	= total stress tensor	$ML^{-1}T^2$, Pa
w	= fracture width field	L, m
z	= fracture height above wellbore	L, m

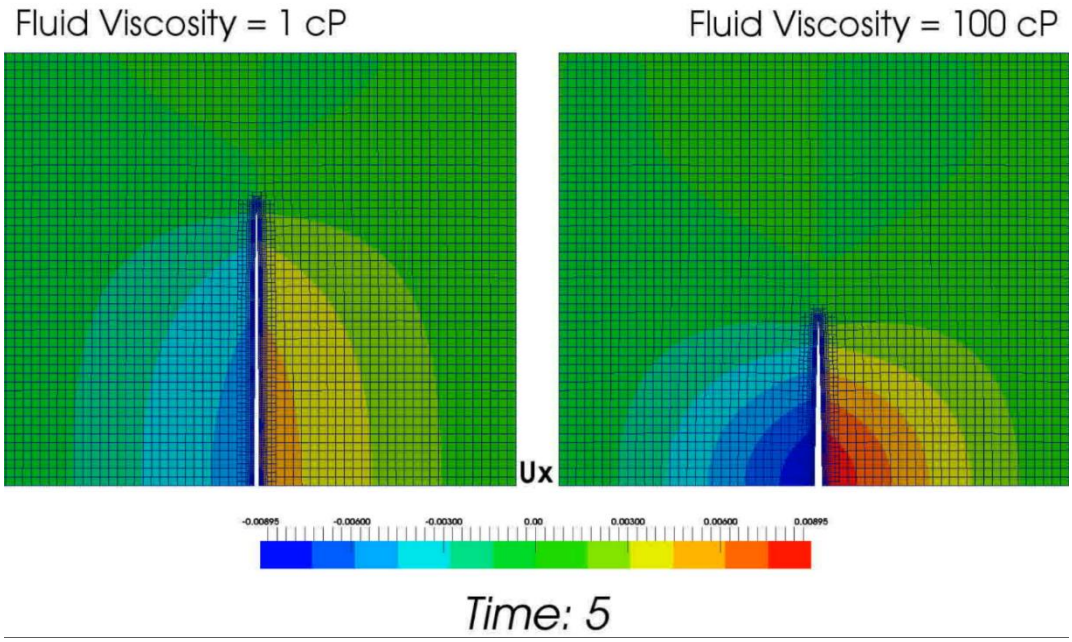

Figure 5.1 Impact of treatment fluid viscosity on fracture propagation using 2-D FSI implementation.

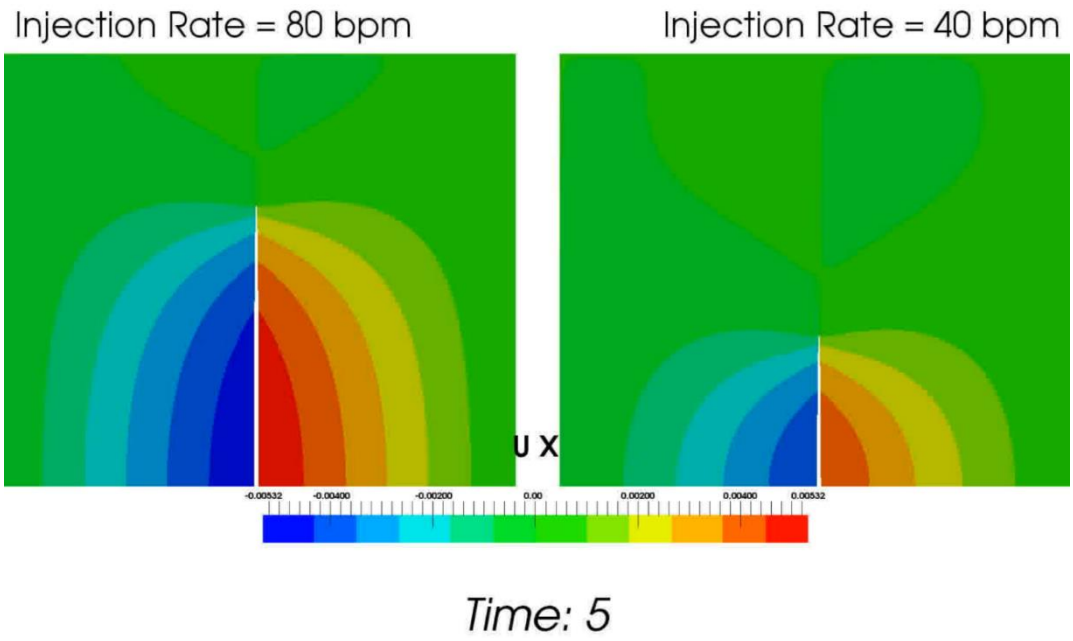

Figure 5.2 Impact of treatment injection rate on fracture propagation using the 2-D FSI implementation.

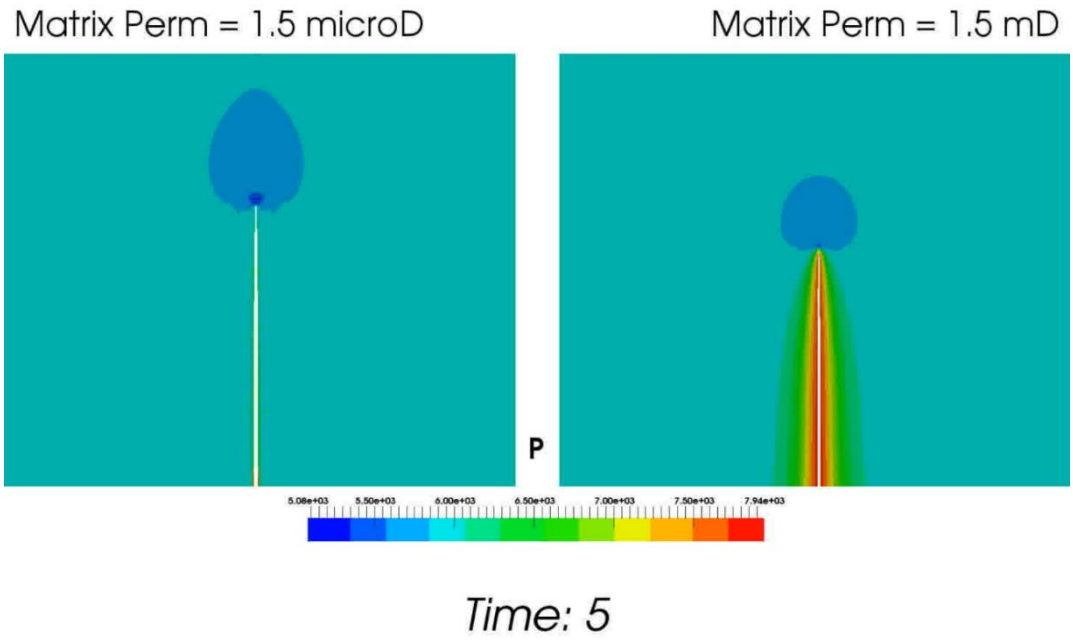

Figure 5.3 Impact of matrix permeability on fracture propagation using the 2-D FSI implementation

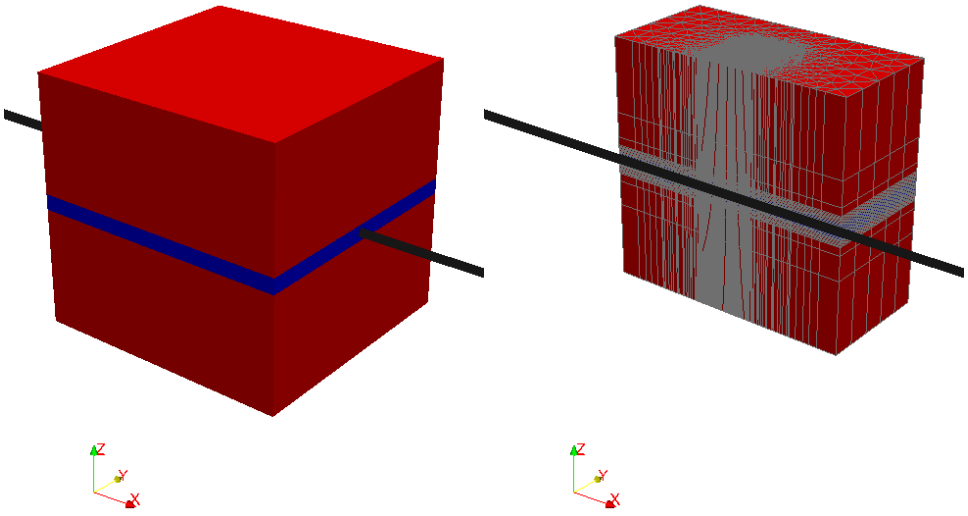

Figure 5.4 Left figure shows the location of the well in the entire grid. The colors show the pay zone and the boundary layers. The right figure shows a vertical clip of mesh and depicts the mesh edges.

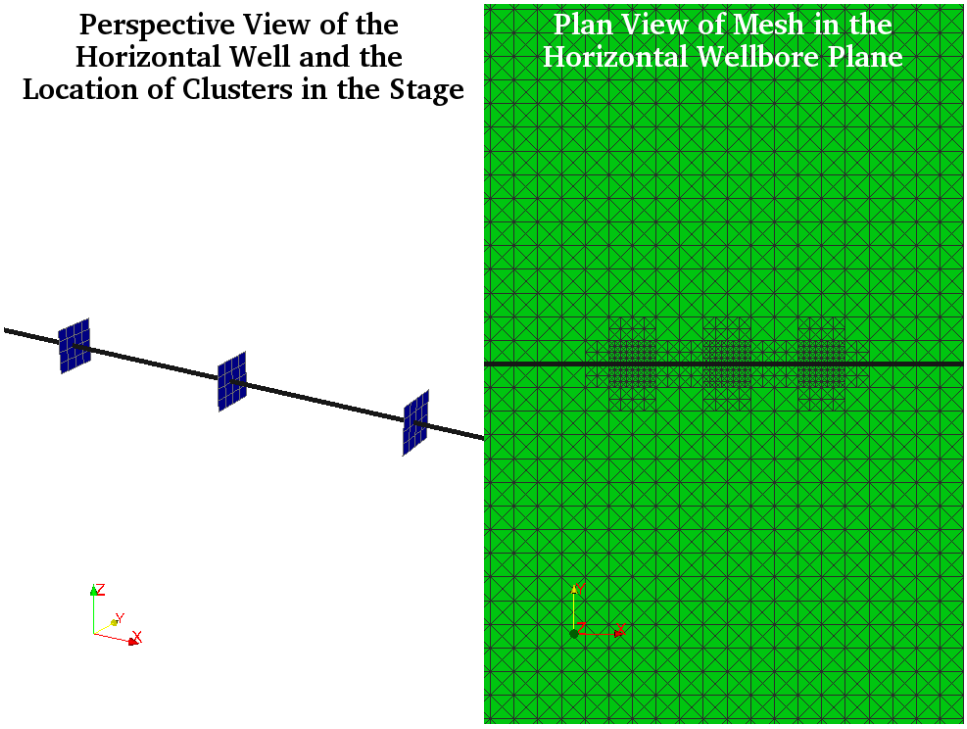

Figure 5.5 Close up view of the location of the clusters and the mesh in the horizontal plane of the well.

Parameter	**Base Case**	**Sensitivity Case**
Young's Modulus	2.9 MMpsi	5.8 MMpsi
Poisson's Ratio	0.2	0.3
Horizontal Stress Contrast	100 psi	400 psi
Injection Rate	60 bpm	100 bpm
Matrix Permeability	1 microDarcy	1 milliDarcy
Number of Clusters per Stage	3	5
Cluster Spacing	32 ft	50 ft
Perforation Coefficient	1e9	4e9

Table 5.1 Base case and sensitivity case parameter values

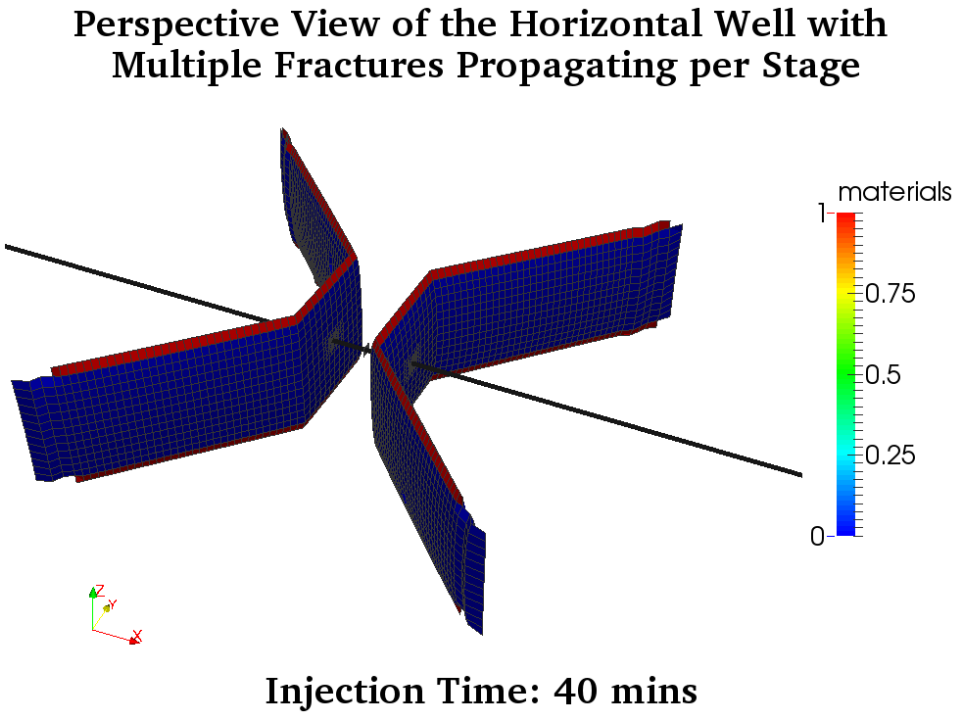

Figure 5.6 Fracture geometry of the created fractures in a horizontal well stage after 40 minutes of injection. The fractures follow the mesh description in the reservoir domain.

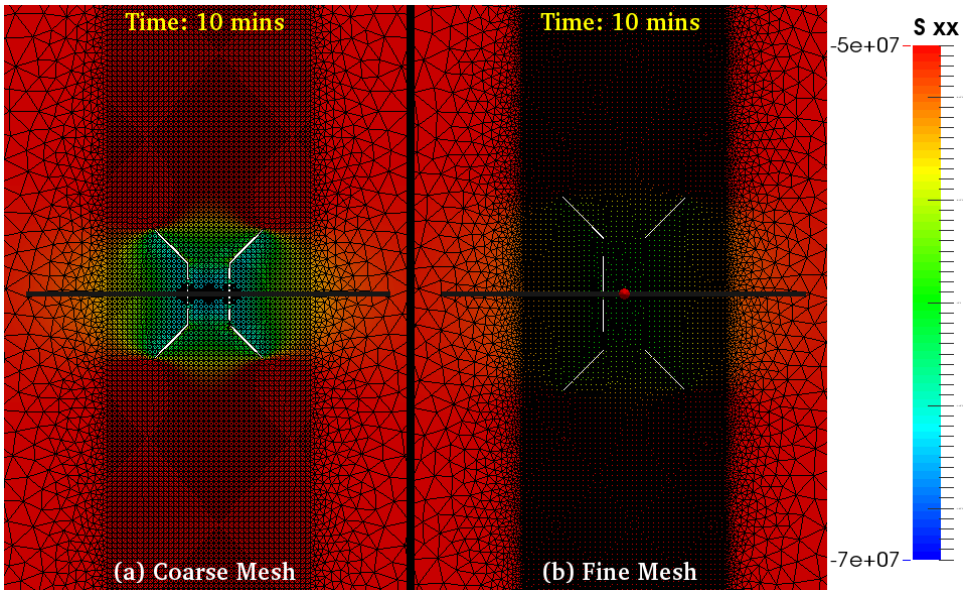

Figure 5.7 Impact of mesh size on fracture trajectory and stress.

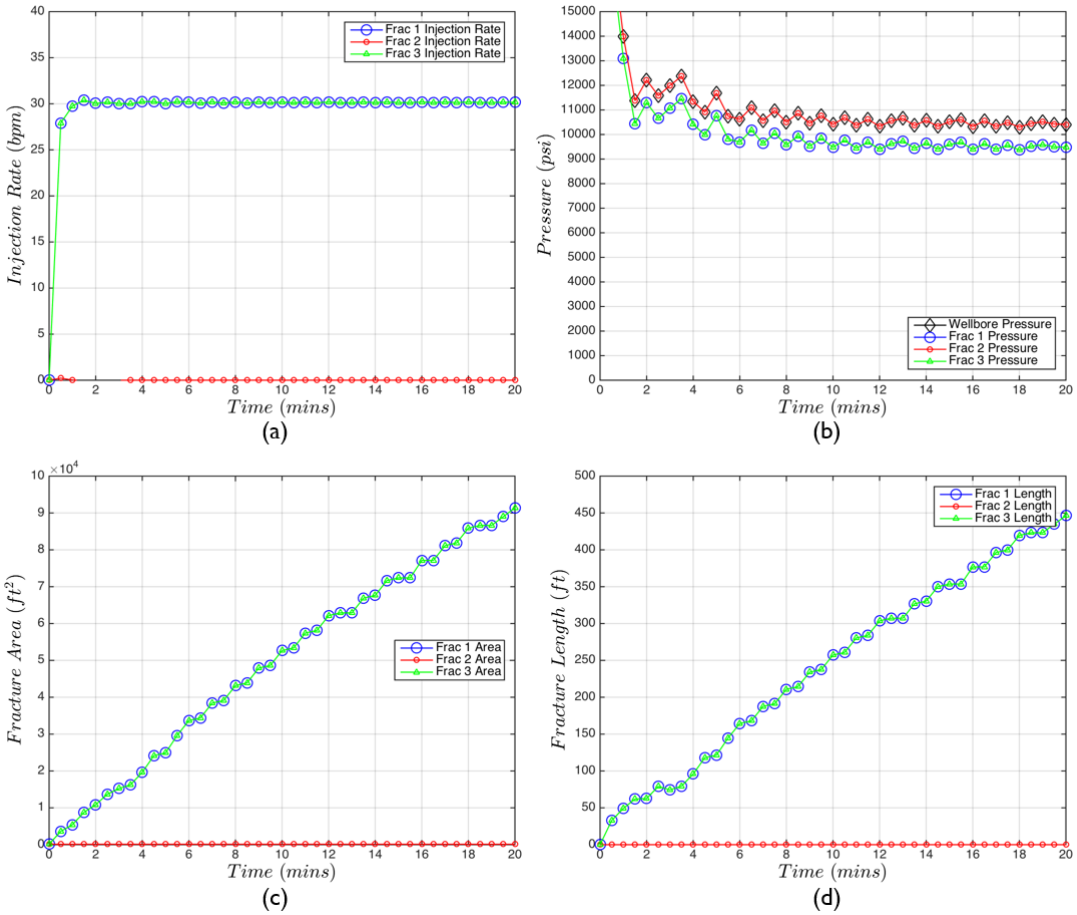

Figure 5.8 Numerical estimates of several fracturing observations. (a) injection rate in multiple fractures, (b) pressure observed in the wellbore and estimated in the fractures, (c) numerical fracture areas, (d) estimated fracture lengths.

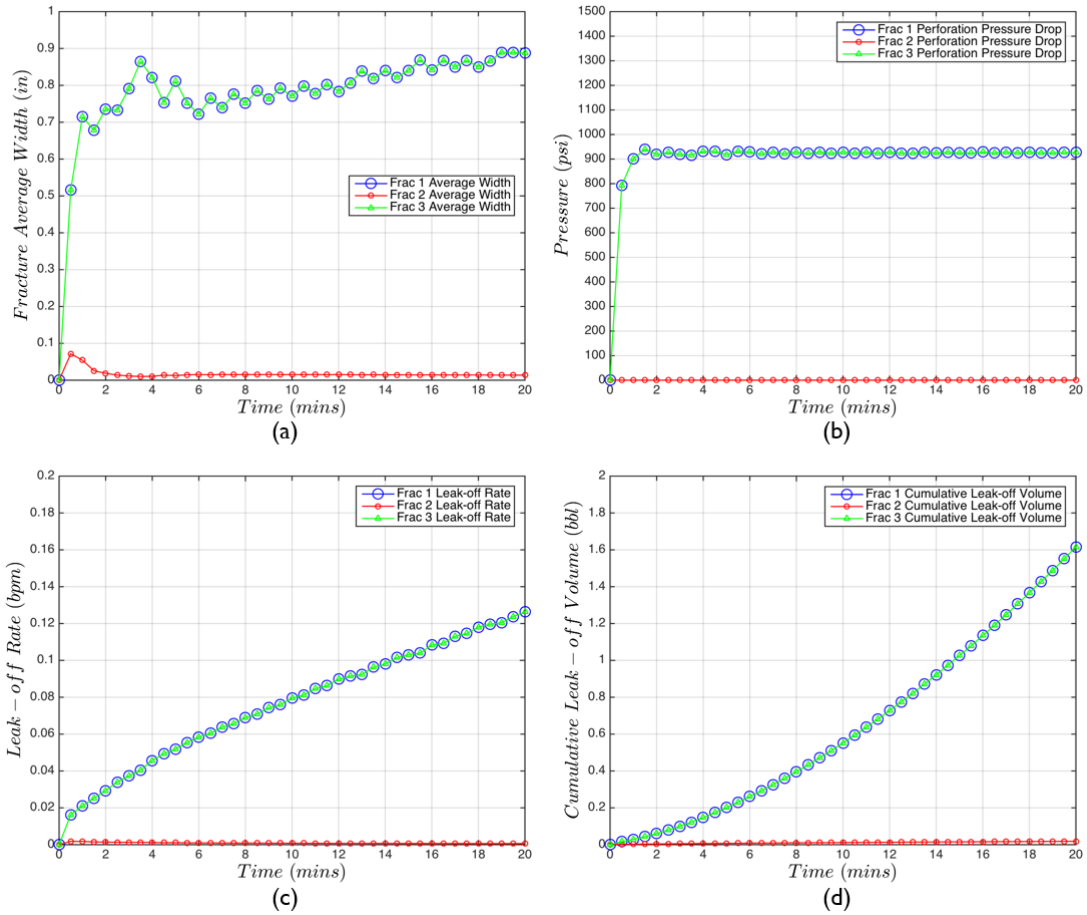

Figure 5.9 Numerical estimates of several fracturing observations. (a) fracture average width, (b) perforation pressure drop for the fractures, (c) leak-off rate from fracture surface, and (d) cumulative leak-off from each fracture.

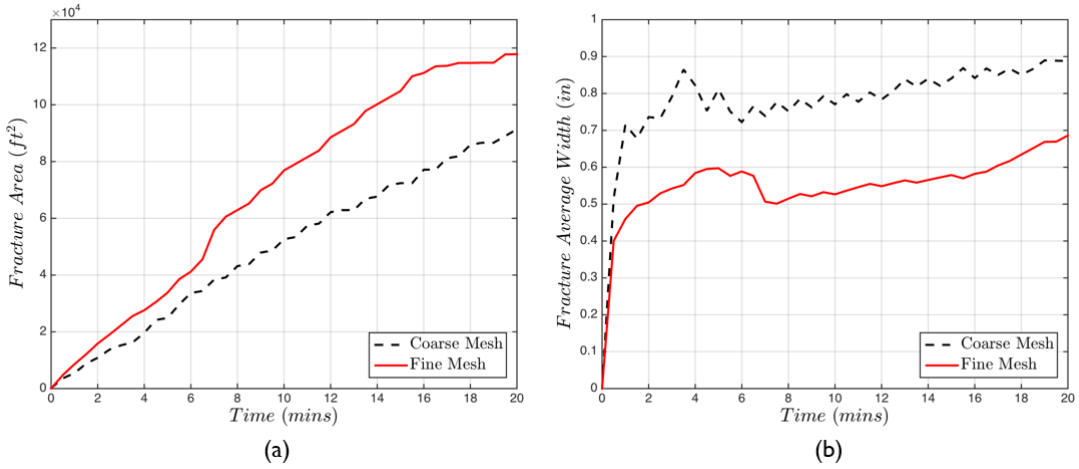

Figure 5.10 Impact of mesh size on (a) fracture area, (b) fracture average width.

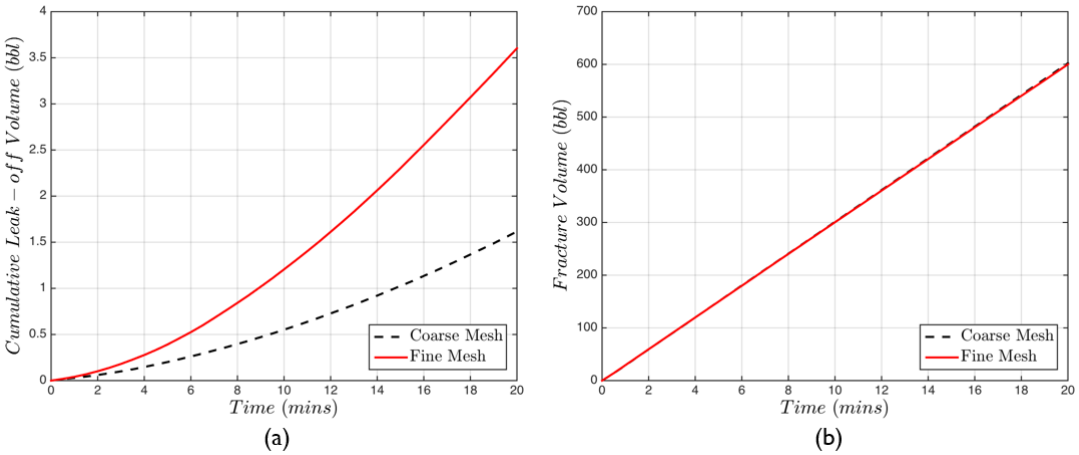

Figure 5.11 Impact of mesh size on (a) cumulative leak-off volume, and (b) fracture volume.

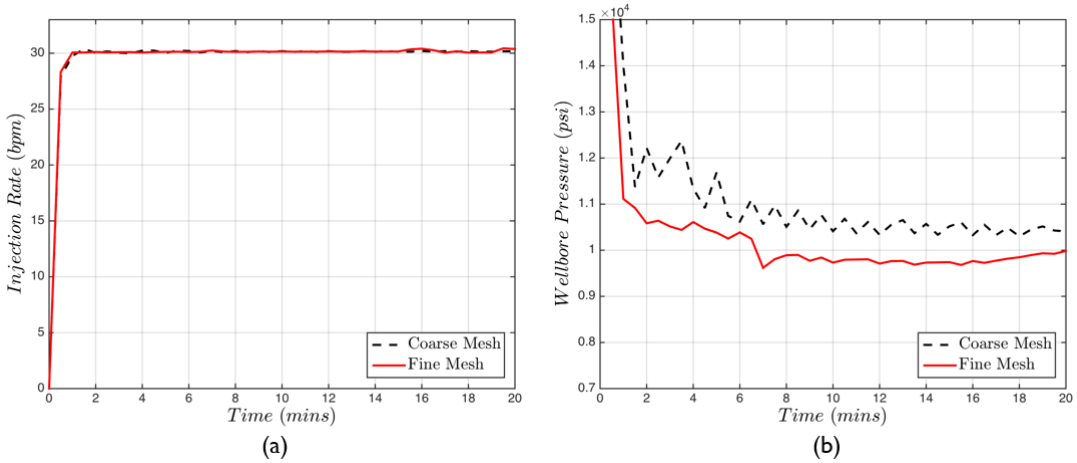

Figure 5.12 Impact of mesh size on (a) fluid rate distribution, (b) wellbore pressure.

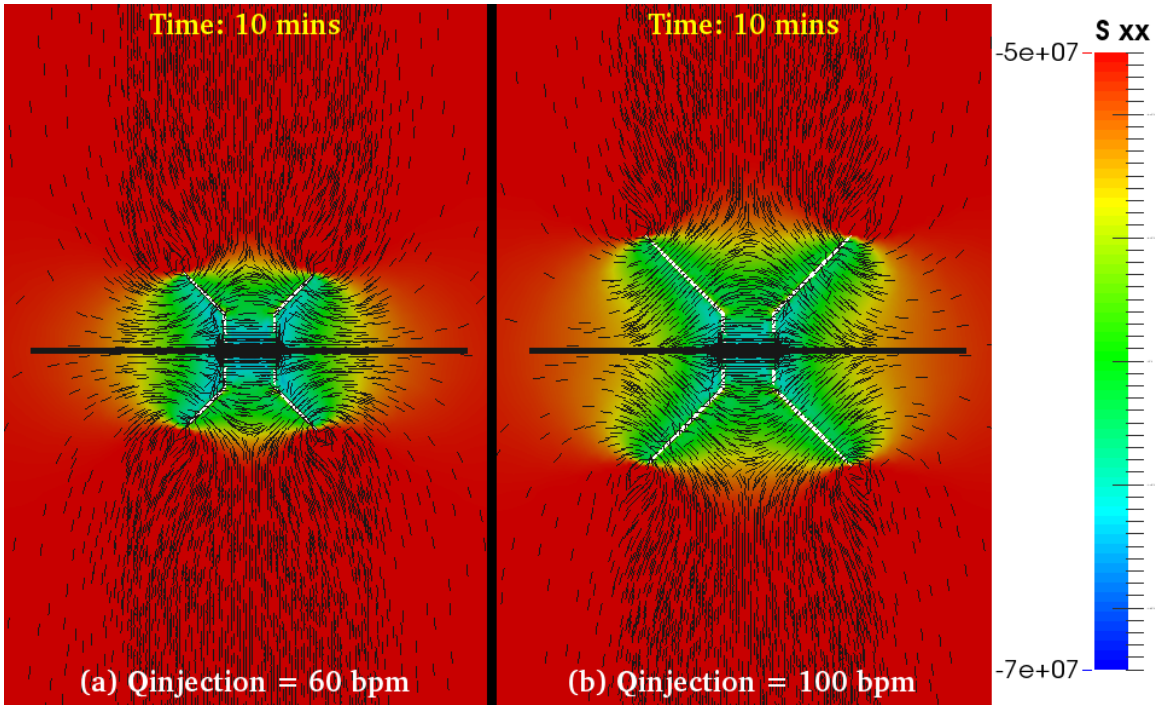

Figure 5.13 Impact of treatment injection rate on fracture trajectory and stress.

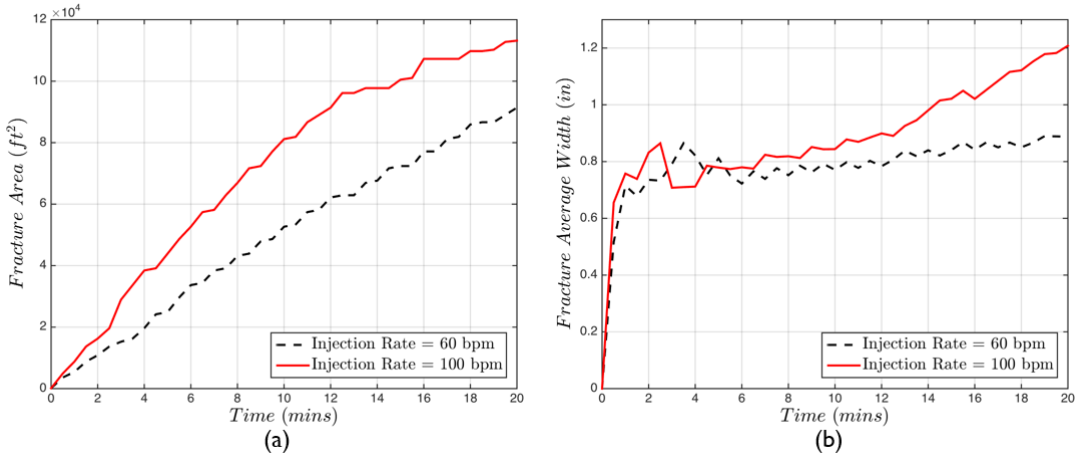

Figure 5.14 Impact of injection rate on (a) created fracture area, and (b) average fracture width.

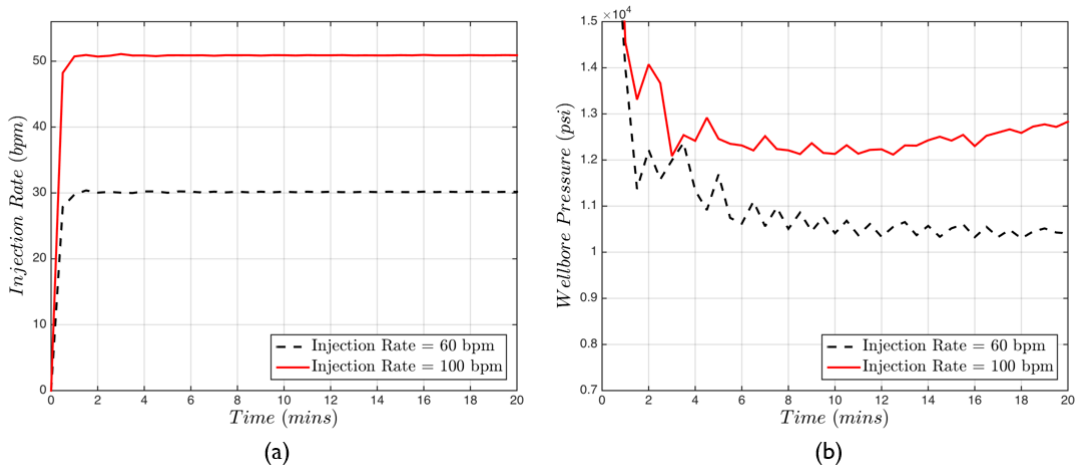

Figure 5.15 Impact of injection rate on (a) fluid distribution, and (b) wellbore pressure.

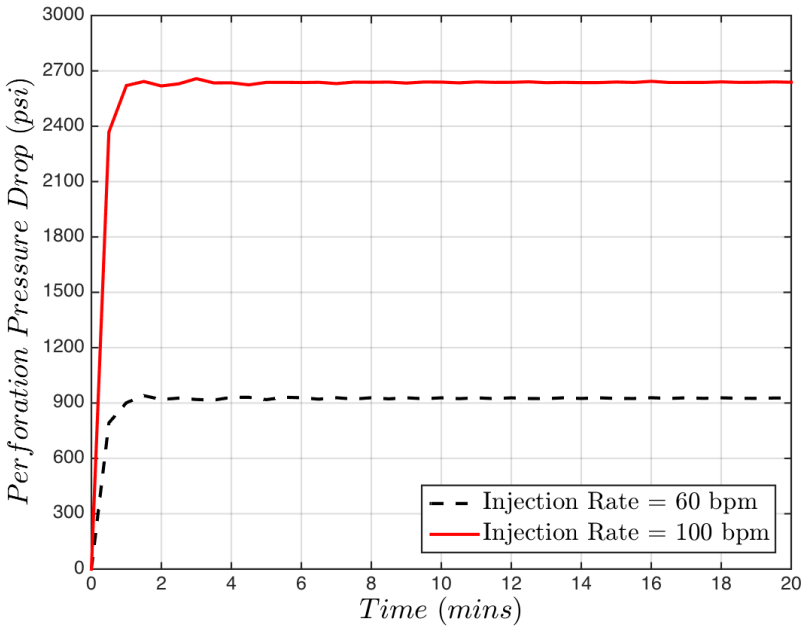

Figure 5.16 Impact of injection rate on perforation pressure drop.

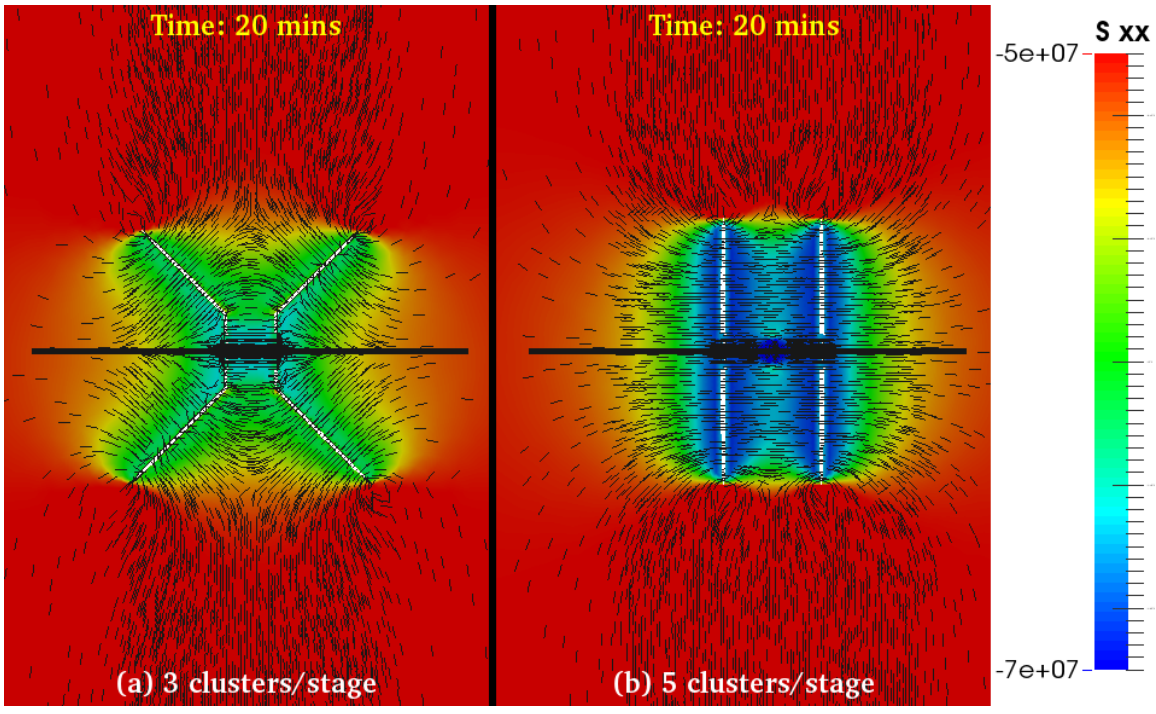

Figure 5.17 Impact of number of clusters per stage with 10 m cluster spacing on fracture trajectory and stress

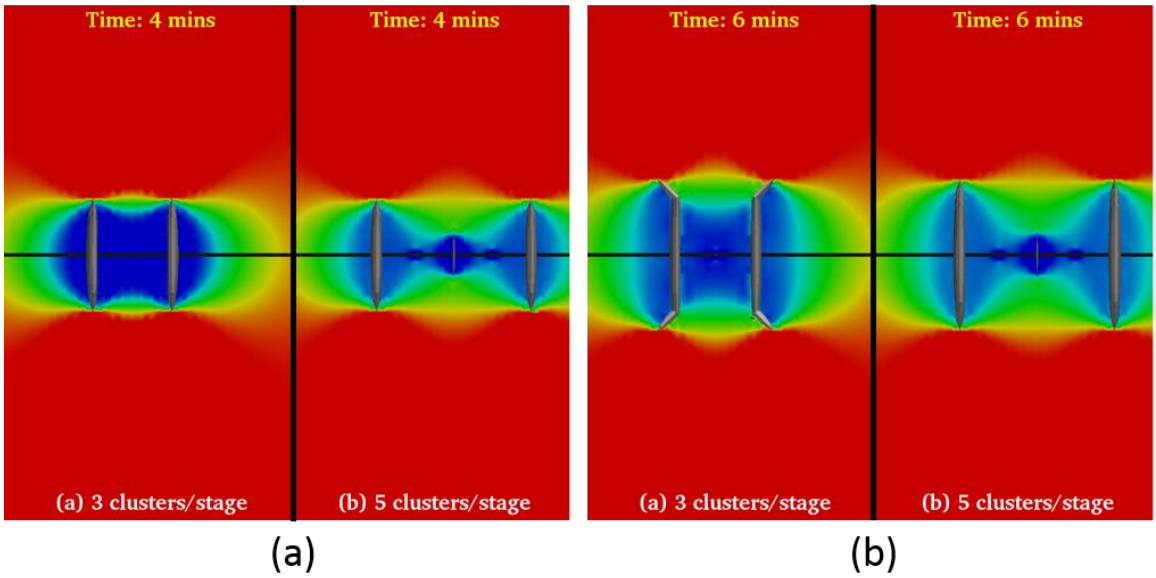

Figure 5.18 Stress relaxation between fractures caused by fracture turning (a) stress interference before fracture turning, and (b) stress interference after fracture turning for the number of clusters per stage parametric analysis case.

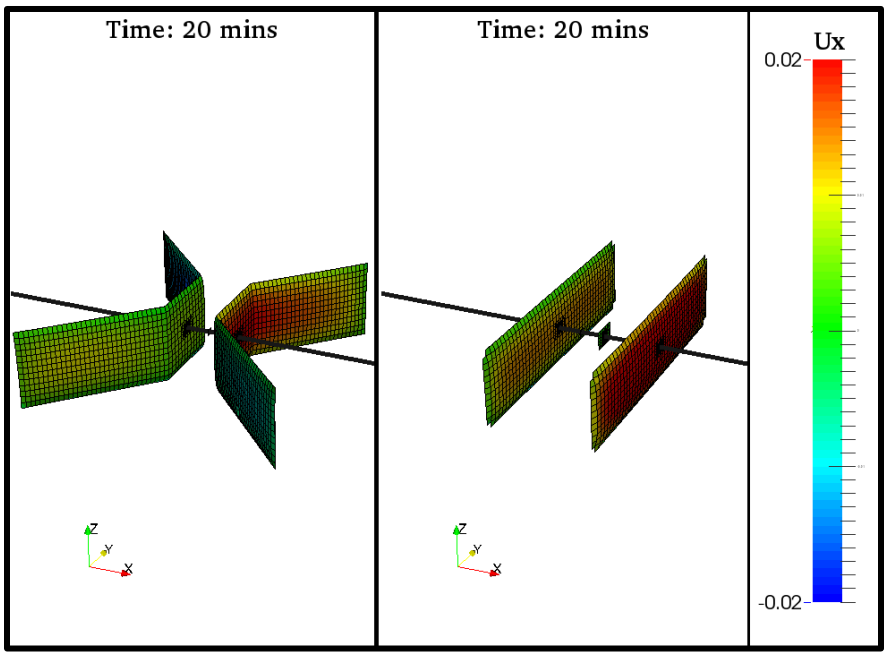

Figure 5.19 Impact of number of clusters per stage on fracture trajectory and width distribution. Left figure shows the resulting fracture trajectory for 3 cluster per stage and the right figure shows the resulting fracture trajectory for 5 clusters per stage. The displacement contours are in *m* units.

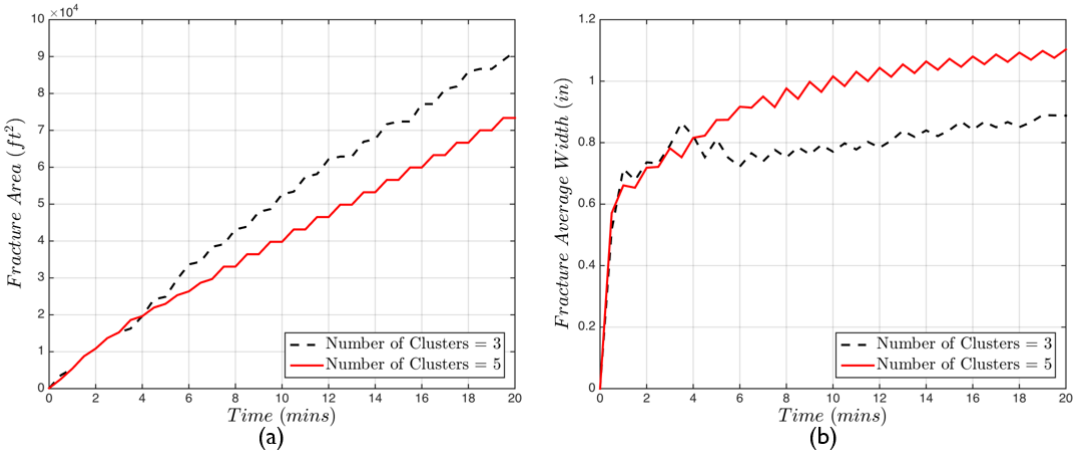

Figure 5.20 Impact of number of clusters on (a) fracture area, and (b) fracture average width.

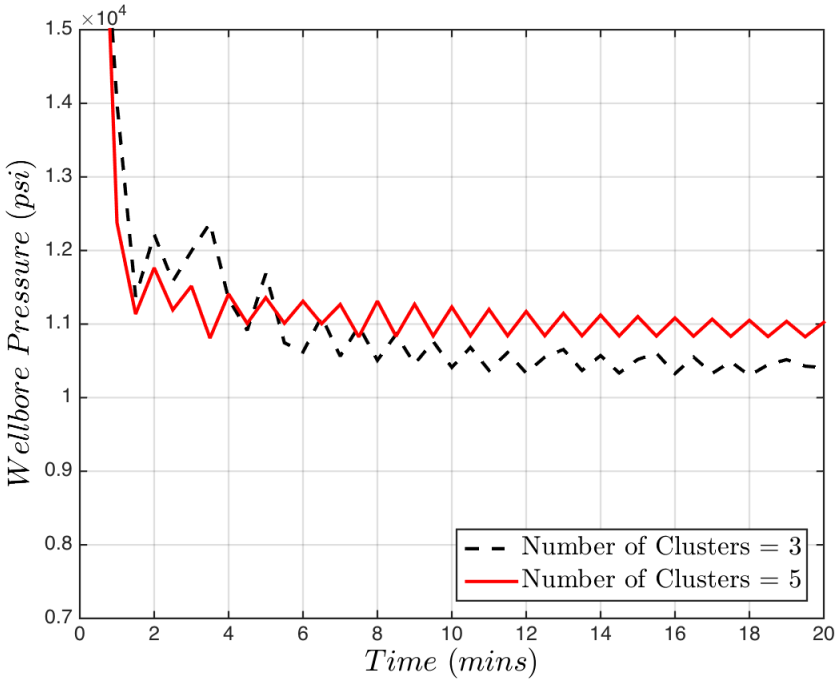

Figure 5.21 Impact of number of clusters on observed pressure

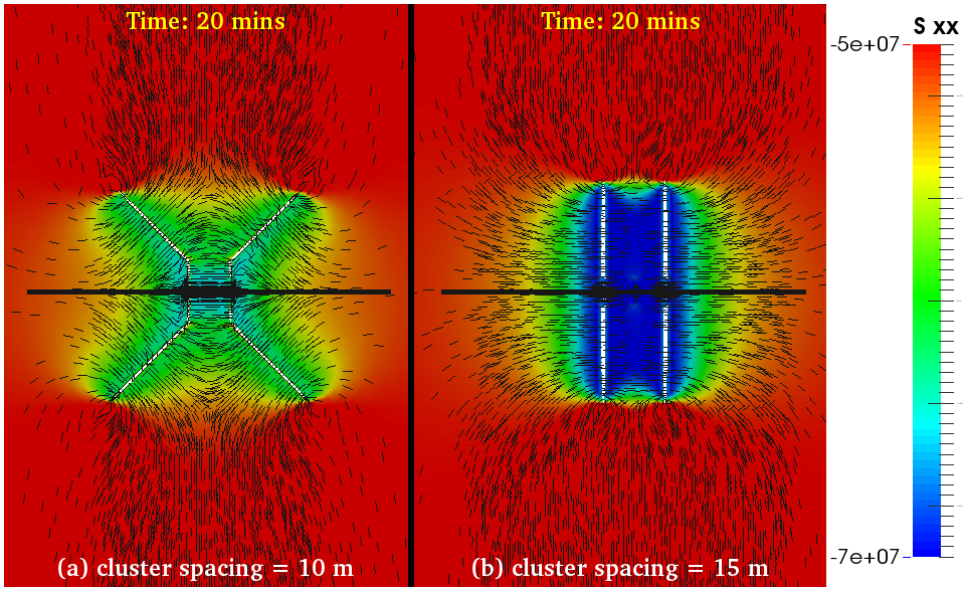

Figure 5.22 Impact of cluster spacing on fracture trajectory and stress.

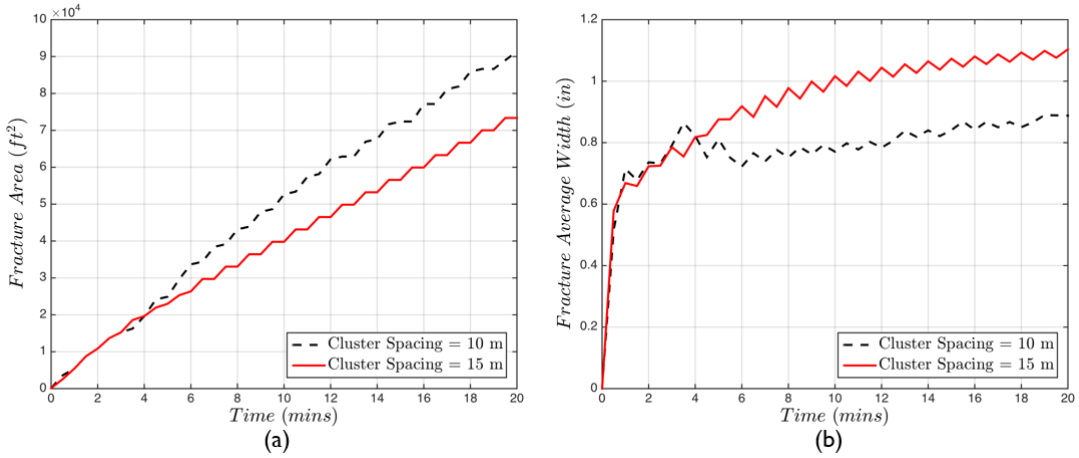

Figure 5.23 Impact of cluster spacing on (a) fracture area, and (b) average fracture width.

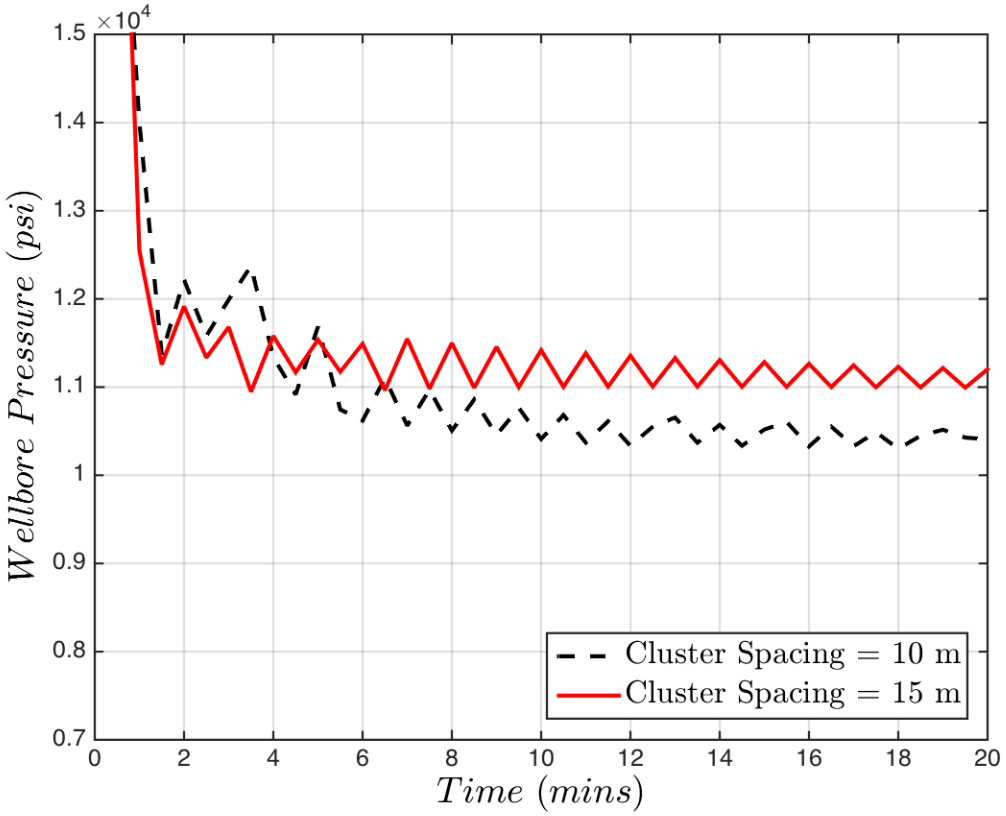

Figure 5.24 Impact of cluster spacing on observed wellbore pressure

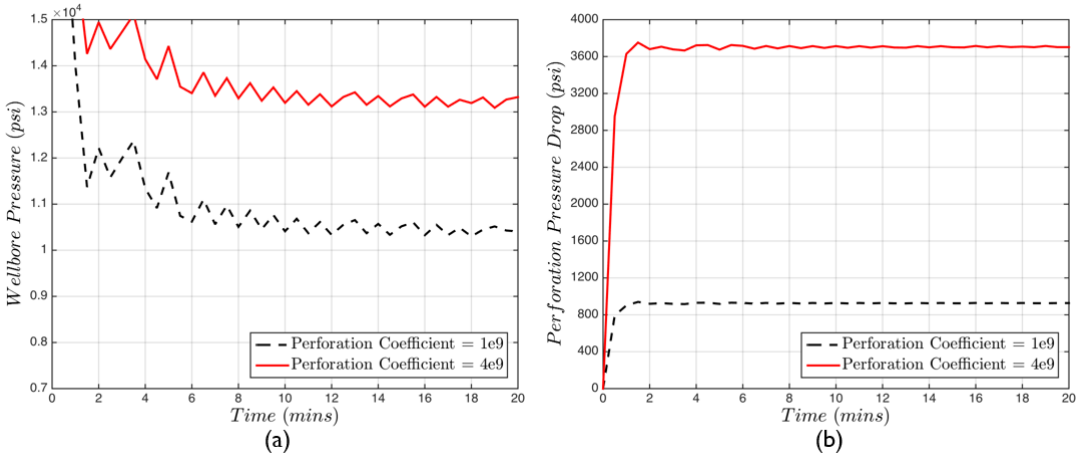

Figure 5.25 Impact of perforation coefficient on (a) wellbore pressure, and (b) perforation pressure drop.

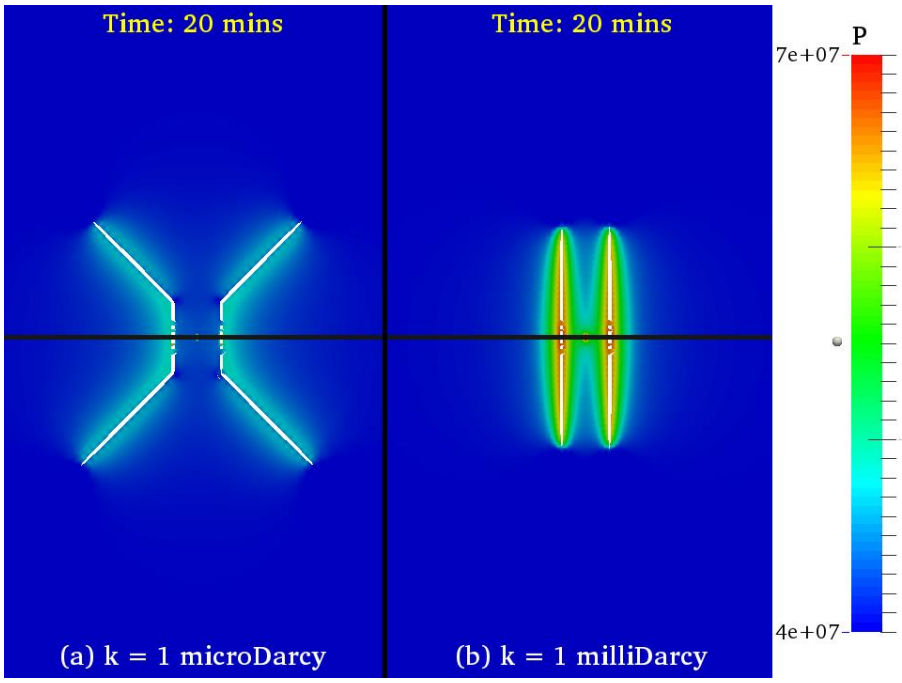

Figure 5.26 Impact of matrix permeability on fracture trajectory and pressure distribution

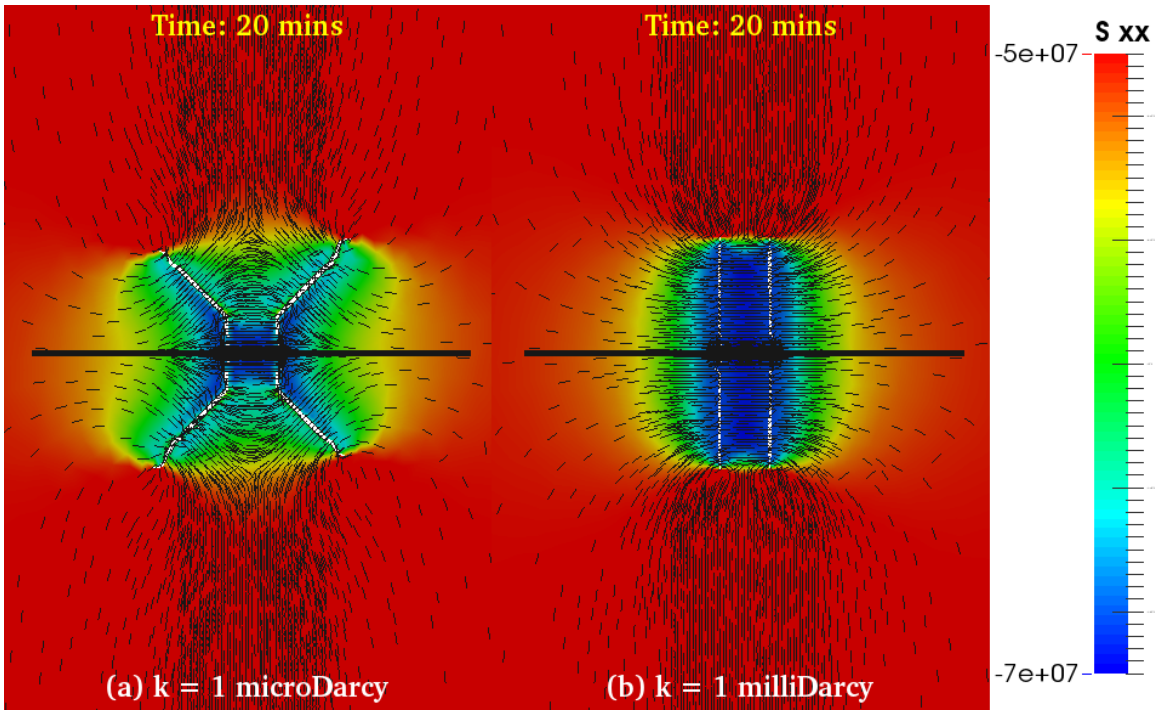

Figure 5.27 Impact of matrix permeability on fracture trajectory and stress.

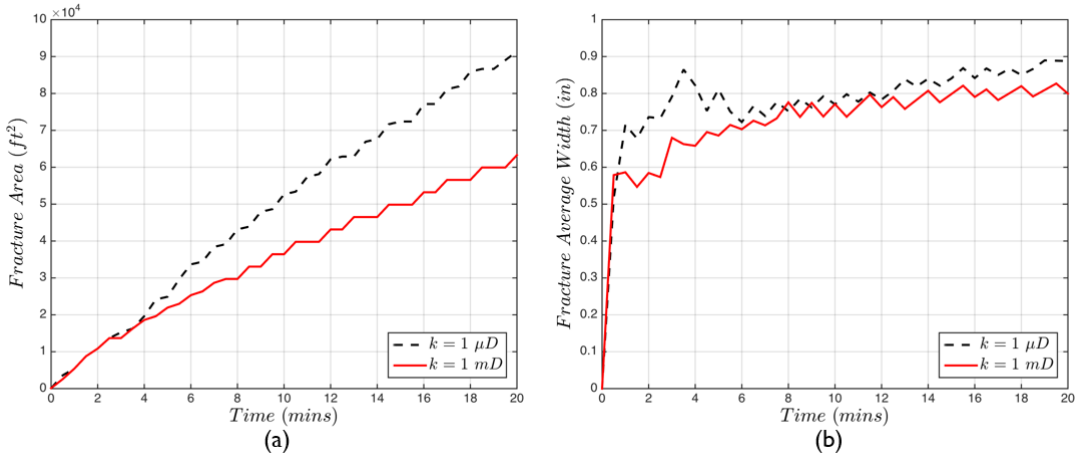

Figure 5.28 Impact of matrix permeability on (a) fracture area, and (b) average fracture width.

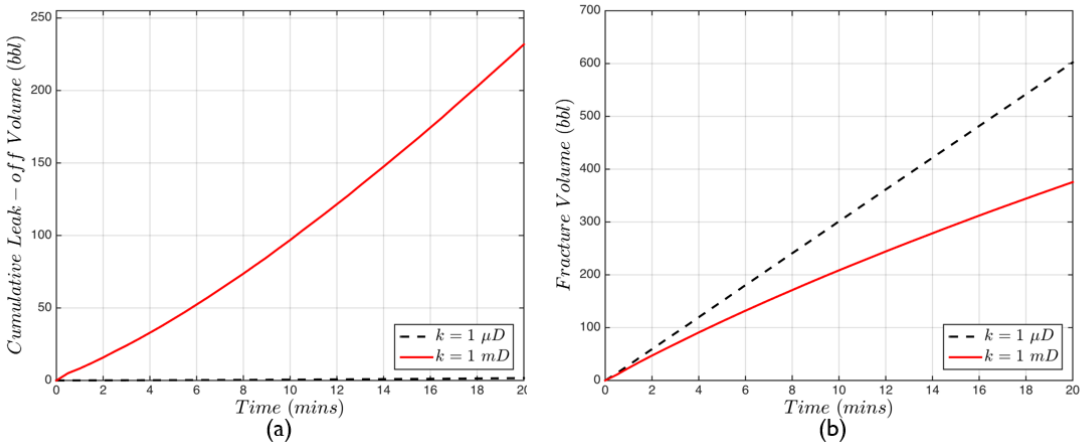

Figure 5.29 Impact of permeability on (a) cumulative leak-off volume and (b) fracture volume.

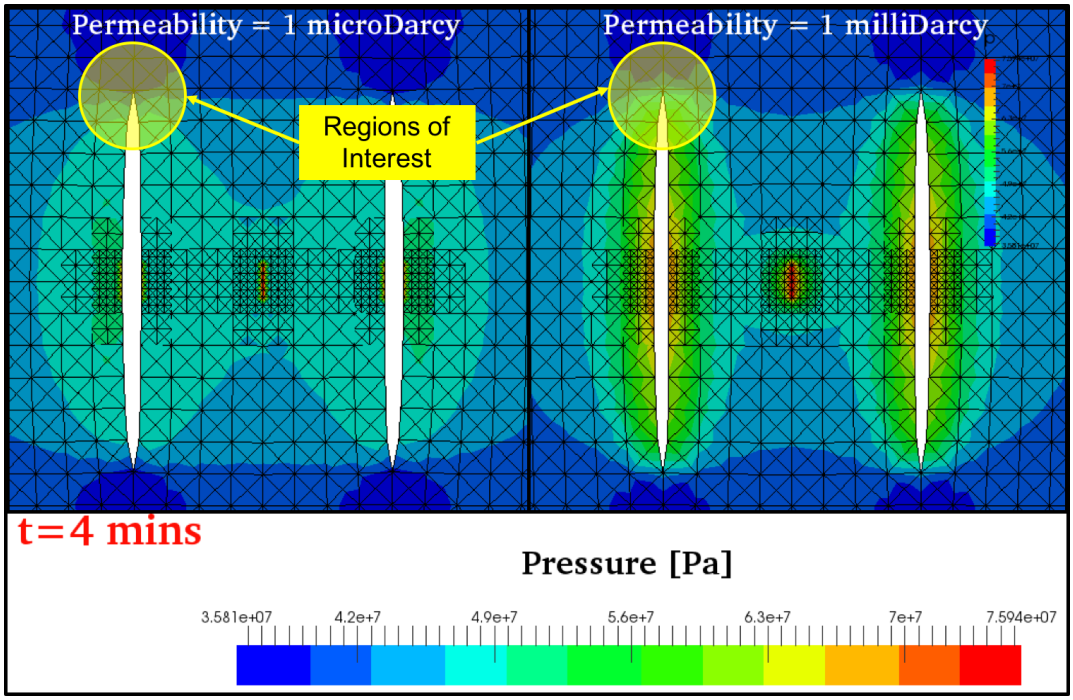

Figure 5.30 Fracture geometry after 4 minutes of injection for the cases of low and high permeability.

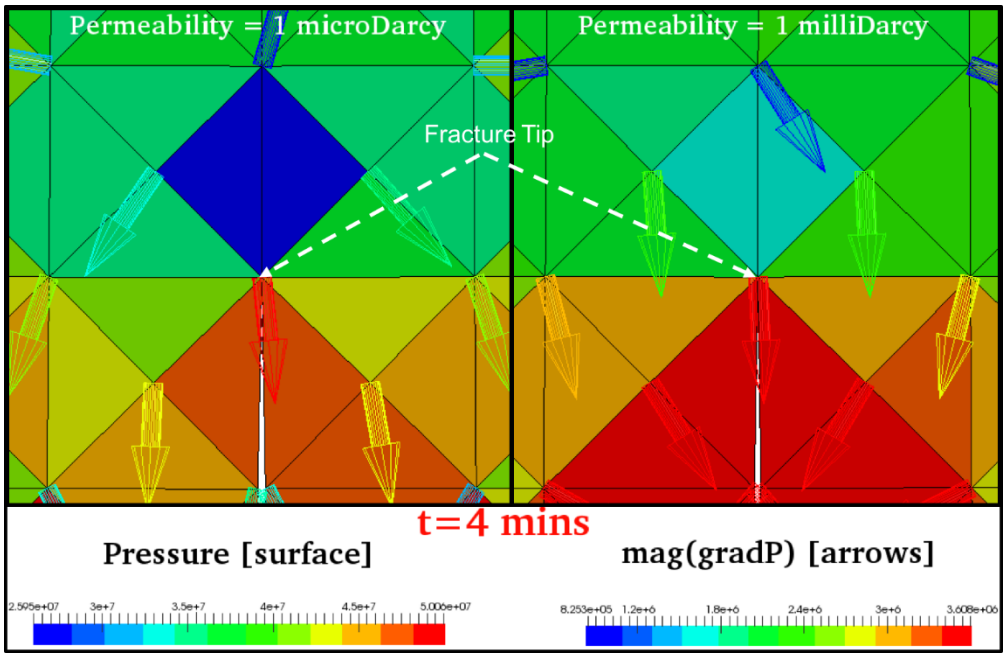

Figure 5.31 Pressure contours and pressure gradient vectors in the vicinity of the fracture tip for the two cases of matrix permeability after 4 minutes of injection.

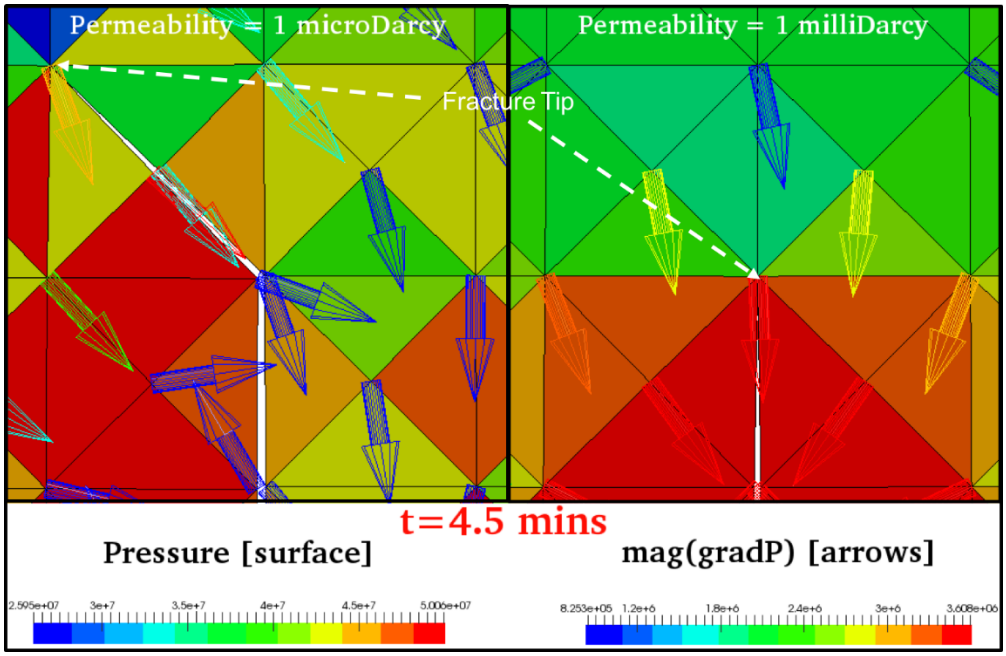

Figure 5.32 Pressure contours and pressure gradient vectors in the vicinity of the fracture tip for the two cases of matrix permeability after 4.5 minutes of injection.

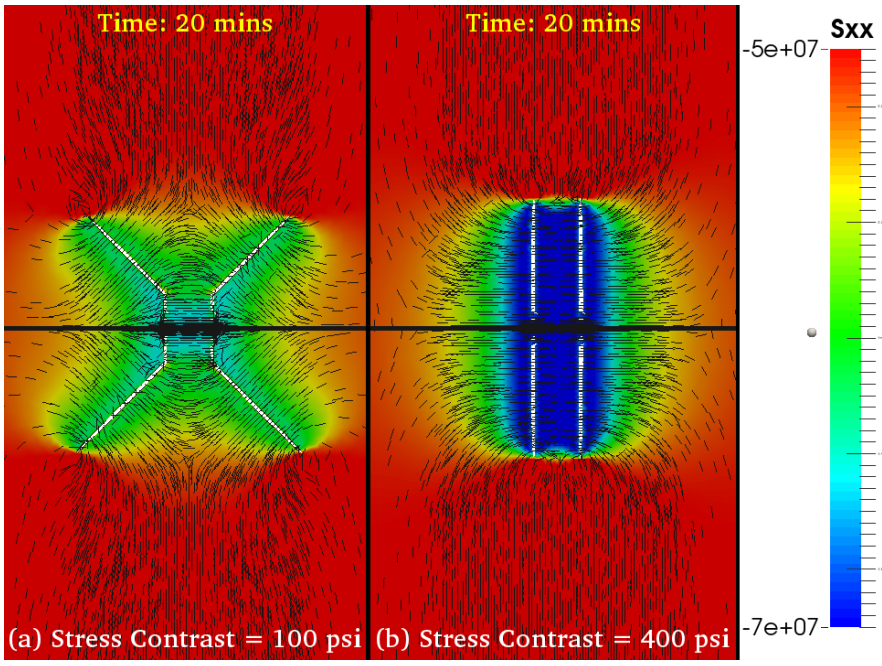

Figure 5.33 Impact of *in-situ* stress contrast on fracture trajectory and the induced stresses

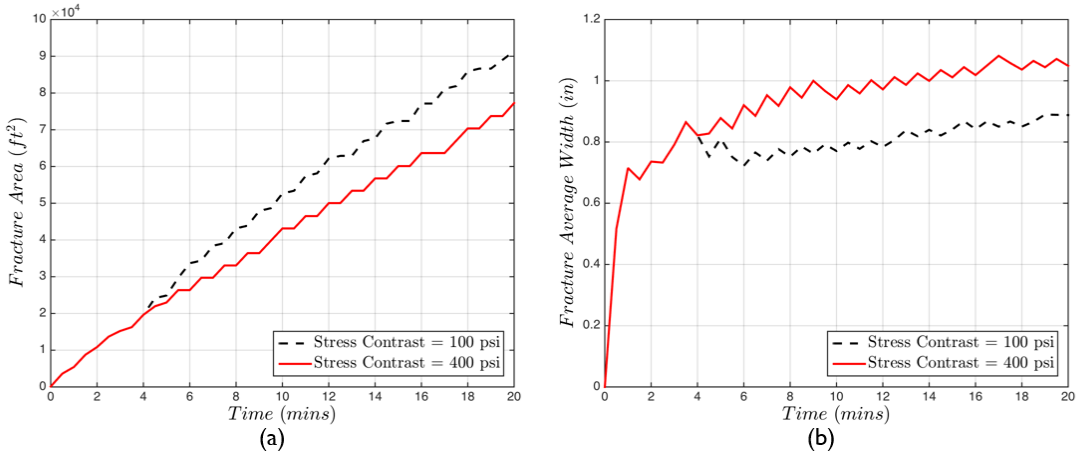

Figure 5.34 Impact of stress contrast on (a) fracture area, and (b) average fracture width.

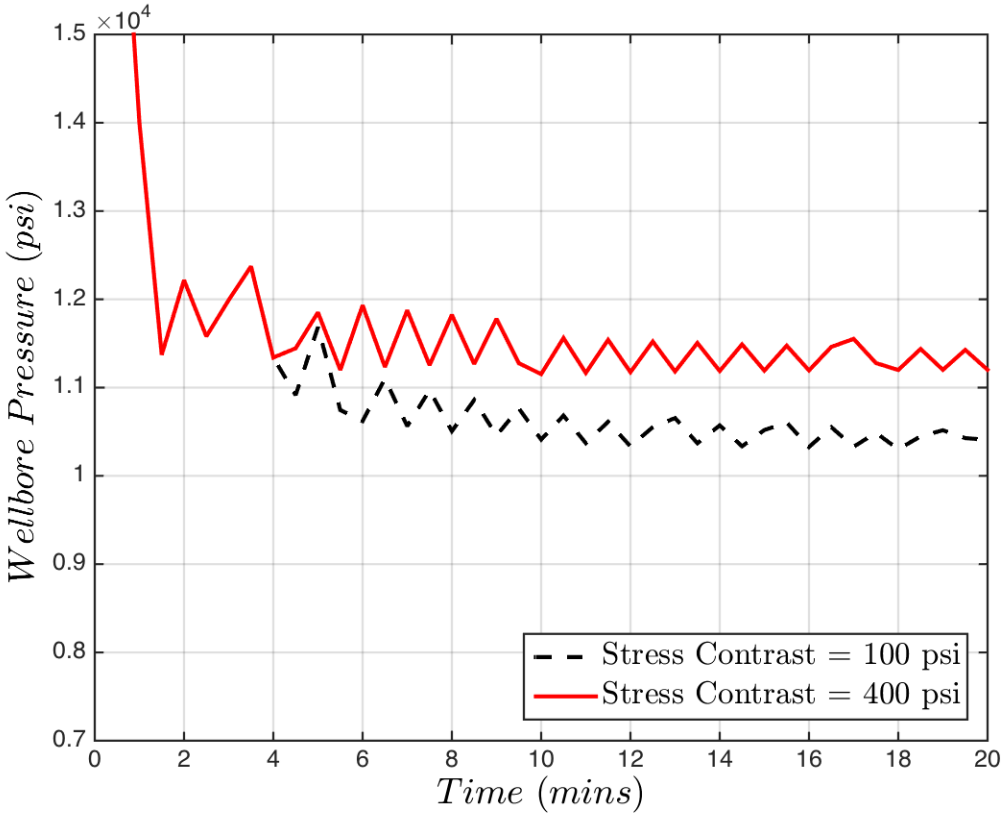

Figure 5.35 Impact of stress contrast on wellbore pressure.

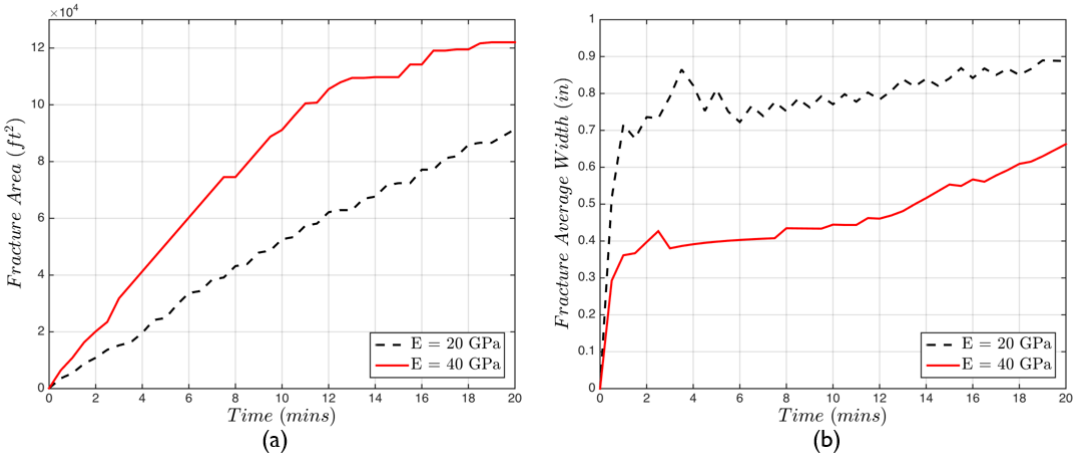

Figure 5.36 Impact of Young's Modulus on (a) fracture area, and (b) average fracture width.

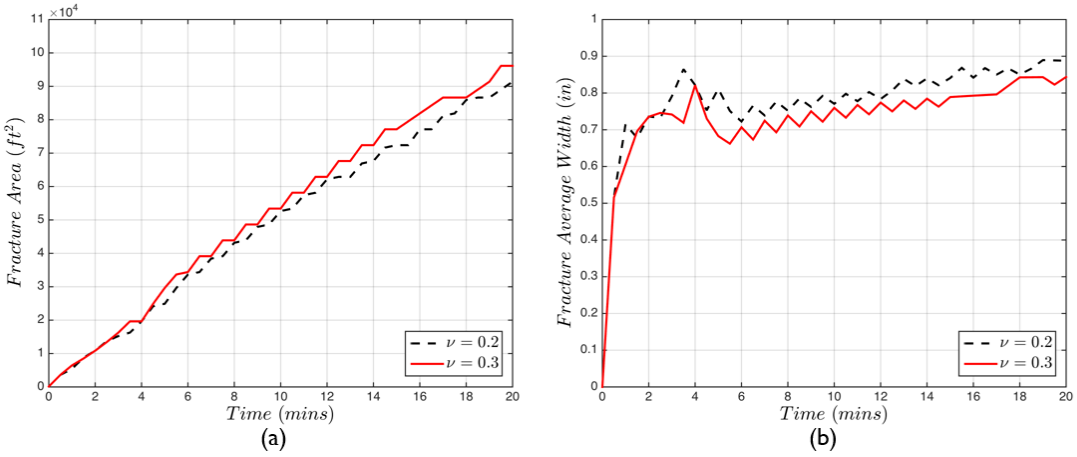

Figure 5.37 Impact on Poisson's ratio on (a) fracture area, and (b) average fracture width.

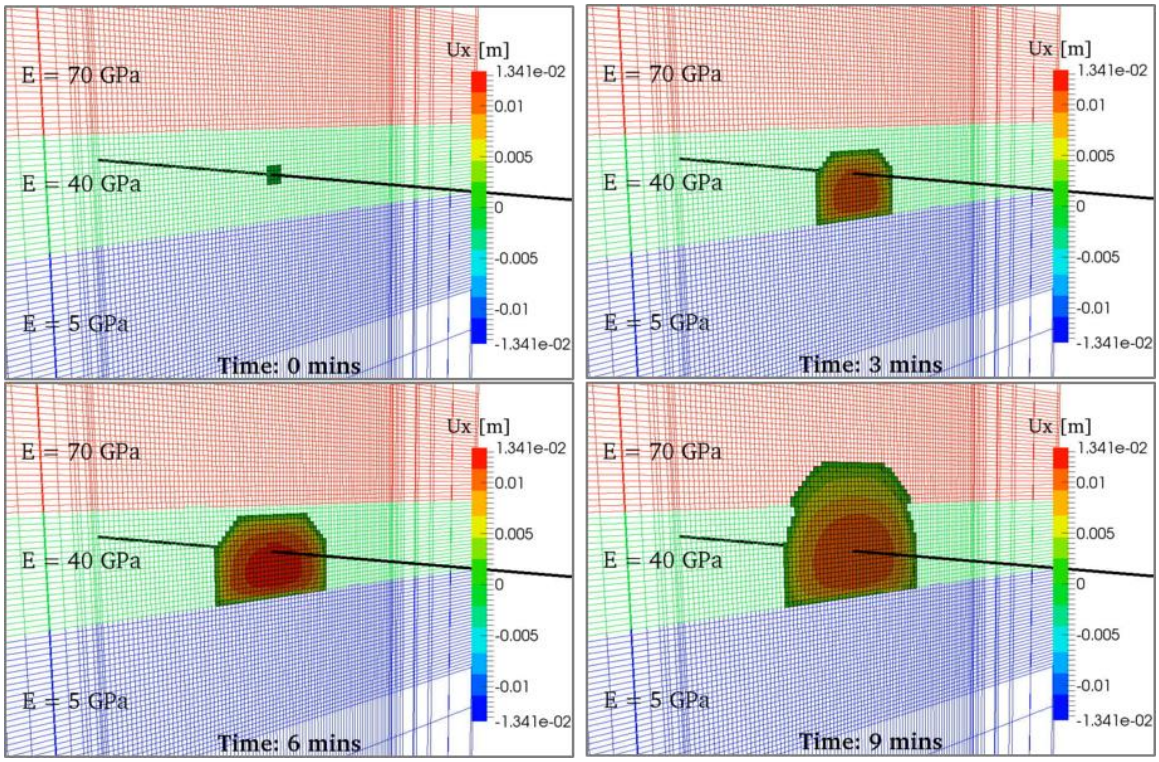

Figure 5.38 Impact of layer heterogeneity on fracture height growth.

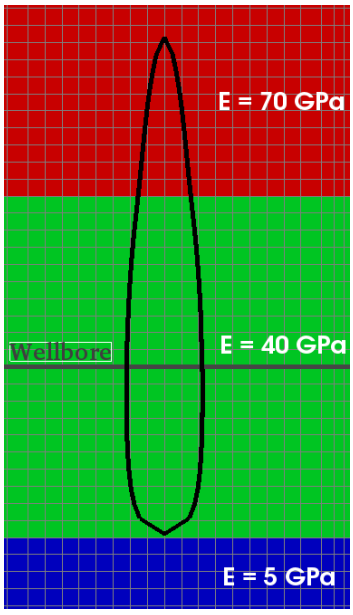

Figure 5.39 Impact of layer heterogeneity on fracture width profile.

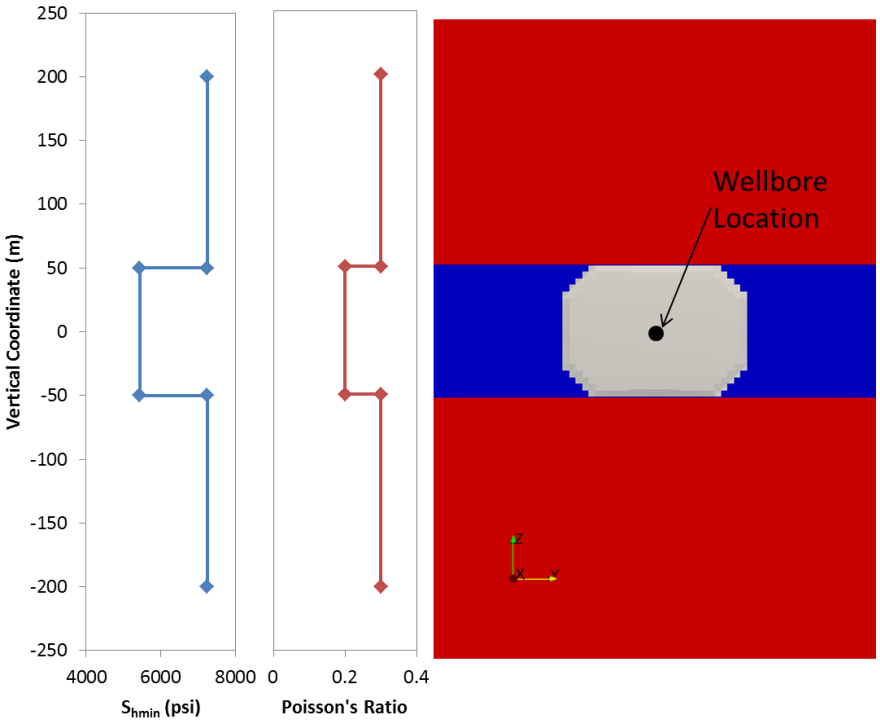

Figure 5.40 Minimum principal stress and Poisson's ratio as a function of vertical coordinate. Horizontal wellbore passes through z = 0. Fracture containment in evident.

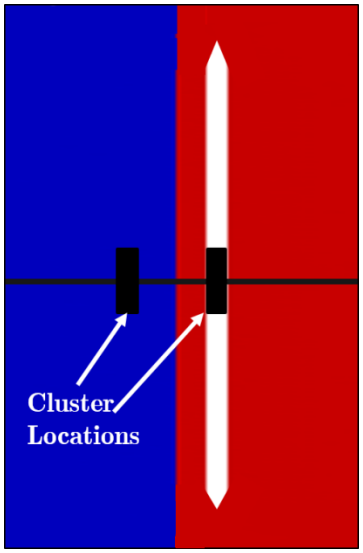

Figure 5.41 Impact of lateral heterogeneity on fracture propagation. The blue region and the red region have contrasting values in all the simulations.

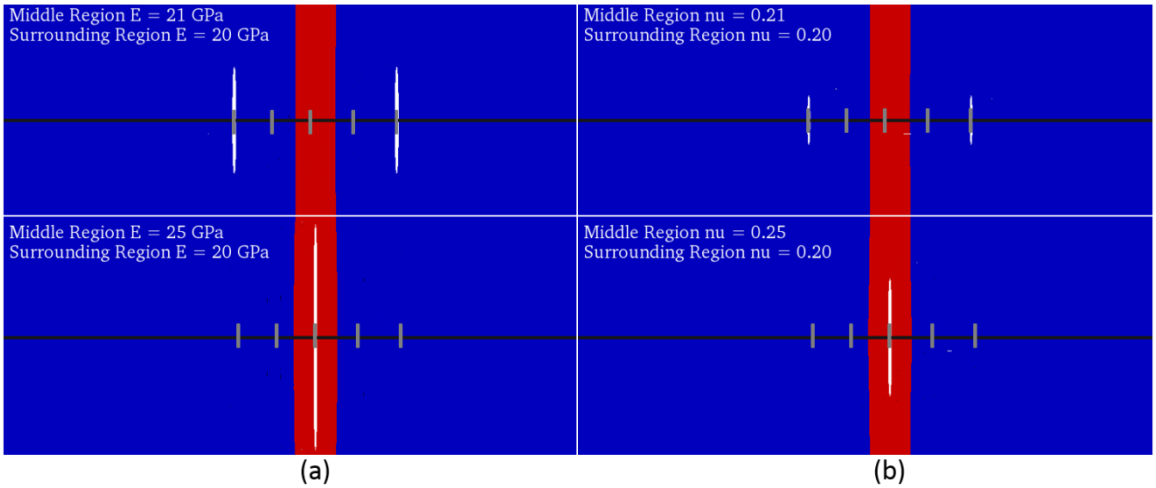

Figure 5.42 Impact of lateral heterogeneity on multiple fracture propagation in a 5 cluster stage (a) variation in Young's modulus, (b) variation in Poisson's ratio. Grey vertical lines represent the clusters in the fracturing stage. The mechanical properties in the red band region depict the lateral heterogeneity.

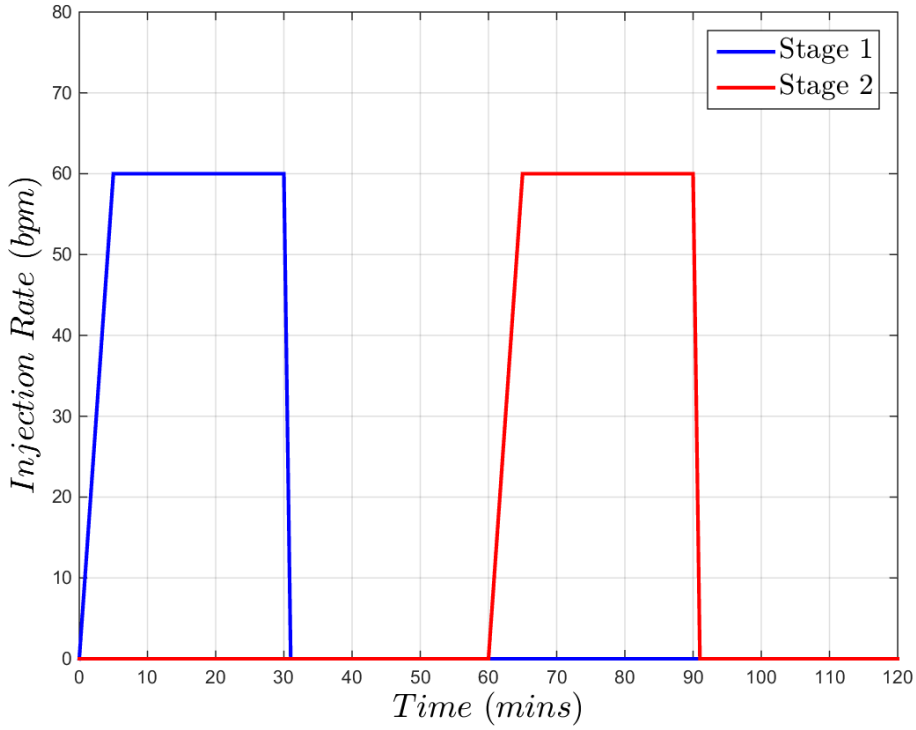

Figure 5.43 Treatment profile for the two fracturing stages.

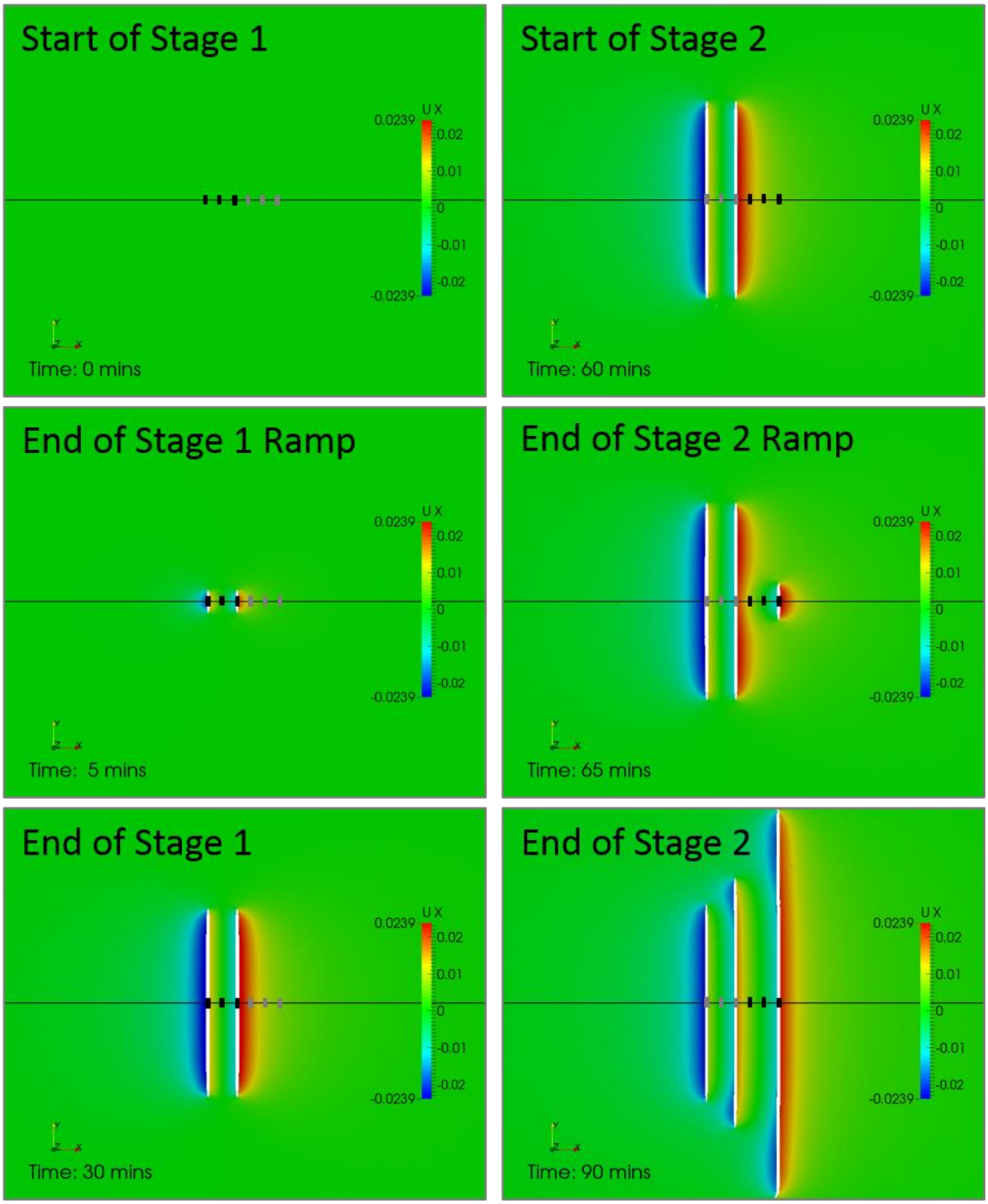

Figure 5.44 Simulation results for propagation of multi-cluster multi-stage fracture propagation showing displacement contours. Active clusters are shown as black vertical lines on the figures.

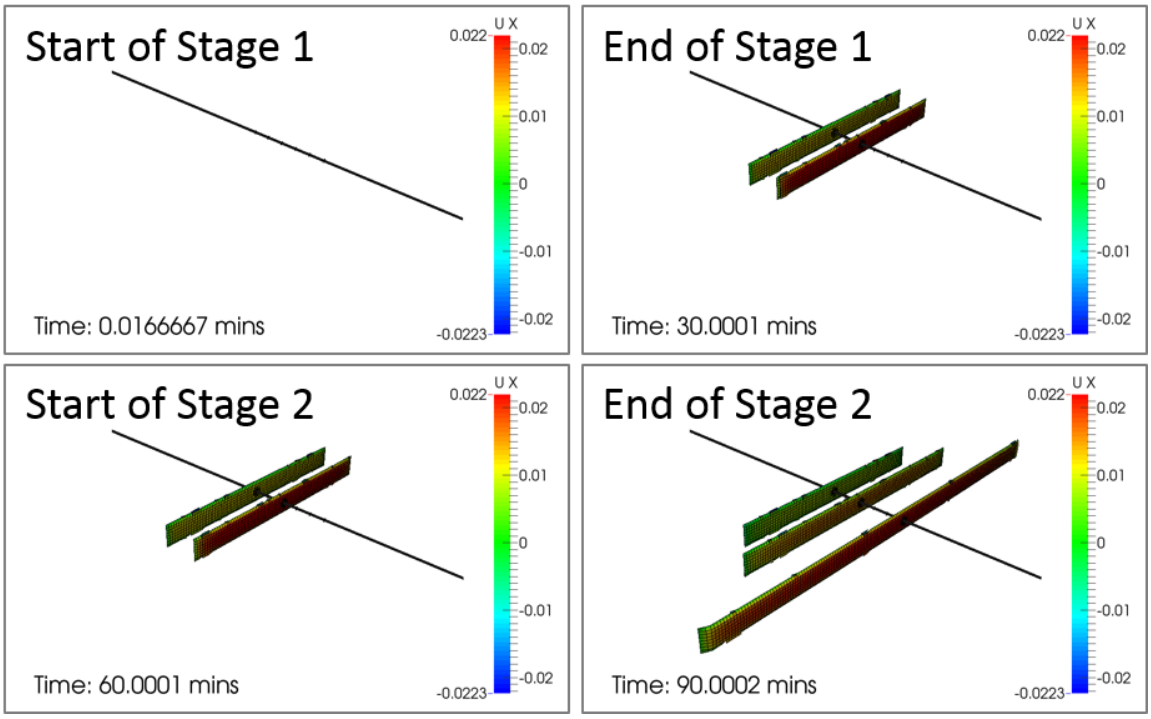

Figure 5.45 Fracture trajectories in multi-cluster multi-stage fracturing simulation.

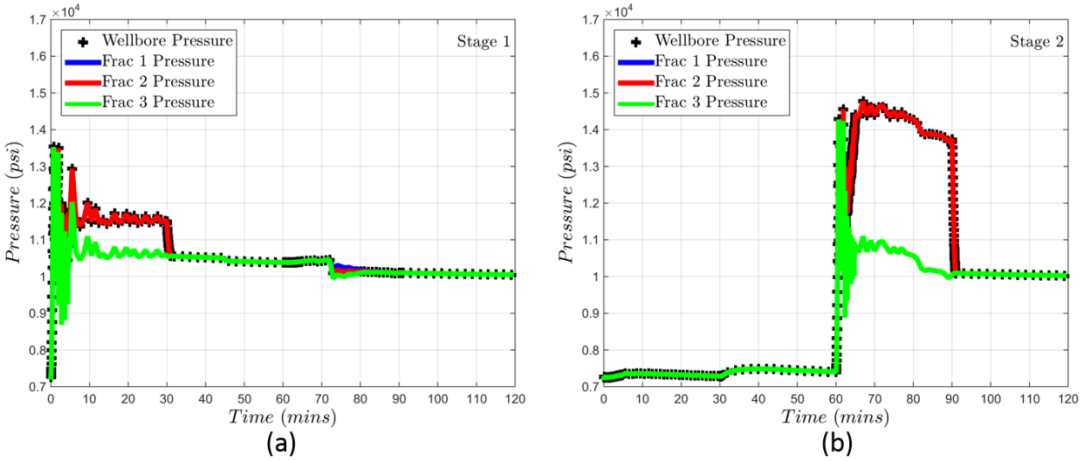

Figure 5.46 Simulated treatment pressure for (a) stage 1, (b) stage 2.

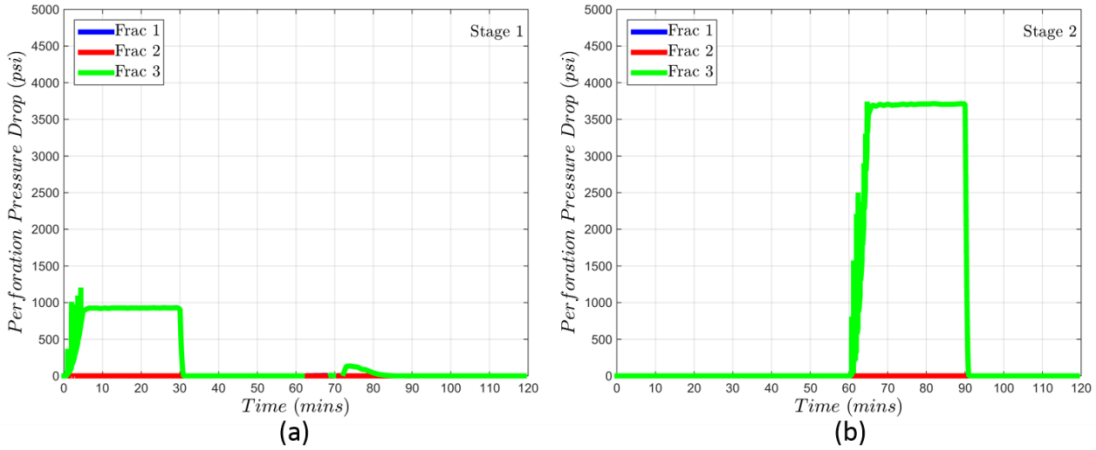

Figure 5.47 Simulated perforation pressure drop for fractures in (a) stage 1, (b) stage 2.

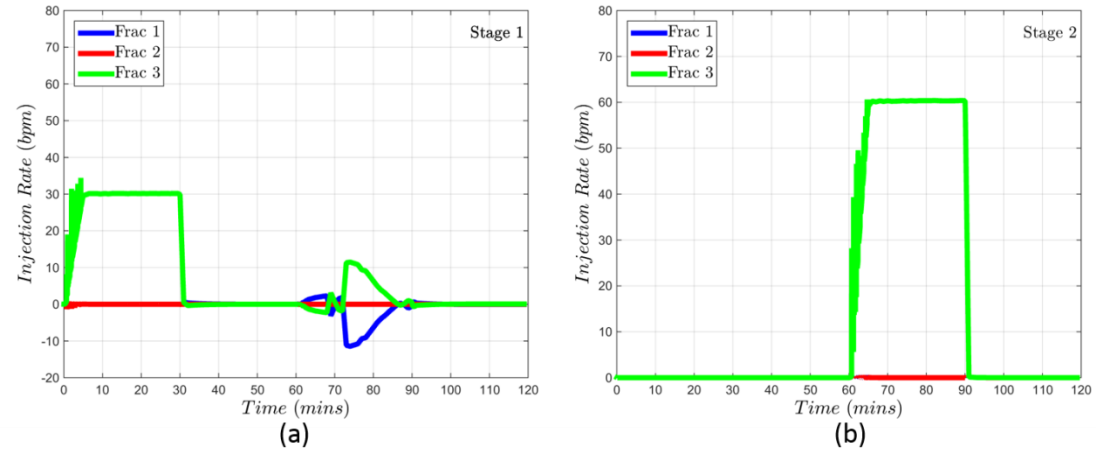

Figure 5.48 Simulated injection rate for fractures in (a) stage 1, (b) stage 2.

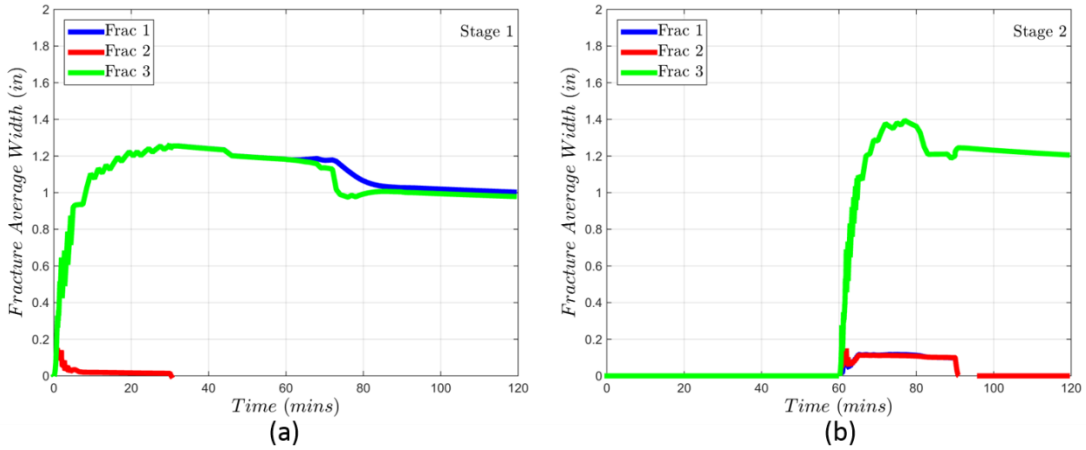

Figure 5.49 Simulated fracture widths for (a) stage 1, (b) stage 2.

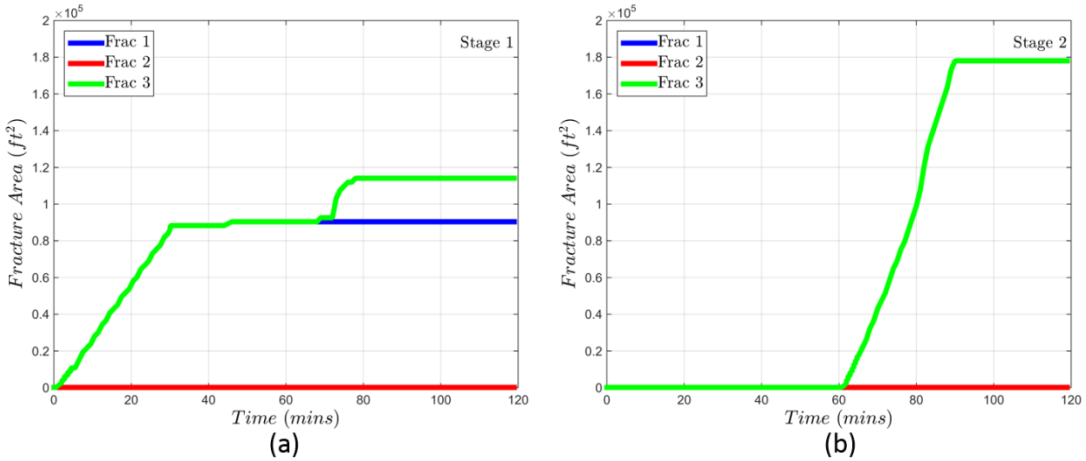

Figure 5.50 Simulated fracture area for (a) stage 1, (b) stage 2.

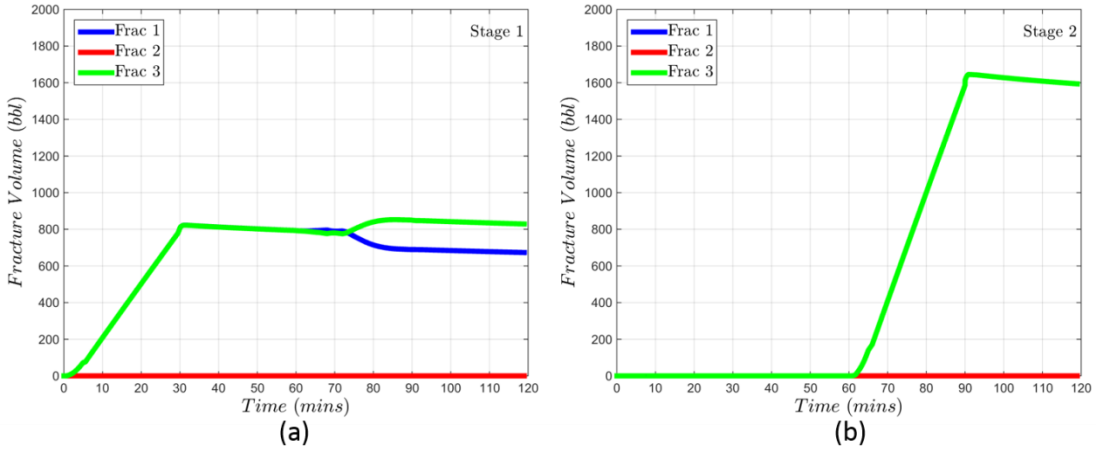

Figure 5.51 Simulated fracture volume for (a) stage 1, (b) stage 2.

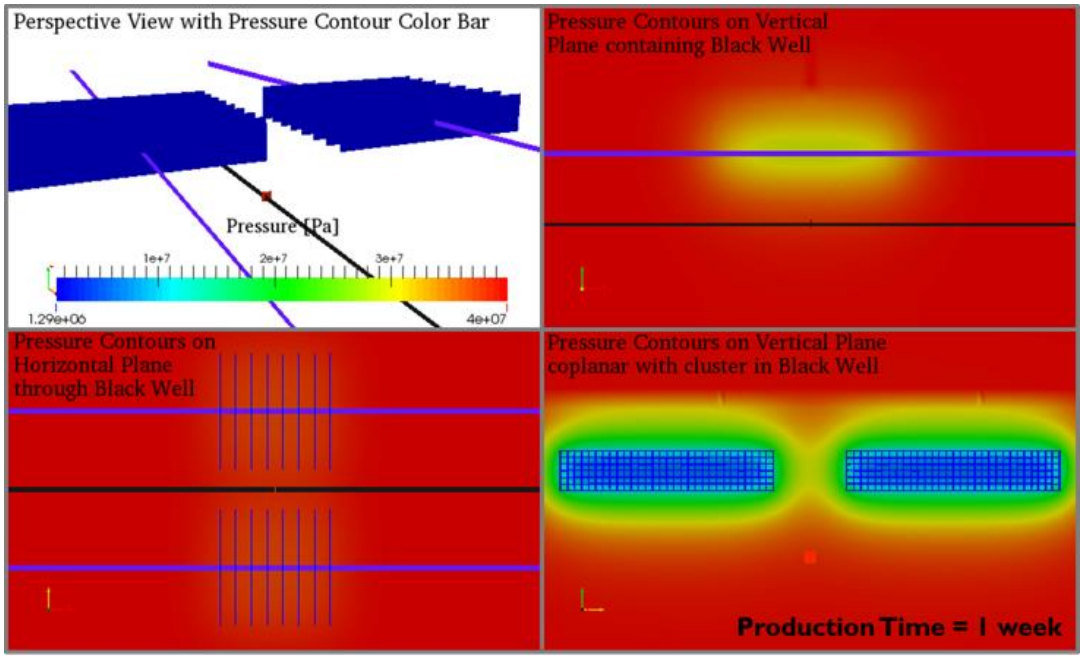

(a)

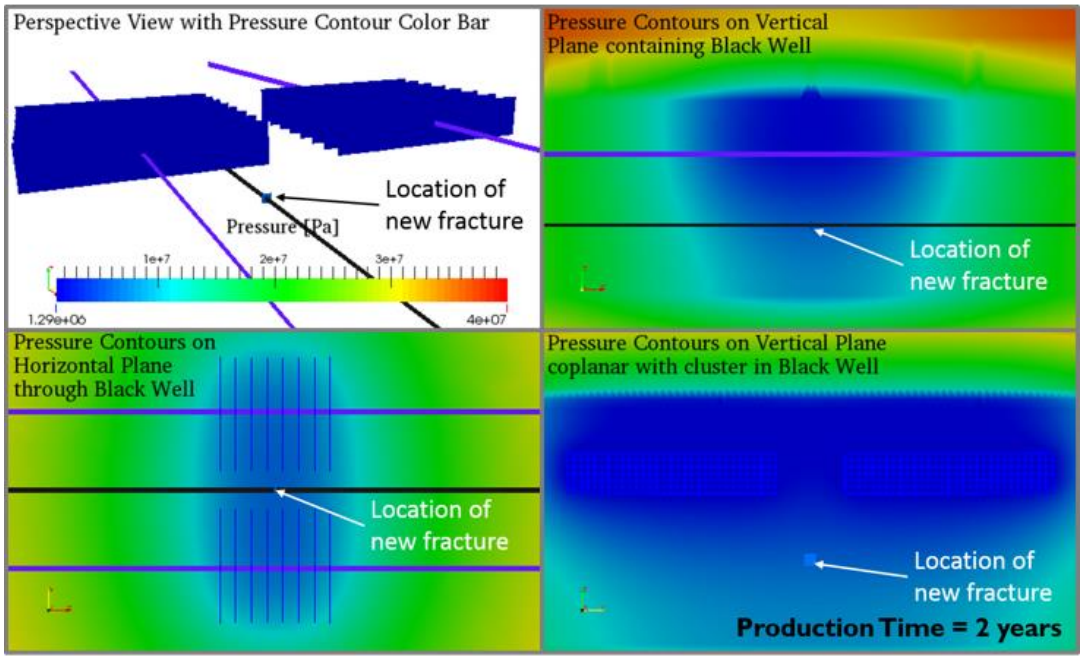

(b)

Figure 5.52 Impact of horizontal well production on pressure depletion in a multi-zone multi-well hydraulic fracturing pad (a) pressure distribution after 1 week of production, (b) pressure distribution after 2 years of production.

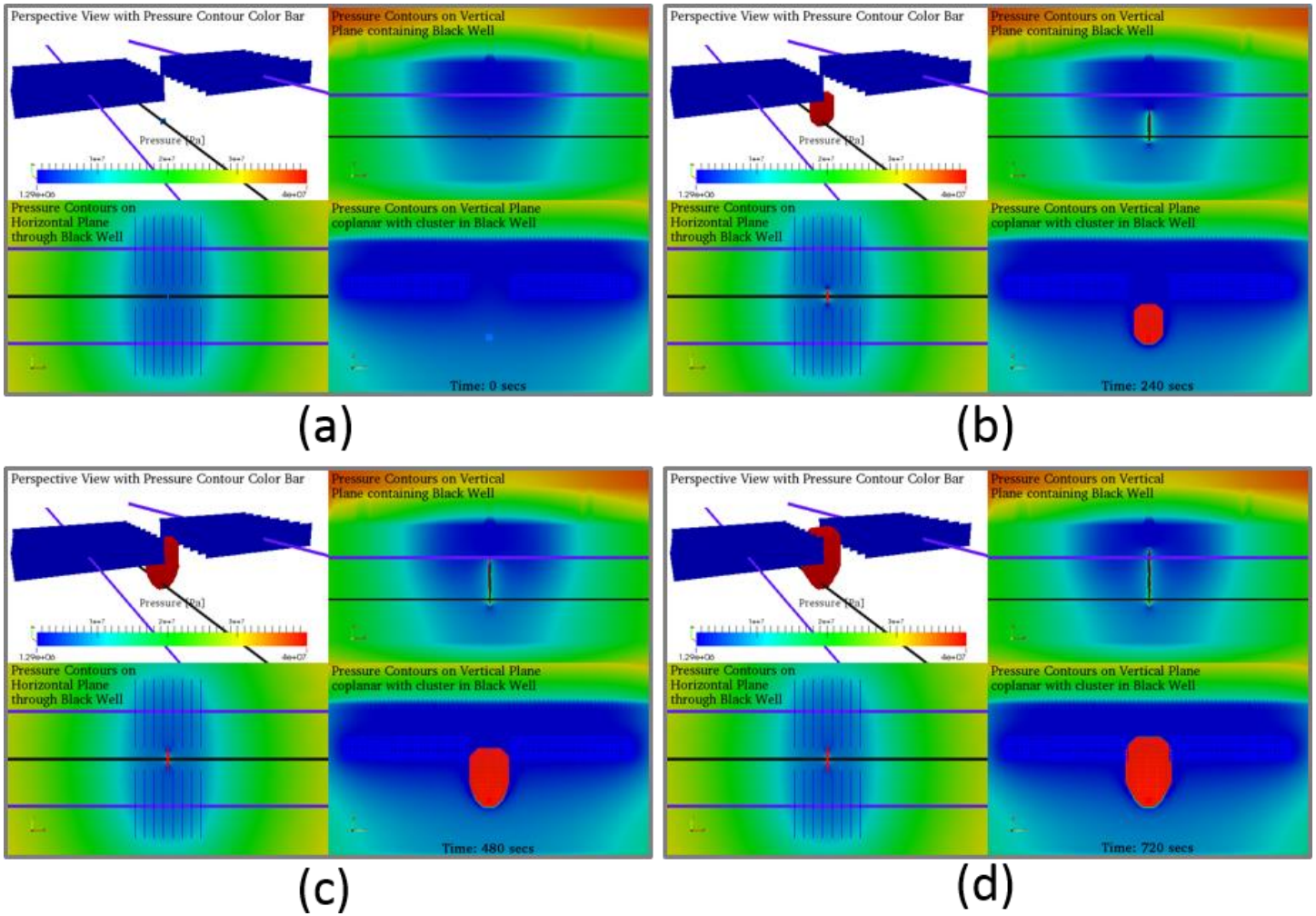

Figure 5.53 Impact of poro-elastic stress interference on hydraulic fracture propagation direction. Hydraulic fracture injection time = (a) 0 min, (b) 4 min, (c) 8 min, and (d) 12 min.

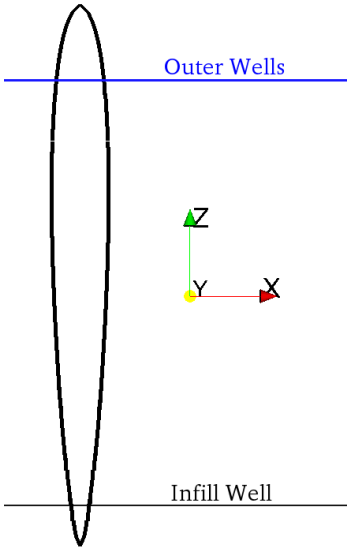

Figure 5.54 Fracture width profile for fracture propagation from an infill well in a depleted reservoir.

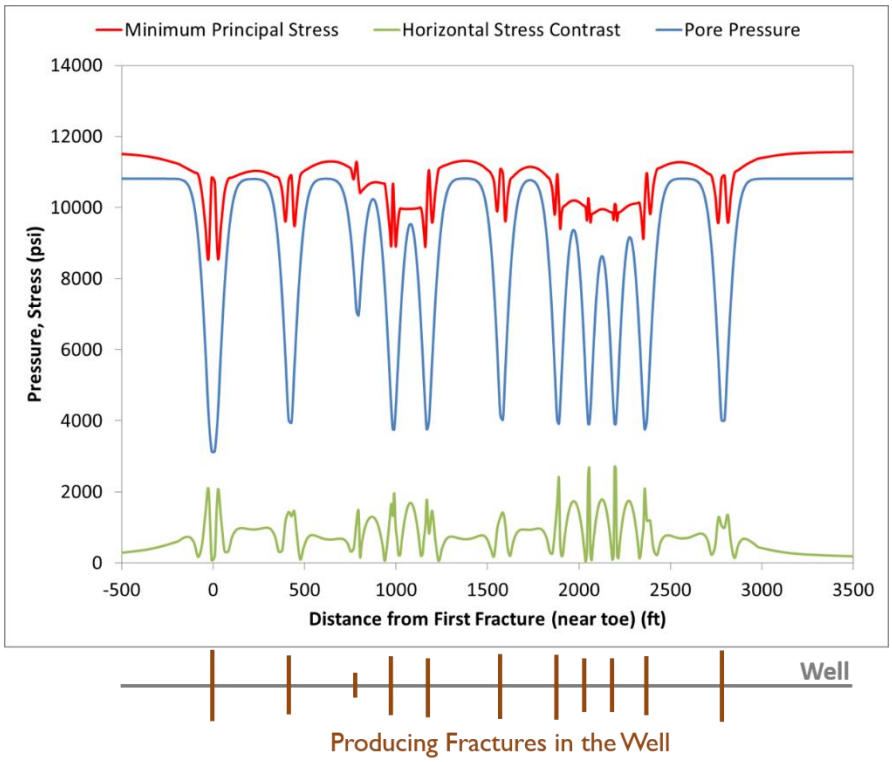

Figure 5.55 Impact of production on stresses in the vicinity of a horizontal well.

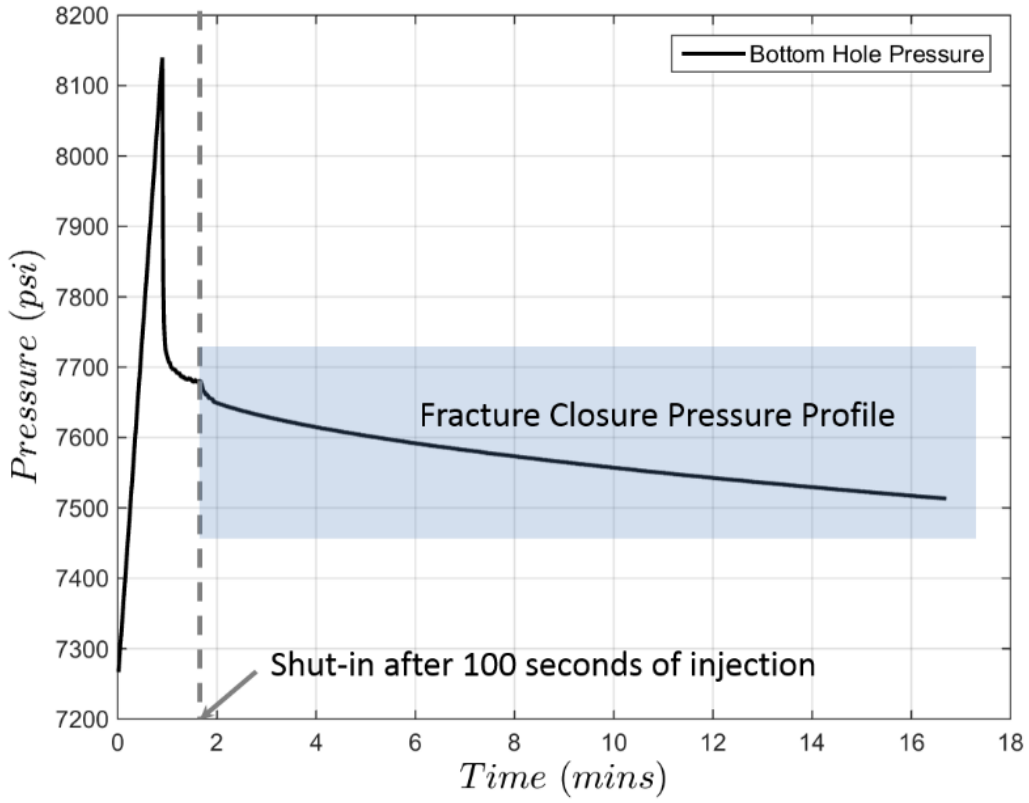

Figure 5.56 Pressure signature of fracture creation and subsequent closure

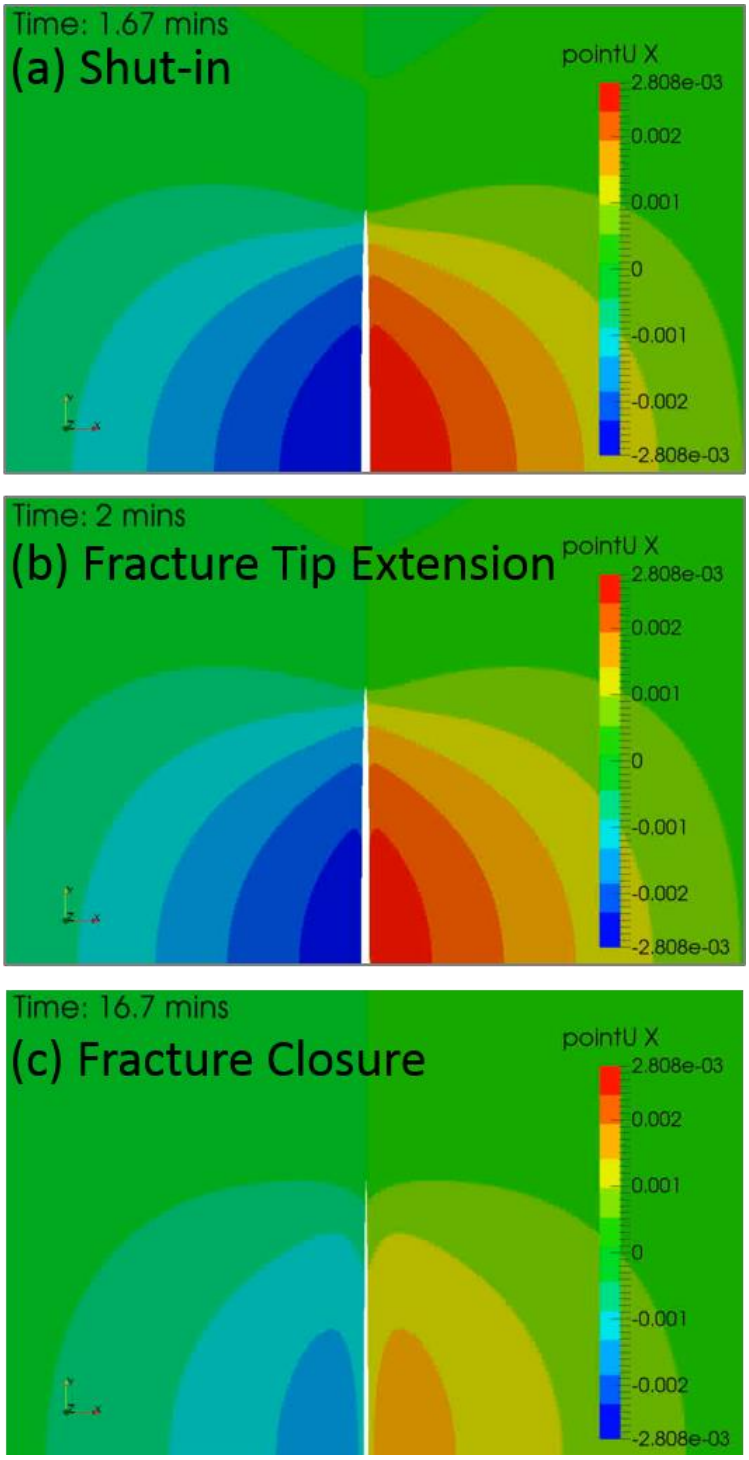

Figure 5.57 Simulation of 2-D fracture closure. (a) Fracture creation by injection of fluid for 100 seconds, (b) Fracture tip extension for approximately 30 seconds, (c) Fracture closure and induced displacements in the domain 900 seconds after shut-in.

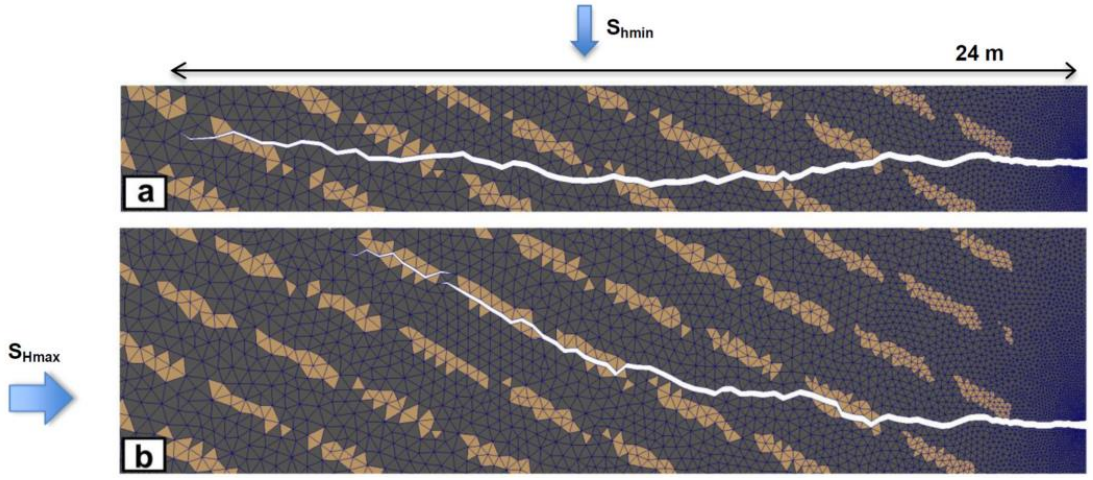

Figure 5.58 Impact of reservoir heterogeneity on fracture propagation (after Bryant et al. 2015) (a) No heterogeneity of parameters, (b) with varying parameters of toughness and critical stress. The lighter color in the figure depicts the location of the potential heterogeneities in the mesh.

Chapter 6: Conclusions

This dissertation presents two approaches to model pad-scale hydraulic fracturing scenarios. In the first approach, static fractures were simulated using a numerical simulator to understand inter-fracture interference. Geomechanical and poro-elastic simulations were conducted to draw conclusions on the impact of fracture stress shadow on fracture trajectory, impact of fracture closure on induced stress shadow, and impact of well spacing and fracture spacing on fracture complexity. Using this analysis, recommendations were made to optimize fracture sequencing scenarios and guide completions engineers.

In the second approach, multiple propagating fractures were simulated to provide a more realistic understanding of pad-scale fracturing. In order to do this, the development of a novel 3-D, finite-volume based, geomechanical, reservoir scale, fracture propagation simulator was undertaken. Numerical experiments showing the impact of various reservoir and operational parameters were presented and several illustrations for the application of the model to pad-scale problems were presented.

In this chapter we summarize the conclusions from the analysis and present recommendations for future work.

6.1 Static Fracture Analysis: Conclusions

1. Fracture spacing (which is affected by both stage spacing and cluster spacing) is the most important operator controlled parameter that can be used to control the extent of fracture interference. Non-intersecting fractures are expected above a critical value of the fracture spacing. Under such conditions transverse fractures are shown to propagate while still being subjected to stress-shadowing effects.

2. The stress shadow induced by fractures creates zones of reduced horizontal stress contrast in the vicinity of these fractures. These zones of low horizontal stress contrast are more conducive to the creation of complex fracture networks which can lead to better reservoir drainage via a natural fracture network.
3. An alternate fracturing sequence has been discussed in previous work (Roussel 2011). This alternate fracturing sequence (sometimes referred to as the Texas Two-Step (East et al. 2011) fracturing sequence) has been hypothesized to reduce the effective fracture spacing in a horizontal wellbore and lead to more efficient completions and possibly larger number of fractures. It has now become feasible to implement this fracturing sequence with the use of new sliding sleeve tools on coiled tubing, that allow single fractures to be pumped in any desired sequence.
4. This alternate fracturing sequence can be effectively used to tap into the natural fracture network. We observed that the stress reorientation caused by the presence of fractures causes the horizontal stress contrast in the middle of the bookend fractures to be reduced to negligible values for a range of bookend fracture spacings. Thus planning the completion design to make this happen can allow the middle fractures to tap into the naturally fractured reservoir.
5. A parametric study to understand the impact of operational and formation parameters was performed. Young's modulus, fracture height, proppant mass, and horizontal stress contrast were found to be the most important operator controlled parameters to optimize fracture spacing in all fracture sequencing scenarios.
6. This optimal fracture spacing is defined as the spacing between fractures that promotes transverse fracture growth away from the wellbore while inducing significant fracture complexity.

7. Using analytical calculations, numerical simulations and field data analysis we showed that the spatial extent of the stress shadow induced by a hydraulic fracture decreases with time because of fluid leak-off and closure of both propped and induced unpropped (IU) fractures.
8. It was shown that a shorter time between adjacent fracture stages in a well can increase the stress interference between the created fractures and can often result in re-stimulation of previously stimulated portions of the reservoir. This can lead to poorer fracture performance.
9. Conversely, if the time between successive fractures in a wellbore is increased the stress shadow region shrinks leading to less interference between fractures and better performing fractures. These effects are shown to be significant through our geomechanical simulations and through interpretation of field data.
10. The closure time for IU fractures is dependent on the amount of fluid pumped, fluid rheology, reservoir permeability and the fracture face area. For unconventional reservoirs with a large number of planes of weaknesses/natural fractures/other local heterogeneities, the volume of fluid leak-off can be increased considerably and hence the closure time can be reduced considerably. The time required for the IU fractures to close is estimated to be of the order of several hours after pumping is ceased. For lower leak-off volumes or smaller fracture area, the time for closure may be of the order of days.
11. A field data set from a pad consisting of 4 wells and a complete set of diagnostic data (microseismic, radioactive tracer, pressure and flow data) was used to understand the impact of fracture spacing, sequencing and design on fracture performance. This field data set validated the hypotheses presented regarding the

impact of fracture spacing, fracture closure, creation of IU fractures and fracture sequencing.

12. The simulations presented in this analysis showed that fracture interference (or stress shadow effects) between fractures in adjacent wells cannot explain the ISIP trends, the microseismic trends and the production trends observed in the zipper fractured wells in the field.
13. The analysis showed, for the first time, that the time interval between adjacent fractures in a wellbore can have a significant impact on the production performance and geometry of fractures in a horizontal wellbore. This has implications in the planning, sequencing and execution of multiple fracture treatments in multiple wellbores in pad drilling and fracturing.
14. The time dependent closure of fractures can now explain why zipper fracturing works better than consecutive fracturing in many applications. The time between successive fractures is more than doubled in a zipper frac sequence of fracturing compared to conventional consecutive fracturing. This allows the IU fractures to close and the stress shadow region to shrink over time leading to less fracture interference (in a given well) when zipper fracs are used.
15. The case study validated the theory that ISIP trends measured during the completion of a horizontal well can act as an inexpensive diagnostic method to evaluate the extent of fracture interference. The up-and-down oscillations of the ISIP from one stage to the next indicates propagation of transverse fractures into previously stimulated regions of the reservoir and suggests an insufficient spacing of the fracture stages.
16. The poro-elastic stress interference induced by a fractured horizontal well that was produced for a period of time can induce stress changes near the produced

horizontal well which can act as a sink for fractures from nearby wells. Thus, fractures from the neighboring wells have an easier time propagating towards a reduced pressure region. This biased fracture propagation can cause fracture hits into producing wells.

17. Well spacing and fracture spacing in a typical pad can be optimized, through geomechanical modeling, to ensure the most effective reservoir drainage. An optimum well spacing exists below which the probability of transverse fractures decreases and above which the probability of fracture complexity decreases in the middle well.
18. Production of the outer wells was simulated and it was shown that the stresses reorient between the producing wells. This reorientation suggests a higher probability of longitudinal fractures in an infill well between the outer wells. The optimal well spacing for infill wells was larger than the pre-production estimate of well spacing.

6.2 Multiple Propagating Fractures: Conclusions

1. A new geomechanics simulator was developed to model pad-scale fracturing problems more efficiently. The pressure equation and the displacement equation in the reservoir were coupled using a segregated iterative fixed point iteration method. The finite volume method was used to model non-linear multi-physics problem of geomechanics and fluid flow in the reservoir and fluid flow within the fracture using the object oriented structure of OpenFOAM.
2. The model allowed us to simulate static fractures and multiple growing fractures. These static fractures can have arbitrary curvatures and the fracture trajectory estimation algorithm can be used to determine the impact of stress shadow on the

fracture trajectory. A fracture closure algorithm was also introduced in this system.

3. The elastic equations included in the model were tested and verified. The stress shadow induced by a penny shaped fracture was shown to be predicted using the model equations.
4. The poro-elastic coupling for the model used in this work was validated using the 1D Biot's consolidation problem.
5. The cohesive zone method used for fracture propagation in this work was described first in Bryant et al. (2015). The uniform fracture pressure formulation was used to validate the fracture propagation model (Lee et al. 2015).
6. Extensive numerical analysis was performed to improve the efficiency of the model:
    - The efficiency of the linear solvers was studied. The time taken for simulations was shown to linearly increase with number of unknowns in the domain.
    - An adaptive mesh refinement procedure was developed to model fracture propagation. This dynamic mesh refinement procedure was shown to speed-up the numerical simulations as well as provide additional degrees of freedom for the fractures to turn.
    - The solvers and methods used in the model have been parallelized and simulations can be performed on multiple cores. The model can be used on high performance computing resources such as Texas Advanced Computing Center's (TACC) High Performance Computing (HPC) resource. The parallelization speed-up was tested and it was shown that the speed-up of the simulations was linear for up to approximately 6000 cells per processor.

- The solution methods use fixed point iteration schemes. It was shown that at solution tolerance values up to 1e-2, the simulation results showed similar fracture propagation lengths and trajectories.
- A new scaling was introduced for simulations run with higher values of relaxation factors. This scaling method prevented the illusion of convergence of the iterative scheme because of a low relaxation factor.
- An adaptive FSI relaxation scheme was incorporated that helped in increasing the simulation efficiency. The simulation results were shown to be very similar to the simulation results obtained for the fixed relaxation factor comparison cases.
- A tighter coupled FSI scheme was also implemented that showed faster solution convergence.

7. Qualitative verification of the FSI model was performed suggesting physical results. Increase in treatment fluid viscosity, decrease in injection rate and increase in matrix permeability suggested shorter fractures. Agreement with these trends was observed from the FSI simulations.
8. Parametric analysis of both operationally controllable parameters and formation properties was conducted. All the case results showed that the stress shadow between fractures caused some clusters in the fracturing stages to not create fractures.
9. The parametric analysis of operational treatment variables showed the following results:
    - Increasing the injection rate induced longer fractures while increasing pressure drop in the perforations. The injection rate did not impact the number of clusters creating dominant fractures.

- Increasing the number of clusters and increasing cluster spacing decreased the stress interference between the propagating fractures and prevented the fractures from turning away from each other. This however, led to multiple inactive clusters in the fracturing stage. Thus, increasing the number of clusters does not support the creation of multiple fractures. The stress shadow between fractures still dominates the fracture creation.
- Decreasing the number of perforations in a cluster and decreasing the diameter of perforations in a cluster resulted in an increase in the fracturing pressure. Perforation parameters such as perforation diameter, number of perforations etc. can be varied to change the perforation pressure drop for the fractures and hence potentially propagate multiple simultaneous fractures from a stage.

10. A parametric analysis of formation properties showed the following results:
    - Reservoir permeability was shown to impact fracture propagation rate as well as the induced stress interference. Higher reservoir permeability induced an increase in pore pressure in the vicinity of the fracture. The poro-elastic impact of hydraulic fracturing reduced the stress interference between simultaneously propagating fractures in the high permeability case. Simulations showed a reduced probability of fracture turning in the higher permeability case.
    - Increased in-situ horizontal stress contrast reduced the probability of fracture interference and reduced the probability of fractures turning away from each other.

- Increased Young's modulus induced fracture width reduction which consequently induced an increase in the fracture area. The increase in Young's modulus also increases the stress interference between the fractures.
- Poisson's ratio did not have a significant impact on the simulated fracture dimensions.
- Fracture height growth was shown to be sensitive to reservoir layer heterogeneity. A fracture propagating in a material layer propagated preferentially towards a softer material layer. Fracture breakthrough into a soft layer from a harder layer was shown to be less probable. Fracture breakthrough into a harder layer from a softer layer was shown to be easier. This knowledge can be used when drilling to optimize the position of a well and the location of clusters in a stage.
- Heterogeneity along the length of a horizontal well was shown to impact the propagation of fractures from the clusters in a stage.
    - Higher Young's modulus and higher Poisson's ratio induced preferred fracture propagation.
    - Higher porosity and higher permeability induced preferred fracture propagation because of the induced poro-elastic impact.
    - This knowledge and customized analysis for field scale heterogeneous situations is recommended to position clusters in a horizontal well in regions of high fracability. This can potentially activate more clusters in a fracturing stage.

11. A two stage multi-cluster simulation was conducted that showed that the fractures in one stage induced a stress shadow on the subsequent stage. This stress shadow

limited the number of active clusters in the next stage. Only the cluster furthest from the previous stage created a fracture.

12. The multi-stage simulation also showed that fractures in a previous stage extended further because of the stress shadow induced by the fractures propagating in the next stage. This can contribute to the explanation of some observations of induced microseismic events observed in stages after fluid injection was stopped in a stage (Fischer et al. 2008). This extension and closure of the fractures in the previous stage can be diagnosed using the shut-in pressure data of the previous stage.
13. The poro-elastic impact of reservoir depletion is observed in the height growth of fractures in an infill well simulation. Fracture growth was observed to be preferentially oriented towards the depleted regions in the reservoir. Such simulations can now be run to simulate fracture hits.
14. There is potential to develop the model to simulate some other pad-scale fracturing scenarios such as re-fracturing, mini-frac analysis (DFIT) and a heterogeneous fracture network.

6.3 Recommended Future Work

Horizontal well fracturing applications were discussed in the current work. There are several other oil and gas field scale applications of the developed model:

1. In order to use the fracturing pressure data as a diagnostic tool more data for estimating the closure pressures for each stage is required. Using accurate values of the net closure pressures from stage-to-stage, a better understanding of fracture orientation and interference can be obtained.

2. Extensions of the model that includes plasticity have been discussed before (Lee et al. 2015; Tang et al. 2015). However, analysis of plastic calculations in unconventional oil and gas applications has not been discussed yet. Bryant et al. (2015) showcased the use of this model for multi-material interfaces and showed the alteration of fracture propagation direction because of simulated heterogeneities. A combination of plasticity and inclusion of characterized heterogeneities in the system can help in simulating shear failure and reproduce microseismic patterns observed in the field.
3. The fracture domain calculations can help in estimating proppant flow as shown in Lee et al. (2015). Similar procedures can allow incorporation of diverting agent (Ramakrishnan et al. 2011; Naceur and Touboul 2013) transport and hence model plugging of selective fractures during re-fracturing.
4. The simultaneous propagation of multiple fractures was discussed in Chapter 4 and 5. This workflow assumed uniform fracture pressure. Implementation of FSI or alternate methods can be used to estimate the pressure drop inside a propagating hydraulic fracture.
5. In this work, the 3-D mesh used is structured in the region of fracture propagation. This structured nature of the mesh makes fracture twisting a difficult possibility. In order to capture 3-D fracture propagation with twisting as shown by other researchers (Rungamornrat et al. 2005; Castonguay et al. 2013) (using boundary element methods), efficient tetrahedral 3-D meshes can be generated and used for the current finite volume discretization schemes. Additional mode II and mode III failure criteria will need to be characterized to achieve fracture twisting.

The intended application of the described model is in realistic pad-scale fracturing scenarios. The large scale of the simulations requires the method to be efficient. Several

additional efforts can be made to make the iterative scheme more numerically efficient for practical use. Some of the proposed developments are listed below:

1. Error driven dynamic refinement of the mesh can cause the regions in the mesh that do not have large error in the calculation to be unrefined and hence save computational time.
2. Parallelization of the dynamic refinement framework will further increase the efficiency of the solution. Research on load-balancing between multiple parallel processors using dynamic refinement has been conducted elsewhere (Menon et al. 2015) and can be used in the current model.
3. The dynamic refinement models currently only works for 2-D cases. Development of these methods for 3-D cases is essential.
4. Other methods such as overset grid or Chimera grids can also be useful in obtaining a refined mesh around the fracture tip (Miller et al. 2014).
5. The parallelization of the numerical methods can be made more efficient by making the Input/Output (IO) methods used more efficient. Currently, the solvers run in parallel by creating individual processor domain folders and writing field calculations to files in these individual processor directories every time step. This increases the number of files written per time step and can be made more efficient using advanced IO methods (Lofstead et al. 2008).
6. The parallelization of the FSI method in use is necessary to conduct large scale fracture propagation simulations.
7. The FSI algorithm can be improved to have better fluid-structure coupling (Blom et al. 2015). The current algorithm relaxes the pressure calculations from the fluid domain and then the relaxed pressure is applied to the solid domain. An alternative method will be to relax the displacements obtained from the solid

domain to define the deformation of the fluid domain. This may lead to better convergence efficiency.

8. The FSI algorithm implemented in this work is 2-D and has been extended to 3-D. Verification of the 3-D FSI procedure using a PKN fracture case will be essential to ensure validity of the developed model.
9. The adaptive FSI relaxation method used can also be further developed to increase the numerical efficiency of the code. Mathematical analysis of the relaxation schemes can enable the incorporation of better adaptive relaxation schemes that can make the numerical simulator more efficient (Degroote et al. 2009, 2010).

Bibliography

Abass, H.H., Hedayati, S., and Meadows, D.L. 1996. Nonplanar Fracture Propagation From a Horizontal Wellbore: Experimental Study. *SPE Prod. & Fac.* **11** (03): 133–137. SPE-24823-PA. http://dx.doi.org/10.2118/24823-PA.

Ajani, A.A., and Kelkar, M.G. 2012. Interference Study in Shale Plays. Presented at the SPE Hydraulic Fracturing Technology Conference, The Woodlands, Texas, 6-8 February. SPE-151045-MS. http://dx.doi.org/10.2118/151045-MS.

Allison, D.B., Curry, S.S., and Todd, B.L. 2011. Restimulation of Wells using Biodegradable Particulates as Temporary Diverting Agents. Presented at the Canadian Unconventional Resources Conference, Calgary, Alberta, Canada, 15–17 November. SPE-149221-MS. http://dx.doi.org/10.2118/149221-MS.

Ames, B.C., and Bunger, A. 2015. Role of Turbulent Flow in Generating Short Hydraulic Fractures With High Net Pressure in Slickwater Treatments. Presented at the SPE Hydraulic Fracturing Technology Conference, The Woodlands, Texas, 3-5 February. SPE-173373-MS. http://dx.doi.org/10.2118/173373-MS.

Bai, M., Green, S., and Suarez-Rivera, R. 2005. Effect of Leakoff Variation on Fracturing Efficiency for Tight Shale Gas Reservoirs. Presented at the 40th U.S. Symposium on Rock Mechanics, Anchorage, Alaska, 25-29 June.

Bai, J., and Lin, A. 2014a. Tightly Coupled Fluid-Structure Interaction Computational Algorithm for Hydraulic Fracturing Simulations. Presented at the 48th US Rock Mechanics/Geomechanics Symposium, Minneapolis, Minnesota, 1-4 June.

Bai, J., and Lin, A. 2014b. Interaction between Multiple Injections Using Tightly Coupled Fluid-Structure Interaction Computational Algorithm. Presented at the Abu Dhabi International Petroleum Exhibition and Conference, Abu Dhabi, UAE, 10-13 November. SPE-171735-MS. http://dx.doi.org/10.2118/171735-MS.

Barenblatt, G.I. 1959. The formation of equilibrium cracks during brittle fracture. General ideas and hypotheses. Axially-symmetric cracks. *J. Appl. Math. Mech.* **23** (3): 622–636. http://dx.doi.org/10.1016/0021-8928(59)90157-1.

Barenblatt, G.I. 1962. The Mathematical Theory of Equilibrium Cracks in Brittle Fracture. *Adv. App. Mech.* **7** : 55–129. http://dx.doi.org/10.1016/S0065-2156(08)70121-2.

Barree, R.D., Barree, V. L., and Craig, D. 2009. Holistic Fracture Diagnostics: Consistent Interpretation of Prefrac Injection Tests Using Multiple Analysis Methods. *SPE Prod. & Oper*. **24** (03): 396–406. SPE-107877-PA. http://dx.doi.org/10.2118/107877-PA.

Berchenko, I., and Detournay, E. 1997. Deviation of hydraulic fractures through poroelastic stress changes induced by fluid injection and pumping. *Int. J. Rock.*

Mech. Min. **34** (6): 1009–1019. http://dx.doi.org/10.1016/S1365-1609(97)80010-X.

Biot, M.A. 1955. Theory of Elasticity and Consolidation for a Porous Anisotropic Solid. *J. App. Phy.* **26** (2): 182-185. http://dx.doi.org/10.1063/1.1721956.

Blom, D.S., van Zuijlen, A.H., and Bijl, H. 2015. Multi-level acceleration with manifold mapping of strongly coupled partitioned fluid–structure interaction. *Comput. Methods in Appl. Mech. Eng.* **296:** 211–231. http://dx.doi.org/10.1016/j.cma.2015.08.004.

Boone, T.J., and Detournay, E.. 1990. Response of a vertical hydraulic fracture intersecting a poroelastic formation bounded by semi-infinite impermeable elastic layers. *Int. J. Rock. Mech. Min. Sci. Geomech Abstr.* **27** (3): 189–197. http://dx.doi.org/10.1016/0148-9062(90)94327-P.

Bouchard, P.O., Bay, F., and Chastel, Y. 2003. Numerical modelling of crack propagation: automatic remeshing and comparison of different criteria. *Comput. Methods. in. Appl. Mech. Eng.* **192** (35-36): 3887–3908. http://dx.doi.org/10.1016/S0045-7825(03)00391-8.

Bouchard, P.O., Bay, F., Chastel, Y. et al. 2000. Crack propagation modelling using an advanced remeshing technique. *Comput. Methods. in Appl. Mech. Eng.* **189** (3): 723–742. http://dx.doi.org/10.1016/S0045-7825(99)00324-2.

Britt, L.K., Smith, M.B., Haddad, Z.A. et al. 2006. Waterfracs: We Do Need Proppant After All. Presented at SPE Annual Technical Conference and Exhibition, San Antonio, Texas. 24-27 September. SPE-102227-MS. http://dx.doi.org/10.2118/102227-MS.

Brown, S., Harstad, H., Lorenz, J. et al. 1995. Geotechnology for Low-Permeability Gas Reservoirs. http://www.netl.doe.gov/kmd/cds/disk7/disk2/WGS%5CGeotechnology%20for%20Low-Permability%20Reservoirs%20(Jun%201995).pdf (downloaded 5 June 2012).

Bruno, M.S., and Nakagawa, F.M. 1991. Pore pressure influence on tensile fracture propagation in sedimentary rock. *Int. J. Rock. Mech. Min. Sci. Geomech. Abstr*. **28** (4): 261–273. http://dx.doi.org/10.1016/0148-9062(91)90593-B.

Bryant, E.C., Hwang, J., and Sharma, M. M. 2015. Arbitrary Fracture Propagation in Heterogeneous Poroelastic Formations Using a Finite Volume-Based Cohesive Zone Model. Presented at the SPE Hydraulic Fracturing Technology Conference, The Woodlands, Texas, 3-5 February. SPE-173374-MS. http://dx.doi.org/10.2118/173374-MS.

Bunger, A., Zhang, X., and Jeffrey, R. 2012. Parameters Affecting the Interaction Among Closely Spaced Hydraulic Fractures. *SPE J.* **17** (1): 292–306. SPE-140426-PA. http://dx.doi.org/10.2118/140426-PA

Cardiff, P., Manchanda, R., Bryant, E.C., et al. 2015. Simulation of Fractures in OpenFOAM: From Adhesive Joints to Hydraulic Fractures. Presented at the 10th OpenFOAM Workshop, Ann Arbor, Michigan.

Carolan, D., Tukovic, Ž., Murphy, N. et al. 2013. Arbitrary Crack Propagation in Multi-Phase Materials using the Finite Volume Method. *Comp. Mat. Sci*. **69**: 153–159. http://dx.doi.org/10.1016/j.commatsci.2012.11.049.

Carrasco, A., DeGeare, J., and Hunter, J. 2014. Achieving a More Efficient Frac Network for Horizontal Development of the Bone Spring Sandstone. Presented at the SPE Hydraulic Fracturing Technology Conference, The Woodlands, Texas, 4-6 February. SPE-168633-MS. http://dx.doi.org/10.2118/168633-MS.

Carrier, B., and Granet, S. 2012. Numerical modeling of hydraulic fracture problem in permeable medium using cohesive zone model. *Eng. Frac. Mech*. **79**: 312–328. http://dx.doi.org/10.1016/j.engfracmech.2011.11.012.

Castonguay, S.T., Mear, M.E., Dean, R.H. et al. 2013. Predictions of the Growth of Multiple Interacting Hydraulic Fractures in Three Dimensions. Presented at the SPE Annual Technical Conference and Exhibition, New Orleans, Louisiana, 30 September–2 October. SPE-166259-MS. http://dx.doi.org/10.2118/166259-MS.

Centurion, S. 2011. Eagle Ford Shale: A Multi-Stage Hydraulic Fracturing, Completion Trends and Production Outcome Study Using Practical Data Mining Techniques. Presented at the SPE Eastern Regional Meeting, Columbus, Ohio, 17-19 August. SPE-149258-MS. http://dx.doi.org/10.2118/149258-MS.

Cheng, Y. 2009. Boundary element analysis of the stress distribution around multiple fractures: implications for the spacing of perforation clusters of hydraulically fractured. Presented at the SPE Eastern Regional Meeting, Charleston, West Virginia, 23-25 September. SPE-125769-MS. http://dx.doi.org/10.2118/125769-MS.

Cipolla, C.L., Hansen, K.K., and Ginty, W.R. 2007. Fracture Treatment Design and Execution in Low Porosity Chalk Reservoirs. *SPE Prod. & Oper.* **22** (1): 94-106. SPE-86485-PA. http://dx.doi.org/10.2118/86485-PA.

Cipolla, C.L., Jensen, L., Ginty, W. et al. 2000. Complex Hydraulic Fracture Behavior in Horizontal Wells, South Arne Field, Danish North Sea. Presented at the SPE Annual Technical Conference and Exhibition, Dallas, Texas, 1-4 October. SPE-62888-MS. http://dx.doi.org/10.2118/62888-MS.

Cipolla, C.L., Lolon, E.P., Mayerhofer, M.J. et al. 2009. The Effect of Proppant Distribution and Un-Propped Fracture Conductivity on Well Performance in Unconventional Gas Reservoirs. Presented at the SPE Hydraulic Fracturing Technology Conference, The Woodlands, Texas, 19-21 January. SPE-119268-MS. http://dx.doi.org/10.2118/119268-MS.

Cipolla, C., Peterman, F., Creegan, T. et al. 2005a. Effect of Well Placement on Production and Frac Design in a Mature Tight Gas Field. Presented at the SPE Annual Technical Conference and Exhibition, Dallas, Texas, 9-12 October. SPE-95337-MS. http://dx.doi.org/10.2118/95337-MS.

Cipolla, C.L., Shucart, J.K., and Lafitte, J.R. 2005b. Evolution of Frac-Pack Design, Modeling, and Execution in the Ceiba Field, Equatorial Guinea. Presented at the SPE Annual Technical Conference and Exhibition, Dallas, Texas, 9-12 October. SPE-95514-MS. http://dx.doi.org/10.2118/95514-MS.

Cipolla, C.L., Warpinski, N.R., Mayerhofer, M.J. et al. 2010. The Relationship Between Fracture Complexity, Reservoir Properties, and Fracture Treatment Design. *SPE Prod and Oper* **25** (4): 438–452. SPE-115769-PA. http://dx.doi.org/10.2118/115769-PA.

Cipolla, C.L., Weng, X., Mack, M. et al. 2011. Integrating Microseismic Mapping and Complex Fracture Modeling to Characterize Fracture Complexity. Presented at the SPE Hydraulic Fracturing Technology Conference and Exhibition, The Woodlands, Texas, 24-26 January. SPE-140185-MS. http://dx.doi.org/10.2118/140185-MS.

Cortez, J., and B. R. Reddy. 2013. Activator Development for Controlling Degradation Rates of Polymeric Degradable Diverting Agents. Presented at the SPE International Symposium on Oilfield Chemistry, The Woodlands, Texas, 8-10 April. SPE-164117-MS. http://dx.doi.org/10.2118/164117-MS.

Coussy, O. 2004. Poromechanics. West Sussex, John Wiley and Sons, Ltd.

Dahi-Taleghani, A., and Olson, J.E. 2011. Numerical Modeling of Multistranded-Hydraulic-Fracture Propagation: Accounting for the Interaction Between Induced and Natural Fractures. *SPE J.* **16** (3): 575-581. SPE-124884-PA. http://dx.doi.org/10.2118/124884-PA.

Dahl, J., Samaripa, J., Spaid, J., et al. 2015. Optimized Fracture Stage and Perforation Placement in Horizontal Wells using a New Calibrated Pulsed-Neutron Log Workflow. Presented at the SPE Annual Technical Conference and Exhibition, Houston, Texas, 28-30 September. SPE-174757-MS. http://dx.doi.org/10.2118/174757-MS.

Dahl, J., Samaripa, J., Spaid, J., et al. 2015. Application of an Engineered Completion Methodology in the Eagle Ford to Improve Economics. Presented at the Unconventional Resources Technology Conference, San Antonio, Texas, 20-22 July. http://dx.doi.org/10.15530/urtec-2015-2153805.

Dahm, T., Hainzl, S., and Fischer, T. 2010. Bidirectional and unidirectional fracture growth during hydrofracturing: Role of driving stress gradients. *J. of Geo. Res.* **115** (B12):322. http://dx.doi.org/10.1029/2009JB006817.

Daneshy, A. 2011. Hydraulic Fracturing of Horizontal Wells: Issues and Insights. Presented at the SPE Hydraulic Fracturing Technology and Conference, The Woodlands, Texas, 24-26 January. SPE-140134-MS. http://dx.doi.org/10.2118/140134-MS.

Degroote, J., Bathe, K.J., and Vierendeels, J. 2009. Performance of a new partitioned procedure versus a monolithic procedure in fluid-structure interaction. *Comp. Struct*. **87** (11-12): 793–801. http://dx.doi.org/10.1016/j.compstruc.2008.11.013.

Degroote, J., Haelterman, R., Annerel, S., et al. 2010. Performance of partitioned procedures in fluid-structure interaction. *Comp. Struct*. **88** (7-8): 446–457. http://dx.doi.org/10.1016/j.compstruc.2009.12.006.

Demirdžić, I., Horman, I., and Martinović, D. 2000. Finite volume analysis of stress and deformation in hygro-thermo-elastic orthotropic body. *Comput. Methods Appl. Mech. Eng.* **190** (8-10): 1221–1232. http://dx.doi.org/10.1016/S0045-7825(99)00476-4

Demirdžić, I., and Martinović, D. 1993. Finite volume method for thermo-elasto-plastic stress analysis. *Comput. Methods Appl. Mech. Eng.* **109** (3-4): 331–349. http://dx.doi.org/10.1016/0045-7825(93)90085-C.

Demirdzic, I., and Muzaferija, S. 1994. Finite-Volume Method for Stress-Analysis in Complex Domains. *Int. J. for Num. Meth. in Eng.* **37** (21): 3751–3766. http://dx.doi.org/10.1002/nme.1620372110.

Demirdžić, I., and Muzaferija, S. 1995. Numerical method for coupled fluid flow, heat transfer and stress analysis using unstructured moving meshes with cells of arbitrary topology. *Comput. Methods Appl. Mech. Eng.* **125** (1-4): 235–255. http://dx.doi.org/10.1016/0045-7825(95)00800-G.

Detournay, E., and Cheng, A.H.-D. 1993. Fundamentals of Poroelasticity. In *Comprehensive Rock Engineering: Principles, Practice and Projects,* first edition, ed. J.A. Hudson and C. Fairhurst, Chap. 5, 113-171. Tarrytown, New York: Permagon Press.

Detournay, E., Cheng, A.H.-D., Roegiers, J.-C., et al. 1989. Poroelasticity considerations in In Situ stress determination by hydraulic fracturing. *Int. J. Rock. Mech. Min. Sci. Geomech. Abstr*. **26** (6): 507–513. http://dx.doi.org/10.1016/0148-9062(89)91428-9.

Dong, C.Y., and de Pater, C. J. 2001. Numerical implementation of displacement discontinuity method and its application in hydraulic fracturing. *Comput. Methods Appl. Mech. Eng.* **191** (8-10): 745–760. http://dx.doi.org/10.1016/S0045-7825(01)00273-0.

East, L., Soliman, M.Y., and Augustine, J.R. 2011. Methods for Enhancing Far-Field Complexity in Fracturing Operations. *SPE Prod. & Oper*. **26** (3): 291–303. SPE-133380-PA. http://dx.doi.org/10.2118/133380-PA.

Ehlig-Economides, C. A., and Economides, M.J. 2000. Formation Characterization: Well and Reservoir Testing. In *Reservoir Stimulation,* third edition, ed. M.J. Economides and K.G. Nolte, Chap. 3, 1-35. New York City, New York, John Wiley and Sons Ltd.

EIA, 2013, Monthly Energy Review, U.S. Energy Information Administration.

EIA, 2015, Drilling Productivity Report, U.S. Energy Information Administration.

Elata, D., and Berryman, J.G. 1996. Contact force-displacement laws and the mechanical behavior of random packs of identical spheres. *Mech. Mat*. **24** (3): 229–240. http://dx.doi.org/10.1016/S0167-6636(96)00034-8

El-rabaa, W. 1982. Experimental Study of Hydraulic Fracture Geometry Initiated From Horizontal Wells. Presented at the SPE Annual Technical Conference and Exhibition, 8-11 October. SPE-19720-MS. http://dx.doi.org/10.2118/19720-MS.

Fairhurst, C. 1964. Measurement of in-situ rock stresses. With particular reference to hydraulic fracturing. *Rock Mech*. *Eng. Geol.* **2**: 129–147.

Fallah, N., Bailey, C., Cross, M., et al. 2000. Comparison of finite element and finite volume methods application in geometrically nonlinear stress analysis. *App. Math. Mod.* **24** (7): 439–455. http://dx.doi.org/10.1016/S0307-904X(99)00047-5.

Fang, C., and Amro, M. 2014. Influence Factors of Fracability in Nonmarine Shale. Presented at the SPE/EAGE European Unconventional Resources Conference and Exhibition, Vienna, Austria. 25-27 Frbruary. SPE-167803-MS. http://dx.doi.org/10.2118/167803-MS.

Fischer, T., Hainzl, S. and Dahm, T. 2009. The creation of an asymmetric hydraulic fracture as a result of driving stress gradients. *Geophy. J. Int*. **179** (1): 634–639. http://dx.doi.org/10.1111/j.1365-246X.2009.04316.x.

Fischer, T., Hainzl, S., Eisner, L., et al. 2008. Microseismic signatures of hydraulic fracture growth in sediment formations: Observations and modeling. *J. Geophy. Res*. **113** (B2): B02307. http://dx.doi.org/10.1029/2007JB005070.

Fisher, M.K., Heinze, J.R., Harris, C.D., et al. 2004. Optimizing Horizontal Completion Techniques in the Barnett Shale Using Microseismic Fracture Mapping. Presented at the SPE Annual Technical Conference and Exhibition, Houston, Texas. 26-29 September. SPE-90051-MS. http://dx.doi.org/10.2118/90051-MS.

Fisher, M.K., Wright, C.A., Davidson, B.M., et al. 2005. Integrating Fracture Mapping Technologies To Improve Stimulations in the Barnett Shale. *SPE Prod. & Fac*. **20** (02): 85–93. SPE-77441-PA. http://dx.doi.org/10.2118/77441-PA.

Fryer, Y.D., Bailey, C., Cross, M., et al. 1991. A control volume procedure for solving the elastic stress-strain equations on an unstructured mesh. *App. Math. Mod*. **15** (11-12): 639–645. http://dx.doi.org/10.1016/S0307-904X(09)81010-X.

Gale, J.F.W., Reed, R.M. and Holder, J. 2007. Natural fractures in the Barnett Shale and their importance for hydraulic fracture treatments. *AAPG Bulletin*. **91** (4): 603–622. http://dx.doi.org/10.1306/11010606061.

Geertsma, J., and F. de Klerk. 1969. A Rapid Method of Predicting Width and Extent of Hydraulically Induced Fractures. *J. Pet. Technol*. **21** (12): 1571-1581. SPE-2458-PA. http://dx.doi.org/10.2118/2458-PA.

Geuzaine, C., and J.-F. Remacle. 2009. Gmsh: A 3-D finite element mesh generator with built-in pre- and post-processing facilities. *Int. J. Num. Meth. Eng*. **79** (11): 1309–1331. http://dx.doi.org/10.1002/nme.2579.

Gidley, J.L. 1989. *Recent Advances in Hydraulic Fracturing*. Richardson, Texas. Society of Petroleum Engineers.

Griffin, LG., Sullivan, R.B., Wolhart, S.L. et al. 2003. Hydraulic Fracture Mapping of the High-Temperature, High-Pressure Bossier Sands in East Texas. Paper SPE 84489 presented at SPE Annual Technical Conference and Exhibition, Denver, Colorado, 5-8 October. http://dx.doi.org/10.2118/84489-MS.

Gupta, J., Zielonka, M., Albert, R., et al. 2012. Integrated Methodology for Optimizing Development of Unconventional Gas Resources. Presented at SPE Hydraulic Fracturing Technology Conference and Exhibition, The Woodlands, Texas, 6-8 February. http://dx.doi.org/10.2118/152224-MS.

Haddad, M., and Sepehrnoori, K. 2014. Simulation of Multiple-Stage Fracturing in Quasibrittle Shale Formations Using Pore Pressure Cohesive Zone Model. Presented at the Unconventional Resources Technology Conference, Denver, Colorado, 25-27 August. http://dx.doi.org/10.15530/urtec-2014-1922219.

Haddad, M., and Sepehrnoori, K. 2015. Integration of XFEM and CZM to Model 3-D Multiple-Stage Hydraulic Fracturing in Quasi-brittle Shale Formations : Solution-Dependent Propagation Direction. Presented at the AADE National Technical Conference and Exhibition, San Antonio, Texas, 8-9 Apr.

Hill, O.F., Ward, A.J., and Clark, C. 1978. Austin Chalk Fracturing Design Using a Crosslinked Natural Polymer as a Diverting Agent. *J. Pet. Technol*. **30** (12): 1795–1804. SPE-6869-PA. http://dx.doi.org/10.2118/6869-PA.

Huckabee, P. T. 2009. Optic Fiber Distributed Temperature for Fracture Stimulation Diagnostics and Well Performance Evaluation. Presented at the SPE Hydraulic Fracturing Technology Conference. Engineers. SPE-118831-MS. http://dx.doi.org/10.2118/118831-MS.

Irwin, G. R. 1957. Analysis of Stresses and Strains Near the End of a Crack Traversing a Plate. Presented at the Applied Mechanics Division Summer Conference, Berkeley, California. 13-15 June.

Ispas, I., Eve, R., Hickman, R. et al. 2012. Laboratory Testing and Numerical Modelling of Fracture Propagation from Deviated Wells in Poorly Consolidated Formations. Presented at the SPE Annual Technical Conference and Exhibition, San Antonio, Texas, 8-10 October. SPE-159262-MS. http://dx.doi.org/10.2118/159262-MS.

Itasca Consulting Group, Inc. 2013, Software – FLAC3D, http://www.itascacg.com/software/flac3d (accessed 19 November 2013).

Ivankovic, A., Demirdzic, I., Williams, J.G. et al. 1994. Application of the finite volume method to the analysis of dynamic fracture problems. *Int. J. Frac*. **66** (4): 357–371. http://dx.doi.org/10.1007/BF00018439.

Ivankovic, A., Karac, A., Dendrinos, E., et al. 2002. Towards Early Diagnosis of Atherosclerosis : The Finite Volume Method for Fluid-Structure Interaction. *Biorheology*. **39** (3-4): 401-407.

Ivankovic, A., Muzaferija, S. and Demirdzic, I. 1997. Finite volume method and multigrid acceleration in modelling of rapid crack propagation in full-scale pipe test. *Comp. Mech*. **20** (1-2): 46–52. http://dx.doi.org/10.1007/s004660050215.

Ivankovic, A., Pandya, K.C. and Williams, J.G. 2004. Crack growth predictions in polyethylene using measured traction–separation curves. *Eng. Frac. Mech*. **71** (4-6): 657–668. http://dx.doi.org/10.1016/S0013-7944(03)00030-4.

Jaeger, J.C. and Cook, N.G.W. 1979. Fundamentals of Rock Mechanics, first edition. London: Chapman and Hall.

Jahandideh, A., and Jafarpour, B. 2014. Optimization of Hydraulic Fracturing Design Under Spatially Variable Shale Fracability. Presented at the SPE Western North American and Rocky Mountain Joint Meeting, Denver, Colorado. 17-18 April. SPE-169521-MS. http://dx.doi.org/10.2118/169521-MS.

Jasak, H. 1996. Error Analysis and Estimation for the Finite Volume Method with Applications to Fluid Flows. University of London, Imperial College of Science. http://dx.doi.org/10.1016/S0020-7683(02)00168-3.

Jasak, H., Jemcov, A., and Tukovic, Z. 2007. OpenFOAM: A C++ library for complex physics simulations. Presented at the International Workshop on Coupled Methods in Numerical Dynamics, Dubrovnik, Croatia, 19-21 Sep.

Jasak, H., and Tukovic, Z. 2007. Automatic mesh motion for the unstructured finite volume method. *Trans. of FAMENA*. **30** (2): 1–18.

Jasak, H., and Tukovic, Z. 2010. Dynamic mesh handling in OpenFOAM applied to fluid-structure interaction simulations. Presented at the European Conference on Computational Fluid Dynamics.

Jasak, H., and Weller, H. 2000. Application of the finite volume method and unstructured meshes to linear elasticity. *Int. J. Num. Meth. Eng*. **48**: 267–287.

Jin, X., Shah, S.N., Roegiers, J., et al. 2014. Fracability Evaluation in Shale Reservoirs - An Integrated Petrophysics and Geomechanics Approach. Presented at the SPE Hydraulic Fracturing Confernece, The Woodlands, Texas, 4-6 February. SPE-168589-MS. http://dx.doi.org/10.2118/168589-MS.

Jin, X., Shah, S.N., Roegiers, J., et al. 2015. An Integrated Petrophysics and Geomechanics Approach for Fracability Evaluation in Shale Reservoirs. *SPE J.* **20** (03): 518–526. SPE-168589-PA. http://dx.doi.org/10.2118/168589-PA.

Kanyanta, V., Ivankovic, A. and Karac, A. 2009. Validation of a fluid-structure interaction numerical model for predicting flow transients in arteries. *J. Biomech*. **42** (11): 1705–1712. http://dx.doi.org/10.1016/j.jbiomech.2009.04.023.

Khoei, A.R., Azadi, H., and Moslemi, H. 2008. Modeling of crack propagation via an automatic adaptive mesh refinement based on modified superconvergent patch recovery technique. *Eng. Frac. Mech*. **75** (10): 2921–2945. http://dx.doi.org/10.1016/j.engfracmech.2008.01.006.

Kias, E., Maharidge, R., and Hurt, R. 2015. Mechanical versus Mineralogical Brittleness Indices Across Various Shale Plays. Presented at the SPE Annual Technical Conference and Exhibition, Houston, Texas, 28-30 September. SPE-174781-MS. http://dx.doi.org/10.2118/174781-MS.

King, G. 2010. Thirty Years of Gas Shale Fracturing: What Have We Learned? Presented at the SPE Annual Technical Conference and Exhibition, Florence, Italy, 19-22 September. SPE-133456-MS. http://dx.doi.org/10.2118/133456-MS.

King, G. E., and Leonard, R.S. 2011. Deciphering Chemical Tracer Results in Multi-Fractured Well Backflow in Shales: A Framework for Optimizing Fracture Design and Application. Presented at the SPE Hydraulic Fracturing Technology Conference, The Woodland, Texas, 24-26 January. SPE-140105-MS. http://dx.doi.org/10.2118/140105-MS.

Kuhlman, R., Perez, J. and Claiborne, E.B. 1992. Microfracture Stress Tests, Anelastic Strain Recovery, and Differential Strain Analysis Assist in Bakken Shale Horizontal Drilling Program. Presented at the SPE Rocky Mountain Regional Meeting, Casper, Wyoming. 18-21 May. SPE-24379-MS. http://dx.doi.org/10.2118/24379-MS.

Lane, C., Laun, L.E., and Schlosser, D. 2013. Reducing Water Volume in Multistage Fracturing Using Sliding Sleeves and Coiled-Tubing-Deployed Resettable Frac Isolation. Presented at the SPE/ICoTA Coiled Tubing & Well Intervention Conference & Exhibition, The Woodlands, Texas. 26-27 March. SPE-163935-MS. http://dx.doi.org/10.2118/163935-MS.

Lecampion, B., and Desroches, J. 2015. Simultaneous initiation and growth of multiple radial hydraulic fractures from a horizontal wellbore. *J. Mech. Phy. Sol*. **82**: 235–258. http://dx.doi.org/10.1016/j.jmps.2015.05.010.

Lee, D., Cardiff, P., Bryant, E.C., et al. 2015. A New Model for Hydraulic Fracture Growth in Unconsolidated Sands with Plasticity and Leak-Off. Presented at the SPE Annual Technical Conference and Exhibition, Houston, Texas. 28-30 September. SPE-174818-MS. http://dx.doi.org/10.2118/174818-MS.

Lofstead, J.F., Klasky, S., Schwan, K., et al. 2008. Flexible IO and integration for scientific codes through the adaptable IO system (ADIOS). Presented at the 6th International Workshop on CLADE. http://dx.doi.org/10.1145/1383529.1383533.

Malhotra, S., Lehman, E.R. and Sharma, M.M. 2014. Proppant Placement Using Alternate-Slug Fracturing. *SPE J.* **19** (05): 974–985. SPE-163851-PA. http://dx.doi.org/10.2118/163851-PA.

Manchanda, R., Roussel, N.P., and Sharma, M.M. 2012. Factors Influencing Fracture Trajectories and Fracturing Pressure Data in a Horizontal Completion. Presented at the 46th US Rock Mechanics/Geomechanics Symposium, Chicago, Illinois. 24-27 June.

Manchanda, R., and Sharma, M.M. 2012. Impact of Completion Design on Fracture Complexity in Horizontal Wells. Presented at the SPE Annual Technical Conference and Exhibition, San Antonio, Texas, 8-10 October. SPE-159899-MS. http://dx.doi.org/10.2118/159899-MS

Manchanda, R., and Sharma, M.M. 2013. Time-Delayed Fracturing: A New Strategy in Multi-Stage, Multi-Well Pad Fracturing. Presented at the SPE Annual Technical Conference and Exhibition, New Orleans, Louisiana, 30 Sep – 2 October. SPE-166489-MS. http://dx.doi.org/10.2118/166489-MS.

Manchanda, R., and Sharma, M.M. 2014. Impact of Completion Design on Fracture Complexity in Horizontal Shale Wells. *SPE Drill. & Compl.* **29** (01): 78–87. SPE-159899-PA. http://dx.doi.org/10.2118/159899-PA.

Manchanda, R., Sharma, M.M., and Holzhauser, S. 2013. Time Dependent Fracture Interference Effects in Pad Wells. Presented at the SPE Unconventional Resources Conference, The Woodlands, Texas, 10-12 April. SPE-164534-MS. http://dx.doi.org/10.2118/164534-MS.

Manchanda, R., Sharma, M.M., and Holzhauser, S. 2014. Time-Dependent Fracture-Interference Effects in Pad Wells. *SPE Prod. & Oper*. **29** (04): 274–287. SPE-164534-PA. http://dx.doi.org/10.2118/164534-PA.

Mayerhofer, M. J., and Economides, M.J. 1997. Fracture-Injection-Test Interpretation: Leakoff Coefficient vs. Permeability. *SPE Prod. & Fac*. **12** (04): 231–236. SPE-28562-PA. http://dx.doi.org/10.2118/28562-PA.

Mayerhofer, M.J., Lolon, E.P., Warpinski, N.R. et al. 2010. What Is Stimulated Reservoir Volume? *SPE Prod. & Oper*. **25** (1): 16–18. SPE-119890-PA. http://dx.doi.org/10.2118/119890-PA.

Mayerhofer, M. J., Lolon, E.P., Youngblood, J.E., et al. 2006. Integration of Microseismic-Fracture-Mapping Results with Numerical Fracture Network Production Modeling in the Barnett Shale. Presented at the SPE Annual Technical Conference and Exhibition, San Antonio, Texas, 24-27 September. SPE-102103-MS. http://dx.doi.org/10.2118/102103-MS.

McClure, M., Babazadeh, M., Shiozawa, S., et al. 2015. Fully Coupled Hydromechanical Simulation of Hydraulic Fracturing in Three-Dimensional Discrete Fracture Networks. Presented at the SPE Hydraulic Fracturing Technology Conference, The Woodlands, Texas, 3-5 February. SPE-173354-MS. http://dx.doi.org/10.2118/173354-MS.

McClure, M.W., Blyton, C.A.J., Jung, H., et al. 2014. The Effect of Changing Fracture Compliance on Pressure Transient Behavior During Diagnostic Fracture Injection Tests. Presented at the SPE Annual Technical Conference and Exhibition, Amsterdam, The Netherlands. 27-29 October. SPE-170956-MS. http://dx.doi.org/10.2118/170956-MS.

McClure, M., and Horne, R.N. 2013. Discrete Fracture Network Modeling of Hydraulic Stimulation: Coupling Flow and Geomechanics. Springer Science & Business. http://dx.doi.org/bfm:978-3-319-00383-2.

Menon, S., Mooney, K.G., Stapf, K.G., et al. 2015. Parallel adaptive simplical re-meshing for deforming domain CFD computations. *J. Comp. Phy*. **298:** 62–78. http://dx.doi.org/10.1016/j.jcp.2015.05.044.

Meyer, B.R., and Bazan, L.W. 2011. A Discrete Fracture Network Model for Hydraulically Induced Fractures - Theory, Parametric and Case Studies. Presented at the SPE Hydraulic Fracturing Technology Conference, The Woodlands, Texas, 24-26 January. SPE-140514-MS. http://dx.doi.org/10.2118/140514-MS.

Miller, S.T., Campbell, R.L., Elsworth, C.W., et al. 2014. An Overset Grid Method for Fluid-Structure Interaction. *World J. Mech*. **04**(07): 217–237. http://dx.doi.org/10.4236/wjm.2014.47023.

Miller, C.K., Waters, G.A., and Rylander, E.I. 2011. Evaluation of Production Log Data from Horizontal Wells Drilled in Organic Shales. Presented at the North American Unconventional Gas Conference and Exhibition, The Woodlands, Texas, 14-16 June. SPE-144326-MS. http://dx.doi.org/10.2118/144326-MS.

Min, K. S., and Ghassemi, A. 2012. Simulation of fracture clusters in unconventional reservoir using fully coupled thermo-hydro-mechanical FEM analysis. Presented at the 46th US Rock Mechanics/Geomechanics Symposium, Chicago, Illinois, 24-27 June.

Molenaar, M., Hill, D., Webster, P., et al. 2011. First downhole application of distributed acoustic sensing (DAS) for hydraulic fracturing monitoring and diagnostics. Presented at the SPE Hydraulic Fracturing Technology Conference, The

Woodlands, Texas, 24-26 Jan. SPE-140561-MS. http://dx.doi.org/10.2118/140561-MS.

Moslemi, H., and Khoei, A.R. 2009. 3-D adaptive finite element modeling of non-planar curved crack growth using the weighted superconvergent patch recovery method. *Eng. Frac. Mech*. **76** (11): 1703–1728. http://dx.doi.org/10.1016/j.engfracmech.2009.03.013.

Mullen, J. 2010. Petrophysical Characterization of the Eagle Ford Shale in South Texas. Presented at the Canadian Unconventional Resources and International Petroleum Conference. SPE-138154-MS, Calgary, Alberta, Canada, 19-21 October. http://dx.doi.org/10.2118/138145-MS.

Mullen, M.J., and Enderlin, M.B. 2012. Fracability Index - More Than Rock Properties. Presented at the SPE Annual Technical Conference and Exhibition, San Antonio, Texas, 8-10 October. SPE-159755-MS. http://dx.doi.org/10.2118/159755-MS.

Naceur, K.B., and E. Touboul. 1990. Mechanisms Controlling Fracture-Height Growth in Layered Media. *SPE Prod. Eng*. **5** (02): 142–150. SPE-16433-PA. http://dx.doi.org/10.2118/16433-PA.

Nagel, N., Gil, I., and Sanchez-Nagel, M. 2011. Simulating Hydraulic Fracturing in Real Fractured Rocks-Overcoming the Limits of Pseudo3D Models. Presented at the SPE Hydraulic Fracturing Technology Conference, The Woodlands, Texas, 24-26 January. http://dx.doi.org/10.2118/140480-MS.

Nagel, N., Sheibani, F., Lee, B., et al. 2014. Fully-Coupled Numerical Evaluations of Multiwell Completion Schemes: The Critical Role of In-Situ Pressure Changes and Well Configuration. Presented at the SPE Hydraulic Fracturing Technology Conference, The Woodlands, Texas, 4-6 February. SPE-168581-MS. http://dx.doi.org/10.2118/168581-MS.

Neuhaus, C., Williams-Stroud, S., Remington, C., et al. 2012. Integrated Microseismic Monitoring for Field Optimization in the Marcellus Shale - A Case Study. Presented at the SPE Canadian Unconventional Resources Conference, Calgary, Alberta, Canada, 30 October – 1 November. SPE-161965-MS. http://dx.doi.org/10.2118/161965-MS.

Nolte, K. G. 1979. Determination of Fracture Parameters from Fracturing Pressure Decline. Presented at the SPE Annual Technical Conference and Exhibition. SPE-8341-MS. http://dx.doi.org/10.2118/8341-MS.

Nordgren, R. P. 1972. Propagation of a Vertical Hydraulic Fracture. *SPE J*. **12** (04): 306–314. SPE-3009-PA. http://dx.doi.org/10.2118/3009-PA.

Olsen, T., Bratton, T., and Thiercelin, M. 2009. Quantifying Proppant Transport for Complex Fractures in Unconventional Formations. Presented at SPE Hydraulic Fracturing Technology Conference, The Woodlands, Texas, 19-21 January. http://dx.doi.org/doi:10.2118/119300-MS.

Olson, J. E. 1993. Joint pattern development: Effects of subcritical crack growth and mechanical crack interaction. *J. Geophy. Res.* **98** (B7): 12251. http://dx.doi.org/10.1029/93JB00779.

Olson, J. E. 2008. Multi-fracture propagation modeling: Applications to hydraulic fracturing in shales and tight gas sands. Presented at the 42nd U.S. Rock Mechanics Symposium (USRMS), San Francisco, California, 29 June-2 July.

OpenFOAM Foundation. 2013. OpenFOAM User Guide.

Ouchi, H., Katiyar, A., York, J., et al. 2015. A fully coupled porous flow and geomechanics model for fluid driven cracks: a peridynamics approach. *Comp Mech.* **55** (3): 561–576. http://dx.doi.org/10.1007/s00466-015-1123-8.

Palisch, T.T., Vincent, M.C. and Handren, P.J. 2010. Slickwater Fracturing: Food for Thought. *SPE Prod. & Oper*. **25** (3): 327-344. SPE-115766-PA. http://dx.doi.org/10.2118/115766-PA.

Peirce, A.P., and Bunger, A.P. 2015. Interference Fracturing: Nonuniform Distributions of Perforation Clusters That Promote Simultaneous Growth of Multiple Hydraulic Fractures. *SPE J.* **20**(2):384-395. SPE-1725000-PA. http://dx.doi.org/10.2118/1725000-PA.

Perkins, T.K., and Gonzalez, J. 1985. The Effect of Thermoelastic Stresses on Injection Well Fracturing. *SPE J.* **25** (01): 78–88. SPE-11332-PA. http://dx.doi.org/10.2118/11332-PA.

Perkins, T.K., and Kern, L.R.. 1961. Widths of Hydraulic Fractures. *J. Pet. Technol*. **13** (9): 937-949. SPE-89-PA. http://dx.doi.org/10.2118/89-PA.

Profit, M.L., Dutko, M. and Yu, J. 2015. Developing a Framework to Simulate the Hydraulic Fracturing of Tight Gas Reservoirs Based on Integrative Adaptive Remeshing and Combined Finite/Discrete Element Approach. Presented at the 49th US Rock Mechanics / Geomechanics Symposium, San Francisco, CA, 28 June – 1 July.

Rafiee, M., Soliman, M.Y., and Pirayesh, E. 2012. Hydraulic Fracturing Design and Optimization: A Modification to Zipper Frac. Presented at SPE Annual Technical Conference and Exhibition, San Antonio, Texas, 8-10 October 2012. SPE-159786-MS. http://dx.doi.org/10.2118/159786-MS.

Ramakrishnan, H., Yuyan, R., and Belhadi, J. 2011. Real-Time Completion Optimization Of Multiple Laterals In Gas Shale Reservoirs: Integration of Geology, Log, Surface Seismic, And Microseismic Information. Presented at the SPE Hydraulic Fracturing Technology Conference, The Woodlands, Texas, 24-26 January. SPE-140543-MS. http://dx.doi.org/10.2118/140542-MS.

Rashid, M. M. 1998. The arbitrary local mesh replacement method: An alternative to remeshing for crack propagation analysis. *Comp. Methods App. Mech. Eng*. **154** (1-2): 133–150. http://dx.doi.org/10.1016/S0045-7825(97)00068-6.

Ribeiro, L., and Sharma, M.M. 2013. Fluid Selection for Energized Fracture Treatments. Presented at the SPE Hydraulic Fracturing Technology Conference, The Woodlands, Texas, 4-6 February. SPE-163867-MS. http://dx.doi.org/10.2118/163867-MS.

Rice, J. R. 1968. Mathematical Analysis In The Mechanics Of Fracture. In H. Liebowitz, ed., Fracture: An Advanced Treatise. N.Y.191–311.

Rios, A., Gutierrez, G., Nagel, N., et al. 2013. Stress Shadow Evaluations For Chicontepec – Evaluating New Completion Options. Presented at the 47th US Rock Mechanics/Geomechanics Symposium, San Francisco, California, 23-26 June.

Roussel, N.P. 2011. Stress Reorientation in Low Permeability Reservoirs. PhD dissertation, University of Texas at Austin, Austin, Texas (August 2011).

Roussel, N.P., Florez, H.A., and Rodriguez, A.A. 2013. Hydraulic Fracture Propagation from Infill Horizontal Wells. Presented at SPE Annual Technical Conference and Exhibition, New Orleans, Louisiana, 30 September - 2 October. http://dx.doi.org/10.2118/166503-MS.

Roussel, N.P., Manchanda, R. and Sharma, M.M. 2012. Implications of Fracturing Pressure Data Recorded during a Horizontal Completion on Stage Spacing Design. Paper SPE 152631 presented at SPE Hydraulic Fracturing Technology Conference and Exhibition, The Woodlands, Texas, 6-8 February. http://dx.doi.org/10.2118/152631-MS.

Roussel, N. P., and Sharma, M.M. 2011a. Optimizing Fracture Spacing and Sequencing in Horizontal-Well Fracturing. *SPE Prod. & Oper*. **26**(02): 173–184. SPE-127986-PA. http://dx.doi.org/10.2118/127986-PA.

Roussel, N.P. and Sharma, M.M. 2011b. Strategies to Minimize Frac Spacing And Stimulate Natural Fractures in Horizontal Completions. Paper SPE 146104 presented at SPE Annual Technical Conference and Exhibition, Denver, Colorado, 30 October-2 November. http://dx.doi.org/10.2118/146104-MS.

Roussel, N. P., and Sharma, M.M. 2012. Method for Determining Spacing of Hydraulic Fractures in a Rock Formation.

Rungamornrat, J., Wheeler, M., and Mear, M. 2005. A Numerical Technique for Simulating Non-planar Evolution of Hydraulic Fractures. Proceedings of SPE Annual Technical Conference and Exhibition, Dallas, Texas, 9-12 October. SPE-96968-MS. http://dx.doi.org/10.2523/96968-MS.

Sahai, V., Jackson, G., Lalehrokh, F., et al. 2013. An Examination of Infill and Offset Drilling Patterns on Field Development for Shale Wells. Presented at the SPE Eastern Regional Meeting, Pittsburgh, Pennsylvania, 20-22 August. SPE-165722-MS. http://dx.doi.org/10.2118/165722-MS.

Sardinha, C.M., Petr, C., Lehmann, J., et al. 2014. Determining Interwell Connectivity and Reservoir Complexity Through Frac Pressure Hits and Production Interference Analysis. Presented at the SPE/CSUR Unconventional Resources Conference – Canada. Calgary, Alberta, Canada, 30 September-2 October. SPE-171628-MS. http://dx.doi.org/10.2118/171628-MS.

Schechter, R.S. 1992. Oil Well Stimulation. Englewood Cliffs, New Jersey: Prentice Hall.

Sesetty, V., and Ghassemi, A. 2012. Simulation of Hydraulic Fractures and their Interactions with Natural Fractures. Paper presented at 46th US Rock Mechanics / Geomechanics Symposium, Chicago, Illinois, 24-27 June.

Shin, D.H., and Sharma, M.M. 2014. Factors Controlling the Simultaneous Propagation of Multiple Competing Fractures in a Horizontal Well. Presented at the SPE Hydraulic Fracturing Technology Conference, The Woodlands, Texas, 4-6 February. SPE-168599-MS. http://dx.doi.org/10.2118/168599-MS.

Singh, V., Roussel, N.P., and Sharma, M.M. 2008. Stress Reorientation and Fracture Treatments in Horizontal Wells. Presented at the SPE Annual Technical Conference and Exhibition, Denver, Colorado, 21-24 September. SPE-116092-MS. http://dx.doi.org/10.2118/116092-MS.

Slone, A.K., Pericleous, K., Bailey, C., et al. 2002. Dynamic fluid–structure interaction using finite volume unstructured mesh procedures. *Comp. Struc*. **80** (5-6): 371–390. http://dx.doi.org/10.1016/S0045-7949(01)00177-8.

Sneddon, I.P. 1946. The Distribution of Stress in the Neighbourhood of a Crack in an Elastic Solid. *Proc. R. Soc. Lond. A* **187** (1009): 229–260. http://dx.doi.org/10.1098/rspa.1946.0077.

Sneddon, I.N., and Elliott, H.A. 1946. The Opening of a Griffith Crack Under Internal Pressure. *Quart. Appl. Math* **4** (3), 262-267.

Stegent, N.A., Wagner, A.L., Mullen, J., et al. 2010. Engineering a Successful Fracture-Stimulation Treatment in the Eagle Ford Shale. Presented at the Tight Gas Completions Conference, San Antonio, Texas, 2-3 November. SPE-136183-MS. http://dx.doi.org/10.2118/136183-MS.

Stylianou, V., and Ivankovic, A. 2002. Finite volume analysis of dynamic fracture phenomena – I. A node release methodology. *Int. J. Frac*. **113** (2): 107–123. http://dx.doi.org/10.1023/A:1015532129150.

Stylianou, V., and Ivankovic, A. 2002. Finite volume analysis of dynamic fracture phenomena – II. A cohesive zone type methodology. *Int. J. Frac*. **113** (2): 125–151. http://dx.doi.org/10.1023/A:1015563602317.

Su, K., Onaisi, A., and Garnier, A. 2014. A Comprehensive Methodology of Evaluation of the Fracability of a Shale Gas Play. Presented at the 2nd Unconventional Resources Technology Conference, Denver, Colorado, 25-27 August. http://dx.doi.org/10.15530/urtec-2014-1932416.

Systemes, D. n.d. ABAQUS FEA: <http://www.3ds.com/products-services/simulia/products/abaqus/> (accessed January 1, 2015).

Tang, T. 2013. Implementation of solid body stress analysis in OpenFOAM. CFD with OpenSource Software.

Tang, T., Hededal, O., and Cardiff, P. 2015. On finite volume method implementation of poro-elasto-plasticity soil model *Int. J. Numer. Anal. Meth. Geomech.* **39** (13): 1410-1430. http://dx.doi.org/10.1002/nag.2361.

Tsui, Y.-Y., Huang, Y.-C., Huang, C.-L., et al. 2013. A Finite-Volume-Based Approach for Dynamic Fluid-Structure Interaction. *Numer. Heat Transf. Part B Fundam.* **64** (4): 326–349. http://dx.doi.org/10.1080/10407790.2013.806691.

Tuković, Ž., Ivanković, A., and Karač, A.. 2013. Finite-volume stress analysis in multi-material linear elastic body. *Int. J. Num. Meth. Eng*. **93** (4): 400–419. http://dx.doi.org/10.1002/nme.4390.

Vermylen, J.P. and Zoback, M.D. 2011. Hydraulic Fracturing, Microseismic Magnitudes, and Stress Evolution in the Barnett Shale, Texas, USA. Presented at the SPE Hydraulic Fracturing Technology Conference and Exhibition, The Woodlands, Texas, 24-26 January. http://dx.doi.org/10.2118/140507-MS.

Walker Jr., R.N., Hunter, J.L., Brake, A.C. et al. 1998. Proppants, We Still Don't Need No Proppants - A Perspective of Several Operators. Presented at the SPE Annual Technical Conference and Exhibition, New Orleans, Louisiana, 27-30 September. http://dx.doi.org/10.2118/49106-MS.

Warpinski, N.R. 1990. Dual Leakoff Behavior in Hydraulic Fracturing of Tight, Lenticular Gas Sands. *SPE Prod. Eng*. **5** (03): 243–252. SPE-18259-PA. http://dx.doi.org/10.2118/18259-PA.

Warpinski, N.R. 1991. Hydraulic Fracturing in Tight, Fissured Media. *J. of Pet. Technol*. **43** (02): 146–209. SPE-20154-PA. http://dx.doi.org/10.2118/20154-PA.

Warpinski, N.R., and Branagan, P.T. 1989. Altered-Stress Fracturing. *J. of Pet. Technol*. **41** (09): 990–997. SPE-17533-PA. http://dx.doi.org/10.2118/17533-PA.

Warpinski, N.R., Branagan, P.T., Sattler, A.R., et al. 1990. Case Study of a Stimulation Experiment in a Fluvial, Tight-Sandstone Gas Reservoir. *SPE Prod. Eng*. **5** (04): 403–410. SPE-18258-PA. http://dx.doi.org/10.2118/18258-PA.

Warpinski, N.R., and Teufel, L.W. 1987. Influence of Geologic Discontinuities on Hydraulic Fracture Propagation (includes associated papers 17011 and 17074). *J of Pet Tech*. **39** (2): 209–220. SPE-13224-PA. http://dx.doi.org/10.2118/13224-PA.

Warpinski, N.R., Wright, T.B., Uhl, J.E. et al. 1996. Microseismic monitoring of the B-Sand Hydraulic Fracture Experiment at the DOE/GRI Multi-Site Project. Presented at the SPE Annual Technical Conference and Exhibition, Denver, Colorado, 6-9 October. http://dx.doi.org/10.2118/36450-MS.

Weijers, L., Wright, C., Mayerhofer, M. et al. 2005. Developing Calibrated Fracture Growth Models for Various Formations and Regions Across the United States. Presented at the SPE Annual Technical Conference and Exhibition, Dallas, Texas, 9-12 October. http://dx.doi.org/10.2118/96080-MS.

Weng, X., Kresse, O., Cohen, C.E., et al. 2011. Modeling of Hydraulic Fracture Network Propagation in a Naturally Fractured Formation. *SPE Prod. & Oper*. **26** (4): 368-380. SPE-140253-PA. http://dx.doi.org/10.2118/140253-PA.

Weng, X., Pandey, V. and Nolte, K.G. 2002. Equilibrium Test-A Method for Closure Pressure Determination. Presented at SPE/ISRM Rock Mechanics Conference, Irving, Texas, 20-23 October. SPE-78173-MS. http://dx.doi.org/10.2118/78173-MS.

Weng, X. and Siebrits, E. 2007. Effect of Production-Induced Stress Field on Refracture Propagation and Pressure Response. Paper SPE 106043 presented at the SPE Hydraulic Fracturing Technology Conference, College Station, Texas, 29-31 January. SPE-106043-MS. http://dx.doi.org/10.2118/106043-MS.

Wolhart, S.L., Harting, T.A., Dahlem, J.E. et al. 2006. Hydraulic Fracture Diagnostics used to Optimize Development in the Jonah Field. Presented at SPE Annual Technical Conference and Exhibition, San Antonio, Texas, 24-27 September. SPE-102528-MS. http://dx.doi.org/10.2118/102528-MS.

Wolhart, S.L., Odegard, C.E., Warpinski, N.R. et al. 2005. Microseismic Fracture Mapping Optimizes Development of Low-Permeability Sands of the Williams Fork Formation in the Piceance Basin. Presented at the SPE Annual Technical Conference and Exhibition, Dallas, Texas, 9-12 October. SPE-95637-MS. http://dx.doi.org/10.2118/95637-MS.

Wong, S.-W., Geilikman, M., and Xu, G. 2013. Interaction of Multiple Hydraulic Fractures in Horizontal Wells. Presented at the SPE Unconventional Gas Conference and Exhibition. SPE-163982-MS. http://dx.doi.org/10.2118/163982-MS.

Wu, K., and Olson, J. 2013. Investigation of the Impact of Fracture Spacing and Fluid Properties for Interfering Simultaneously or Sequentially Generated Hydraulic

Fractures. *SPE Prod. & Oper*. **28** (4): 4–6. SPE-163821-PA. http://dx.doi.org/10.2118/163821-PA.

Wu, K., and Olson, J.E. 2015. Simultaneous Multifracture Treatments: Fully Coupled Fluid Flow and Fracture Mechanics for Horizontal Wells. *SPE J*. **20** (02): 337–346. SPE-167626-PA. http://dx.doi.org/10.2118/167626-PA.

Wu, H., and Pollard, D. 2002. Imaging 3-D fracture networks around boreholes. *AAPG Bull.* **86** (4): 593–604. http://dx.doi.org/10.1306/61EEDB52-173E-11D7-8645000102C1865D.

Xu, W., Thiercelin, M., Ganguly, U. et al. 2010. Wiremesh: A Novel Shale Fracturing Simulator. Presented at CPS/SPE International Oil and Gas Conference and Exhibition, Beijing, China, 8-10 June. SPE-132218-MS. http://dx.doi.org/10.2118/132218-MS.

Yamamoto, K., T. Shimamoto, and S. Sukemura. 2004. Multiple Fracture Propagation Model for a Three-Dimensional Hydraulic Fracturing Simulator. *Int. J. Geomech.* **4** (1): 46–57. http://dx.doi.org/10.1061/(ASCE)1532-3641(2004)4:1(46).

Yi, S., and M. M. Sharma. 2015. A Methodology for Designing Fluid Diversion in Refracturing Operations in Horizontal Wells. (*in press*)

Zhai, Z. and Sharma, M.M. 2007. Estimating Fracture Reorientation because of Long Term Fluid Injection / Production. Presented at Production and Operations Symposium, Oklahoma City, Oklahoma, 31 March-3 April. SPE-106387-MS. http://dx.doi.org/10.2118/106387-MS.

Zienkiewicz, O. C., and J. Z. Zhu. 1992. The superconvergent patch recovery (SPR) and adaptive finite element refinement. *Comp. Methods App. Mech. Eng*. **101** (1-3): 207–224. http://dx.doi.org/10.1016/0045-7825(92)90023-D.

Zoback, M.D. 2007. Reservoir Geomechanics. Cambridge: University Press.

Vita

Ripudaman Manchanda enrolled in the graduate program in the Department of Petroleum and Geosystems Engineering at The University of Texas at Austin in 2012 to pursue a Ph.D. in Petroleum Engineering. Manchanda holds a B.Tech degree in chemical engineering from Indian Institute of Technology Guwahati, Assam, India, and a M.S.E. degree in petroleum engineering from The University of Texas at Austin.

Permanent email: ripu.manchanda@gmail.com

This dissertation was typed by the author.